

THE MINISTRY OF SCIENCE AND HIGHER EDUCATION OF THE RUSSIAN FEDERATION



ST. PETERSBURG STATE  
POLYTECHNICAL UNIVERSITY  
**JOURNAL**

---

Physics  
and Mathematics

---

**VOLUME 13, No.2,  
2020**

Peter the Great St. Petersburg  
Polytechnic University  
2020

# ST. PETERSBURG STATE POLYTECHNICAL UNIVERSITY JOURNAL. PHYSICS AND MATHEMATICS

## JOURNAL EDITORIAL COUNCIL

*A.I. Borovkov*, vice-rector for perspective projects;  
*V.A. Glukhikh*, full member of RAS;  
*D.A. Indeitsev*, corresponding member of RAS;  
*A.I. Rudskoy*, full member of RAS, deputy head of the editorial council;  
*R.A. Suris*, full member of RAS;  
*D.A. Varshalovich*, full member of RAS;  
*A.E. Zhukov*, corresponding member of RAS.

## JOURNAL EDITORIAL BOARD

*V.K. Ivanov* – Dr. Sci. (phys.-math.), prof., SPbPU, St. Petersburg, Russia, – editor-in-chief;  
*A.E. Fotiadi* – Dr. Sci. (phys.-math.), prof., SPbPU, St. Petersburg, Russia, – deputy editor-in-chief;  
*V.M. Kapralova* – Candidate of Phys.-Math. Sci., associate prof., SPbPU, St. Petersburg, Russia, – executive secretary;  
*V.I. Antonov* – Dr. Sci. (phys.-math.), prof., SPbPU, St. Petersburg, Russia;  
*I.B. Bezprozvanny* – Dr. Sci. (biology), prof., The University of Texas Southwestern Medical Center, Dallas, TX, USA;  
*A.V. Blinov* – Dr. Sci. (phys.-math.), prof., SPbPU, St. Petersburg, Russia;  
*A.S. Cherepanov* – Dr. Sci. (phys.-math.), prof., SPbPU, St. Petersburg, Russia;  
*D.V. Donetski* – Dr. Sci. (phys.-math.), prof., State University of New York at Stony Brook, NY, USA;  
*D.A. Firsov* – Dr. Sci. (phys.-math.), prof., SPbPU, St. Petersburg, Russia;  
*A.S. Kheifets* – Ph.D., prof., Australian National University, Canberra, Australia;  
*O.S. Loboda* – Candidate of Phys.-Math. Sci., associate prof., SPbPU, St. Petersburg, Russia;  
*J.B. Malherbe* – Dr. Sci. (physics), prof., University of Pretoria, Republic of South Africa;  
*V.M. Ostryakov* – Dr. Sci. (phys.-math.), prof., SPbPU, St. Petersburg, Russia;  
*V.E. Privalov* – Dr. Sci. (phys.-math.), prof., SPbPU, St. Petersburg, Russia;  
*E.M. Smirnov* – Dr. Sci. (phys.-math.), prof., SPbPU, St. Petersburg, Russia;  
*A.V. Solov'yov* – Dr. Sci. (phys.-math.), prof., MBN Research Center, Frankfurt am Main, Germany;  
*A.K. Tagantsev* – Dr. Sci. (phys.-math.), prof., Swiss Federal Institute of Technology, Lausanne, Switzerland;  
*I.N. Toptygin* – Dr. Sci. (phys.-math.), prof., SPbPU, St. Petersburg, Russia;  
*E.A. Tropp* – Dr. Sci. (phys.-math.), prof., SPbPU, St. Petersburg, Russia.

The journal is included in the List of leading peer-reviewed scientific journals and other editions to publish major findings of theses for the research degrees of Doctor of Sciences and Candidate of Sciences.

The publications are presented in the VINITI RAS Abstract Journal and Ulrich's Periodical Directory International Database.

The journal is published since 2008 as part of the periodical edition 'Nauchno-tekhnicheskie vedomosti SPb-GPU'.

The journal is registered with the Federal Service for Supervision in the Sphere of Telecom, Information Technologies and Mass Communications (ROSKOMNADZOR). Certificate ПИ № ФС77-52144 issued December 11, 2012.

The journal is distributed through the CIS countries catalogue, the «Press of Russia» joint catalogue and the «Press by subscription» Internet catalogue. The subscription index is **71823**.

The journal is in the **Web of Science** (Emerging Sources Citation Index) and the **Russian Science Citation Index** (RSCI) databases.

© Scientific Electronic Library (<http://www.elibrary.ru>).

No part of this publication may be reproduced without clear reference to the source.

The views of the authors may not represent the views of the Editorial Board.

Address: 195251 Politeknicheskaya St. 29, St. Petersburg, Russia.

Phone: (812) 294-22-85.

<http://ntv.spbstu.ru/physics>

© Peter the Great St. Petersburg Polytechnic University, 2020

# Contents

## Condensed matter physics

<b>Gorokhovatsky Yu.A., Demidova N.S., Temnov D.E.</b> <i>Electric charge relaxation in the polyethylene with mineral inclusions of diatomite.....</i>	5
<b>Tregulov V.V.</b> <i>The efficiency of solar energy conversion by the CdS/por-Si/p-Si heterostructure: the dopant effect.....</i>	12

## Simulation of physical processes

<b>Levchenya A.M., Trunova S.N., Kolesnik E.V.</b> <i>Assessment of RANS turbulence models capabilities based on computational results for free convection developing near a suddenly heated vertical plate.....</i>	21
--	----

## Mathematical physics

<b>Petrichenko M.R., Musorina T.A.</b> <i>Fractional differentiation operation in the Fourier boundary problems....</i>	33
<b>Berdnikov A.S., Solovyev K.V., Krasnova N.K.</b> <i>Chains of fundamental mutually homogeneous functions with a common real eigenvalue.....</i>	44
<b>Berdnikov A.S., Solovyev K.V., Krasnova N.K.</b> <i>General formulas for chains of fundamental mutually homogeneous functions with a common pair of complex conjugate eigenvalues.....</i>	60

## Experimental technique and devices

<b>Maisheev V.A., Sandomirskiy Yu.E., Chesnokov M.Yu., Chesnokov Yu.A., Yanovich A.A.</b> <i>Devices for steering particle beams in the accelerators based on crystals curved by scratching the grooves on the surface.....</i>	75
---	----

## Physical electronics

<b>Tsybin O.Yu., Makarov S.B., Dyubo D.B., Kuleshov Yu.V., Goncharov P.S., Martynov V.V., Shunovich N.A.</b> <i>An electrically powered ion accelerator with contact ionization for perspective electrically powered thrusters.....</i>	84
---	----

## Physical optics

<b>Koreshev S.N., Smorodinov D.S., Frolova M.A., Starovoitov S.O.</b> <i>Imaging properties of computer-generated holograms: phase distribution effect in the objects' space.....</i>	99
---	----

## Radiophysics

<b>Kostromitin A.O., Liokumovich L.B., Skliarov P.V., Kotov O.I.</b> <i>The fiber-optic interferometric schemes with multiplexed sensitive elements: an analysis of output optical power level.....</i>	108
---	-----

## Nuclear Physics

- Borisov V.S., Berdnikov Ya.A., Berdnikov A.Ya., Kotov D.O., Mitrankov I.M.** *Production of  $K^*$ -mesons in the copper-gold nuclei collisions at  $\sqrt{s_{NN}} = 200$  GeV.....* 121
- Larionova M.M., Berdnikov Ya.A., Berdnikov A.Ya., Mitrankov I.M., Kotov D.O.** *Measurement of  $\phi$ -meson's nuclear modification factors in the collisions of proton beams with aluminum nuclei at an energy of 200 GeV.....* 130

## Mechanics

- Frolova K.P.** *Determination of the effective Young's modulus of medium with microstructure typical for hydrogen degradation.....* 137

DOI: 10.18721/JPM.13201

UDC: 538.9

## **ELECTRIC CHARGE RELAXATION IN THE POLYETHYLENE WITH MINERAL INCLUSIONS OF DIATOMITE**

*Yu.A. Gorokhovatsky, N.S. Demidova, D.E. Temnov*

Herzen State Pedagogical University of Russia, St. Petersburg, Russian Federation

The paper considers methods for increasing stability of polyethylene's electret state by adding diatomite particles to its composition. The results of analyzing the IR spectra, the involved materials' temporal and temperature stability are presented. Mechanisms for improving the stability of the composite polyethylene's electret state are discussed.

**Keywords:** electret state, polyethylene, diatomite, thermoactivation spectroscopy

**Citation:** Gorokhovatsky Yu.A., Demidova N.S., Temnov, D.E. Electric charge relaxation in the polyethylene with mineral inclusions of diatomite, St. Petersburg Polytechnical State University Journal. Physics and Mathematics. 13 (2) (2020) 5–11. DOI: 10.18721/JPM.13201

This is an open access article under the cc by-nc 4.0 license (<https://creativecommons.org/licenses/by-nc/4.0/>)

## **РЕЛАКСАЦИЯ ЭЛЕКТРИЧЕСКОГО ЗАРЯДА В ПОЛИЭТИЛЕНЕ С МИНЕРАЛЬНЫМИ ВКЛЮЧЕНИЯМИ ДИАТОМИТА**

*Ю.А. Гороховатский, Н.С. Демидова, Д.Э. Темнов*

Российский государственный педагогический университет им. А.И. Герцена,  
Санкт-Петербург, Российская Федерация

В работе рассматриваются методы повышения стабильности электретного состояния полиэтилена путем добавления в его состав частиц диатомита. Приводятся результаты исследования ИК-спектров, временной и температурной стабильности исследуемых материалов. Обсуждаются механизмы улучшения стабильности электретного состояния композитного полиэтилена.

**Ключевые слова:** электретное состояние, полиэтилен, диатомит, термостимулированная спектроскопия

**Ссылка при цитировании:** Гороховатский Ю.А., Демидова Н.С., Темнов Д.Э. Релаксация электрического заряда в полиэтилене с минеральными включениями диатомита // Научно-технические ведомости СПбГПУ. Физико-математические науки. 2020. Т. 13. №2. С. 9–16. DOI: 10.18721/JPM.13201

Статья открытого доступа, распространяемая по лицензии CC BY-NC 4.0 (<https://creativecommons.org/licenses/by-nc/4.0/>)

### Introduction

Polyethylene is one of the most widely used polymeric materials. At the moment, the polyethylene's electret properties are studied to create the active packages. One of the ways to increase the electret state stability is the creation of the composite material [1, 2]. Studies performed in Ref. [3] showed that adding aerosil in polyethylene leads to a significant improvement in the electret state stability of the obtained composite material. Aerosil is a very pure amorphous non-porous silicon dioxide with a particle size of 5 to 40 nm. Diatomite is another modification of silica. Diatomite is a more promising material for creating composites based on polyethylene because of its low cost.

In the work, the electret stability of composite polyethylene with diatomite has been compared with pure polyethylene films' stability using various methods.

We used such methods as thermostimulated potential relaxation, isothermal potential relaxation, depolarization with registration of short-circuit currents of a pre-charged dielectric and IR spectroscopy. The film thickness was about 1 mm.

### Experimental technique

Samples were made by rolling and subsequent pressing. The Kazan National Research Technological University equipment was used. High pressure polyethylene, the brand 15313-003, GOST 7699-78 was used for creating the composite material. Mixing of the starting polyethylene with the filler was carried out in a mixing chamber. The mixing chamber consisted of 2 half cylinders containing horizontally rotating rolls. For the better distribution of filler particles, the rolls rotated in the opposite directions and had different rotation speeds. The temperature in the mixing chamber was 420–430 K.

The films were created using the pressing method in accordance with GOST 12019-66. The mold was a frame between two polished plates. Lavsan film was used to prevent the pressed sample's adhesion to the mold plates. The mold with the composite material was placed between the cooling plates, which, in turn, were placed between the heated plates. After the sample heating, the press plates were closed to create the necessary pressure and withstood the necessary time. After that, the samples were cooled by water, then the pressure was removed from the plates, the press was opened and the samples were removed.

Diatomite distribution was monitored using a Nikon Eclipse LV150 optical microscope. IR spectra were obtained by means of a FSM 1202 Fourier spectrometer. When studying the electret state stability by the isothermal and thermally stimulated potential relaxation methods, the films were polarized in a corona discharge at 5 kV.

Electrically active defects' activation energy was calculated using the Tikhonov regulatory algorithms.

### Experimental results and discussion

Our study of the composite materials without treatment did not show a significant effect of diatomite on their electret properties. Earlier it had been shown that the main mechanism of deterioration the polyethylene's electret properties was the presence of water molecules in it [4 – 7]. Diatomite, being a natural mineral, also contains water, which can impair the composite's electret properties. To reduce the amount of physically absorbed water in the composite structure, before studying the properties, samples were annealed in a muffle furnace for 1 h at a temperature  $T = 400$  K.

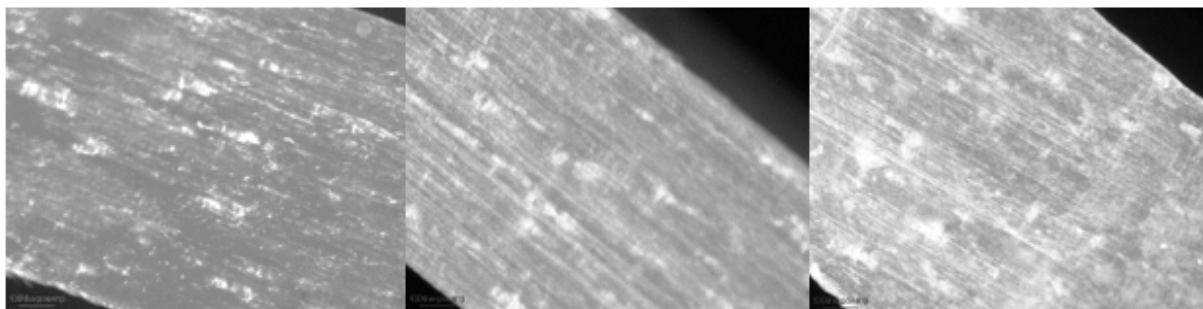


Fig. 1. Optical images of slices of the polyethylene films including diatomite; a filler content (% vol.) is 2 (left), 4 (in the center) and 6 (right)



Fig. 2. IR transmission spectra of LDPE (1) and of the composite of LDPE + 6 % diatomite (2).  
The presence of water is highlighted

The addition of diatomite to polyethylene leads to its gray color, so that the distribution of the filler in the polyethylene film can be controlled optically.

Fig. 1 shows the optical images of polyethylene film's slices with a diatomite concentration of 2, 4, and 6 % vol. Analysis of the filler distribution showed a uniform pattern of diatomite in the polyethylene film.

The optical spectroscopy method is highly effective in studying the physical and physicochemical properties of water-containing polymer objects [8 – 10]. Fig. 2 shows the infrared (IR) transmission spectra of the initial *low density polyethylene* (LDPE) and composite polyethylene with 6 % diatomite. Absorption bands in the region of 1500–1650  $\text{cm}^{-1}$  are associated with the presence of water dissolved in the polymer. These

spectra show the presence of water in the initial LDPE film and its substantial decrease with the addition of diatomite (see Fig. 2).

In order to study directly the electret state stability in the composite polyethylene, the films were investigated by the isothermal potential relaxation method at a temperature of 343 K. The films were polarized in a corona discharge at 5 kV for 360 s. The polarization temperature was 360 K.

Fig. 3 shows the time dependence of the electric potential relaxation for films of pure polyethylene and polyethylene with the different diatomite content. The graphs show a significant increase in the stability of polyethylene films when diatomite is introduced into their composition.

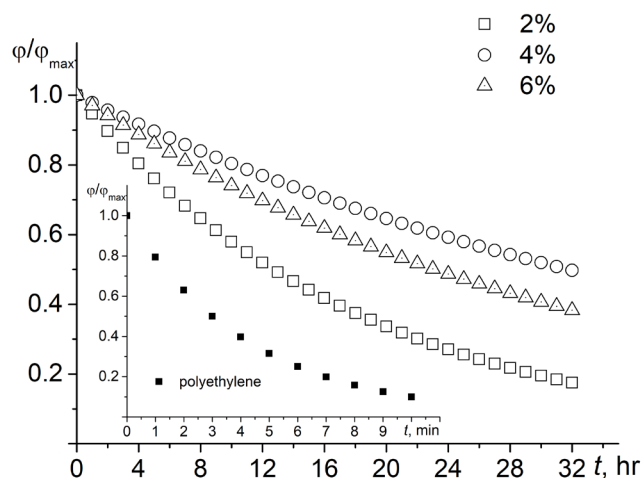


Fig. 3. The time dependences of the surface potential relaxation for pure polyethylene film (in the inset) and composite polyethylene with the different diatomite content



The diatomite adding into the polyethylene films leads to the stability increasing that it is obvious from the spectra obtained by thermostimulated potential relaxation method (Fig. 4). The thermally stimulated potential relaxation spectra were obtained both for the unannealed and annealed films of the polyethylene with 4 % diatomite; these curves are compared in Fig. 4. The graphs show a significant improvement of the composite polyethylene film's electret state stability after annealing. Thus, nonannealed films of composite polyethylene with diatomite did not exhibit high electret stability.

The electrically active defects' activation energy is one of the main characteristics of the relaxation process of electric charge decay [11]. To calculate this parameter, the study of pure and composite polyethylene was carried out by the method of thermally stimulated depolarization (TSD). A TSC-II setup by Setaram (France) was used for measurements. Sensitive electrometer Keithley 6517 is the main measuring device of the setup. The thermostimulated currents were measured in the temperature range between 290 and 380 K at the fixed heating rate. The heating rate was from  $5 \cdot 10^{-2}$  to  $1,5 \cdot 10^{-1}$  K/s. The samples

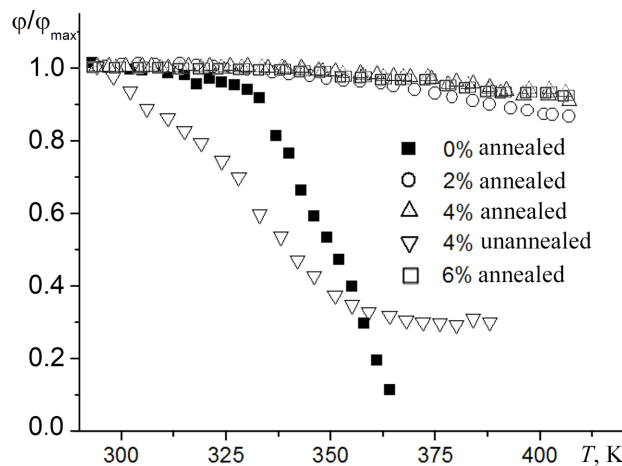


Fig. 4. The temperature dependences of the surface potential relaxation for the pure annealed polyethylene films and the composite polyethylene (unannealed and annealed) with the different diatomite content

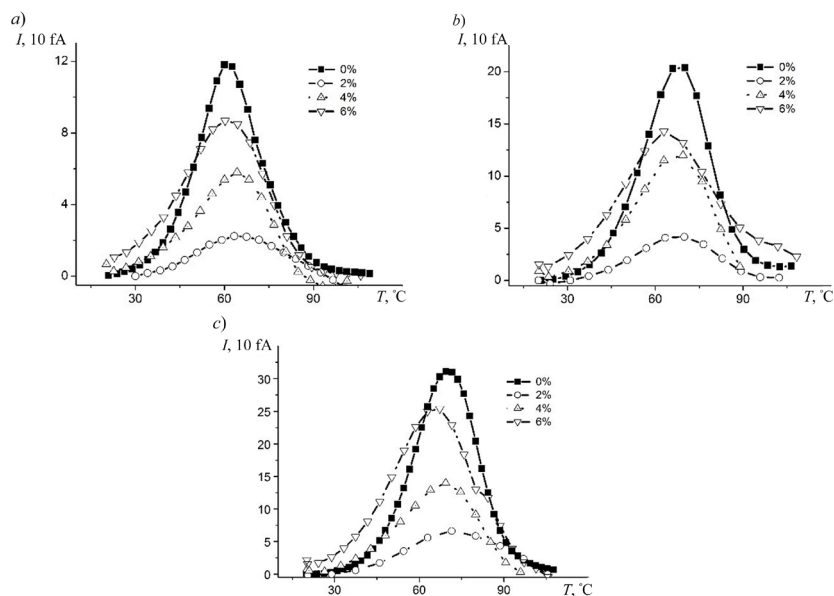


Fig. 5. Thermally stimulated depolarization spectra of the pure polyethylene films and of the composite polyethylene ones with diatomite. The heating rates (K/s) were  $5 \cdot 10^{-2}$  (a),  $1,0 \cdot 10^{-1}$  (b) and  $1,5 \cdot 10^{-1}$  (c). For pure polyethylene films, the current value was reduced by 10 times





were polarized in the electric field  $E = 500$  V/mm at a polarization temperature  $T_p = 343$  K, during a polarization time of 300 s. After the electric field exposure for 300 s, the samples were cooled in the applied field with a rate of  $3,3 \cdot 10^{-2}$  K/s up to 293 K. The thermostimulated currents' spectra are shown in Fig. 5.

TSD data were processed using Tikhonov's regularizing algorithms. Fig. 6 shows the reconstructed distribution functions of the electrically active defects. It can be seen from the graphs that the maxima shift towards the higher energy and the distribution broadens with increasing the diatomite concentration. Table shows the values of the electrically active defects' activation energy for all the compositions. The activation energy value obtained in this work for electrically active defects for polyethylene without filler is in good agreement with the results of our previous studies [12].

### Summary

Our study showed that the creation of composite polyethylene based on diatomite could increase the electret stability of LDPE. The adding diatomite to polyethylene leads to increasing the charge traps' activation energy, at least up to a concentration of 6 vol%. Diatomite can be used for creating composite polyethylene to increase its electret stability in order to create active packages. It is important to continue further studies of the electret stability of polyethylene composite films with a higher concentration of diatomite and to study other fillers containing silicon dioxide.

The research was supported by the Russian Foundation for Basic Research (Grant No. 19-32-90271) and the Ministry of Science and Higher Education of the Russian Federation (Project No. FSZN-2020-0026).

Table  
The values of the electrically active defects' activation energy  
for pure and composite LDPE films

Diatomite concentration, % vol.	Activation energy, eV
0	$1.1 \pm 0.1$
2	$1.4 \pm 0.1$
4	$2.2 \pm 0.2$
6	$2.6 \pm 0.3$

Footnote. Tikhonov's regularizing algorithms were used.

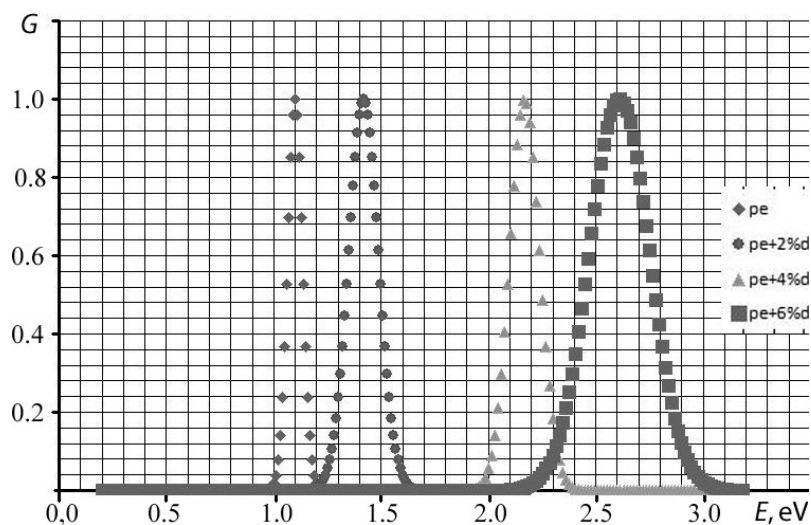


Fig. 6. The energy distribution functions of electrically active defects in the pure polyethylene (pe) and the composite one with the different diatomic (d) content (% vol.)

## REFERENCES

1. Goldade V.A., Electret composite materials based on polymers: Main properties and new fields of application, *Mechanics of Composite Materials*. 34 (2) (1998) 107–114.
2. Gorokhovatsky Yu., Temnov D., Electret state in composite polymer materials based on low density polyethylene and polypropylene, *Applied Mechanics and Materials*. 752–753 (April) (2015) 225–231.
3. Temnov D., Fomicheva E., Tazenzov B., et al., Electrets properties of polyethylene films with starch and aerosol, *Journal of Materials Science and Engineering A*. 3 (7) (2013) 494–498.
4. Bordovsky G.A., Gorokhovatsky Y.A., Temnov D.E., Electret properties of polyethylene films with nano-dimension inclusions of SiO<sub>2</sub>, *Scientific Papers of the Institute of Electrical Engineering Fundamentals of Wrocław Technical University Conferences*. (2007) 194–197.
5. Guzhova A.A., Galikhanov M.F., Gorokhovatsky Y., et al., Improvement of polylactic acid electret properties by addition of fine barium titanate, *Journal of Electrostatics*. 79 (February) (2016) 1–6.
6. Kreuer K.D., On the development of proton conducting polymer membranes for hydrogen and methanol fuel cells, *Journal of Membrane Science*. 185 (1) (2001) 29–39.
7. Shim W.S., Lee Y.H., Yeo I.H., et al., Polypyrrole/thermally sensitive polyelectrolyte composite, *Synthetic Metals*. 104 (2) (1999) 119–127.
8. Okumura S., Nakashima S., Water diffusivity in rhyolitic glasses as determined by in situ IR spectroscopy, *Physics and Chemistry of Minerals*. 31 (3) (2004) 183–189.
9. Kitano H., Nagaoka K., Tada S., et al., Structure of water incorporated in amphoteric polymer thin films as revealed by FT-IR spectroscopy, *Macromolecular Bioscience*. 8 (1) (2008) 77–85.
10. Karulina E.A., Temnov D.E., Chistyakova O.V., Demidova N.S., The study of the sorbed water content in composite polymers by Fourier spectroscopy, “Physics of Dielectrics (Dielectrics-2017)”, *Proceedings of the 14-th International Conference* (2017) 35–37.
11. Sessler G.M. (Ed.), *Electrets (Topics in Applied Physics, Vol. 33)*, Second Ed., Springer-Verlag, Berlin, Heidelberg, 1987.
12. Gorokhovatsky Yu., Temnov D., Thermostimulated relaxation of surface potential and thermostimulated discharge currents in dielectrics, *Izvestia of Herzen State Pedagogical University*. (8(38)) (2007) 24–34.

*Received 04.05.2020, accepted 15.05.2020.*

## THE AUTHORS

### **GOROKHOVATSKY Yuriy A.**

*Herzen State Pedagogical University of Russia*  
48 Moyka Emb., St. Petersburg, 191186, Russian Federation  
gorokh-yu@yandex.ru

### **DEMIDOVA Natalya S.**

*Herzen State Pedagogical University of Russia*  
48 Moyka Emb., St. Petersburg, 191186, Russian Federation  
demidov\_evg@mail.ru

### **TEMNOV Dmitry E.**

*Herzen State Pedagogical University of Russia*  
48 Moyka Emb., St. Petersburg, 191186, Russian Federation  
tde@herzen.spb.ru

## СПИСОК ЛИТЕРАТУРЫ

1. Гольдаде В.А. Электретные композитные материалы на основе полимеров: основные свойства и новые области применения. // *Механика композитных материалов*. 1998. Т. 34. № 2. С. 153–162.
2. Gorokhovatsky Yu., Temnov D. Electret state in composite polymer materials based on low density polyethylene and polypropylene // *Applied Mechanics and Materials*. 2015. Vols. 752–753. April. Pp. 225–231.



3. **Temnov D., Fomicheva E., Tazekov B., Karulina E., Gorokhovatsky Yu.** Electrets properties of polyethylene films with starch and aerosil // *Journal of Materials Science and Engineering A*. 2013. Vol. 3. No. 7. C. 494–498.
4. **Bordovsky G.A., Gorokhovatsky Y.A., Temnov D.E.** Electret properties of polyethylene films with nano-dimension inclusions of  $\text{SiO}_2$  // *Scientific Papers of the Institute of Electrical Engineering Fundamentals of Wroclaw Technical University Conferences*. 2007. Pp. 194–197.
5. **Guzhova A.A., Galikhanov M.F., Gorokhovatsky Y., Temnov D.E., Fomicheva E.E., Karulina E.A., Yovcheva T.A.** Improvement of polylactic acid electret properties by addition of fine barium titanate // *Journal of Electrostatics*. 2016. Vol. 79. February. Pp. 1–6.
6. **Kreuer K.D.** On the development of proton conducting polymer membranes for hydrogen and methanol fuel cells // *Journal of Membrane Science*. 2001. Vol. 185. No. 1. Pp. 29–39.
7. **Shim W.S., Lee Y.H., Yeo I.H., Lee J.Y., Lee D.S.** Polypyrrole/thermally sensitive polyelectrolyte composite // *Synthetic Metals*. 1999. Vol. 104. No. 2. Pp. 119–127.
8. **Okumura S., Nakashima S.** Water diffusivity in rhyolitic glasses as determined by in situ IR spectroscopy // *Physics and Chemistry of Minerals*. 2004. Vol. 31. No. 3. Pp. 183–189.
9. **Kitano H., Nagaoka K., Tada S., Gemei-Ide M., Tanaka M.** Structure of water incorporated in amphoteric polymer thin films as revealed by FT-IR spectroscopy // *Macromolecular Bioscience*. 2008. Vol. 8. No. 1. Pp. 77–85.
10. **Карулина Е.А., Темнов Д.Ф., Чистякова О.В., Демидова Н.С.** Исследование содержания сорбированной воды в композитных полимерах методом Фурье-спектроскопии // «Физика диэлектриков (Диэлектрики 2017-)». Материалы XIV Международной конференции. СПб., 29 мая – 2 июня 2017 г. Т. 1. СПб.: Изд-во РГПУ им. А.И. Герцена, 2017. С. 35–37.
11. **Сесслер Г.** Электреты. М.: Мир, 1983. 487 с.
12. **Гороховатский Ю.А., Темнов Д.Э.** Термостимулированная релаксация поверхностного потенциала и термостимулированные токи короткого замыкания в предварительно заряженном диэлектрике // *Известия РГПУ им. А.И. Герцена. Естественные и точные науки*. 2007. № 8 (38). С. 24–34.

*Статья поступила в редакцию 04.05.2020, принята к публикации 15.05.2020.*

## СВЕДЕНИЯ ОБ АВТОРАХ

**ГОРОХОВАТСКИЙ Юрий Андреевич** — доктор физико-математических наук, заведующий кафедрой общей и экспериментальной физики Российского государственного педагогического университета им. А.И. Герцена, Санкт-Петербург, Российская Федерация.

191186, Российская Федерация, г. Санкт-Петербург, наб. р. Мойки, 48  
gorokh-yu@yandex.ru

**ДЕМИДОВА Наталья Сергеевна** — аспирантка кафедры общей и экспериментальной физики Российского государственного педагогического университета им. А.И. Герцена, Санкт-Петербург, Российская Федерация.

191186, Российская Федерация, г. Санкт-Петербург, наб. р. Мойки, 48  
demidov\_evg@mail.ru

**ТЕМНОВ Дмитрий Эдуардович** — кандидат физико-математических наук, доцент кафедры общей и экспериментальной физики Российского государственного педагогического университета им. А.И. Герцена, Санкт-Петербург, Российская Федерация.

191186, Российская Федерация, г. Санкт-Петербург, наб. р. Мойки, 48  
tde@herzen.spb.ru

DOI: 10.18721/JPM.13202

UDC 538.91

## THE EFFICIENCY OF SOLAR ENERGY CONVERSION BY THE CDS/*POR-SI*/*P-SI* HETEROSTRUCTURE: THE DOPANT EFFECT

V.V. Tregulov

Ryazan State University named for S. Yesenin,

Ryazan, Russian Federation

In this paper, the effect of the distribution profile of the doping acceptor impurity concentration in the base region of the CdS/*por-Si*/*p-Si* heterostructure on the efficiency of solar energy conversion parameters has been studied. It was established that the solar energy conversion efficiency depended on the degree of a doping acceptor impurity depletion of the near-surface *p-Si* layer in the *por-Si*/*p-Si* heterojunction. The distribution profile of the impurity concentration in this space is formed during the growth of a porous silicon layer. This profile is controlled through changing the technological parameters of the process of a porous film growing: the current density and the duration time of the electrochemical etching. A gain in the conversion efficiency of solar energy was explained by an increase in the penetration depth of the electric field into the base region due to formation of a certain type of the impurity concentration distribution profile. In the final, this profile promotes the rapid carry-away of charge carriers generated by the light from the base region. This carry-away occurs before the carrier recombination moment involving traps.

**Keywords:** porous silicon, heterojunction, photovoltaic converter, solar cell, capacitance–voltage characteristic

**Citation:** Tregulov V.V. The efficiency of solar energy conversion by the CdS/*por-Si*/*p-Si* heterostructure: the dopant effect, St. Petersburg Polytechnical State University Journal. Physics and Mathematics. 13 (2) (2020) 12–20. DOI: 10.18721/JPM.13202

This is an open access article under the cc by-nc 4.0 license (<https://creativecommons.org/licenses/by-nc/4.0/>)

## ВЛИЯНИЕ ЛЕГИРУЮЩЕЙ ПРИМЕСИ НА ЭФФЕКТИВНОСТЬ ПРЕОБРАЗОВАНИЯ СОЛНЕЧНОЙ ЭНЕРГИИ ГЕТЕРОСТРУКТУРОЙ CDS/*POR-SI*/*P-SI*

В.В. Трегулов

Рязанский государственный университет имени С.А. Есенина,

г. Рязань, Российская Федерация

В работе исследуется влияние профиля распределения концентрации легирующей акцепторной примеси в базовой области гетероструктуры CdS/*por-Si*/*p-Si* на параметры, характеризующие эффективность преобразования солнечной энергии. Установлено, что указанная эффективность зависит от степени обеднения легирующей акцепторной примесью приповерхностного слоя дырочного кремния (*p-Si*), входящего в структуру гетероперехода *por-Si*/*p-Si*. Профиль распределения концентрации примеси в данной области формируется в ходе роста слоя пористого кремния. Управление характером профиля распределения осуществляется через изменение технологических параметров процесса роста пористой пленки: плотностью тока и длительностью электрохимического травления. Повышение эффективности преобразования солнечной энергии объясняется увеличением глубины проникновения электрического поля внутрь базовой области за счет формирования определенного вида профиля распределения концентрации примеси. В конечном итоге вид профиля способствует быстрому выносу из базовой области носителей заряда, генерируемых светом; вынос происходит до момента рекомбинации носителей при участии ловушек.



**Ключевые слова:** пористый кремний, гетеропереход, фотовольтаический преобразователь, солнечный элемент, вольт-фарадная характеристика

**Ссылка при цитировании:** Трегулов В.В. Влияние легирующей примеси на эффективность преобразования солнечной энергии гетероструктурой CdS/*por*-Si/*p*-Si // Научно-технические ведомости СПбГПУ. Физико-математические науки. 2020. Т. 2 № .13. С. 17–26. DOI: 10.18721/JPM.13202

Статья открытого доступа, распространяемая по лицензии CC BY-NC 4.0 (<https://creativecommons.org/licenses/by-nc/4.0/>)

## Introduction

Currently quite a lot of interest is being shown in the study of the solar photovoltaic converter based on the CdS/*por*-Si/*p*-Si heterostructure [1, 2]. The CdS film plays the role of an optical window and significantly expands the spectral sensitivity region of the photovoltaic converter [3, 4]. The *por*-Si layer is a buffer that reduces the mechanical stresses arising between the silicon substrate and the CdS film due to the difference in the lattice constants (about 7 %) [4, 5]. In addition, the *por*-Si film reduces the reflectivity of the front surface of the CdS/*por*-Si/*p*-Si photovoltaic converter [4]. An important advantage of the CdS/*por*-Si/*p*-Si heterostructure is the absence of the need to form a *p* – *n* junction by diffusion in *p*-Si. This will reduce the complexity of the manufacturing process of the photovoltaic cells and its cost, which is important in mass production. Thus the CdS/*por*-Si/*p*-Si heterostructure is relevant for use in solar energy.

In this regard the urgent task is to develop solutions aimed at increasing the efficiency of the CdS/*por*-Si/*p*-Si heterostructure as a solar energy converter.

One way to solve this problem is to increase the collection efficiency of charge carriers generated by light in the absorbing region of the photovoltaic converter. It is well known that the separation of photogenerated charge carriers occurs under the influence of an electric field concentrated in the space charge region (SCR) of the photovoltaic converter barrier layer (in our case, a heterojunction). Due to the strong electric field the carriers are removed from the SCR before they have time to recombine through the participation of traps [6]. Thus, to increase the efficiency of carrier separation, it is advisable to create conditions for expanding the region located inside the absorbing layer in which the strongest electric field is concentrated. For this purpose, it is desirable to set up a concentration gradient of the dopant in the surface region of the absorbing layer of the photovoltaic converter [6, 7]. According to Ref. [6] these methods

lead to an increase in the efficiency of solar energy conversion due to an increase in open circuit voltage and short circuit current.

The experimental samples studied in this work are similar to the CdS/*por*-Si/*p*-Si heterostructure investigated in Ref. [8] where it was shown the largest contribution to the photocurrent to make by charge carriers absorbed in *p*-Si. In addition, the SCR of the studied heterostructure was almost completely concentrated in the surface region of the *p*-Si heterojunction of the *por*-Si/*p*-Si. Thus, the base region of the CdS/*por*-Si/*p*-Si heterostructure is located in the near-surface *p*-Si layer close to the *por*-Si/*p*-Si heterojunction. The charge carriers generated by light are separated by the electric field of the *por*-Si/*p*-Si heterojunction [8].

The high-frequency capacitance – voltage (*C* – *V*) characteristics of *por*-Si/*p*-Si structures were studied, and in this case the *por*-Si film was formed by anodic electrochemical etching at various values of the etching duration  $t_{et}$  and the anode current density  $J_{et}$  [9, 10]. It was found that with an increase in  $J_{et}$  and  $t_{et}$  in silicon, a depleted dopant region was formed near the *por*-Si/Si heterojunction.

In this paper, the influence of the distribution profile of the acceptor dopant concentration on the solar energy conversion efficiency for the absorbing *p*-Si layer of the CdS/*por*-Si/*p*-Si heterostructure has been investigated.

In order to control this distribution profile, a *por*-Si film of the samples under investigation was formed at different values of the etching duration  $t_{et}$  and the anode current density  $J_{et}$ .

## The technology of manufacturing experimental samples

For the preparation of experimental CdS/*por*-Si/*p*-Si samples the *p*-type single-crystal silicon wafers with a specific resistance of 1 Ohm·cm doped with boron and a surface orientation of (100) were used. The concentration of the doping acceptor impurity in the silicon wafers was  $1.5 \cdot 10^{16} \text{ cm}^{-3}$ . The *por*-Si film was made by the technique of anodic



Table

Information on the experimental samples

No.	$J_{et}$ , mA/cm <sup>2</sup>	$t_{et}$ , min	$U_{oc}$ , mV	$J_{sc}$ , mA/cm <sup>2</sup>	FF, arb.unit.	$\eta$ , %	$N_t$ , cm <sup>-3</sup>
1	10	12	365	12.1	0.6	3.4	$4.2 \cdot 10^{13}$
2	18	10	487	16.5	0.7	5.7	$9.7 \cdot 10^{13}$
3	30	7	475	14.2	0.7	4.6	$2.0 \cdot 10^{14}$
4	45	5	270	9.6	0.6	1.6	$2.3 \cdot 10^{14}$

Symbols:  $J_{et}$  is the anode current density,  $t_{et}$  is the etching duration,  $U_{oc}$  is the open circuit voltage,  $J_{sc}$  is the short-circuit current density, FF is the filling factor of the current-voltage characteristic,  $\eta$  is the efficiency,  $N_t$  is the concentration of traps.

electrochemical etching in the galvanostatic mode. An electrolyte consisting of HF and C<sub>2</sub>H<sub>5</sub>OH in a ratio of 1:1 was used. Several samples were made with different values of  $J_{et}$  and  $t_{et}$  (See Table). The time  $t_{et}$  values for the samples were chosen so that the *por*-Si film thickness at different  $J_{et}$  values was approximately the same. After the *por*-Si film was grown, the surface of the samples was etched in an aqueous HF solution (10 %) for 10 min. The *por*-Si film thickness for all samples was  $2.2 \pm 0.3 \mu\text{m}$ .

A CdS film was formed on the surface of a *por*-Si layer by the method of chemical bath deposition (from aqueous solutions). A CdCl<sub>2</sub> solution with a concentration of 0.44 M was used as a source of cadmium ions. A N<sub>2</sub>H<sub>4</sub>CS (thiourea) solution with a concentration of 0.22M was used as a source of sulfur ions. A concentrated aqueous NH<sub>4</sub>OH (ammonia) solution was used as a complexing agent. At first, an ammonia solution was added to the CdCl<sub>2</sub> one until the precipitate completely dissolved, then the same volume of an aqueous thiourea solution was added to the resulting solution. The temperature of the solution was brought to 90° C, substrates with a *por*-Si film were immersed in it, and a CdS film was grown for 20 min. The CdS layer on the back side of *p*-Si was completely etched with a 30% HCl solution. Samples were washed with distilled water and dried in the oven. For all samples, the CdS film thickness was  $1.8 \pm 0.2 \mu\text{m}$ .

For electrical measurements, ohmic contacts were formed on opposite surfaces of the sample to the *p*-Si substrate and the CdS film by soldering indium.

### The used investigation technique

In order to study the distribution profile of the dopant concentration in the base region of the structure given above, the  $C - V$  characteristics were measured at a frequency of 1 MHz at a reverse bias. The reverse bias corresponds to the application of a positive value of the constant bias voltage  $U$  to the contact on the CdS surface and negative  $U$  to the contact on the *p*-Si. The measurements of the samples were carried out using an E7-20 digital immitance meter (MNIPI, Belarus) at a temperature of 300 K. It is known that the high-frequency  $C - V$  characteristic  $C(U)$  measured at reverse bias reflects the dependence of the capacitance barrier component on the applied voltage and allows one to determine the impurity concentration in the base region of the studied semiconductor structure:

$$N_b = \frac{2}{q\epsilon\epsilon_0 S^2} \cdot \left( \frac{dC(U)^{-2}}{dU} \right)^{-1}, \quad (1)$$

where  $q$  is the electron charge,  $\epsilon$  is the dielectric constant of the semiconductor material of the base region of the studied heterostructure (silicon),  $\epsilon_0$  is the vacuum dielectric constant,  $S$  is the sample area [7].

The value of the  $x$  coordinate is calculated by the formula [7]:

$$x = \frac{\epsilon\epsilon_0 S}{C(U)}. \quad (2)$$

The combined use of formulas (1) and (2) allows us to calculate the distribution profile of the concentration of the dopant  $N_b(x)$  in the



base region of the investigated semiconductor structure.

The calculation of the distribution profile of the electric field in the SCR of the studied samples was carried out as follows [7]:

$$E(x) = -\frac{q}{\epsilon\epsilon_0} N_b(x) \cdot (x - W), \quad (3)$$

where  $W$  is the width of the SCR.

The main characteristics of solar photovoltaic converters with heterojunctions are significantly affected by surface states, and also traps with energy levels located in the bulk of the base region [6]. In order to obtain information about traps, we studied the  $C - V$  hysteresis measured at a frequency of 1 MHz in the region of reverse biases.

Despite the fact that at high frequencies the charge in traps with deep energy levels does not have time to follow the measuring signal, it affects the value of  $W$  and the value of the high-frequency capacitance [11]. To evaluate the influence of traps, one can compare the  $C - V$  characteristic, measured with the forward bias of a constant bias voltage from 0 to a certain limiting value  $U_m$  ( $C_{in}(U)$ ), and measured with a reverse scan from  $U_m$  to 0 ( $C_{out}(U)$ ). In the absence of traps, the  $C_{in}(U)$  and  $C_{out}(U)$  curves should coincide completely. In the presence of traps a hysteresis phenomenon is observed – the  $C_{in}(U)$ , and  $C_{out}(U)$  curves differ [12]. Thus, by analyzing the width of the hysteresis band formed by the  $C_{in}(U)$  and  $C_{out}(U)$  curves, we can obtain information about traps in the SCR.

The value of the barrier capacitance is determined by the ratio of the charge increment in the SCR to the magnitude of the voltage change [7]:

$$C = \frac{dQ}{dU}. \quad (4)$$

Hence, the charge  $Q$  concentrated in the SCR, when the constant bias voltage changes from  $U_1$  to  $U_2$ , can be expressed as follows:

$$Q = \int_{U_1}^{U_2} C(U) dU. \quad (5)$$

On the other hand, the charge  $Q$  is determined by the volume concentrations of the dopant  $N_b$  and of the traps  $N_t$ , as well as the SCR thickness  $W$ :

$$Q = q(N_b + N_t)WS. \quad (6)$$

Given the hysteresis of the  $C - V$  curves and using Eqs. (5) and (6), for the concentration of traps we can write the following expression:

$$N_t = \frac{1}{qWS} \int_0^{U_m} |C_{in}(U) - C_{out}(U)| dU, \quad (7)$$

where  $U_m$  is the limiting value of the constant bias voltage to which the constant bias voltage  $U$  is scanned.

To evaluate the efficiency of solar energy conversion by CdS/*por*-Si/*p*-Si samples, we measured the open circuit voltage  $U_{oc}$ , short-circuit current density  $J_{sc}$ , filling factor of the current – voltage characteristic FF and efficiency  $\eta$  under illumination under AM1.5.

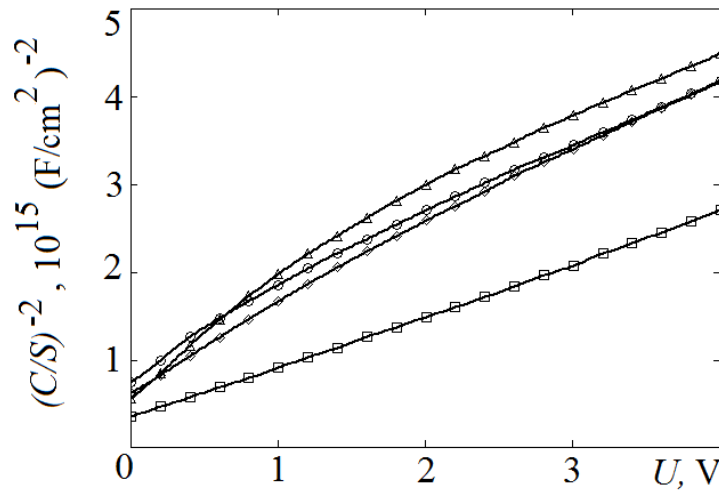


Fig. 1. Capacitance – voltage characteristics of samples No. 1 ( $\square$ ), No. 2 ( $\diamond$ ), No. 3 ( $\circ$ ), No. 4 ( $\Delta$ ), measured at a frequency of 1 MHz with reverse bias;  $S$  is the sample area



### Experimental results

Capacitance – voltage characteristics of the samples under study, measured in the region of reverse biases, are shown in Fig. 1 in the form of the dependence  $(C/S)^{-2} = f(U)$ . For sample No. 1, the graph in Fig. 1 is close to a straight line. For samples No. 2 – No. 4, the dependence  $(C/S)^{-2} = f(U)$  noticeably deviates from the linear one, which indicates the presence of an impurity concentration gradient in the base region (see Fig. 1).

The profiles of the distribution dopant concentration  $N_b(x)$  in the surface layer of the base region of the samples under study, calculated by Eqs. (1) and (2), are shown in Fig. 2. For sample No.1, the  $N_b$  value varies slightly with the  $x$  coordinate and is close to the acceptor impurity concentration ( $1.5 \cdot 10^{16} \text{ cm}^{-3}$ )

in silicon wafers used as a substrate for the manufacture of the samples. For sample No. 2, the value  $N_b$  increases linearly with increasing  $x$  to a value close to  $1.5 \cdot 10^{16} \text{ cm}^{-3}$ . Samples No. 3 and No. 4 are characterized by a more complex dependence  $N_b(x)$ . Thus, for samples No. 2 – No. 4 an acceptor impurity is depleted in the surface layer of the base region directly adjacent to the *por*-Si/*p*-Si heterojunction. With an increase in  $x$  the value of  $N_b$  tends to a value close to  $1.5 \cdot 10^{16} \text{ cm}^{-3}$ .

The electric field distribution profile  $E(x)$  for the studied samples calculated by Eq. (3) is presented in Fig. 3. Sample No. 1 exhibits a linear dependence  $E(x)$  with a sharp heterojunction. The maximum value of  $E$  for samples No. 1 – No. 3 practically coincides. The region width bounded by the dependence

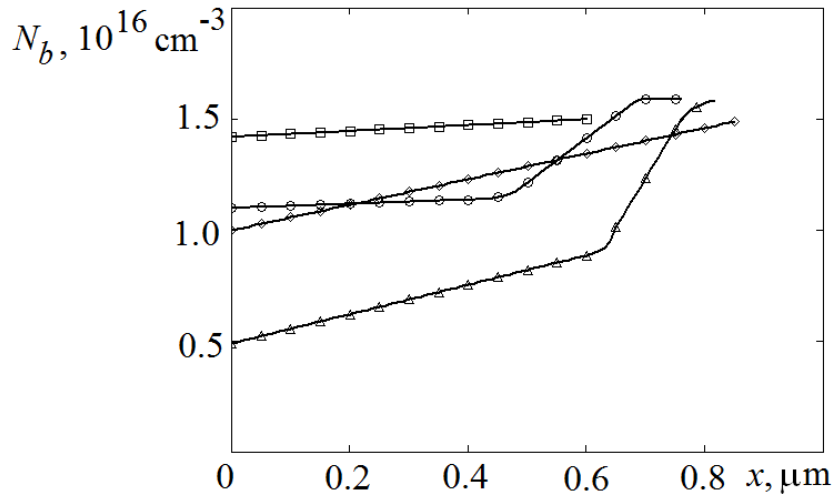


Fig. 2. Distribution profiles of the concentration of acceptor impurities in the base region of samples No. 1 (□), No. 2 (◇), No. 3 (○), No. 4 (Δ)

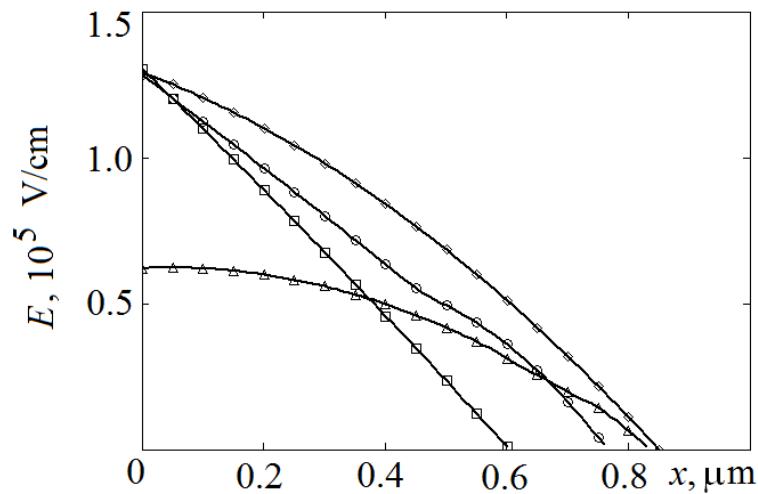


Fig. 3. The distribution profiles of the electric field in the base region of samples No. 1 (□), No. 2 (◇), No. 3 (○), No. 4 (Δ)

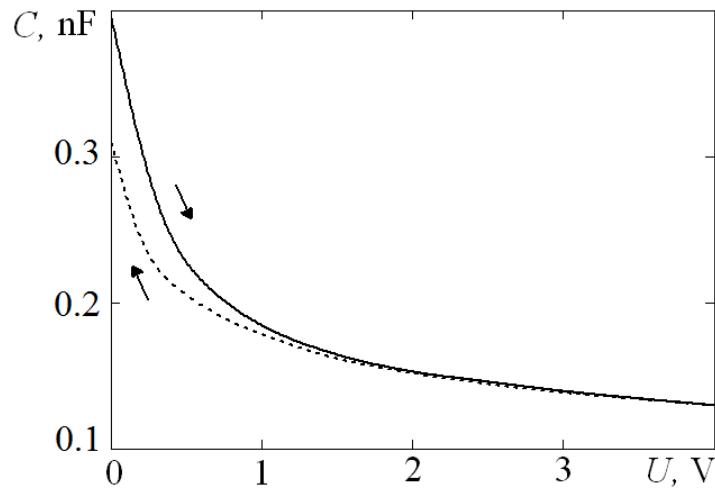


Fig. 4. Capacitance – voltage characteristics of sample No. 2 for a forward sweep of a constant bias voltage (solid line) and reverse (dashed line)

$E(x)$  is maximum value for sample No. 2.

In order to estimate the traps concentration  $N_t$  the  $C - V$  characteristics of the samples were measured at direct  $C_{in}(U)$  and reverse  $C_{out}(U)$  scans of a constant bias voltage  $U$  in the range 0 – 4 V. For all the samples studied the behavior of the  $C_{in}(U)$  and  $C_{out}(U)$  is almost identical. The curves  $C_{in}(U)$  and  $C_{out}(U)$  for sample No. 2 are shown in Fig. 4. The  $C_{in}(U)$  and  $C_{out}(U)$  curves noticeably differ in the range of  $U$  values from 0 to 2 V; for  $U > 2$  V this difference practically disappears (see Fig. 4). This behavior of the curves in Fig. 4 can be explained by a more noticeable effect on the barrier capacitance of traps localized at the *por*-Si/*p*-Si heterojunction (surface states) as compared to traps located in the bulk of the base region of the samples.

The values of  $U_{oc}$ ,  $J_{sc}$ , FF and  $\eta$ , characterizing the efficiency of solar energy conversion of the studied samples, are presented in Table. The highest efficiency of solar energy conversion is characterized by sample No. 2; sample No. 3 is close to it; sample No. 4 has the lowest conversion efficiency compared to samples No. 1 – No. 3 (see Table).

### Discussion of the experimental results

The efficiency of a solar photovoltaic converter with a heterojunction is significantly affected by surface states and traps located in the volume of the absorbing region [6]. However, it is impossible to draw an unambiguous conclusion about the effect of the concentration  $N_t$  on the solar energy conversion efficiency of experimental samples from the Table. So, sample No. 4 has significantly lower values

of  $U_{oc}$ ,  $J_{sc}$ , and  $\eta$  compared to sample No. 3. Moreover, for these samples the value of  $N_t$  changes slightly. Sample No. 2, characterized by the highest conversion efficiency  $\eta$ , has an  $N_t$  value close to samples No. 3 and No. 4. At the same time sample No. 1 which occupies an intermediate place between samples No. 3 and No. 4 in terms of conversion efficiency  $\eta$ , is characterized by the lowest  $N_t$  value of all the samples studied. Moreover, the  $N_t$  value of sample No. 1, is significantly less than for the remaining samples. Thus, the value of  $N_t$  does not have a decisive influence on the parameters characterizing the conversion efficiency of the studied samples.

An analysis of the hysteresis for the  $C - V$  characteristics (see Fig. 4) shows that the capacitance decreases upon reverse sweep  $U$ . In Ref. [11] the decrease in the SCR capacitance was explained by the emptying of the traps of minority charge carriers. This situation can be illustrated by zone diagrams in Fig. 5.

The SCR of a width  $W$  is almost completely concentrated in the surface *p*-Si layer near the *por*-Si/*p*-Si heterojunction. At this heterojunction, surface states characterized by energy levels of  $E_{ss}$  are localized, and traps with energy levels of  $E_t$  can also be contained in the bulk of the *p*-Si base region (see Fig. 5). It was shown [8], that the of current flow mechanisms in the studied CdS/*por*-Si/*p*-Si heterostructure are determined by the traps with activation energies occupying a wide range of values. For the purpose of simplification, only one volumetric energy level  $E_t$  is shown in Fig. 5. At  $U = 0$  V (see Fig. 5,a), the band bending in the *p*-Si region is determined by the value of the diffusion potential  $V_{bi}$ . In this case

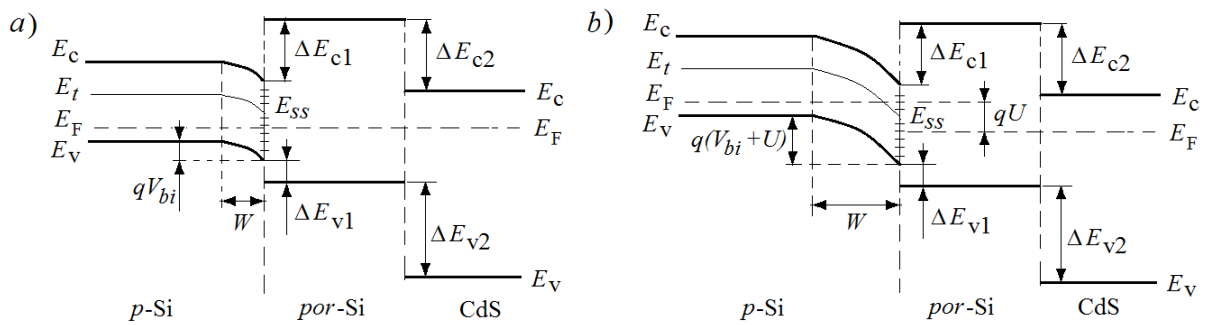


Fig. 5. The band diagram of the CdS/por-Si/p-Si heterostructure at  $U = 0$  V (a) and for some value of reverse bias  $U$  (b); see explanations in the text

the energy levels of the  $E_t$  and  $E_{ss}$  traps located within the SCR of the por-Si/p-Si heterojunction are filled with charge carriers if they are below the Fermi level  $E_F$  and emptied if they are above  $E_F$ .

In the reverse bias (see Fig. 5,b), the band bending in the SCR increases by the value of the applied voltage  $U$ , the energy levels of the traps below  $E_F$  are filling with carriers. Upon subsequent change in the scanning direction  $U$  to 0 V the bending of the zones decreases, and a transition to the conditions shown in Fig. 5,a takes place. This is accompanied by the depletion of the energy levels of the  $E_t$  and  $E_{ss}$  traps. Moreover, the dominant contribution to the relaxation process is made by the energy levels of minority carrier traps in the p-Si layer.

The most probable cause of the observed differences in the efficiency parameters of the studied samples (see Table) may be the difference in the character of the dependence  $E(x)$  in the SCR of the base region of the por-Si/p-Si heterojunction (see Fig. 3). In turn, the form of the dependence  $E(x)$  is determined by the distribution dopant concentration profile  $N_b(x)$  (see Fig. 2). Referring to Figs. 2 and 3, depletion of the p-Si surface region by an acceptor impurity for samples No. 2 and No. 3 leads to a noticeable extension of the  $E(x)$  curves towards an increase in  $x$  as compared to that of sample No. 1, for which the  $N_b$  value weakly depends on  $x$  within the SCR. Moreover, the efficiencies of samples No. 2 and 3 are significantly higher as compared to that of sample No. 1. The near-surface layer of the p-Si region of sample No. 4 is more depleted in acceptor impurity than those of samples No. 1 – No. 3 (see Fig. 2). As a result, the electric field inside the SCR is noticeably lower for sample No. 4 than those for the remaining samples (see Fig. 3). Sample No. 4 exhibits the lowest conversion efficiency of solar energy as compared to those for the rest of the studied samples.

Thus, an increase in the conversion efficiency

of solar energy of the studied samples can be explained by an increase in the penetration depth of a strong electric field into the base region. The charge carriers generated by the light inside this region are carried away by the electric field before they have time to recombine through the participation of traps. Thus, the depletion of the doping impurity in the near-surface p-Si layer which is in the immediate vicinity of the por-Si/p-Si heterojunction, is an aid to the expansion of the region in which the strongest electric field is concentrated. At the same time an increase in the depletion of the base region with an alloying impurity observed for sample No. 4 leads to a decrease in the electric field strength (see Fig. 3) and a decrease in the efficiency of solar energy conversion (see Table).

The depletion of the p-Si surface region occurs during the formation of a por-Si film. One of the causes of depletion may be the partial etching of impurity atoms from the surface of silicon crystallites during the formation of a porous layer [13]. Another cause of the depletion may be a partial compensation of the main dopant by defects, including those having deep energy levels localized on the surface of silicon crystallites [9, 13].

Numerous studies have shown that por-Si films formed on single-crystal silicon substrates are complexly structured [14 – 16]. The por-Si film is formed by silicon crystallites separated by pores. The average crystallite diameter increases as it moves from the outer surface of the por-Si film to the single-crystal substrate [16]. Thus, a clearly defined boundary between the porous film and the single crystal substrate may be absent. As a result, the por-Si/p-Si heterojunctions of the samples studied in this work can be located inside the largest silicon crystallites in the lower region of the por-Si film. The states localized on the crystallite surface can contribute to partial



compensation of the acceptor dopant in the surface layer of the base region of the samples under study.

### Summary

The relationship between the distribution profile of the dopant acceptor impurity in the base region of the CdS/*por*-Si/*p*-Si heterostructure and the solar energy conversion efficiency parameters has been established. It was shown that the conversion efficiency depends on the degree of depletion of the *p*-Si surface layer doping with an acceptor impurity located in the immediate vicinity of the *por*-Si/*p*-Si heterojunction. The formation of this depletion region occurs as a result of a *por*-Si film growing. By changing the main parameters of the *por*-Si growth process ( $t_{et}$  and  $J_{et}$ ) one can

control the impurity distribution profile and the efficiency of solar energy conversion. Thus, in order to increase its efficiency, one of the directions of optimizing the technology of the solar photovoltaic converter based on the CdS/*por*-Si/*p*-Si heterostructure is the selection of  $t_{et}$  and  $J_{et}$  parameters for *por*-Si film growing. An important advantage is a forming of the depleted region not requiring a separate technological operation. The concentration distribution profile is formed in the process of growing the *por*-Si layer. In production conditions this will reduce the cost of manufacturing a photovoltaic converter.

The obtained data can be useful in the development of solar photovoltaic converters and optical sensors based on the CdS/*por*-Si/*p*-Si heterostructure.

### REFERENCES

1. Hasoon S.A., Ibrahim I.M., Raad M.S., et al., Fabrication of nanostructure CdS thin film on nanocrystalline porous silicon, International Journal of Current Engineering and Technology. 4 (2) (2014) 594–601.
2. Jafarov M.A., Nasirov E.F., Jahangirova S.A., Nano-CdS/porous silicon heterojunction for solar cell, International Journal of Scientific and Engineering Research. 6 (7) (2015) 849–853.
3. Sharma B.L., Purohit R.K., Semiconductor heterojunctions, Pergamon Press, Oxford, New York, 1974.
4. Mamedov H.M., Kukevecz A., Konya Z., et al., Electrical and photoelectrical characteristics of c-Si/*porous*-Si/CdS heterojunctions, Russian Physics Journal. 61 (9) (2019) 1660–1666.
5. Eesa M.W., Abdullah M.M., Porous silicon effect on the performance of CdS nanoparticles photodetector, International Journal of Current Engineering and Technology. 4 (6) (2016) 1372–1376.
6. Fahrenbuch A.L., Bube R.H., Photovoltaic solar energy conversion, Fundamentals of solar cells, Academic Press, New York, 1983.
7. Sze S.M., Physics of semiconductor devices: Second Ed., John Wiley and Sons, New York, Chichester, Brisbane, Toronto, Singapore, 1981.
8. Tregulov V.V., Litvinov V.G., Ermachikhin A.V., Study of current flow mechanisms in a CdS/*por*-Si/*p*-Si heterostructure, Semiconductors. 52 (7) (2018) 891–896.
9. Timokhov D.F., Timokhov F.P., Determination of structure parameters of porous silicon by the photoelectric method, Journal of Physical Studies. 8 (2) (2004) 173–177.
10. Hadi H.A., Abood T.H., Mohi A.T., Karim M.S., Impact of the etching time and current density on capacitance-voltage characteristics of *p*-type of porous silicon, World Scientific News. 67 (2) (2017) 149–160.
11. Berman L.S., Lebedev A.A., Emkostnaya spektroskopiyaglubokihcentrovvpoluprovodnikah [Deep-center capacity spectroscopy in semiconductors] Nauka, Leningrad, 1981 (In Russian).
12. Voitsekhovskii A.V., Nesmelov S.N., Dzyadukh S.M., Electrical characterizations of MIS structures based on variable-gap *n(p)*-HgCdTe grown by MBE on Si(013) substrates, Infrared Physics and Technology. 87 (December) (2017) 129–133.
13. Zhang X.G., Electrochemistry of silicon and its oxide, Kluwer Academic Publishers, New York, Boston, Dordrecht, London, Moscow, 2004.
14. Goryachev D.N., Belyakov L.V., Sreseli O.M., Formation of thick porous silicon layers with insufficient minority carrier concentration, Semiconductors. 38 (6) (2004) 712–716.
15. Venger E.F., Gorbach T.Ya., Kirillova S.I., et al., Changes in properties of a porous silicon/silicon system during gradual etching off of the porous silicon layer, Semiconductors. 36 (3) (2002) 330–335.
16. Melnik N.N., Tregulov V.V., Photoluminescence and Raman studies of the structure of a thick porous silicon film, Bulletin of the Lebedev Physics Institute. 42 (3) (2015) 77–80.

Received 20.03.2020, accepted 04.05.2020.

## THE AUTHOR

**TREGULOV Vadim V.**

*Ryazan State University named for S. Yesenin*

46, Svobody St., Ryazan, 390000, Russian Federation

trww@yandex.ru

## СПИСОК ЛИТЕРАТУРЫ

1. Hasoon S.A., Ibrahim I.M., Raad M.S., Al-Haddad, Mahmood S.S. Fabrication of nanostructure CdS thin film on nanocrystalline porous silicon // International Journal of Current Engineering and Technology. 2014. Vol. 4. No. 2. Pp. 594–601.
2. Jafarov M.A., Nasirov E.F., Jahangirova S.A. Nano-CdS/porous silicon heterojunction for solar cell // International Journal of Scientific and Engineering Research. 2015. Vol. 6. No. 7. Pp. 849–853.
3. Шарма Б.Л., Пурохит Р.К. Полупроводниковые гетеропереходы. Пер. с англ. М.: Сов. радио, 232. 1979 с.
4. Мамедов Г.М., Кукевич А., Коня З., Кордаш К., Шах С.И. Электрические и фотоэлектрические характеристики гетеропереходов *c*-Si/пористый-Si/CdS // Известия высших учебных заведений. Физика. 2018. Т. 61. № 9. С. 96–101.
5. Eesa M.W., Abdullah M.M. Porous silicon effect on the performance of CdS nanoparticles photodetector // International Journal of Current Engineering and Technology. 2016. Vol. 4. No. 6. Pp. 1372–1376.
6. Фаренбух А., Бьюб Р. Солнечные элементы: Теория и эксперимент: Пер. с англ. М.: Энергоатомиздат, 1987. 280 с.
7. Зи С.М. Физика полупроводниковых приборов: Пер. с англ. В 2 тт. Т. 1. М.: Мир, 1984. 456 с.
8. Трегулов В.В., Литвинов В.Г., Ермачихин А.В. Исследование механизмов токопрохождения в гетероструктуре CdS/*por*-Si/*p*-Si / Физика и техника полупроводников // 2018. Т. 52. № 7. С. 751–756.
9. Timokhov D.F., Timokhov F.P. Determination of structure parameters of porous silicon by the photoelectric method // Journal of Physical Studies. 2004. Vol. 8. No. 2. Pp. 173–177.
10. Hadi H.A., Abood T.H., Mohi A.T., Karim M.S. Impact of the etching time and current density on Capacitance–Voltage characteristics of *p*-type of porous silicon // World Scientific News. 2017. Vol. 67. No. 2. Pp. 149–160.
11. Берман Л.С., Лебедев А.А. Емкостная спектроскопия глубоких центров в полупроводниках. Л.: Наука, 1981. 176 с.
12. Voitsekhovskii A.V., Nesmelov S.N., Dzyadukh S.M. Electrical characterizations of MIS structures based on variable-gap *n(p)*-HgCdTe grown by MBE on Si(013) substrates // Infrared Physics and Technology. 2017. Vol. 87. December. Pp. 129–133.
13. Zhang X.G. Electrochemistry of silicon and its oxide. New York, Boston, Dordrecht, London, Moscow: Kluwer Academic Publishers, 2004. 510 p.
14. Горячев Д.Н., Беляков Л.В., Сресели О.М. Формирование толстых слоев пористого кремния при недостаточной концентрации неосновных носителей // Физика и техника полупроводников. 2004. Т. 38. № 6. С. 739–744.
15. Венгер Е.Ф., Горбач Т.Я., Кириллова С.И., Примаченко В.Е., Чернобай В.А. Изменение свойств системы пористый Si/Si при постепенном травлении слоя пористого Si // Физика и техника полупроводников. 2002. Т. 3 № 36. С. 349–354.
16. Мельник Н.Н., Трегулов В.В. Исследование структуры толстой пленки пористого кремния методами фотолюминесценции и комбинационного рассеяния света // Краткие сообщения по физике ФИАН. Т. 42. № 3. 2015. С. 19–24.

*Статья поступила в редакцию 20.03.2020, принята к публикации 04.05.2020.*

## СВЕДЕНИЯ ОБ АВТОРЕ

**ТРЕГУЛОВ** Вадим Викторович — кандидат технических наук, доцент кафедры общей и теоретической физики и методики преподавания физики Рязанского государственного университета имени С.А. Есенина, г. Рязань, Российская Федерация.

390000, Российская Федерация, г. Рязань, ул. Свободы, 46

trww@yandex.ru



DOI: 10.18721/JPM.13203

УДК 532.517

**ASSESSMENT OF RANS TURBULENCE MODELS CAPABILITIES  
BASED ON COMPUTATIONAL RESULTS FOR FREE CONVECTION  
DEVELOPING NEAR A SUDDENLY HEATED VERTICAL PLATE***A.M. Levchenya, S.N. Trunova, E.V. Kolesnik*

Peter the Great St. Petersburg Polytechnic University, St. Petersburg, Russian Federation

The results of testing several RANS turbulence models in solving a problem of free air convection temporal development near the surface of a suddenly heated infinite vertical plate have been presented in the paper. The solution results with the use of the different models were compared with the literature data obtained by direct numerical simulation. Numerical solutions were carried out using the four models, two of them based on the isotropic turbulent viscosity concept and the rest ones involved solving the transport equations of the Reynolds stress tensor components. The flow and heat transfer characteristics for different stages of boundary layer development, from laminar to turbulent, were analyzed. Based on a comparison with the literature data on direct numerical simulation, conclusions about the predictive capabilities of the RANS models considered were drawn.

**Keywords:** free convection, RANS simulation, time-developing, direct numerical simulation, boundary layer

**Citation:** Levchenya A.M., Trunova S.N., Kolesnik E.V., Assessment of RANS turbulence models capabilities based on computational results for free convection developing near a suddenly heated vertical plate, St. Petersburg Polytechnical State University Journal. Physics and Mathematics. 13 (2) (2020) 21–32. DOI: 10.18721/JPM.13203

This is an open access article under the CC BY-NC 4.0 license (<https://creativecommons.org/licenses/by-nc/4.0/>)

**ОЦЕНКА ВОЗМОЖНОСТЕЙ RANS-МОДЕЛЕЙ  
ТУРБУЛЕНТНОСТИ ПО РЕЗУЛЬТАТАМ РАСЧЕТОВ  
СВОБОДНОЙ КОНВЕКЦИИ, РАЗВИВАЮЩЕЙСЯ ВБЛИЗИ  
ВНЕЗАПНО НАГРЕТОЙ ВЕРТИКАЛЬНОЙ ПЛАСТИНЫ***А.М. Левченя, С.Н. Трунова, Е.В. Колесник*Санкт-Петербургский политехнический университет Петра Великого,  
Санкт-Петербург, Российская Федерация

В работе представлены результаты тестирования нескольких RANS-моделей турбулентности на примере решения задачи развития во времени свободной конвекции воздуха у поверхности внезапно нагретой безграничной вертикальной пластины. Результаты решения с использованием различных моделей сопоставлены с литературными данными, полученными методом прямого численного моделирования. Численные решения получены с применением четырех моделей, две из которых основаны на концепции изотропной турбулентной вязкости, а остальные предполагают решение уравнений переноса компонент тензора рейнольдсовых напряжений. Получены характеристики течения и теплообмена на разных стадиях развития пограничного слоя — от ламинарного режима до турбулентного. На основе сопоставления полученных результатов с данными прямого численного моделирования сделаны выводы о предсказательных возможностях рассмотренных RANS-моделей турбулентности.

**Ключевые слова:** свободная конвекция, RANS-моделирование, прямое численное моделирование, пограничный слой

**Ссылка при цитировании:** Левченко А.М., Трунова С.Н., Колесник Е.В. Оценка возможностей RANS-моделей турбулентности по результатам расчетов свободной конвекции, развивающейся вблизи внезапно нагретой вертикальной пластины // Научно-технические ведомости СПбГПУ. Физико-математические науки. 2020. Т. 132 №. С. 27–40. DOI: 10.18721/JPM.13203

Статья открытого доступа, распространяемая по лицензии CC BY-NC 4.0 (<https://creativecommons.org/licenses/by-nc/4.0/>)

### Introduction

Free-convection flow near the surface of a vertical heated plate has long been the focus of attention because correctly predicting heat transfer in boundary layers is important for many practical applications. The Time-Developing approach considering the temporal evolution of the flow is an efficient computational method for analysis of developing boundary layers.

The approach basically consists in describing the temporal evolution of a boundary layer instead of the spatial evolution (the Spatial approach), which is usually observed in practice. Thus, time serves as a sort of coordinate axis along which the flow evolves. In contrast with other methods simulating flow evolution along the longitudinal (spatial) axis, this approach allows to significantly reduce the size of the computational domain and consequently the total computation time.

The Time-Developing approach is very popular for simulations of dynamic turbulent boundary layers on plates in axial flow [1, 2]. In particular, Ref. [1] discussed a laminar-turbulent transition in a boundary layer at high

turbulence. For this purpose, Time-Developing Direct Numerical Simulation (TDDNS) was used to solve a model problem of a boundary layer evolving on an infinite plate in isotropic turbulent fluid of zero mean velocity, with the plate suddenly set in motion in its plane. The method was used in [3] to solve problems of free convection for the first time, while [4] presented promising and detailed computational results based on this method.

Although only DNS methods can yield the most complete data on the laminar-turbulent transition, whether semi-empirical RANS turbulence models can provide a satisfactory description of the transition is still open to question [5]. Furthermore, it is undoubtedly interesting to assess the efficiency of different turbulence models for simulations of the flow in fully developed turbulent free-convection boundary layers, both for the models based on isotropic turbulent viscosity [6] and for Reynolds stress models [7].

Notably, the choice of suitable turbulence models is especially critical for simulation of complex free-convection flows, including free-convection layers perturbed by different

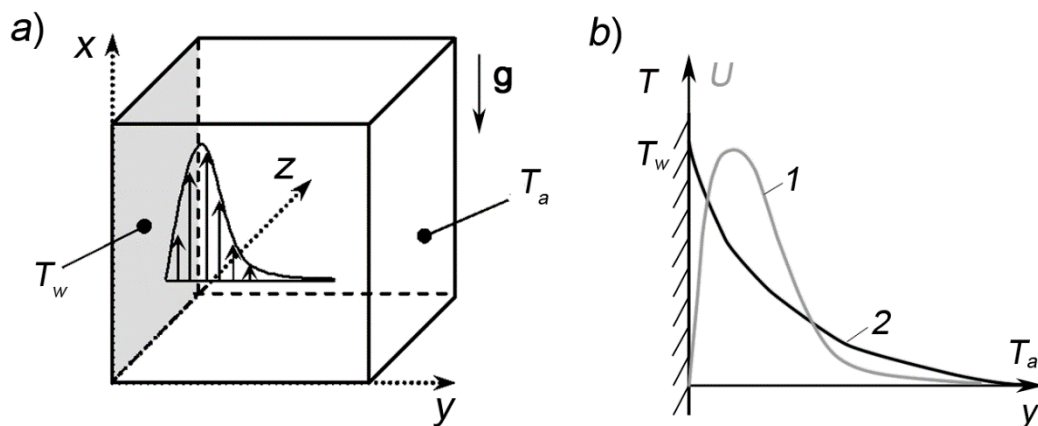


Fig. 1. Schematic for problem statement of turbulent free-convection boundary layer developing along an infinite heated vertical plate: *a* corresponds to the plate (shaded) with the surrounding ambient (cube); *b* to velocity (1) and temperature (2) distributions of the ambient air depending on the distance from the plate





kinds of obstacles. For example, [8] reports on RANS simulations (using the SST  $k-\omega$  model) for flow around a cylinder of finite height mounted on a vertical heated plate, while a recent paper [9] presents simulations and experiments the same configuration.

The goal of this study consisted in assessing the performance of several RANS turbulence models by comparing the numerical solutions that we obtained with the test (reference) data from literature [4] for a model problem on the time evolution of free convection along an infinite vertical plate. We used the ANSYS Fluent 18.2 package for the computations.

#### TDDNS method as a source of test data

We consider a model problem of free convection developing along an infinite suddenly heated vertical plate. The flow diagram is shown in Fig. 1. The parameters of the problem in this section (described identically to [4]) correspond to the conditions of earlier well-known experiments [10] on a free-convection layer developing along a vertical plate (along the spatial coordinate). The parameters are given in Table.

The mathematical model taken for describing turbulent free convection of incompressible Newtonian fluid with constant physical properties is based on a system of unsteady 3D Navier–Stokes equations complemented with an energy balance equation, taking into account buoyancy effects in the gravity field in the Boussinesq approximation:

$$\begin{aligned} \frac{\partial u_j}{\partial x_j} &= 0; \\ \rho \frac{\partial u_i}{\partial t} + \rho u_j \frac{\partial u_i}{\partial x_j} &= -\frac{\partial p}{\partial x_i} + \frac{\partial \tau_{ij}}{\partial x_j} - \rho \beta_T (T - T_a) g_i, \\ i &= 1, 2, 3; \\ \rho c_p \frac{\partial T}{\partial t} + \rho c_p u_j \frac{\partial T}{\partial x_j} &= \frac{\partial q_j}{\partial x_j}. \end{aligned} \quad (1)$$

Here  $u_i$  are the components of the velocity vector  $\mathbf{V}$  in Cartesian coordinates ( $x \equiv x_1$ ,  $y \equiv x_2$ );  $p$  (Pa) is the pressure,  $T$  (K) is the temperature,  $\rho$  (kg/m<sup>3</sup>) is the density and  $c_p$  (J/(kg·K)) is the heat capacity of the air.

The components of the viscous stress tensor  $\tau$  and the heat flux density vector  $\mathbf{q}$  due to molecular thermal conductivity are found, respectively, using Fourier's law and Newton's law of viscosity:

$$q_j = -\lambda \left( \partial T / \partial x_j \right), \quad j = 1, 2, 3, \quad (2)$$

$$\tau_{ij} = \mu \left( \frac{\partial u_i}{\partial x_j} + \frac{\partial u_j}{\partial x_i} \right), \quad i, j = 1, 2, 3. \quad (3)$$

The space shaped as a rectangular parallelepiped adjacent to the plate acts as the computational domain in TDDNS computations (Fig. 1,a). The outer boundary parallel to the wall is assumed to be permeable, with constant pressure  $p$  and temperature  $T_a$  given. Periodic

Table

Problem parameters

Parameter	Notation	Unit	Value
Plate temperature	$T_w$	K	333.15
Ambient temperature	$T_a$	K	289.15
Ambient density	$\rho$	kg/m <sup>3</sup>	1.135
Ambient viscosity	$\mu$	Pa·s	$1.906 \cdot 10^{-5}$
Ambient thermal conductivity	$\lambda$	W/(m·K)	0.0274
Heat capacity at constant pressure	$c_p$	J/(kg·K)	1006
Coefficient of thermal expansion	$\beta$	1/K	$3,458 \cdot 10^{-3}$
Prandtl number	Pr	—	0.71

Notes. 1. Physical properties of the air were assumed to be constant, computed at the average temperature  $T_f = (T_w + T_a)/2$ .

2. Coefficient  $\beta$  was computed at the temperature  $T = T_a$ .

3. Prandtl number  $Pr = c_p \mu / \lambda$ .

conditions are imposed in homogeneous coordinates (vertical ( $x$ ) and transverse ( $z$ )). After the flow fields are computed, they are averaged along the homogeneous coordinates (along the  $x$  and  $z$  axes) at the next time step, so that the unsteady problem can be considered statistically one-dimensional, where the averaged parameters of the flow change only along the  $y$  axis (Fig. 1,  $b$ ).

The notion of integral thickness of the velocity boundary layer is introduced to construct the dimensionless parameters characterizing the given flow at different instants in time. This quantity can be found by the following formula (integration with respect to  $y$  is performed over the entire ambient):

$$\delta = \int_0^{\infty} \frac{u}{U_m} dy. \quad (4)$$

Dimensionless temperature is also introduced:

$$\theta = (T - T_a) / (T_w - T_a). \quad (5)$$

The thickness of the temperature boundary layer  $\delta_T$  is defined as the coordinate  $y$ , where  $\theta = 0.01$ .

The Grashof number, the Nusselt number, and the dimensionless friction constructed based on the boundary layer thickness are defined as follows:

$$Gr_\delta = g\beta\Delta T\delta^3/\nu^2, \quad (6)$$

$$Nu_\delta = q_w\delta/(\lambda\Delta T), \quad (7)$$

$$\bar{\tau} = \tau_w/(\rho g\beta\Delta T\delta). \quad (8)$$

where  $\Delta T = T_w - T_a$  is the temperature difference between the plate and the ambient.

Detailed data on the TDDNS model are given in [4] for the skin friction coefficient and the Nusselt number depending on the Grashof number, along with data on the mean velocity and temperature profiles and turbulence characteristics at different  $Gr_\delta$ ; these data are used for comparison in our study.

#### Problem statement based on the RANS approach

The given time-developing flow is simulated based on Reynolds-averaged Navier–Stokes equations (RANS), initially introducing averaging along homogeneous coordinates ( $x$  and  $z$ ). As a result, we obtain unsteady one-dimensional equations with respect to the

mean axial component of velocity  $u$  and the mean temperature  $T$ :

$$\begin{aligned} \rho \frac{\partial u}{\partial t} &= \frac{\partial (\tau_{xy} + \tau_{t,xy})}{\partial y} - \rho\beta_T (T - T_a)g, \\ \rho c_p \frac{\partial T}{\partial t} &= \frac{\partial}{\partial y} (q_y + q_{t,y}). \end{aligned} \quad (9)$$

In this case, the transverse velocity  $v$  is taken to equal zero.

Considering the resulting unsteady one-dimensional problem, we can see that only two components of the turbulent stress tensor and the heat flux vector remain; these are  $\tau_{t,xy}$  and  $q_{t,y}$ , reflecting turbulent transfer along a normal to the wall:

$$\tau_{t,xy} = -\rho \overline{u'v'}, \quad (10)$$

$$q_{t,y} = -\rho c_p \overline{v'T'}, \quad (11)$$

(the prime denotes the fluctuating components, the overbar denotes averaging in homogeneous coordinates).

System of equations (9) is *open* in order to find a method for computing the turbulent components of the stress tensor (10) and the heat flux density vector (11). To this end, we used semi-empirical turbulence models (described below).

Notably, we obtained the solutions below using the ANSYS Fluent general-purpose code, where one-dimensional problems are solved as two-dimensional by introducing conditions for translation homogeneity. The no-slip condition and constant temperature  $T_w$  are imposed on the wall. The outer boundary parallel to the wall is assumed to be permeable with constant pressure and temperature given. Periodic conditions are imposed for the homogeneous coordinate  $x$ . It is assumed that the air has the temperature  $T_a$  at the initial time and is generally stationary. At the same time, there is initial turbulence in the region, characterized by the following parameters: turbulence intensity  $I = 0.1\%$ , turbulent to molecular viscosity ratio  $\nu_t/\nu = 0.1$ .

#### Turbulence models

Let us describe the general (three-dimensional) formulation of the turbulence models available in the ANSYS Fluent code that we used for our computations. These are two models based on the Boussinesq hypothesis (SST  $k-\omega$  and RNG  $k-\varepsilon$ ), and two Reynolds stress models (DRSM Stress-omega and DRSM StressBSL).



According to the Boussinesq hypothesis, the components of the turbulent stress tensor and the turbulent heat flux with averaged flow parameters are related as:

$$\tau_{t,ij} = \mu_t \left( \frac{\partial u_i}{\partial x_j} + \frac{\partial u_j}{\partial x_i} \right) + \frac{2}{3} k \delta_{ij}, \quad (12)$$

$$\tau_{t,ij} = \mu_t \left( \frac{\partial u_i}{\partial x_j} + \frac{\partial u_j}{\partial x_i} \right) + \frac{2}{3} k \delta_{ij}, \quad (13)$$

where  $k = 1/2 \overline{u_i' u_i'}$  is the turbulent kinetic energy,  $\mu_t$  is the turbulent viscosity,  $\lambda_t$  is the turbulent thermal conductivity;

$$\lambda_t = c_p \mu_t / \text{Pr}_t. \quad (14)$$

Expression (14) is based on the hypothesis that the processes of turbulent transfer of momentum and heat are similar, introducing the turbulent Prandtl number  $\text{Pr}_t$  whose value is taken to be constant in the computations. The system is closed by the semi-empirical turbulence model to find the turbulent viscosity  $\mu_t$ . The results below were obtained using the SST  $k$ - $\omega$  and RNG  $k$ - $\varepsilon$  models described in [11, 12].

In case of differential Reynolds stress models, the following differential equation is solved for each of the six independent components of the Reynolds stress tensor:

$$\begin{aligned} \rho \frac{\partial}{\partial t} \overline{u_i' u_j'} + \rho u_k \frac{\partial}{\partial x_k} \overline{u_i' u_j'} = \\ = (D_{ij}^m + D_{ij}^t) + P_{ij} + \phi_{ij} - \varepsilon_{ij}, \end{aligned} \quad (15)$$

where  $D_{ij}^m$ ,  $D_{ij}^t$  are the terms reflecting molecular and turbulent diffusive transfer, respectively;  $P_{ij}$  is the generation term;  $\phi_{ij}$  is the term responsible for redistribution of energy between tensor components,  $\varepsilon_{ij}$  is the dissipation term.

The equations for the terms related to molecular diffusion  $D_{ij}^m$  and generation  $P_{ij}$  are written as follows (no closure relations are necessary in this case):

$$D_{ij}^m = \frac{\partial}{\partial x_k} \left( \mu \frac{\partial \overline{u_i' u_j'}}{\partial x_k} \right), \quad (16)$$

$$P_{ij} = -\rho \left[ \overline{u_i' u_k'} \frac{\partial u_j}{\partial x_k} + \overline{u_j' u_k'} \frac{\partial u_i}{\partial x_k} \right]. \quad (17)$$

As other terms of Eq. (15),  $D_{ij}^t$ ,  $\phi_{ij}$ ,  $\varepsilon_{ij}$ , contain higher-order moments, they are computed using closures relating these terms and the averaged flow parameters.

Let us describe the specific form of the relations for the two models used in this study:

Stress-omega (referred to as DRSM SO, i.e., Differential Reynolds Stress Model Stress-Omega),

StressBSL (referred to as DRSM BSL, i.e., Differential Reynolds Stress Model Stress-BSL).

These models differ by certain closure relations and constant values.

Similar to molecular diffusion, we introduce the coefficient of turbulent diffusion proportional to turbulent viscosity for the term reflecting turbulent transfer:

$$D_{ij}^t = \frac{\partial}{\partial x_k} \left( \frac{\mu_t}{\sigma_k} \frac{\partial \overline{u_i' u_j'}}{\partial x_k} \right). \quad (18)$$

According to the DRSM SO model, the coefficient  $\sigma_k = 2$ .

The coefficient  $\sigma_k$  on the DRSM BSL model is defined by the relation

$$\sigma_k = F_1 \sigma_{k,1} + (1 - F_1) \sigma_{k,2}. \quad (19)$$

where  $\sigma_{k,1} = 2.0$ ,  $\sigma_{k,2} = 1.0$ , and function  $F_1$  is defined using the formulas:

$$F_1 = \tanh(\Phi_1^4), \quad (20)$$

$$\Phi_1 = \min \left[ \max \left( \frac{\sqrt{k}}{0.09 \omega y}, \frac{500 \mu}{\rho y^2 \omega} \right) \frac{4 \rho k}{\sigma_{\omega,2} D_{\omega}^+ y^2} \right], \quad (21)$$

$$\begin{aligned} D_{\omega}^+ = \max \left( 2 \rho \frac{1}{\omega} \frac{\partial k}{\partial x_j} \frac{\partial \omega}{\partial x_j}, 10^{-10} \right), \\ \sigma_{\omega,2} = 1.168, \end{aligned} \quad (22)$$

where  $y$  is the distance to the wall.

The term responsible for redistribution of energy between tensor components has the following form:

$$\begin{aligned} \phi_{ij} = -C_1 \rho \beta_{RSM}^* \omega \left[ \overline{u_i' u_j'} - 2/3 \delta_{ij} k \right] - \\ - \hat{\alpha}_0 \left[ P_{ij} - 1/3 P_{kk} \delta_{ij} \right] - \\ - \hat{\beta}_0 \left[ D_{ij} - 1/3 P_{kk} \delta_{ij} \right] - k \hat{\gamma}_0 \left[ S_{ij} - 1/3 S_{kk} \delta_{ij} \right], \end{aligned} \quad (23)$$

$$D_{ij} = -\rho \left[ \overline{u_i' u_k'} \frac{\partial u_k}{\partial x_j} + \overline{u_j' u_k'} \frac{\partial u_k}{\partial x_i} \right], \quad (24)$$

$$S_{ij} = \frac{1}{2} \left[ \frac{\partial u_j}{\partial x_i} + \frac{\partial u_i}{\partial x_j} \right]. \quad (25)$$

The coefficient  $\beta_{RSM}^*$  is defined as follows for the DRSM SO model:

$$\beta_{RSM}^* = \beta^* f_\beta^*, \quad \beta^* = 0.09, \quad (26)$$

$$f_\beta^* = \begin{cases} 1, & \chi_k \leq 0 \\ \frac{1 + 640\chi_k^2}{1 + 400\chi_k^2}, & \chi_k > 0 \end{cases}, \quad (27)$$

$$\chi_k = \frac{1}{\omega^3} \frac{\partial k}{\partial x_j} \frac{\partial \omega}{\partial x_j}. \quad (28)$$

The coefficient  $\beta_{RSM}^* = \beta^*$  for the DRSM BSL model.

The rest of the constants are given using the following formulas (identical for both models):

$$\begin{aligned} \hat{\alpha}_0 &= \frac{8 + \tilde{N}_2}{11}, \quad \hat{\beta}_0 = \frac{8\tilde{N}_2 - 2}{11}, \\ \hat{\gamma}_0 &= \frac{60\tilde{N}_2 - 4}{55}, \end{aligned} \quad (29)$$

where  $C_1 = 1.80$ ,  $C_2 = 0.52$ . (30)

The dissipation term is calculated by introducing an additional scalar variable, the specific dissipation  $\omega$ :

$$\varepsilon_{ij} = 2/3 \delta_{ij} \rho \beta_{RSM}^* k \omega. \quad (31)$$

The value of the constant  $\beta_{RSM}^*$  is found in the same manner as for the term  $\varphi_{ij}$  (see Eqs. (26)–(28)).

The turbulent kinetic energy is calculated as follows:

$$k = 1/2 \overline{u_i' u_i'}. \quad (32)$$

Turbulent viscosity is calculated by the following formula:

$$\mu_t = \alpha^* \frac{\rho k}{\omega}, \quad \alpha^* = 1. \quad (33)$$

We need to define specific dissipation  $\omega$  to close the system. For this purpose, the differential transport equation for  $\omega$  is solved together with the equations for the components of the Reynolds stress tensor (15). According to the DRSM SO model, this equation is written as

$$\begin{aligned} \rho \frac{\partial \omega}{\partial t} + \rho u_k \frac{\partial \omega}{\partial x_k} = \\ = \frac{\partial}{\partial x_k} \left( \Gamma_\omega \frac{\partial \omega}{\partial x_k} \right) + G_\omega - Y_\omega + S_\omega, \end{aligned} \quad (34)$$

$$\Gamma_\omega = \mu + \mu_t / \sigma_\omega, \quad \sigma_\omega = 2. \quad (35)$$

The terms  $G_\omega$ ,  $Y_\omega$ ,  $S_\omega$  are found in accordance with the  $k$ - $\omega$  turbulence model [13].

According to the DRSM BSL model, an additional (cross-diffusion) term is added to Eq. (34) with respect to  $\omega$ :

$$D_\omega = 2(1 - F_1) \rho \frac{1}{\omega \sigma_{\omega,2}} \frac{\partial k}{\partial x_j} \frac{\partial \omega}{\partial x_j}, \quad (36)$$

where the values of the function  $F_1$  are calculated by Eqs. (20)–(22).

The remaining terms are calculated in accordance with the BSL  $k$ - $\omega$  turbulence model.

The gradient hypothesis (13), (14) is used to calculate the turbulent heat flux components required to close the averaged energy equation; the turbulent Prandtl number is taken equal to 0.85.

### Computational aspects

The computational domain is a rectangle on the  $xy$  plane. Its outer boundary is located 0.5 m away from the plate. The computational grid contained 200 cells along the  $y$  axis and 5 cells along the homogenous coordinate  $x$ . The grid was refined towards the plate surface to provide values less than unity for the dimensionless distance  $y^+$  from the center of the first near-wall cell to the wall for the entire computational time. The time step  $dt$  was taken equal to 0.005 s. To analyze the influence of the time step on the computational results, we also performed computations where the time step was twice as short.

The computations were run in the ANSYS Fluent 18.2 package. We used the non-iterative fractional step method to advance in time.

At the stage of preliminary computations, we analyzed the influence of numerical factors on the quality of the solutions obtained. Fig. 2,a shows the time dependence of  $y^+$  for all turbulence models. Evidently,  $y^+$  takes values less than unity throughout the computations. Fig. 2,b shows the time dependences for the boundary layer thickness  $\delta$  (calculated as integral thickness using Eq. (4)) for the SST  $k$ - $\omega$  model, obtained with different time steps. The differences are apparently insignificant.

### Computational results and discussion

**Influence of turbulence model on the growth in boundary layer thickness.** Fig. 3 shows the time dependences of integral thickness of the velocity boundary layer, as well as the relationships between temperature and velocity layer thicknesses; these dependencies were obtained

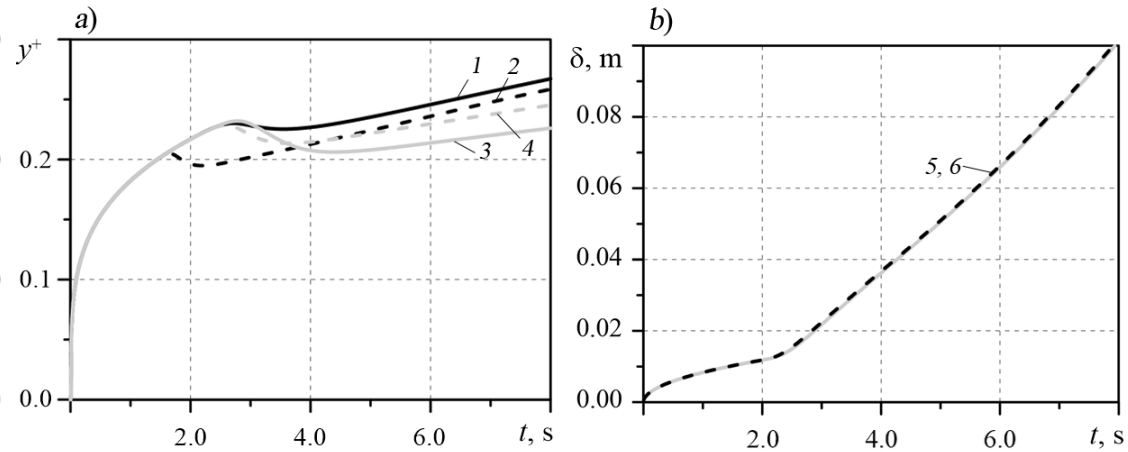


Fig. 2. Time dependences of dimensionless distance  $y^+$  (a) and boundary layer thickness (b). Comparison of computational results obtained with different models (a) and influence of time step (b). SST  $k-\omega$  (curve 1 and Fig. 2,b), RNG  $k-\varepsilon$  (curve 2), DRSM SO (3) and DRSM BSL (4) models were used; time steps  $dt = 0.0050$  (5) and  $0.0025$  s (6) were taken

using the given turbulence models. Fig. 3,a shows three pronounced phases in the evolution of the boundary layer: at first its thickness grows conforming to unsteady laminar layer patterns (until approximately 2 s in time), then we observe a short period with pseudo-processes of laminar-turbulent transition, and after that the boundary layer follows the turbulent flow regime (dependence of thickness  $\delta$  on time is close to linear).

Comparing the results obtained using different models, we can conclude that all models yield similar predictions for the phase of laminar boundary layer (as expected), while the transition point and the peculiarities in the growth of the boundary layer in the region with developed turbulence depend on the model applied.

The DRSM SO model yields the fastest thickness growth of the turbulent velocity boundary layer, while the SST  $k-\omega$  model yields the slowest growth. Apparently, the transition to turbulence (a point of characteristic change of dependences in Fig. 3) occurs simultaneously for all models except the RNG  $k-\varepsilon$  model, where this transition occurs much earlier. This model also differs by the behavior of the ratio between the temperature layer thickness and integral velocity layer thickness: while this variable reaches a nearly constant value at  $t > 3$  s in computations by other models, it decreases over time in this model.

**Comparison with the data of direct numerical simulation.** We compared the obtained computational results with the TDDNS results given in [4].

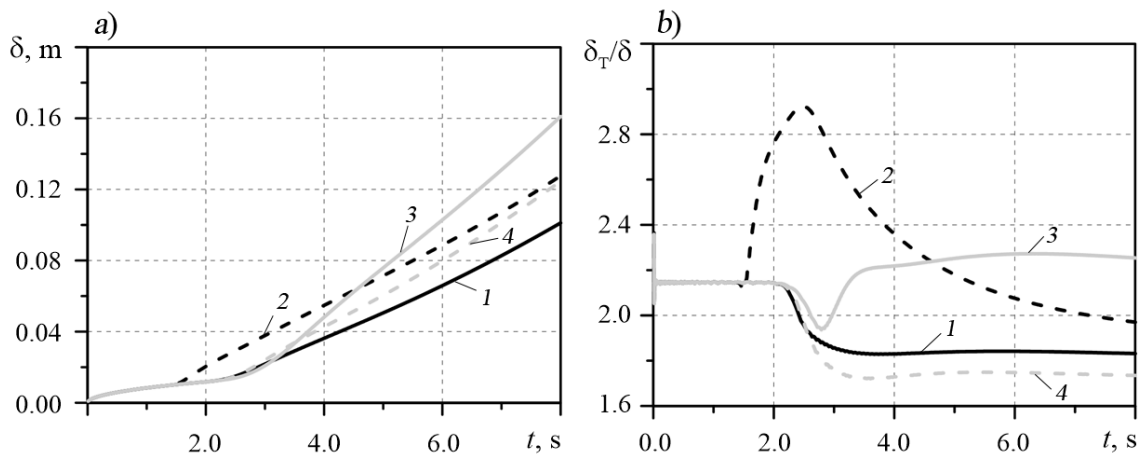


Fig. 3. Time dependences of integral thickness of velocity boundary layer (a) and ratios between temperature layer thickness and integral velocity layer thickness (b). Results are given for different models: SST  $k-\omega$  (1), RNG  $k-\varepsilon$  (2), DRSM SO (3), DRSM BSL (4)



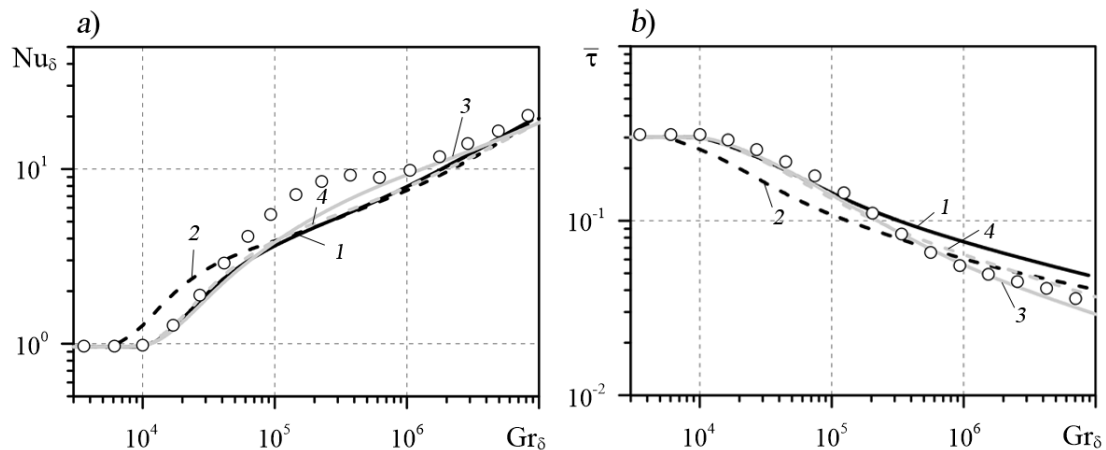


Fig. 4. Comparison of computed dependences of Nusselt number (a) and dimensionless friction (b) on Grashof number (lines) with TDDNS data (symbols);  $Nu_\delta$  and  $Gr_\delta$  were constructed based on boundary layer thickness. The curves are numbered the same as in Fig. 3

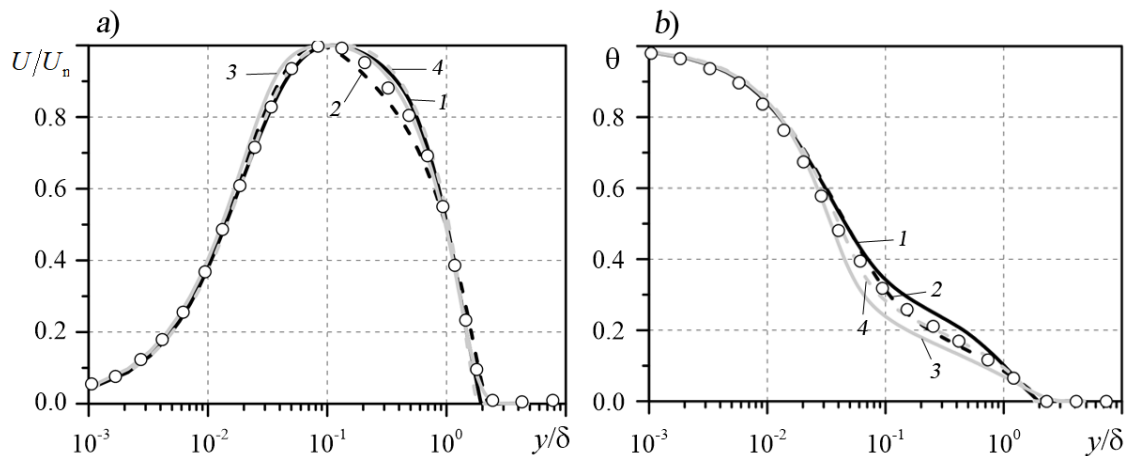


Fig. 5. Comparison of computed profiles of normalized velocity (a) and temperature (b) (lines) with TDDNS data (symbols);  $Gr_\delta = 5.94 \cdot 10^6$ . The curves are numbered the same as in Figs. 3 and 4

Fig. 4 shows the dependences for the Nusselt number and the dimensionless friction on the Grashof number constructed with respect to the integral thickness of the boundary layer (see Eqs. (6)–(8)), as well as the TDDNS results. We should note that the obtained dependences differ insignificantly and are in good agreement with the TDDNS data for the stages of laminar and fully turbulent flow. However, pronounced differences appear in the behavior of the curves at the stage of transition to turbulence: direct numerical simulation predicts a local maximum for the dependence of  $Nu_\delta$  on  $Gr_\delta$ , while RANS simulations indicate that  $Nu_\delta$  changes monotonically. Moreover, all the curves lie below the TDDNS points (a difference up to 50%). At the same time, all the

dependences obtained with different models generally exhibit the same behavior in all cases, except for the earlier turbulence transition predicted by the RNG  $k-\varepsilon$  model (as mentioned above).

Analyzing the distributions of dimensionless friction over time, we found that the DRSM SO model yields the best agreement with the direct numerical simulation data, while the SST  $k-\omega$  model predicts slightly overestimated values for developed turbulence.

Fig. 5 shows a comparison of the TDDNS data with the profiles of dimensionless velocity and temperature at  $Gr_\delta = 5.94 \cdot 10^6$  (corresponds to the stage of developed turbulent flow). The results indicate that the velocity profiles obtained in all computations are in fairly good agreement

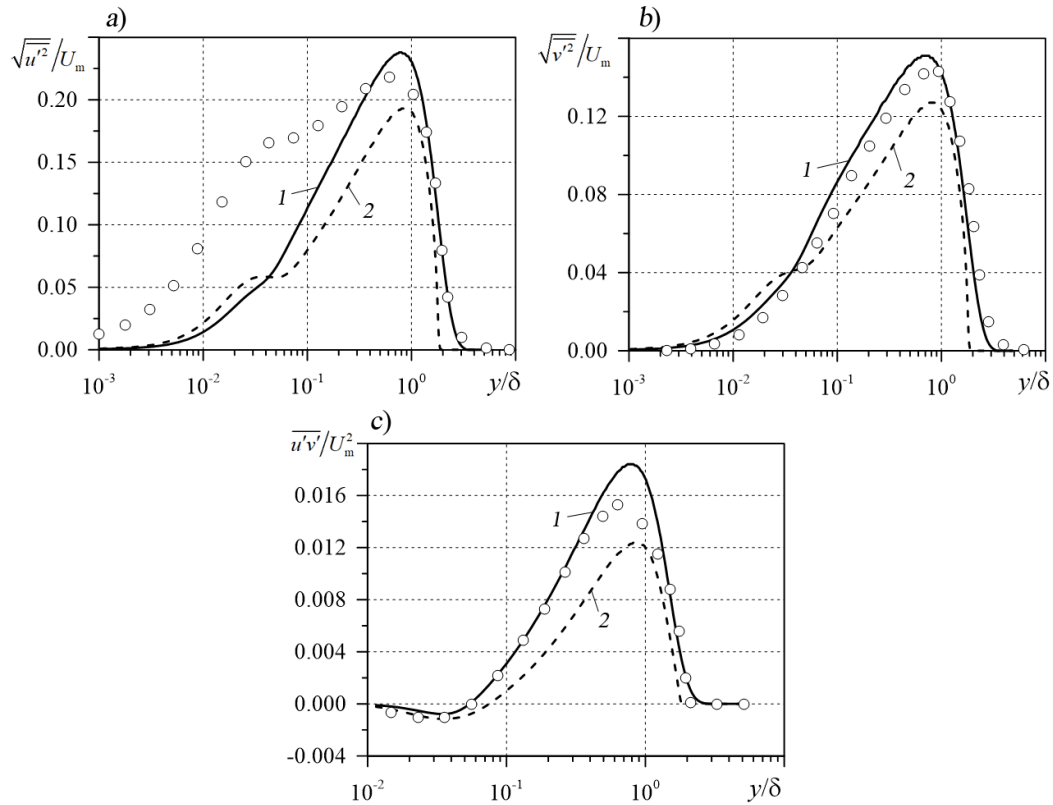


Fig. 6. Comparison of computed fluctuation intensity profiles for axial (a) and transverse (b) velocity components, and turbulent shear stress profile (c) (lines) with TDDNS data (symbols).

Results are given for different models: DRSM SO (1), DRSM BSL (2)

with the TDDNS data. There is some divergence with TDDNS only in the outer region of the boundary layer, where velocity decreases: the RNG  $k-\varepsilon$  yields underestimated results, while all the other models produce overestimated ones but these discrepancies do not exceed 5%. As for the temperature distribution, DRSM BSL and RNG  $k-\varepsilon$  produced the best agreement with the TDDNS data. Two other models yield significant differences in the outer region of the boundary layer: the SST  $k-\omega$  model yields a 15–20% overestimation of temperature, and the DRSM SO model a 20–25% underestimation.

Fig. 6 shows a comparison of the predicted distributions of stress tensor components along the  $y$  coordinate with the direct numerical simulation results for the computations performed using the Reynolds stress models (DRSM SO and DRSM BSL). The fluctuation intensity of the axial velocity component computed using both DRSM models appears to be significantly underestimated in the inner region of the boundary layer. The computed distributions of the remaining tensor components are in good agreement with the TDDNS data, with the DRSM SO model yielding the best agreement.

## Conclusion

We tested two semi-empirical RANS turbulence models based on Boussinesq's hypothesis and two Reynolds stress models for the problem of free convection developing near a suddenly heated vertical plate. The results obtained by Time-Developing Direct Numerical Simulation were used as test data [4].

Analyzing the results of the computations carried out with different models, we found that the rate with which the thickness of the boundary layer grows at the stage of laminar-turbulent transition and in the developed turbulent layer phase largely depends on the model used. The DRSM SO model predicts the fastest growth in the thickness of the velocity turbulent boundary layer, while the SST  $k-\omega$  model predicts the slowest growth rate.

The predictions for the dependences of the Nusselt number and the normalized friction on the Grashof number constructed based on the characteristic thickness of the growing layer are in good agreement with the TDDNS data for the stages of laminar and fully turbulent flow; the results obtained with different models differ insignificantly in this case. The DRSM SO



model yields a slightly better agreement with the TDDNS data for dimensionless friction.

The normalized velocity profiles computed for the turbulent layer phase are in a good agreement with the TDDNS data for all models considered. Analysis of the temperature profiles revealed that DRSM BSL and RNG  $k-\varepsilon$  are in best agreement with the test data. The DRSM SO and SST  $k-\omega$  models give significant differences in the outer region of the boundary layer (around 20 %).

The DRSM models give fairly accurate predictions for the profiles of turbulent shear stress and fluctuation intensity of the transverse

velocity component but the fluctuation intensity predicted for the axial velocity component turns out to be significantly underestimated in the inner region of the boundary layer.

The computations and analysis of the results allow to conclude that the DRSM SO model is capable of providing the best agreement with the test data [4], obtained using the TDDNS method out of all the RANS turbulence models under consideration.

The study was sponsored by Russian Science Foundation Grant no. 18-19-00082.

## REFERENCES

1. Ustinov M.V., Numerical modeling of laminar-turbulent transition in a boundary layer at a high freestream turbulence level, *Fluid Dynamics*. 41 (6) (2006) 923–937.
2. Huang Z.F., Zhou H., Luo J.S., Direct numerical simulation of a supersonic turbulent boundary layer on a flat plate and its analysis, *Science China. Ser. G: Physics, Mechanics & Astronomy*. 48 (5) (2005) 626 – 640.
3. Tsuji T., Kajitani T., Turbulence characteristics and heat transfer enhancement of a natural convection boundary layer in water along a vertical plate, *Proceedings of the 13th International Heat Transfer Conference (IHTC-13)*. Sydney, Australia, August 13–18. 2006. USA: Bigell House Inc, 2006.
4. Abedin M.Z., Tsuji T., Hattori Y., Direct numerical simulation for a time-developing natural-convection boundary layer along a vertical plate, *International Journal of Heat and Mass Transfer*. 52 (19–20) (2009) 1723–1734.
5. Abdollahzadeh M., Esmailpour M., Vizinho R., et al., Assessment of RANS turbulence models for numerical study of laminar-turbulent transition in convection heat transfer, *International Journal of Heat and Mass Transfer*. 115, B (December) (2017) 1288–1308.
6. Henkes R.A.W.M., Hoogendoorn C.J., Comparison of turbulence models for the natural convection boundary layer along a heated vertical plate, *International Journal of Heat and Mass Transfer*. 32 (1) (1989) 157–169.
7. Peeters T.W.J., Henkes R.A.W.M., The Reynolds-stress model of turbulence applied to the natural-convection boundary layer along a heated vertical plate, *International Journal of Heat and Mass Transfer*. 35 (2) (1992) 403–420.
8. Smirnov E.M., Levchenya A.M., Zhukovskaya V.D., RANS-based numerical simulation of the turbulent free convection vertical-plate boundary layer disturbed by a normal-to-plate circular cylinder, *International Journal of Heat and Mass Transfer*. 144 (December) (2019) 118573.
9. Chumakov Yu.S., Levchenya A.M., Khrapunov E.F., An experimental study of the flow in the area of influence of a cylinder immersed in the free convective boundary layer on a vertical surface, *St. Petersburg State Polytechnical University Journal. Physics and Mathematics*. 13 (1) (2020) 66–77.
10. Tsuji T., Nagano Y., Characteristics of a turbulent natural convection boundary layer along a vertical flat plate, *International Journal of Heat and Mass Transfer*. 31 (8) (1988) 1723–1734.
11. Menter F.R., Kuntz M., Langtry R., Ten years of industrial experience with the SST turbulence model turbulence, *Turbulence, Heat and Mass Transfer*, Vol. 4. *Proceedings of the Fourth International Symposium on Turbulence, Heat and Mass Transfer*, Antalya, Turkey, 12–17 October, 2003, Pp. 625–632.
12. Orszag S.A., Yakhot V., Flannery W.S., et al., Renormalization group modeling and turbulence simulations, In: *Proceedings of the International Conference on Near-Wall Turbulent Flows*, Tempe, Arizona, USA, 15–17 March (1993) 1031.
13. Wilcox D.C., *Turbulence modeling for CFD*, 2<sup>nd</sup> edition, DCW Industries, Inc. La Canada, California, 1998.
14. Menter F.R., Two-equation eddy-viscosity turbulence models for engineering applications, *AIAA Journal*. 32 (8) (1994) 1598–1605.

*Received 31.03.2020, accepted 29.04.2020.*



## THE AUTHORS

**LEVCHENYA Alexander M.**

*Peter the Great St. Petersburg Polytechnic University*

29 Politechnicheskaya St., St. Petersburg, 195251, Russian Federation

levchenya\_am@spbstu.ru

**TRUNOVA Seraphima N.**

*Peter the Great St. Petersburg Polytechnic University*

29 Politechnicheskaya St., St. Petersburg, 195251, Russian Federation

seraphimatr@yandex.ru

**KOLESNIK Elizaveta V.**

*Peter the Great St. Petersburg Polytechnic University*

29 Politechnicheskaya St., St. Petersburg, 195251, Russian Federation

kolesnik\_ev@mail.ru

## СПИСОК ЛИТЕРАТУРЫ

1. Устинов М.В. Численное моделирование ламинарно-турбулентного перехода в пограничном слое при повышенной степени турбулентности потока // Известия РАН. Механика жидкости и газа. 2006. № 6. С. 77–93.
2. Huang Z.F., Zhou H., Luo J.S. Direct numerical simulation of a supersonic turbulent boundary layer on a flat plate and its analysis // Science China. Ser. G: Physics, Mechanics & Astronomy. 2005. Vol. 48. No. 5. Pp. 626–640.
3. Tsuji T., Kajitani T. Turbulence characteristics and heat transfer enhancement of a natural convection boundary layer in water along a vertical plate // Proceedings of the 13th International Heat Transfer Conference (IHTC-13). Sydney, Australia, August 13–18. 2006. USA: Bigell House Inc, 2006.
4. Abedin M.Z., Tsuji T., Hattori Y. Direct numerical simulation for a time-developing natural-convection boundary layer along a vertical plate // International Journal of Heat and Mass Transfer. 2009. Vol. 52. No. 19–20. Pp. 1723–1734.
5. Abdollahzadeh M., Esmailpour M., Vizinho R., Younesi A., Pascoa J.C. Assessment of RANS turbulence models for numerical study of laminar-turbulent transition in convection heat transfer // International Journal of Heat and Mass Transfer. 2017. Vol. 115. Part B. December. Pp. 1288–1308.
6. Henkes R.A.W.M., Hoogendoorn C.J. Comparison of turbulence models for the natural convection boundary layer along a heated vertical plate // International Journal of Heat and Mass Transfer. 1989. Vol. 32. No. 1. Pp. 157–169.
7. Peeters T.W.J., Henkes R.A.W.M. The Reynolds-stress model of turbulence applied to the natural-convection boundary layer along a heated vertical plate // International Journal of Heat and Mass Transfer. 1992. Vol. 35. No. 2. Pp. 403–420.
8. Smirnov E.M., Levchenya A.M., Zhukovskaya V.D. RANS-based numerical simulation of the turbulent free convection vertical-plate boundary layer disturbed by a normal-to-plate circular cylinder // International Journal of Heat and Mass Transfer. 2019. Vol. 144. December. P. 118573.
9. Чумаков Ю.С., Левченя А.М., Храпунов Е.Ф. Экспериментальное исследование течения в зоне влияния цилиндра, погруженного в свободноконвективный пограничный слой на вертикальной поверхности // Научно-технические ведомости СПбГПУ. Физико-математические науки. 2020. Т. 13. № 1. С. 66–77.
10. Tsuji T., Nagano Y. Characteristics of a turbulent natural convection boundary layer along a vertical flat plate // International Journal of Heat and Mass Transfer. 1988. Vol. 31. No. 8. Pp. 1723–1734.
11. Menter F.R., Kuntz M., Langtry R. Ten years of industrial experience with the SST turbulence model // Turbulence, Heat and Mass Transfer. Vol. 4. Proceedings of the Fourth International Symposium on Turbulence, Heat and Mass Transfer. Antalya, Turkey. 12–17 October, 2003. Pp. 625–632.
12. Orszag S. A., Yakhot V., Flannery W. S., Boysan F., Choudhury D., Maruzewski J., Patel B. Renormalization group modeling and turbulence simulations // Proceedings of

the International Conference on Near-Wall Turbulent Flows, Tempe, Arizona, USA., 15–17 March 1993. P. 1031.

13. **Wilcox D.C.** Turbulence modeling for CFD. 2<sup>nd</sup> edition. La Canada, California: DCW

Industries, 1998. 457 p.

14. **Menter F. R.** Two-equation eddy-viscosity turbulence models for engineering applications // AIAA Journal. 1994. Vol. 32. No. 8. Pp. 1598–1605.

*Статья поступила в редакцию 31.03.2020, принята к публикации 29.04.2020.*

### СВЕДЕНИЯ ОБ АВТОРАХ

**ЛЕВЧЕНЯ Александр Михайлович** — кандидат физико-математических наук, доцент Высшей школы прикладной математики и вычислительной физики Санкт-Петербургского политехнического университета Петра Великого, Санкт-Петербург, Российская Федерация.

195251, Российская Федерация, г. Санкт-Петербург, Политехническая ул., 29

levchenya\_am@spbstu.ru

**ТРУНОВА Серафима Николаевна** — студентка магистратуры Института прикладной математики и механики Санкт-Петербургского политехнического университета Петра Великого, Санкт-Петербург, Российская Федерация.

195251, Российская Федерация, г. Санкт-Петербург, Политехническая ул., 29

seraphimatr@yandex.ru

**КОЛЕСНИК Елизавета Владимировна** — ассистент Высшей школы прикладной математики и вычислительной физики Санкт-Петербургского политехнического университета Петра Великого, Санкт-Петербург, Российская Федерация.

195251, Российская Федерация, г. Санкт-Петербург, Политехническая ул., 29

kolesnik\_ev@mail.ru

DOI: 10.18721/JPM.13204

УДК 530.1

## FRACTIONAL DIFFERENTIATION OPERATION IN THE FOURIER BOUNDARY PROBLEMS

*M.R. Petrichenko, T.A. Musorina*

Peter the Great St. Petersburg Polytechnic University, St. Petersburg, Russian Federation

We use the algebra of unbounded differentiation  $t$  operators acting on the ring of differentiable functions. The analytical representation of the fractional degree of the  $t$  operator is used to construct the resolvents of three boundary problems for the Fourier equation. Periodic solutions of limiting Fourier problems in the algebra of differentiation operators coincide with classical solutions. The  $t + 2$  extension is a continuous spectrum of the Fourier transform and allows us to obtain exact solutions of three limit problems for a domain of any dimension  $d > 1$ .

**Keywords:** differential equation, Abel–Liouville formula, ring of operators, inverse operator, carrier, distribution

**Citation:** Petrichenko M.R., Musorina T.A., Fractional differentiation operation in the Fourier boundary problems, St. Petersburg Polytechnical State University Journal. Physics and Mathematics. 13 (2) (2020) 33–43. DOI: 10.18721/JPM.13204

This is an open access article under the CC BY-NC 4.0 license (<https://creativecommons.org/licenses/by-nc/4.0/>)

## ОПЕРАЦИЯ ДРОБНОГО ДИФФЕРЕНЦИРОВАНИЯ В ПРЕДЕЛЬНЫХ ЗАДАЧАХ ФУРЬЕ

*М.Р. Петриченко, Т.А. Мусорина*

Санкт-Петербургский политехнический университет Петра Великого,

Санкт-Петербург, Российская Федерация

Применяется алгебра неограниченных операторов дифференцирования  $t$ , действующая над кольцом дифференцируемых функций. Аналитическое представление дробной степени оператора  $t$  используется для построения резольвент трех предельных задач для уравнения Фурье. Периодические решения предельных задач Фурье в алгебре операторов дифференцирования совпадают с классическими решениями. Расширение  $t + 2$  – непрерывный спектр преобразования Фурье, позволяет получить точные решения трех предельных задач для области любой размерности  $d > 1$ .

**Ключевые слова:** дифференциальное уравнение, формула Лиувилля, кольцо операторов, обратный оператор, носитель, распределение

**Ссылка при цитировании:** Петриченко М.Р., Мусорина Т.А. Операция дробного дифференцирования в предельных задачах Фурье // Научно-технические ведомости СПбГПУ. Физико-математические науки. 2020. Т. 13. № 2. С. 41–52. DOI: 10.18721/JPM.13204

Статья открытого доступа, распространяемая по лицензии CC BY-NC 4.0(<https://creativecommons.org/licenses/by-nc/4.0/>)

## Introduction

The classic theory of thermal stability of wall structures developed by Seliverstov [1] uses the methods of Fourier series theory and, in a certain sense, originates from these methods. This is hardly accidental, as the author of the study was an expert in Fourier series theory. The methods of trigonometric series are sufficient if the boundary temperature distributions of external sources belong to  $L_p$  ( $p > 1$ ) on a set of times  $t$ . Fourier series converge almost everywhere on such a set. However, the above condition is redundant for applied problems. While the temperature distribution of the sources is typically continuous at best, according to Titchmarsh [2], it was impossible to prove similar statements for convergence of Fourier series almost everywhere [2, pp. 420–421]. The methods for expanding Fourier series are inconvenient for mixed boundary problems, especially if the external heat source depends on parameter  $t$  (time).

This study focuses on the methods for solving boundary problems for the Fourier equation in the form of equalities containing functions of differential operators, comparing the distributions obtained with the known exact solutions.

The significance of our study is in offering potential solutions for solving problems related to thermal stability of construction barriers.

## Key approaches to obtaining the solutions

We have formulated and proved the following statements.

1. The solutions for the second and third boundary problems for the Fourier equation are obtained by solving the first boundary problem inverting the differentiation operator.

2. Support measures for the distribution of the primitive  $x(t, s)$ ,  $\delta_x$  and the primitive derivative  $y := -\partial x / \partial s$ ,  $\delta_y$  satisfy the inequality  $\delta_y / \delta_x \geq 1$  in the first-kind boundary problem.

3. Increasing the dimension of the domain does not increase the support measures of the distribution.

Statement 3 implies that the thermal resistance of a half-space does not exceed the thermal resistance of a half-plane. In turn, the thermal resistance of a half-plane does not exceed the thermal resistance of a half-line.

As an auxiliary technique, we use the following representation of the Taylor series (shift) for functions  $f(t)$ , analytic on half-line  $t > 0$ ,  $f \in C^\infty(0, \infty) \setminus$

$$f(t+s) = \exp(s\partial_t) f(t),$$

and its inversion

$$f(t) = \exp(-s\partial_t) f(t+s),$$

containing integer powers of the differential operator  $\partial_t$ .

**Simple expressions for measures of the supports  $\delta_{x,y}$**

Using the operator norms of fractional powers of the operator  $\partial_t$  allows to obtain simple expressions for measures of the supports  $\delta_{x,y}$ .

**Preliminary considerations.** Fractional differentiation is related to the solution of the Cauchy problem for an ordinary differential equation of arbitrary positive integer (natural) order  $s > 0$ .

Let

$$t \in \mathcal{D}(x) \subset \mathcal{C}^{(s)}(R^1), y \in \mathcal{G}(x) \subseteq \mathcal{L}_1^{(loc)}(R^1).$$

then the Cauchy problem

$$\begin{aligned} \partial_t^s x &= y, \partial_t^r x(0) = 0, \\ r &= 0(1)s - 1, \partial_t := d/dt \end{aligned} \quad (1)$$

has the following solution [3]:

$$x(t) = \frac{1}{(s-1)!} \int_0^t (t-\tau)^{s-1} y(\tau) d\tau, \quad (2)$$

or, in symbolic form,

$$x(t) = \partial_t^{-s} y(t). \quad (2a)$$

Given non-integer  $s$ , Eq. (2) can be extended:

$$\begin{aligned} \partial_t^{-s} y(t) &= \frac{1}{\Gamma(s)} \int_0^t (t-\tau)^{s-1} y(\tau) d\tau, \\ \Gamma(s) &:= (s-1)!, s > 0. \end{aligned} \quad (2b)$$

If  $s = \sigma + i\rho$ ,  $\sigma > 0$ , Eq. (2b) takes the form

$$\begin{aligned} \partial_t^{-(\sigma+i\rho)} y(t) &= \frac{1}{\Gamma(\sigma+i\rho)} \times \\ &\times \int_0^t (t-\tau)^{\sigma-1} \left( \cos(\rho \ln(t-\tau)) + \right. \\ &\left. + i \sin(\rho \ln(t-\tau)) \right) y(\tau) d\tau. \end{aligned}$$

Let  $s=1/2$ . Then, by virtue of expression (2b), we obtain Abel's formula:



$$\begin{aligned}\partial_t^{-1/2}y(t) &= \frac{1}{\sqrt{\pi}} \int_0^t \frac{y(\tau)}{\sqrt{t-\tau}} d\tau = \\ &= \frac{2}{\sqrt{\pi}} \int_0^{\sqrt{t}} y(t-z^2) dz.\end{aligned}\quad (2c)$$

The formula obtained (2c) can be used to calculate the derivatives of the powers of  $t$ , for instance,

$$\begin{aligned}\partial_t^{-1/2}1 &= 2\sqrt{t/\pi}, \partial_t^{1/2}1 = 1/\sqrt{t\pi}, \\ \partial_t^{-1/2}t &= \frac{4\sqrt{t^3}}{3\sqrt{\pi}}, \partial_t^{1/2}t = \frac{2\sqrt{t}}{\sqrt{\pi}},\end{aligned}$$

furthermore, for any  $n > 0$ :

$$\begin{aligned}\partial_t^{-1/2}t^n &= t^{n+1/2} \frac{\Gamma(n+1)}{\Gamma(n+3/2)}, \\ \partial_t^{1/2}t^n &= t^{n-1/2} \frac{(n+1/2)\Gamma(n+1)}{\Gamma(n+3/2)}.\end{aligned}$$

Clearly, the kernel of the operator  $\partial_t^{-s}$ ,  $N(\partial_t^{-s})$ , contains only one element,  $y = 0$ , for any  $0 < s < 1$ .

**Commutation.** By definition, the following expression holds true:

$$\begin{aligned}\partial_t^{1/2}y(t) &= \frac{1}{\sqrt{\pi}} \frac{d}{dt} \int_0^t \frac{y(t-\tau)}{\sqrt{\tau}} d\tau = \\ &= \frac{y(0)}{\sqrt{t\pi}} + \frac{1}{\sqrt{\pi}} \int_0^t \frac{\partial_t y(t-\tau)}{\sqrt{\tau}} d\tau = \\ &= \frac{y(0)}{\sqrt{t\pi}} + \partial_t^{-1/2}(\partial_t y(t)),\end{aligned}$$

or

$$(\partial_t \partial_t^{-1/2} - \partial_t^{-1/2} \partial_t) y(t) = \frac{y(0)}{\sqrt{t\pi}}. \quad (3)$$

If  $y(0) = 0$ , then the operator  $\partial_t$  commutes with its negative fractional power, e.g.,  $-1/2$ :

$$(\partial_t \partial_t^{-1/2} - \partial_t^{-1/2} \partial_t) y(t) = 0, \quad (3a)$$

or, in symmetric form,

$$\partial_t^{-1/2} = \partial_t^{-1} \partial_t^{-1/2} \partial_t, \partial_t = \partial_t^{-1/2} \partial_t \partial_t^{1/2}.$$

It follows then that the operator  $\partial_t$  and its fractional powers are self-similar in case of commutation.

If

$$y(t \pm t_0) - y(t) = 0, \forall |t| > 0, t_0 > 0$$

in the Cauchy problem (1) is a primitive period, and a periodic solution is sought, so that

$$x(t \pm t_0) - x(t) = 0, \forall |t| > 0,$$

the periodic condition can be replaced by the homogeneous condition [3]:

$$\partial_t^r x(-\infty) = 0, \quad r = 0(1)s - 1,$$

and then the solution to the periodic Cauchy problem takes the form

$$\begin{aligned}\partial_t^{-s}x(t) &= \frac{1}{\Gamma(s)} \int_{-\infty}^t (t-\tau)^{s-1} y(\tau) d\tau = \\ &= \frac{1}{\Gamma(s)} \int_0^\infty \omega^{s-1} y(t-\omega) d\omega.\end{aligned}$$

Let  $s = 1/2$ , and then the previous formula takes the form

$$\partial_t^{-1/2}x = \frac{2}{\sqrt{\pi}} \int_0^\infty y(t-z^2) dz. \quad (2d)$$

Thus, the commutator in the periodic boundary problem equals zero, and the fractional power of the operator  $\partial_t$  is permutable with its inverse power.

Relations (2)–(2d) are known as the Abel–Liouville identities [13]. Applications to different mechanics problems are presented in Caputo's study (unfortunately, the original text was unavailable to us but it is cited in many later studies, for example, in [5–17] and references therein).

**Extension 1.** For any  $s > 0$ , inversion of the fractional differential operator has the form

$$\partial_t^{-s}x = \frac{1}{\Gamma(s+1)} \int_0^t y(t-z^{1/s}) dz$$

for a non-periodic problem and

$$\partial_t^{-s}x = \frac{1}{\Gamma(s+1)} \int_0^\infty y(t-z^{1/s}) dz$$

for a periodic one.

Indeed, if

$$y(t \pm 1) - y(t) = 0, \forall |t| > 0,$$

then the Cauchy condition for all derivatives takes the Lyapunov form:



$$\partial_t^s x(-\infty) = 0.$$

**Extension 2.** Let us consider an equation depending on the parameter  $\lambda$ :

$$(\partial_t - \lambda)x(t) = y(t).$$

Evidently, the kernel  $N(\partial_t - \lambda)$  of the operator  $\partial_t - \lambda$  consists of the exponents  $x(t) = \exp(\lambda t)$ . Therefore, the solution to the equation is

$$x = (\partial_t - \lambda)^{-1} y + z, z \in \mathcal{U}(\partial_t - \lambda).$$

The equation

$$(\partial_t - \lambda)^n x(t) = y(t)$$

has the solution

$$x(t) = (\partial_t - \lambda)^{-n} y(t) + (z),$$

$$(z) \in \mathcal{U}((\partial_t - \lambda)^n);$$

evidently,

$$\mathcal{U}(\partial_t - \lambda) \subset \mathcal{U}(\partial_t - \lambda)^2 \subset \dots \subset \mathcal{U}(\partial_t - \lambda)^n.$$

Integral representation of the solution to the homogeneous Cauchy problem has the form

$$x(t) = \frac{1}{(n-1)!} \int_0^t (t-\tau)^{n-1} \exp(\lambda(t-\tau)) y(\tau) d\tau.$$

Here the kernel consists of functions

$$P_{n-1}(t) \exp(\lambda t) = z(t) \in \mathcal{U}(\partial_t - \lambda)^n,$$

where  $P_s(t)$  is a polynomial of degree  $s$ .

Let us continue solving the homogenous Cauchy problem for fractional values of  $n$ :

$$\begin{aligned} x(t) &= (\partial_t - \lambda)^{-n} y(t) = \\ &= \frac{1}{\Gamma(n)} \int_0^t (t-\tau)^{n-1} \exp(\lambda(t-\tau)) y(\tau) d\tau. \end{aligned}$$

Let  $n=1/2$ ; then

$$\begin{aligned} x(t) &= (\partial_t - \lambda)^{-1/2} y(t) = \\ &= \frac{1}{\sqrt{\pi}} \int_0^t \frac{\exp(\lambda(t-\tau))}{\sqrt{t-\tau}} y(\tau) d\tau = \\ &= \frac{2}{\sqrt{\pi}} \int_0^{\sqrt{t}} \exp(\lambda z^2) y(t-z^2) dz. \end{aligned}$$

It is sufficient for integrals to converge that the following condition hold true for the real part of the number  $\lambda$ :  $\text{Re} \lambda < 0$ .

Similarly, the periodic solution takes the form

$$\begin{aligned} x(t) &= (\partial_t - \lambda)^{-1/2} y(t) = \\ &= \frac{2}{\sqrt{\pi}} \int_0^\infty \exp(\lambda z^2) y(t-z^2) dz. \end{aligned}$$

**Extension 3.** Given arbitrary  $n > 0$ , the inversion equations for the fractional powers of the operator take the form:

$$x(t) = \frac{1}{\Gamma(n+1)} \int_0^{t^n} \exp(\lambda z^{1/n}) y(t-z^{1/n}) dz,$$

for a non-periodic problem and

$$x(t) = \frac{1}{\Gamma(n+1)} \int_0^\infty \exp(\lambda z^{1/n}) y(t-z^{1/n}) dz,$$

for a periodic problem, while  $\text{Re} \lambda < 0$ .

This extension is thoroughly explored in monograph [13] but the authors but apparently did not use the trivial substitution  $\sqrt[n]{t} = z$ . This substitution is convenient because it allows to represent the fractional differential operator as a probability integral. Indeed, the integrand in Eq. (2d) can be expanded in a Taylor series:

$$x(t-z^2) = \exp(-z^2 \partial_t) x(t),$$

then the left-hand side of Eq. (2d) is obtained immediately.

Nash's and Kuiper's studies (discussed in Gromov's monograph [18]) formulated the so-called  $h$ -principle: differential operators  $R$  connecting partial derivatives are regarded as algebraic relations for partial derivatives.

The  $h$ -principle is substantiated in [18], accompanied by a list of publications up to 1990. Sobolev spaces of functions with (generalized) derivatives of fractional order were considered by Slobodetskii in a series of studies [19, 20], developing Bakelman's earlier ideas [21] on the geometric theory of equations.

### Analysis of Fourier boundary problems for half-line $s > 0$

**First boundary problem.** Let us consider the first boundary problem in an unbounded domain  $t > 0$ ,  $s > 0$ :

$$\frac{\partial x}{\partial t} = \frac{\partial^2 x}{\partial s^2}, x(t, 0) = x_0(t). \quad (4)$$

We find a formal solution to this boundary problem by separation of variables.





Let

$$x(t, s) = \exp(-s\alpha) x_0(t), \quad (5)$$

While the parameter  $\alpha > 0$ , which guarantees a decrease in  $x(t, s)$ , uniform with respect to  $t$ . In this case, substituting equality (5) in the equation of problem (4) leads to the condition

$$\exp(-s\alpha)(\partial_t - \alpha^2) x_0(t) = 0,$$

from which it follows that  $\alpha = \partial_t^{1/2}$ , and, by virtue of equality (5), the solution of boundary problem (4) has the form

$$x(t, s) = \exp(-s\partial_t^{1/2}) x_0(t). \quad (6)$$

**Verification of solution (6).** Step 1. The classical solution for boundary problem (4) has the following form:

$$x(t, s) = \frac{2}{\sqrt{\pi}} \int_0^{\frac{s}{2\sqrt{t}}} x_0\left(t - \frac{s^2}{4z^2}\right) \exp(-z^2) dz. \quad (7)$$

Let us expand the function  $x_0\left(t - \frac{s^2}{4z^2}\right)$  into a Taylor series in powers of  $\frac{s^2}{4z^2}$ :

$$x_0\left(t - \frac{s^2}{4z^2}\right) = \exp\left(-\frac{s^2\partial_t}{4z^2}\right) x_0(t).$$

Solution (7) then takes the form [4]:

$$x(t, s) = \frac{2}{\sqrt{\pi}} \int_0^{\frac{s}{2\sqrt{t}}} \exp\left(-z^2 - \frac{s^2\partial_t}{4z^2}\right) dz (x_0(t)). \quad (7a)$$

However, it is known from the course on analysis of infinitely small quantities, developed by de la Vallée Poussin [3], that

$$\frac{2}{\sqrt{\pi}} \int_0^{\frac{s}{2\sqrt{t}}} \exp(-u^2 - \alpha/u^2) du = \exp(-2\sqrt{\alpha}).$$

Therefore, if the lower limit in the integral in (7a) equals zero, then Eq. (7a) coincides with Eq. (6). Thus, Eq. (7a) takes the following form:

$$x(t, s) = \exp(-s\partial_t^{1/2}) x_0(t) - \frac{2}{\sqrt{\pi}} \int_0^{\frac{s}{2\sqrt{t}}} \exp\left(-z^2 - \frac{s^2\partial_t}{4z^2}\right) dz \cdot x_0(t). \quad (7b)$$

Consequently, given that  $\frac{s}{2\sqrt{t}} \ll 1$ , Eqs. (7b) and (6) yield close results.

Step 2. If  $x_0(t)$  is a periodic time function, i.e.,

$$x_0(t \pm t_0) = x_0(t),$$

where  $t_0 < 0$  is a primitive period, then, instead of solutions (7), (7a) and (7b), we obtain a solution in the form

$$x(t, s) = \frac{2}{\sqrt{\pi}} \int_0^{\frac{s}{2\sqrt{t}}} x_0\left(t - \frac{s^2}{4z^2}\right) \exp(-z^2) dz, \quad (7c)$$

and solutions (7c) and (6) are then identical. To confirm this, it is sufficient to expand the integrand in solution (7c) in a Taylor series:

$$\begin{aligned} x(t, s) &= \frac{2}{\sqrt{\pi}} \int_0^{\frac{s}{2\sqrt{t}}} \exp\left(-z^2 - \frac{s^2\partial_t}{4z^2}\right) dz \cdot x_0(t) = \\ &= \exp(-s\partial_t^{1/2}) x_0(t), \end{aligned}$$

which proves the identity.

Thus, Eq. (6) and its corollaries hold true for a boundary value  $x(t, 0) = x_0(t)$ , periodic with respect to the parameter  $t$ , i.e., for the solution of the quasi-steady boundary problem of thermal conductivity.

**The second boundary problem.** Eq. (6)

implies that the derivative  $y(t, s) = -\frac{\partial x}{\partial s}$  is calculated as follows:

$$y(t, s) = \partial_t^{1/2} \exp(-s\partial_t^{1/2}) x_0(t). \quad (8)$$

Let  $s=0$ . By virtue of expression (8),

$$\begin{aligned} y(t, 0) &:= y_0(t) = \partial_t^{1/2} x_0(t), \\ x_0(t) &= \partial_t^{-1/2} y_0(t), \end{aligned}$$

and by virtue of solution (6), the solution to the second boundary problem takes the form

$$x(t, s) = \exp(-s\partial_t^{1/2}) \partial_t^{-1/2} y_0(t). \quad (9)$$

**The third boundary problem.** The given problem is formulated as follows for the Fourier equation:

$$\left(\frac{\partial x}{\partial s}\right)_{s=0} + \beta(x_e - x_0) = 0, \quad (10)$$

where  $x_e$  is the potential of an external source,  $\beta$  is the transfer coefficient.

Equality (10) then takes the form

$$(\partial_t + \beta) x_0(t) = \beta x_e,$$

which implies that

$$\begin{aligned} x_0(t) &= (\partial_t + \beta)^{-1} (\beta x_e), \\ x(t, s) &= \exp(-s \partial_t^{1/2}) \left( (\partial_t + \beta)^{-1} (\beta x_e) \right). \end{aligned} \quad (11)$$

So, if the boundary parameters  $y_0$ ,  $x_e$ ,  $\beta$  are periodic time functions, then solutions (9) and (11) coincide with the classical solutions.

### Measure of distribution supports for half-line $s > 0$

We define the support  $\text{supp}(x(t, s))$  of the distribution  $x(t, s)$  as a set of values of the coordinate  $s$  on which the distribution  $x(t, s)$  is concentrated. If the distribution  $x(t, s)$  has continuous density, we can define the support as the thickness of the  $x$ -layer with respect to the density limit,  $x_0(t)$ :

$$\delta_x(t) := \frac{1}{x_0} \int_0^\infty x(t, s) ds.$$

By virtue of solution (6), the thickness of the  $x$ -layer is expressed as

$$\delta_x(t) = \frac{\partial_t^{-1/2} x_0(t)}{x_0(t)}.$$

If the distribution  $x_0(t)$  is periodic, the given thickness follows the expression

$$\delta_x(t) = \frac{2}{\sqrt{\pi} x_0(t)} \int_0^\infty x_0(t - z^2) dz.$$

Similarly, the thickness of  $y$ -layer is expressed as

$$\begin{aligned} \delta_y(t) &:= \frac{1}{y_0(t)} \int_0^\infty y(t, s) ds = \frac{x_0(t)}{\partial_t^{1/2} x_0(t)} = \\ &= \frac{\sqrt{\pi}}{2} \frac{x_0(t)}{\int_0^\infty \dot{x}(t - z^2) dz}, \end{aligned}$$

where the dot denotes the derivative with respect to the entire argument  $t - z^2$ .

**Lemma 1.** *The ratio between the layer thicknesses (form parameter), expressed by the formula*

$$\begin{aligned} \delta_y / \delta_x &= \frac{x_0^2}{\partial_t^{1/2} x_0 \cdot \partial_t^{-1/2} x_0} = \\ &= \frac{\pi x_0^2(t)}{2} \left( \frac{d}{dt} \left( \int_0^\infty x_0(t - z^2) dz \right)^2 \right)^{-1}, \end{aligned}$$

has a value of at least unity for any bounded distribution  $x_0(t)$ .

**Proof.** Indeed, the above expression can be written as

$$\delta_y / \delta_x = \frac{\pi}{2} \frac{\partial_t^{-1} x_0^2}{(\partial_t^{-1} x_0)^2} \geq \frac{\pi}{2} > 1.$$

Here we use the Cauchy inequality to estimate the integrals.

To illustrate that the lemma proved holds true, let us provide an example which allows to calculate the support lengths directly. The distribution  $x(t, s)$  for a straight line (ray)  $s > 0$  takes the form

$$x(t, s) = \text{erfc}\left(\frac{s}{2\sqrt{t}}\right),$$

where

$$x(t, 0) : x_0(t) - 1 = x(0, s) = 0.$$

Then we obtain the following equations:

$$y(t, s) := -\frac{\partial x}{\partial s} = \frac{1}{\sqrt{t\pi}} \exp\left(-\frac{s^2}{4t}\right),$$

$$y(t, 0) := y_0(t) = \frac{1}{\sqrt{t\pi}},$$

$$\delta_x = 2\sqrt{\frac{t}{\pi}},$$

$$\delta_y = \sqrt{t\pi},$$

$$\delta_y / \delta_x = \pi / 2.$$

The lemma is proved.

**Lemma 2.** *Let*

$$f(x) := \int_x^\infty \exp(-at^m) dt, f(0) = \int_0^\infty \exp(-at^m) dt,$$

where  $a, m$  are positive constants, and

$$-f'(x) := \phi(x) = \exp(-ax^m), -f(0) = 1.$$

Then the ratio between the support lengths of function  $f(x)$  and its derivative  $f'(x) = \phi(x)$  ( $\delta_\phi$  and  $\delta_f$ , respectively) has a value no less than unity:

$$\mathfrak{K} := \delta_\phi / \delta_f = \frac{1}{m} \frac{(\Gamma(1/m))^2}{\Gamma(2/m)} \geq 1.$$

**Proof.** Indeed, the following equations hold true:



$$\delta_f = \frac{\int_0^\infty t \exp(-at^m) dt}{\int_0^\infty \exp(-at^m) dt},$$

$$\delta_\varphi = \int_0^\infty \exp(-at^m) dt,$$

$$\mathfrak{H} = \frac{\left( \int_0^\infty \exp(-at^m) dt \right)^2}{\int_0^\infty t \exp(-at^m) dt},$$

and it remains to rewrite the integrals in Euler form.

The Lemma is proved.

The results of Lemma 2 can be rewritten differently, if we use a duplication formula for the function  $\Gamma(z)$  [2, 3]:

$$\mathfrak{H} = \frac{\pi}{2^{2/m-1} m} \frac{\Gamma(1/m)}{\Gamma(1/m + 1/2)}.$$

Let  $m = 1$ , then  $\mathfrak{H} = 1$ ; if  $m = 2$ , then  $\mathfrak{H} = \pi/2$ . It is easy to use the asymptotic form of the  $\Gamma$ -function to prove that  $\mathfrak{H} \rightarrow \infty$  as  $m \rightarrow \infty$ .

Thus, the measure (length) of the distribution support for decreasing integer distributions of the order  $m > 1$ , the measure (length) of the distribution support does not exceed the measure of the distribution support derivative.

The quantity  $\delta_y/\delta_x$  in problems of thermal conductivity of wall structures is the ratio of absolute to effective thermal resistance of one-dimensional heat conducting medium (of the half-line  $s > 0$ ) [22].

#### Fourier boundary problems

for half-plane  $s > 0$ ,  $|u| < \infty$

Let

$$D(x) = (t, s, u: t > 0, s > 0, |u| < \infty),$$

where  $u$  is the second coordinate.

The Fourier equation

$$\frac{\partial x}{\partial t} = \nabla_{s,u}^2 x$$

and the first-kind boundary condition

$$x(t, 0, u) = x_0(t, u)$$

are satisfied.

We define the transformation

$$x(t, s, u), \hat{x} = \hat{x}(t, s)$$

that is integral with respect to the argument  $u$  as

$$\hat{x}(t, s) := \int_{-\infty}^{\infty} x(t, s, v) \exp(i\omega v) dv,$$

where the circumflex  $\hat{\phantom{x}}$  denotes the Fourier transform of the function  $x(t, s, u)$  with respect to the argument  $u$ .

The Fourier transform of the function  $x(t, s, u)$  satisfies the partial differential equation:

$$\left( \frac{\partial}{\partial t} + \omega^2 \right) \hat{x} = \frac{\partial^2 \hat{x}}{\partial s^2}. \quad (12)$$

Eq. (11) can be obtained from Eq. (4) by replacing the operator  $\partial_t$  with the operator

$$\partial_{t,\omega} = \partial_t + \omega^2,$$

where  $\omega$  is the spectral number.

The first-kind boundary condition is formulated as

$$\hat{x}(t, 0) = \hat{x}_0(t). \quad (13)$$

Then, similar to solution (6), we obtain:

$$\hat{x}(t, s) = \exp(-s \partial_{t,\omega}^{1/2}) \hat{x}_0(t). \quad (6a)$$

Next, the solution to the second boundary problem has the form

$$\hat{x}(t, s) = \exp(-s \partial_{t,\omega}^{1/2}) \partial_{t,\omega}^{-1/2} \hat{y}_0(t),$$

$$\hat{y}_0(t) := - \left( \frac{\partial \hat{x}}{\partial s} \right)_{s=0}. \quad (9a)$$

Finally, the solution to the third boundary problem follows the expression

$$\hat{x}(t, s) = \exp(-s \partial_{t,\omega}^{1/2}) \times$$

$$\times \left( \left( \partial_{t,\omega} + \beta \right)^{-1} \left( \beta \hat{x}_e \right) \right). \quad (11a)$$

As a result, Eqs. (6a), (9a) and (11a) coincide with the exact solutions of the periodic boundary problems and are obtained from the solutions to one-dimensional problems by replacing the operator  $\partial_t$  with the operator  $\partial_{t,\omega}$ .

**Generalization of analysis.** The Fourier equation with respect to the coordinates  $s, u_1, \dots, u_{d-1}$  for the case  $d > 1$  has the following form:

$$\frac{\partial x}{\partial t} = \frac{\partial^2 x}{\partial s^2} + \sum_{i=1}^{d-1} \frac{\partial^2 x}{\partial u_i^2},$$

Applying  $(d - 1)$ -fold Fourier transform, the equation is written as

$$\left( \frac{\partial}{\partial t} + \Omega^2 \right) \hat{x} = \frac{\partial^2 \hat{x}}{\partial s^2}, \Omega^2 := \sum_{i=1}^{d-1} \omega_i^2.$$

The solution to the first boundary problem in traditional notation has the form

$$\hat{x}(t, s) = \exp(-s \partial_{t, \Omega}^{1/2}) \hat{x}_0, \quad (6b)$$

where we introduce the following notation for  $(d - 1)$ -fold Fourier transform

$$\begin{aligned} \hat{x}_0(t, \omega_1, \dots, \omega_{d-1}) &= \frac{1}{(2\pi)^{d-1}} \times \\ &\times \int_0^\infty dv_1 \dots \int_0^\infty dv_{d-1} x_0(t, 0, v_1, \dots, v_{d-1}) \times \\ &\times \exp\left(i \sum_{i=1}^{d-1} \omega_i v_i\right). \end{aligned}$$

The inverse Fourier transform should be represented as

$$\begin{aligned} x_0(t, 0, u_1, \dots, u_{d-1}) &= \int_0^\infty d\omega_1 \dots \int_0^\infty d\omega_{d-1} \hat{x}_0 \times \\ &\times (t, \omega_1, \dots, \omega_{d-1}) \exp\left(-i \sum_{i=1}^{d-1} \omega_i u_i\right). \end{aligned}$$

If  $x_0(t, 0, u_1, \dots, u_{d-1})$  is a periodic function of the argument  $t$ , then Eq. (6b) coincides with the exact solution to the first Fourier boundary problem. Eqs. (9a) and (11a) also hold true if the subscript  $\omega$  is replaced with  $\Omega$ .

Let us return to the thermal conductivity problem mentioned at the end of the section "Measure of distribution supports for half-line  $s > 0$ ". It can be proved that if the dimension of an infinite domain occupied by scalar

heat-conducting medium increases, its thermal resistance does not increase with an increase in the dimension of the domain  $d > 1$ .

Indeed, for any value  $d > 1$ ,

$$\left\| \partial_t + \sum_{1 \leq i \leq d-1} \omega_i^2 \right\|^{-s} \leq \left\| \partial_t^{-s} \right\| \leq \left\| \partial_t \right\|^{-s}.$$

## Conclusion

Using the algebra of unbounded differentiation operators and reviewing the results of the analysis carried out, we have drawn the following conclusions.

1. The unbounded operator of fractional differentiation over a ring of continuous functions can be inverted (known as the Abel–Liouville formula). The inverse operator is bounded on functions from the set  $L_1(0, t)$ , where  $t \leq \infty$ . The solutions for the second and third Fourier boundary problems are obtained by inverting the differentiation operator of the first boundary problem.

2. The operator  $\partial_t$  in a quasi-steady (periodic) boundary problem commutes with any fractional inverse power. There are no operator powers in aperiodic commutation problems.

3. In case of decreasing integer distributions of order  $m > 1$ , the support measure (length) of the distribution  $x(t, s)$  does not exceed the support measure corresponding to the derivative of the distribution  $y(t, s) = \partial x / \partial s$ . In other words, the thickness of the heat flux boundary layer (decreasing distribution of order  $m > 1$ ) should be no less than the thickness of the temperature boundary layer.

4. Increasing the dimension of the domain  $D(x)$  of the sought-for function  $x(t, s)$  does not increase the measures of the supports  $\text{supp}(x)$  and  $\text{supp}(y)$ , where  $y = \|\nabla x\|$  ( $\|\nabla x\|$  is the Euclidian norm of the scalar function  $x(t, s)$ ). The support measure (length) of the distribution  $x(t, s)$  does not exceed the support measure corresponding to the derivative of the distribution for any decreasing integer distributions of order  $m > 1$ . Therefore, the thermal resistance of the domain  $D(x)$  does not increase along with increasing dimension: the heat flux vector  $\mathbf{y}$  gains an additional component (additional degree of freedom).



## REFERENCES

1. **Selivestrov G.A.**, Mathematical theory of thermostable, *Matematicheskii Sbornik*. 38 (3–4) (1931) 70–73.
2. **Titchmarsh E.C.**, The theory of functions, 2nd Ed., Oxford University Press, Oxford, 1939.
3. **De la Vallée-Poussin Ch.-J.**, Cours d'analyse infinitésimale, Paris, 1914.
4. **Zhukova-Malitskaya G.K., Kuzmin Yu.N.**, *Matematicheskaya fizika [Mathematical physics]*, Leningrad Polytechnic Institute Publishing, Leningrad, 1974, P. 81, Example 185 (in Russian).
5. **Metzler R., Klafter J.**, The random walk's guide to anomalous diffusion: a fractional dynamic approach, *Physics Reports*. 339 (1) (2000) 1–77.
6. **Samko S.G., Kilbas A.A., Marichev O.I.**, *Integraly i proizvodnyye drobnogo poryadka i nekotoryye ikh prilozheniya [Integrals and derivatives of fractional order and their applications]*, Nauka i Tekhnika, Minsk, 1987 (in Russian).
7. **Nakhushev A.M.**, *Drobnoye ischisleniye i yego primeneniye [Fractional calculus and its application]*, Fizmatlit, Moscow, 2003 (in Russian).
8. **Pskhu A.V.**, Solution of a boundary value problem for a fractional partial differential equation, *Differential Equations*. 39 (8) (2003) 1150–1158.
9. **Pskhu A.V.**, *Uravneniya v chastnykh proizvodnykh drobnogo poryadka [Fractional partial differential equations]*, Nauka, Moscow, 2005 (in Russian).
10. **Kilbas A.A., Srivastava H.M., Trujillo J.J.**, *Theory and applications of fractional differential equations*, Elsevier, Amsterdam, 2006.
11. **Le Mehaute A., Tenreiro Machado J.A., Trigeassou J.C., Sabatier J. (Eds.)**, *Fractional differentiation and its applications*, Bordeaux University, Bordeaux, 2005.
12. **Gazizov R.K., Kasatkin A.A., Lukashchuk S.Yu.**, Fractional differential equations: change of variables and nonlocal symmetries, *Ufa Mathematical Journal*. 4 (4) (2012) 54–67.
13. **Zenyuk D.A., Orlov Yu.N.**, On the application of Riemann – Liouville fractional calculus to the analysis of probability distributions, *Keldysh Institute preprints*, 2014, 018. URL: <http://library.keldysh.ru/preprint.asp?id=2014>.
14. **Gazizov R.K., Kasatkin A.A., Lukashchuk S.Yu.**, Simmetriynnye svoystva differentsialnykh uravneniy perenos drobnogo poryadka [Symmetrical properties of fractional differential transfer equations], *Transactions of Mavlyutov Institute of Mechanics, Ufa Scientific Centre of the Russian Academy of Sciences*. 9(1) (2012) 59–64 (in Russian).
15. **Gazizov R.K., Kasatkin A.A., Lukashchuk S.Yu.**, Symmetry properties of fractional diffusion equations, *Physica Scripta*. (T136) (2009) 014016.
16. **Ibragimov N.H. (Ed.)**, *CRC handbook of Lie group analysis of differential equations*, Vol. 1. Symmetries, exact solutions, and conservation laws, CRC Press Inc., Boca Raton (1994).
17. **Akhatov I.Sh., Gazizov R.K., Ibragimov N.Kh.**, Nelokalnyye simmetrii. Evristicheskiy podkhod [Nonlocal symmetries, Heuristic approach], In: *Itogi Nauki i Tekhniki, Seriya "Sovremennyye Problemy Matematiki. Noveyshie Dostizheniya"*, VINITI, Moscow. 34 (1989) 3–83.
18. **Gromov M.**, *Partial differential relations*, Springer-Verlag, Berlin, Heidelberg, 1980.
19. **Slobodetskiĭ L.N.**, Obobshchennyye prostranstva Soboleva i ikh prilozheniya k krayevym zadacham v chastnykh proizvodnykh [Generalized Sobolev spaces and their application to boundary problems in partial derivatives], *Uchenyye Zapiski of LSPI named after Herzen*. 197 (1958) 54–112.
20. **Slobodetskiĭ L.N.**, Estimates in  $L_p$  of solutions of elliptic systems, *Dokl. Akad. Nauk SSSR*, 123 (4) (1958) 616–619 (in Russian).
21. **Bakelman I.Ya.**, *Geometricheskiye metody resheniya ellipticheskikh uravneniy [Geometric methods for solving elliptic equations]*, Fizmatlit, Moscow, 1962 (in Russian).
22. **Musorina T.A., Zaborova D.D., Petrichenko M.R.**, Mathematical apparatus for determination of homogenous scalar medium thermal resistance, *Vestnik MGSU*. 14 (8) (2019) 1037–1045 (in Russian).

*Received 31.10.2019, accepted 05.04.2020.*



## THE AUTHORS

### PETRICHENKO Mikhail R.

*Peter the Great St. Petersburg Polytechnic University*

29 Politechnicheskaya St., St. Petersburg, 195251, Russian Federation

fonpetrich@mail.ru

### MUSORINA Tatiana A.

*Peter the Great St. Petersburg Polytechnic University*

29 Politechnicheskaya St., St. Petersburg, 195251, Russian Federation

flamingo-93@mail.ru

## СПИСОК ЛИТЕРАТУРЫ

1. Селивестров Г.А. Математическая теория теплоустойчивости // Математический сборник. 1931. Т. 38. 3–4. С. 70–73.
2. Титчмарш Е. Теория функций. Пер. с англ. В.А. Рохлина М.: Наука, 1980. 464 с.
3. Валле-Пуссен Ш.-Ж. Курс анализа бесконечно малых. Пер. с франц. Г.М. Фихтенгольца. В 2 тт. Т. 2. Москва – Ленинград: Гос. изд-во технико-теоретической лит-ры, 1933. 464 с.
4. Жукова-Малицкая Г.К., Кузьмин Ю.Н., Математическая физика. Ленинград: Изд-во ЛПИ, 1974. С. 81, задача 185.
5. Metzler R., Klafter J. The random walk's guide to anomalous diffusion: A fractional dynamic approach // Physics Reports. 2000. Vol. 339. No. 1. Pp. 1–77.
6. Самко С.Г., Килбас А.А., Маричев О.И. Интегралы и производные дробного порядка и некоторые их приложения. Минск: Наука и техника, 1987. 688 с.
7. Нахушев А.М. Дробное исчисление и его применение. М.: Физматлит, 2003. 272 с.
8. Псху А.В. Решение краевых задач для дифференциального уравнения с частными производными дробного порядка // Дифференциальные уравнения. 2003. Т. 39. 8. С. 1092–1099.
9. Псху А.В. Уравнения в частных производных дробного порядка. М.: Наука, 2005. 199 с.
10. Kilbas A.A., Srivastava H.M., Trujillo J.J. Theory and applications of fractional differential equations. Amsterdam: Elsevier, 2006. 272 p.
11. Le Mehauté A., Tenreiro Machado J.A., Trigeassou J.C., Sabatier J. (Eds.) Fractional differentiation and its applications. In 3 Vols. Vol. 1. Bordeaux: Bordeaux University, 2005. 251 p.
12. Газизов Р.К., Касаткин А.А., Лукашук С.Ю. Уравнения с производными дробного порядка: замены переменных и нелокальные симметрии // Уфимский математический журнал. 2012. Т. 4. 4. С. 54–68.
13. Зенюк Д.А., Орлов Ю.Н. О применении дробного исчисления Римана – Лиувилля для описания распределений вероятностей // Препринты ИПМ им. М.В. Келдыша. 2014. 18. 21 с. Режим доступа: <http://library.keldysh.ru/preprint.asp?id=2014>.
14. Газизов Р.К., Касаткин А.А., Лукашук С.Ю. Симметричные свойства дифференциальных уравнений переноса дробного порядка // Труды Института механики им. Р.Р. Мавлютова УНЦ РАН. 2012. Т. 9. 1. С. 59–64.
15. Gazizov R.K., Kasatkin A.A., Lukashchuk S.Yu. Symmetry properties of fractional diffusion equations // Physica Scripta. 2009. No. T136. P. 014016.
16. Ibragimov N.H. (Ed.). CRC handbook of Lie group analysis of differential equations. Vol. 1. CRC Press, Boca Raton, 1994. 430 p.
17. Ахатов И.Ш., Газизов Р.К., Ибрагимов Н.Х. Нелокальные симметрии. Эвристический подход // Итоги науки и техники. Серия «Современные проблемы математики. Новейшие достижения». М.: ВИНТИ, 1989. Т. 34. С. 3–83.
18. Громов М. Дифференциальные соотношения с частными производными. М.: Мир, 1990. 534 с.
19. Слободецкий Л.Н. Обобщенные пространства Соболева и их приложения к краевым задачам в частных производных // Ученые записки ЛГПИ им. Герцена. 1958. Т. 197. С. 54–112.
20. Слободецкий Л.Н. Оценка в  $L_p$  решений эллиптических систем // Доклады Академии наук СССР. 1958. Т. 123. 4. С. 616–619.
21. Бакельман И.Я. Геометрические методы решения эллиптических уравнений. М.: Физматлит, 1962. 340 с.
22. Мусорина Т.А., Заборова Д.Д., Петриченко М.Р. Математический аппарат для определения термического сопротивления скалярной среды // Вестник МГСУ. 2019. Т. 14. 8. С. 1037–1045.

Статья поступила в редакцию 31.10.2019, принята к публикации 05.04.2020.



## СВЕДЕНИЯ ОБ АВТОРАХ

**ПЕТРИЧЕНКО Михаил Романович** — доктор технических наук, профессор Высшей школы гидротехнического и энергетического строительства Санкт-Петербургского политехнического университета Петра Великого, Санкт-Петербург, Российская Федерация.

195251, Российская Федерация, г. Санкт-Петербург, Политехническая ул., 29  
fonpetrich@mail.ru

**МУСОРИНА Татьяна Александровна** — ассистент Высшей школы гидротехнического и энергетического строительства Санкт-Петербургского политехнического университета Петра Великого, Санкт-Петербург, Российская Федерация.

195251, Российская Федерация, г. Санкт-Петербург, Политехническая ул., 29  
flamingo-93@mail.ru

DOI: 10.18721/JPM.13205

УДК 517.51; 517.28; 517.983; 537.213, 537.8

## CHAINS OF FUNDAMENTAL MUTUALLY HOMOGENEOUS FUNCTIONS WITH A COMMON REAL EIGENVALUE

*A.S. Berdnikov<sup>1</sup>, K.V. Solovyev<sup>2,1</sup>, N.K. Krasnova<sup>2</sup>*

<sup>1</sup>Institute for Analytical Instrumentation of the Russian Academy of Sciences,  
St. Petersburg, Russian Federation

<sup>2</sup>Peter the Great St. Petersburg Polytechnic University, St. Petersburg, Russian Federation

This work continues our studies in properties of the mutually homogeneous functions (MHF) being a generalization of Euler homogeneous functions. MHF can be used in the synthesis of electric and magnetic fields for electron systems and ion-optical ones with special properties. A chain of functions corresponding to multiple real eigenvalues of the matrix of basic functional relations for MHF has been considered. Functional relations answering such functions were derived. General formulas for the solutions of the obtained functional relations were derived. The obtained functions were shown to be a refinement of the associated homogeneous functions introduced by Gel'fand. Typical differential and integral properties of the obtained functions were investigated, and a generalization of the Euler theorem was proved (Euler criterion) for differentiable functions.

**Keywords:** functional equation, homogeneous function, associated homogeneous function, mutually homogeneous functions

**Citation:** Berdnikov A.S., Solovyev K.V., Krasnova N.K., Chains of fundamental mutually homogeneous functions with a common real eigenvalue, St. Petersburg Polytechnical State University Journal. Physics and Mathematics. 13 (2) (2020) 44–59. DOI: 10.18721/JPM.13205

This is an open access article under the CC BY-NC 4.0 license (<https://creativecommons.org/licenses/by-nc/4.0/>)

## ЦЕПОЧКИ ФУНДАМЕНТАЛЬНЫХ ВЗАИМНО-ОДНОРОДНЫХ ФУНКЦИЙ С ОБЩИМ ВЕЩЕСТВЕННЫМ СОБСТВЕННЫМ ЧИСЛОМ

*А.С. Бердников<sup>1</sup>, К.В. Соловьев<sup>2,1</sup>, Н.К. Краснова<sup>2</sup>*

<sup>1</sup>Институт аналитического приборостроения Российской академии наук,  
Санкт-Петербург, Российская Федерация;

<sup>2</sup>Санкт-Петербургский политехнический университет Петра Великого,  
Санкт-Петербург, Российская Федерация

Данная работа продолжает изучение свойств взаимно-однородных функций (ВОФ), которые являются обобщением функций, однородных по Эйлеру; ВОФ могут использоваться при синтезе электрических и магнитных полей электронно- и ионно-оптических систем со специальными свойствами. Рассматривается цепочка функций, соответствующая кратным вещественным собственным значениям матрицы базовых функциональных уравнений для ВОФ. Выведены функциональные соотношения, характеризующие такие функции, а также общие формулы для функций, являющихся решениями полученных функциональных соотношений. Показано, что полученный класс функций представляет собой уточнение присоединенных однородных функций Гельфанда. Исследованы типичные дифференциальные и интегральные свойства полученного класса функций, а для дифференцируемых функций доказано обобщение теоремы Эйлера (критерий Эйлера).

**Ключевые слова:** функциональное уравнение, однородная функция, присоединенная однородная функция, взаимно-однородные функции



**Ссылка при цитировании:** Бердников А.С., Соловьев К.В., Краснова Н.К. Цепочки фундаментальных взаимно-однородных функций с общим вещественным собственным числом // Научно-технические ведомости СПбГПУ. Физико-математические науки. 2020. Т. 2 № .13. С. 53–71. DOI: 10.18721/JPM.13205

Статья открытого доступа, распространяемая по лицензии CC BY-NC 4.0 (<https://creativecommons.org/licenses/by-nc/4.0/>)

## Introduction

This paper continues a series of studies [1–4] considering the properties of homogeneous harmonic functions and their applications for synthesis of electric and magnetic fields for electron and ion-optical systems with special properties [5–8]. Carrying on where [9] left off, our work heavily relies on the results presented therein.

A function  $f(x_1, x_2, \dots, x_n)$  is called Euler-homogeneous with the degree of homogeneity equal to  $p$  if the identity

$$f(\lambda x_1, \lambda x_2, \dots, \lambda x_n) = \lambda^p f(x_1, x_2, \dots, x_n). \quad (1)$$

holds true for any real values of  $\lambda$ .

The main properties and theorems on Euler-homogeneous functions are described in monograph [10]. In particular, any homogeneous function of degree  $p$  can be represented as

$$\begin{aligned} f(x_1, x_2, \dots, x_n) = \\ = x_1^p h(x_2/x_1, x_3/x_1, \dots, x_n/x_1), \end{aligned} \quad (2)$$

where  $h(t_2, t_3, \dots, t_n)$  is a certain function of  $(n-1)$  variables, while any function taking the form (2) is homogeneous with the degree  $p$ .

The function  $f(x_1, x_2, \dots, x_n)$  is called positively homogeneous in Euler terms with the degree  $p$  if identity (1) holds true for any positive real values of  $\lambda$ , while the identity is not guaranteed to hold for negative real values of  $\lambda$  (for example, function  $f(x) \neq x$ ). Imposing a constraint that  $\lambda > 0$ , in particular, allows to safely operate random real degrees of homogeneity in Eq. (1): additional steps need to be taken for a random real degree  $p$  to determine the power function  $\lambda^p$  at negative values of  $\lambda$  to satisfy the condition

$$\lambda_1^p \lambda_2^p = (\lambda_1 \lambda_2)^p.$$

Positively homogeneous function  $f(x_1, x_2, \dots, x_n)$  of degree  $p$  can be represented in the form:

$$\begin{aligned} \text{if } x_1 > 0 \quad f(x_1, x_2, \dots, x_n) = \\ = x_1^p h(x_2/x_1, x_3/x_1, \dots, x_n/x_1); \end{aligned} \quad (3)$$

$$\begin{aligned} \text{if } x_1 < 0 \quad f(x_1, x_2, \dots, x_n) = \\ = (-x_1)^p g(x_2/x_1, x_3/x_1, \dots, x_n/x_1), \end{aligned} \quad (4)$$

where  $h(t_2, t_3, \dots, t_n)$  and  $g(t_2, t_3, \dots, t_n)$  are functions of  $(n-1)$  variables independent of each other (in general).

Eqs. (3) and (4) are obtained from relation (1) by substituting into it the values  $\lambda = +1/x_1$  for  $x_1 > 0$  and  $-1/x_1$  for  $x_1 < 0$ , if the functions  $h(t_2, t_3, \dots, t_n)$  and  $g(t_2, t_3, \dots, t_n)$  are defined as follows:

$$h(t_2, t_3, \dots, t_n) = f(+1, t_2, t_3, \dots, t_n),$$

$$g(t_2, t_3, \dots, t_n) = f(-1, -t_2, -t_3, \dots, -t_n).$$

If  $x_1 = 0$ , the function  $f(0, x_2, x_3, \dots, x_n)$  is positively Euler-homogeneous of degree  $p$  with less variables, so parametrization of the form (3), (4) can be applied to it. A recursive process of constructing complete parametrization for a positively homogeneous function  $f(x_1, x_2, \dots, x_n)$  stops when a set of variables  $x_1, x_2, \dots, x_n$  is exhausted.

Consider the functions taking the form

$$\begin{aligned} \text{if } x_1 > 0: \quad f_{p,k}(x_1, x_2, \dots, x_n) = \\ = (1/k!) x_1^p (q \ln x_1)^k \times \\ \times h(x_2/x_1, x_3/x_1, \dots, x_n/x_1), \end{aligned} \quad (5)$$

$$\begin{aligned} \text{if } x_1 < 0: \quad f_{p,k}(x_1, x_2, \dots, x_n) = \\ = (1/k!) (-x_1)^p (q \ln (-x_1))^k \times \\ \times g(x_2/x_1, x_3/x_1, \dots, x_n/x_1), \end{aligned} \quad (6)$$

where  $p, q$  are real constants;  $k$  is an integer index ( $k = 0, 1, 2, \dots$ );  $h(t_2, t_3, \dots, t_n)$ ,  $g(t_2, t_3, \dots, t_n)$  are certain functions of  $(n-1)$  variables; the values of the variable  $x_1$  satisfy the condition  $x_1 \neq 0$ .

Given the functional relations

$$\begin{aligned} f_i(\lambda x_1, \lambda x_2, \dots, \lambda x_n) = \\ = \sum a_{ij}(\lambda) f_j(x_1, x_2, \dots, x_n), \end{aligned} \quad (7)$$

where  $i, j = 1, 2, \dots, k$ , and the functions  $a_{ij}(\lambda)$  are unknown in advance, then, in a particular case when all eigenvalues of the matrix  $\|a_{ij}(\lambda)\|$  are real numbers  $p$  equal to each other (see [9]), functions taking the form (5), (6) may qualify as possible solutions to functional equations of the form (7).

Using direct substitution, we can confirm that for  $\forall \lambda > 0$ , functions (5), (6) satisfy the functional relations

$$f_{p,k}(\lambda x_1, \lambda x_2, \dots, \lambda x_n) = \sum_{j=0,k} a_{k-j}(\lambda) f_{p,j}(x_1, x_2, \dots, x_n), \quad (8)$$

where  $a_j(\lambda) = (1/j!) \lambda^p (q \ln \lambda)^j$ .

The objectives of this study are, firstly, developing general formulae for the functions satisfying functional equations (8) provided that functions  $a_j(\lambda)$  take the form

$$a_j(\lambda) = (1/j!) \lambda^p (q \ln \lambda)^j,$$

and, secondly, proving certain important theorems on the obtained class of real functions of multiple variables.

Relationship of functions (5) with associated homogeneous Gel'fand functions

Functions (5) and (6) satisfying functional relations (8) are a refinement of associated homogeneous Gel'fand functions as defined in [11, 12]. However, these studies falsely assume that the system of functional relations (8) is a bidiagonal matrix with functions  $a(\lambda)$  for the main diagonal and  $b(\lambda)$  for the auxiliary one, unknown in advance. Unfortunately, while this insignificant mistake in the formal definition did not affect the other fundamental results obtained in [11, 12], was further uncritically disseminated in subsequent publications by other authors [13–20]. We could only find mentions of this inaccuracy in [21, 22] but even in these instances the authors omitted the factor  $1/k!$  in the respective formulae from consideration. This shortcoming is absent in earlier formulae presented in [23]. Moreover, no analysis of the *general* solution was performed in [21–23] for the obtained functional equations after verifying the required functional relations for the given functions (i.e., after obtaining a particular solution).

It is easy to prove at least for differentiable functions<sup>1</sup> that a bidiagonal system of functional equations (8) can have nondegenerate solutions different from the null equation only when  $a(\lambda) = \lambda^p$  and  $b(\lambda) = \lambda^p (q \ln \lambda)$ . At the same time, these solutions (if they exist) must have a form of linear combinations with constant factors composed of functions (7) [21]. Unfortunately,

even when  $k = 3$ , functions (7) do not satisfy the system of bidiagonal relations (8), and we can prove that these functional relations have essentially no solutions for  $k \geq 3$  [21].

One of the goals of this work is to reintroduce mathematical rigor to associated homogeneous Gel'fand functions, as well as to study some interesting properties of the obtained functions.

We should stress that we consider a rather narrow subclass of functions that is the closest to associated homogeneous Gel'fand functions. The general solution for functional equations (8) with the functions  $a_j(\lambda)$  unknown in advance is far more extensive, and we are in fact planning another publication on this subject.

### General formulae

So as not to confuse the constructions we consider with the associated homogeneous functions in terms of Gel'fand definitions [11, 12], let us add the following definition.

**Definition.** A semi-infinite chain of functions  $f_{p,k}(x_1, x_2, \dots, x_n)$ , where  $k = 0, 1, 2, \dots$ , and the functions  $f_{p,k}(x_1, x_2, \dots, x_n)$  satisfy the functional relations

$$f_{p,k}(\lambda x_1, \lambda x_2, \dots, \lambda x_n) = \sum_{j=0,k} (1/(k-j)!) \lambda^p (q \ln \lambda)^{k-j} \times f_{p,j}(x_1, x_2, \dots, x_n), \quad (9)$$

for all  $\lambda > 0$  is called fundamental associated homogeneous functions of degree  $p$  and order  $k$ .

Changing the order of summation, relations (9) can be written in an equivalent form as

$$f_{p,k}(\lambda x_1, \lambda x_2, \dots, \lambda x_n) = \sum_{j=0,k} (1/j!) \lambda^p (q \ln \lambda)^j \times f_{p,k-j}(x_1, x_2, \dots, x_n).$$

Parameter  $q$  is responsible for normalization of the fundamental associated homogeneous functions and does not affect the rest of their properties. After substituting

$$f_{p,j}(x_1, x_2, \dots, x_n) = q^j F_{p,j}(x_1, x_2, \dots, x_n),$$

the parameter  $q$  is reduced in functional relations (9), and functions  $F_{p,j}(x_1, x_2, \dots, x_n)$  take the meaning of normalized fundamental associated homogeneous functions corresponding to the choice  $q = 1$ .

We need to find the general formulae for the functions satisfying functional relations (9), similar to formulae (3) and (4). The solution is provided by the following theorem.

<sup>1</sup> For this conclusion, it is actually sufficient to impose that each of the functions  $a(\lambda)$  and  $b(\lambda)$  is continuous in at least one point of  $\lambda > 0$ . Rigorous proof of this statement is not complicated but lies beyond the scope of our study.





**Theorem 1.** Chain of fundamental associated homogeneous functions  $f_{p,k}(x_1, x_2, \dots, x_n)$  of degree  $p$  and order  $k$ , obeying functional relations (9) for all  $\forall \lambda > 0$ , has the following one-to-one representation for  $x_1 \neq 0$ :

$$\begin{aligned} & \text{if } x_1 > 0 \quad f_{p,k}(x_1, x_2, \dots, x_n) = \\ & = \sum_{j=0,k} (1/(k-j)!) x_1^p (q \ln x_1)^{k-j} \times \quad (10) \\ & \quad \times h_j(x_2/x_1, x_3/x_1, \dots, x_n/x_1); \\ & \text{if } x_1 < 0 \quad f_{p,k}(x_1, x_2, \dots, x_n) = \\ & = \sum_{j=0,k} (1/(k-j)!) (-x_1)^p \\ & \quad (q \ln (-x_1))^{k-j} \times \quad (11) \\ & \quad \times g_j(x_2/x_1, x_3/x_1, \dots, x_n/x_1), \end{aligned}$$

where  $g_j(t_2, t_3, \dots, t_n)$ ,  $h_j(t_2, t_3, \dots, t_n)$  are real functions of  $(n-1)$  variables, which have a one-to-one correspondence with functions  $f_{p,k}(x_1, x_2, \dots, x_n)$ .

The reverse is also true: a chain of functions given by Eqs. (10) and (11) obeys functional relations (9) for  $x_1 \neq 0$  with randomly chosen functions  $g_j(t_2, t_3, \dots, t_n)$  and  $h_j(t_2, t_3, \dots, t_n)$ .

When  $x_1 = 0$  and  $x_2 \neq 0$ , parametrization for fundamental associated homogeneous functions  $f_{p,k}(0, x_2, x_3, \dots, x_n)$  of degree  $p$  and order  $k$  is constructed similar to Eqs. (10), (11). Complete parametrization for functions  $f_{p,k}(x_1, x_2, \dots, x_n)$  is repeated recursively until the set of variables  $x_1, x_2, \dots, x_n$  is exhausted.

**Proof.** Let us confine ourselves to considering only the case when  $x_1 > 0$ , since the case when  $x_1 < 0$  is derived from it by substituting  $x_1 = -x_1$ , with relations (9) remaining unchanged.

When  $k = 0$ , relations (9) transform into homogeneity relation (1), while the function  $f_{p,0}(x_1, x_2, \dots, x_n)$  turns out to be a positively homogeneous function of degree  $p$  which is defined at  $x_1 > 0$ . Consequently, Eq. (10) holds true with  $k = 0$ , as it coincides with Eq. (3) for positively homogeneous functions, while the function  $h_0(t_2, t_3, \dots, t_n)$  is mapped one-to-one using the obtained function  $f_{p,0}(x_1, x_2, \dots, x_n)$ .

Let us employ mathematical induction.

Suppose Eqs. (10) are proved for all values of  $k$  satisfying the inequality  $0 \leq k < m$ . Let us write the function  $f_{p,m}(x_1, x_2, \dots, x_n)$  for  $x_1 > 0$  as

$$\begin{aligned} & f_{p,m}(x_1, x_2, \dots, x_n) = x_1^p \\ & \quad H(x_1, x_2, \dots, x_n) + \quad (12) \\ & + \sum_{j=0,m-1} (1/(m-j)!) x_1^p (q \ln x_1)^{m-j} \times \\ & \quad \times h_j(x_2/x_1, x_3/x_1, \dots, x_n/x_1), \end{aligned}$$

where the functions  $h_j(t_2, t_3, \dots, t_n)$  for  $j = 0, 1, m-1$  have been already defined at the previous steps of the proof. It is required to find the form that the function  $H(x_1, x_2, \dots, x_n)$ , which has a meaning at  $x_1 > 0$ , should take for the identity

$$\begin{aligned} & f_{p,m}(\lambda x_1, \lambda x_2, \dots, \lambda x_n) - \\ & - \lambda^p f_{p,m}(x_1, x_2, \dots, x_n) - \\ & - \sum_{k=0,m-1} (1/(m-k)!) \lambda^p (q \ln \lambda)^{m-k} \times \\ & \quad \times f_{p,k}(x_1, x_2, \dots, x_n) = 0. \end{aligned} \quad (13)$$

to hold true for  $\forall \lambda > 0$ .

After simplifying expression (13) given that the functions  $f_{p,k}(x_1, x_2, \dots, x_n)$  can be replaced by relations (10) for  $0 \leq k < m$ , we obtain the condition:

$$\text{if } \forall \lambda > 0, x_1 > 0$$

$$H(\lambda x_1, \lambda x_2, \dots, \lambda x_n) = H(x_1, x_2, \dots, x_n).$$

Consequently, the function  $H(x_1, x_2, \dots, x_n)$  must be a positively homogeneous function of zero degree, defined for  $x_1 > 0$ . This condition is necessary and sufficient to fulfil equality (13), because all algebraic transformations simplifying expression (13) are reversible.

According to Eq. (3), when  $x_1 > 0$ , the function  $H(x_1, x_2, \dots, x_n)$  can be represented as

$$H(x_1, x_2, \dots, x_n) =$$

$$= h_m(x_2/x_1, x_3/x_1, \dots, x_n/x_1),$$

where  $h_m(t_2, t_3, \dots, t_n)$  is a certain new function of  $(n-1)$  variables.

Next, if we substitute the values  $x_1 = 1$  into equality (12), we obtain the condition

$$f_{p,m}(1, x_2, \dots, x_n) = h_m(x_2, x_3, \dots, x_n),$$

which implies a one-to-one correspondence between the functions  $f_{p,m}$  and  $h_m$ .

Thus, with  $x_1 > 0$ , Eq. (10) holds true for  $k = m$  as well.

Theorem 1 is proved.

The chain of associated homogeneous functions can be also represented in parameterized form by other means. For example, a method for constructing the most generalized type of parametrization can be formulated as the following theorem.

**Theorem 2.** Suppose  $\omega_p(x_1, x_2, \dots, x_n)$  is a positively homogeneous function of degree  $p$ ,  $\psi_q(x_1, x_2, \dots, x_n)$  is a positively homogeneous function of degree  $q \neq 0$ , and  $\psi_2(x_1, x_2, \dots, x_n)$ ,  $\psi_3(x_1, x_2, \dots, x_n)$ , ...,  $\psi_n(x_1, x_2, \dots, x_n)$  are positively homogeneous functions of zero degree.

Let these functions be defined at any point of the domain  $\Omega$ . Additionally, suppose that the function  $\omega_p$  does not become zero in the domain  $\Omega$ , the function  $\psi_q$  is strictly positive, the functions  $\psi_2, \psi_3, \dots, \psi_n$  are functionally independent.

Then the fundamental associated homogeneous functions  $f_{p,k}(x_1, x_2, \dots, x_n)$ , which obey the functional relations (9) for  $\forall \lambda > 0$ , can be mapped one-to-one as follows in the domain  $\Omega$ :

$$f_{p,k}(\mathbf{x}) = \sum_{j=0,k} (1/(k-j)!) \omega_p(\mathbf{x}) (\ln \psi_q(\mathbf{x}))^{k-j} \times h_j(\psi_2(\mathbf{x}), \psi_3(\mathbf{x}), \dots, \psi_n(\mathbf{x})), \quad (14)$$

where  $\mathbf{x} = (x_1, x_2, \dots, x_n)$ , and  $h_j(t_2, t_3, \dots, t_n)$  are certain real functions of  $(n-1)$  variables.

**Proof.** When  $k=0$ , the function  $f_{p,0}(x_1, x_2, \dots, x_n)$  is a positively homogeneous function of degree  $p$ , while the function

$$f_{p,0}(x_1, x_2, \dots, x_n) / \omega_p(x_1, x_2, \dots, x_n)$$

is a well-defined positively homogeneous function of zero degree. It can be represented as  $h_0(\psi_2, \psi_3, \dots, \psi_n)$ , as it is functionally dependent on the functionally independent functions  $\psi_2, \psi_3, \dots, \psi_n$ . Indeed, if we can find such a positively homogeneous function  $\psi(x_1, x_2, \dots, x_n)$  of zero degree, which forms a functionally independent set with the functions

$$\psi_2(x_1, x_2, \dots, x_n),$$

$$\psi_3(x_1, x_2, \dots, x_n), \dots, \psi_n(x_1, x_2, \dots, x_n),$$

then the free variables  $x_1, x_2, \dots, x_n$  can be expressed in terms of functionally independent positively homogeneous functions  $\psi, \psi_2, \dots, \psi_n$  of zero degree. Then any function of the variables  $x_1, x_2, \dots, x_n$  would be a positively homogeneous functions of zero degree. This cannot be true, so the corresponding function  $h_0(\psi_2, \psi_3, \dots, \psi_n)$  must exist, and thus, Eq. (14) is fulfilled for  $k=0$ . Further proof by induction repeats the proof of Theorem 1 practically verbatim.

Theorem 2 is proved.

Using Eqs. (14), the entire space  $R^n$  is divided into non-intersecting conic<sup>2</sup> domains  $\Omega_s$ , for each of which the selected functions  $\omega_p(x_1, x_2, \dots, x_n)$  and  $\psi_q(x_1, x_2, \dots, x_n)$  do not become zero<sup>3</sup>, and the functions

$$\psi_2(x_1, x_2, \dots, x_n),$$

$$\psi_3(x_1, x_2, \dots, x_n), \dots, \psi_n(x_1, x_2, \dots, x_n)$$

form a functionally independent set of positively homogeneous functions of zero degree. Generally speaking, we construct parametrization (14) for each of the domains  $\Omega_s$  using a separate set of functions  $h_j(t_2, t_3, \dots, t_n)$  unrelated to the functions  $h_j(t_2, t_3, \dots, t_n)$  used for other domains. The boundaries between the conic domains are conic surfaces of smaller dimensions, along which the given functions  $f_{p,k}(x_1, x_2, \dots, x_n)$  act as fundamental associated homogeneous functions of smaller dimensions, with parametrization constructed by a similar algorithm.

Importantly, parametrization of fundamental associated homogeneous functions  $f_{p,k}(x_1, x_2, \dots, x_n)$  is partitioned into several independent branches as a result; moreover, such a partition depends on the selected auxiliary functions  $\omega_p(x_1, x_2, \dots, x_n)$  and  $\psi_q(x_1, x_2, \dots, x_n)$ , and, to a lesser degree, on the functions

$$\psi_2(x_1, x_2, \dots, x_n),$$

$$\psi_2(x_1, x_2, \dots, x_n), \dots, \psi_n(x_1, x_2, \dots, x_n),$$

and does not reflect the inner structure of the chain of functions parameterized.

Partitioning the space  $R^n$  into several independent branches can be avoided as the following theorem implies.

**Theorem 3.** A chain of fundamental associated homogeneous functions  $f_{p,k}(x_1, x_2, \dots, x_n)$ , which adheres to functional relations (9) for all  $\forall \lambda > 0$  can be mapped one-to-one as follows:

$$f_{p,k}(\mathbf{x}) = \sum_{j=0,k} (1/(k-j)!) r^p (q \ln r)^{k-j} \times h_j(x_1/r, x_2/r, \dots, x_n/r), \quad (15)$$

where  $\mathbf{x} = (x_1, x_2, \dots, x_n)$ ,  $r = \sqrt{x_1^2 + x_2^2 + \dots + x_n^2}$  and  $h_j(t_1, t_2, \dots, t_n)$  are arbitrary real functions given on the surface of a unit hypersphere

$$t_1^2 + t_2^2 + \dots + t_n^2 = 1,$$

with a one-to-one correspondence to the functions  $f_{p,k}(x_1, x_2, \dots, x_n)$ .

**Proof.** If  $k=0$ , we can establish that Eq. (15) holds true for a positively homogeneous function  $f_{p,0}(x_1, x_2, \dots, x_n)$  after substituting  $\lambda = 1/r$  into homogeneity relation (1) and using the function  $h_0(t_1, t_2, \dots, t_n) = f_{p,0}(t_1, t_2, \dots, t_n)$  (recall that each of the functions  $h_j(t_1, t_2, \dots, t_n)$  is defined only for the surface of a unit hypersphere  $t_1^2 + t_2^2 + \dots + t_n^2 = 1$ ). Further proof by induction repeats the proof of Theorem 1 practically verbatim.

<sup>2</sup> The domain  $\Omega$  is called a hypercone, if it follows from the condition  $\mathbf{x} \in \Omega$  that the condition  $\lambda \mathbf{x} \in \Omega$  is also satisfied for any points  $\lambda \mathbf{x}$  at random values  $\lambda > 0$ .

<sup>3</sup> If the function  $\psi_q$  is negative in the given domain, it is replaced by  $-\psi_q$ .



Theorem 3 is proved.

Relations (9) imply that the linear combination with constant coefficients comprised from several chains of fundamental associated homogeneous functions of degree  $p$  and order  $k$  is also a chain of fundamental associated homogeneous functions of degree  $p$  and order  $k$ . Besides, if  $f_{p,k}(x_1, x_2, \dots, x_n)$  is a chain of fundamental associated homogeneous functions of degree  $p$  and order  $k$ , then a new chain of functions

$$g_{p,k}(x_1, x_2, \dots, x_n) = f_{p,k-1}(x_1, x_2, \dots, x_n)$$

with an index shift, supplemented by a leading zero  $g_{p,0}(x_1, x_2, \dots, x_n) = 0$ , is also a chain of fundamental associated homogeneous functions of degree  $p$  and order  $k$ .

Eqs. (10), (11) (as well as (14) or (15)) illustrate the validity of Gel'fand's hypothesis that any chains of associated homogeneous functions of degree  $p$  and order  $k$  are obtained from the main chains with a nonzero first term by shifting the index  $k$  and subsequent summation. At the same time, all elements of the main chain of functions are reconstructed one-to-one by to its first term according to a certain rule; the accurate formulation of this rule reflects the researcher's preferences and, generally speaking, can be different for the same initial function. In case of the theorems proved above, the respective chains of fundamental associated homogeneous functions have the form

a) for Eqs. (10), (11):

$$\begin{aligned} & \text{if } x_1 > 0 \quad f_{p,k}^{(j)}(x) = \\ & = (x_1^p / k!) (q \ln x_1)^k \times \\ & \times h_j(x_2/x_1, x_3/x_1, \dots, x_n/x_1); \\ & \text{if } x_1 < 0: \quad f_{p,k}^{(j)}(x) = \\ & = ((-x_1)^p / k!) (q \ln (-x_1))^k \times \\ & \times g_j(x_2/x_1, x_3/x_1, \dots, x_n/x_1); \end{aligned}$$

b) for Eq. (14):

$$\begin{aligned} f_{p,k}^{(j)}(x) &= \omega_p(x) / k! (\ln \psi(x))^k \times \\ & \times h_j(\psi_2(x), \psi_3(x), \dots, \psi_n(x)); \end{aligned}$$

c) for Eq. (15):

$$\begin{aligned} f_{p,k}^{(j)}(x) &= \\ & = (r^p / k!) (q \ln r)^k h_j(x_1/r, x_2/r, \dots, x_n/r). \end{aligned}$$

**Remark.** As follows from Eqs. (14), the fundamental associated homogeneous functions are actually linear combinations of chains of functions taking the form

$$\begin{aligned} & (1/k!) R_p(x_1, x_2, \dots, x_n) \times \\ & \times (\ln S_q(x_1, x_2, \dots, x_n))^k, \end{aligned}$$

where  $R_p(x_1, x_2, \dots, x_n)$  are random positively homogeneous functions of degree  $p$ , and  $S_q(x_1, x_2, \dots, x_n)$  are fixed positively homogeneous functions of degree  $q$ , for which we also shift the index  $k$  and supplement the shifted chains with leading zeros.

The situation will not change and no new functions can be obtained if we demand that the functions  $S_q(x_1, x_2, \dots, x_n)$  are random positively homogeneous functions of degree  $q$ .

In particular, this approach allows to formulate the fundamental associated homogeneous functions more elegantly without using artificially derived variables  $x_1$ . Changing the selected function  $S_q(x_1, x_2, \dots, x_n)$  makes the current main chains secondary, and, vice versa, the chains that were previously secondary the main ones. Because of this, the definition of the main chains of fundamental associated homogeneous functions is fairly arbitrary and depends on the selected parametrization of fundamental associated homogeneous functions.

#### Differentiation and integration of associated homogeneous functions

If an Euler-homogeneous function  $f(x_1, x_2, \dots, x_n)$  of degree  $p$  is differentiable, then its derivatives with respect to the variables  $x_1, x_2, \dots, x_n$  are homogeneous functions of degree  $(p-1)$  [10]. A similar statement is valid for the associated homogeneous functions. Let us formulate and prove the following theorem.

**Theorem 4** (on differentiation). *If  $f_{p,k}(x_1, x_2, \dots, x_n)$  is a chain of fundamental associated homogeneous functions of degree  $p$  and order  $k$ , and the functions  $f_{p,k}(x_1, x_2, \dots, x_n)$  are differentiable, then their first partial derivatives  $\partial f_{p,k} / \partial x_i$  with respect to the variables  $x_1, x_2, \dots, x_n$  form chains of fundamental associated homogeneous functions of degree  $(p-1)$  and order  $k$ .*

**Proof.** The statement of the theorem follows from a term-by-term differentiation of the right and the left-hand sides of Eq. (9) with respect to the variable  $x_i$ .

Theorem 4 is proved.

A similar statement is valid for integration.

**Theorem 5** (on integration). *If  $f_{p,k}(x_1, x_2, \dots, x_n)$  is a chain of fundamental associated homogeneous functions of degree  $p$  and order  $k$ , then integrals represented as*

$$F_{p,k}(x_1, x_2, \dots, x_n) = \int_0^{x_i} f_{p,k}(x_1, x_2, \dots, x_{i-1}, t, x_{i+1}, \dots, x_n) dt$$

(if they exist) form a chain of fundamental associated homogeneous functions of degree  $(p + 1)$  and order  $k$ .

Significantly, the initial point of integration is zero.

**Proof.** The proof follows from term-by-term differentiation with respect to the variable  $t$  in the interval  $t \in [0, x_i]$  of relation (8) after substituting  $x_i \rightarrow t$  in it in view of the equality

$$\int_0^{x_i} f_{p,k}(\lambda x_1, \lambda x_2, \dots, \lambda x_{i-1}, \lambda t, \lambda x_{i+1}, \dots, \lambda x_n) dt = \frac{1}{\lambda} \int_0^{\lambda x_i} f_{p,k}(\lambda x_1, \lambda x_2, \dots, \lambda x_{i-1}, \tau, \lambda x_{i+1}, \dots, \lambda x_n) d\tau.$$

Theorem 5 is proved.

It is also possible to consider the integrals

$$F_{p,k}(x_1, \dots, x_n) = \int_{a_k}^{x_i} f_{p,k}(x_1, \dots, x_{i-1}, t, x_{i+1}, \dots, x_n) dt + g_k(x_1, \dots, x_{i-1}, x_{i+1}, \dots, x_n),$$

where the functions  $g_k(x_1, x_2, \dots, x_{i-1}, x_{i+1}, \dots, x_n)$  are such that the obtained functions  $f_{p,k}(x_1, x_2, \dots, x_n)$  form a chain of fundamental associated homogeneous functions of degree  $(p + 1)$  and order  $k$ . We can prove that such functions  $g_k$  do indeed exist and can be expressed in terms of the functions  $f_{p,k}(x_1, x_2, \dots, x_n)$  with a one-to-one correspondence up to the additive elements in the form of fundamental associated homogeneous functions of degree  $(p + 1)$  and order  $k$  depending on the variables  $x_1, x_2, \dots, x_{i-1}, x_{i+1}, \dots, x_n$ . The proof of this statement is given in the following section.

**Theorem 6** (on fractional differentiation). *If  $f_{p,k}(x_1, x_2, \dots, x_n)$  is a chain of fundamental associated homogeneous functions of degree  $p$  and order  $k$ , then their fractional derivatives  $F_{p,k}(x_1, x_2, \dots, x_n)$  of order  $\alpha \in (0, 1)$  (Riemann–Liouville integrals of order  $\alpha$  [24–26]), expressed as*

$$F_{p,k}(x_1, x_2, \dots, x_n) = \frac{1}{\Gamma(m - \alpha)} \frac{d^m}{dx_i^m} \int_0^{x_i} (x_i - t)^{m - \alpha - 1} \times f_{p,k}(x_1, x_2, \dots, x_{i-1}, t, x_{i+1}, \dots, x_n) dt,$$

form a chain of fundamental associated homogeneous functions of degree  $(p - \alpha)$  and order  $k$  (if such integrals exist, in particular, if  $m - \alpha > 0$ ).

Significantly, the initial point of integration is zero.

**Proof.** The proof follows from term-by-term application of the linear convolution operator  $L[f]$  to relation (8):

$$L[f(x_1, x_2, \dots, x_n)] = \int_0^{x_i} (x_i - t)^{m - \alpha - 1} \times f(x_1, x_2, \dots, x_{i-1}, t, x_{i+1}, \dots, x_n) dt,$$

where we should also take into account the equality

$$\int_0^{x_i} (x_i - t)^{m - \alpha - 1} \times f_{p,k}(\lambda x_1, \lambda x_2, \dots, \lambda x_{i-1}, \lambda t, \lambda x_{i+1}, \dots, \lambda x_n) dt = \frac{1}{\lambda^{m - \alpha}} \int_0^{\lambda x_i} (\lambda x_i - \tau)^{m - \alpha - 1} \times f_{p,k}(\lambda x_1, \lambda x_2, \dots, \lambda x_{i-1}, \tau, \lambda x_{i+1}, \dots, \lambda x_n) d\tau.$$

As a result, we obtain a chain of fundamental associated homogeneous functions of degree  $(m + p - \alpha)$  and order  $k$ , which, after  $m$ -fold differentiation with respect to the variable  $x_i$ , becomes a chain of fundamental associated homogeneous functions of degree  $(p - \alpha)$  and order  $k$ .

Theorem 6 is proved.

**Theorem 7** (on convolution with a generalized Abel kernel). *If  $f_{p,k}(x_1, x_2, \dots, x_n)$  is a chain of fundamental associated homogeneous functions of degree  $p$  and order  $k$ , then provided that there the corresponding integrals exist, their convolution with the generalized Abel kernel expressed as*

$$F_{p,k}(x_1, x_2, \dots, x_n) = \int_0^{x_1} \dots \int_0^{x_n} (x_1^{k_1} - t_1^{k_1})^{\frac{\mu_1 - 1}{k_1}} \dots (x_n^{k_n} - t_n^{k_n})^{\frac{\mu_n - 1}{k_n}} \times f_{p,k}(t_1, t_2, \dots, t_n) dt_1 \dots dt_n,$$





where  $\forall \mu_i > 0$ , forms a chain of fundamental associated homogeneous functions of degree  $p + \mu_1 + \dots + \mu_n$  and order  $k$ . The result for partial convolution with respect to the variables  $x_1, x_2, \dots, x_m$  is a chain of fundamental associated homogeneous functions of degree  $p + \mu_1 + \dots + \mu_m$  and order  $k$ .

Significantly, the initial point of integration is zero.

**Proof.** The proof follows from term-by-term application of convolution with the Abel kernel to relation (8) in view of the equality

$$\begin{aligned} & \int_0^{x_1} \dots \int_0^{x_n} (x_1^{k_1} - t_1^{k_1})^{\frac{\mu_1-1}{k_1}} \dots (x_n^{k_n} - t_n^{k_n})^{\frac{\mu_n-1}{k_n}} \times \\ & \times f_{p,k}(\lambda t_1, \lambda t_2, \dots, \lambda t_n) dt_1 \dots dt_n = \\ & = \frac{1}{\lambda^{\mu_1} \dots \lambda^{\mu_n}} \int_0^{\lambda x_1} \dots \int_0^{\lambda x_n} ((\lambda x_1)^{k_1} - \tau_1^{k_1})^{\frac{\mu_1-1}{k_1}} \dots \times \\ & \times ((\lambda x_n)^{k_n} - \tau_n^{k_n})^{\frac{\mu_n-1}{k_n}} f_{p,k}(\tau_1, \tau_2, \dots, \tau_n) d\tau_1 \dots d\tau_n. \end{aligned}$$

Theorem 7 is proved.

### Euler's criterion

Let us recall Euler's theorem on homogeneous functions [10]:

**Euler's theorem** (Euler's criterion for homogeneous functions). *If the function  $f(x_1, x_2, \dots, x_n)$  is continuously differentiable in any point of space  $R^n$ , then for it to be Euler-homogeneous of degree  $p$ , it is necessary and sufficient that in any point of space  $R^n$  the following condition is satisfied*

$$\begin{aligned} & x_1 \partial f / \partial x_1 + x_2 \partial f / \partial x_2 + \dots + \\ & + x_n \partial f / \partial x_n = pf. \end{aligned} \quad (16)$$

Relation (13) is obtained through differentiation of identical equation

$$f(\lambda x_1, \lambda x_2, \dots, \lambda x_n) = \lambda^p f(x_1, x_2, \dots, x_n)$$

for a homogeneous function of degree  $p$  with respect to parameter  $\lambda$  in point  $\lambda = 1$ , therefore, its necessity is obvious. However, it is highly non-trivial that condition (16) is not only necessary but sufficient for the function  $f(x_1, x_2, \dots, x_n)$  differentiable everywhere to be Euler-homogeneous of degree  $p$ . The proof of this theorem can be found, for example, in monograph [10].

Euler's criterion (16) works for continuously differentiable positively homogeneous functions of degree  $p$  as well. The only difference is that in this case the function  $f(x_1, x_2, \dots, x_n)$  can have

no derivative at point  $x_1 = x_2 = \dots = x_n = 0$  and, consequently, condition (16) is violated at this point.

**Theorem 8** (generalization of Euler's criterion). *For the functions  $f_{p,k}(x_1, x_2, \dots, x_n)$  continuously differentiable everywhere to form a chain of fundamental associated homogeneous functions of degree  $p$  and order  $k$ , it is necessary and sufficient that the following equations are fulfilled at all points of space  $R^n$ , possibly except for point  $x_1 = x_2 = \dots = x_n = 0$ :*

$$\begin{aligned} & x_1 \partial f_{p,k} / \partial x_1 + x_2 \partial f_{p,k} / \partial x_2 + \dots + \\ & + x_n \partial f_{p,k} / \partial x_n = p f_{p,k} + q f_{p,k-1}. \end{aligned} \quad (17)$$

**Proof.** The necessity of relation (17) follows from differentiation of relation (9) as a composite function of  $\lambda$  at point  $\lambda = 1$  (continuous differentiability is required here so that we could safely differentiate relation (9) as a composite function). The remaining task is to prove the sufficiency of relation (17).

When  $k = 0$ , the sufficiency of criterion (17) follows from Euler's theorem on homogeneous functions. Next, we apply the method of mathematical induction.

Suppose the statement is proved for all values of the index  $k$  in the interval  $0 \leq k \leq m-1$ . Consider the function

$$\Phi_m(\lambda) = f_{p,m}(\lambda x_1, \lambda x_2, \dots, \lambda x_n) / \lambda^p -$$

$$- \sum_{k=0, m} f_{p, m-k}(x_1, x_2, \dots, x_n) (q \ln \lambda)^k / k!,$$

with summation carried out with respect to the index  $1 \leq k \leq m$ .

This expression coincides with identity (9), whose right and left-hand sides were divided by  $\lambda^p$ , up to the substitution of the summation index. The derivative of the function  $\Phi_m(\lambda)$  with respect to the parameter  $\lambda$  is transformed to

$$\begin{aligned} d\Phi_m(\lambda)/d\lambda &= (1/\lambda^{p+1}) [\lambda x_1 \partial f_{p,m}(\lambda x)/\partial x_1 + \\ &+ \lambda x_2 \partial f_{p,m}(\lambda x)/\partial x_2 + \dots + \\ &+ \lambda x_n \partial f_{p,m}(\lambda x)/\partial x_n - \\ &- p f_{p,m}(\lambda x) - q f_{p, m-1}(\lambda x) + \\ &+ q f_{p, m-1}(\lambda x) - q \sum_{k=1, m} f_{p, m-k}(x) \lambda^p \times \\ &\times (q \ln \lambda)^{k-1} / (k-1)!] = 0, \end{aligned}$$

because relation (17) for the function  $f_{p,m}(x_1, x_2, \dots, x_n)$  is fulfilled, including at point  $(\lambda x_1, \lambda x_2, \dots, \lambda x_n)$ , and the function



$f_{p,m-1}(x_1, x_2, \dots, x_n)$  satisfies condition (9) by inductive assumption. Therefore,  $\Phi_m(\lambda) = \text{const}$  and, in particular,  $\Phi_m(\lambda) = \Phi_m(1)$ .

However, as it is easy to verify, the condition  $\Phi_m(\lambda) = \Phi_m(1)$  means that relation (9) is fulfilled for the functions  $f_{p,m}(x_1, x_2, \dots, x_n)$ . Consequently, if condition (17) is satisfied for  $\forall k \geq 0$  at all points of space  $R^n$ , except possibly the origin of coordinates, then relation (9) is satisfied for  $\forall k \geq 0$ .

Theorem 8 is proved.

**Note.** To provide the condition  $\Phi_m(\lambda) = \Phi_m(1) = \text{const}$ , the derivative  $\Phi'_m(\lambda)$  must exist and become zero at any point of the segment connecting the points  $(\lambda x_1, \lambda x_2, \dots, \lambda x_n)$  and  $(x_1, x_2, \dots, x_n)$ . If equality (14) is violated for at least one intermediate point, or at least the derivative  $\Phi'_m(\lambda)$  exhibits discontinuities at one intermediate point, then the function  $\Phi_m(\lambda)$  can be decomposed into piecewise constant steps. This is exactly why violation of continuous differentiability of the function at zero provides only positive Euler homogeneity for the function  $f(x_1, x_2, \dots, x_n)$ , and not the general Euler homogeneity.

**Theorem 9** (on integrating fundamental associated homogeneous functions). *If  $f_{p,k}(x_1, x_2, \dots, x_n)$  is a chain of fundamental associated homogeneous functions of degree  $p$  and order  $k$ , then there exist such functions  $g_k(x_2, x_3, \dots, x_n)$  for which the functions*

$$F_{p,k}(x_1, x_2, \dots, x_n) = \int_{a_k}^{x_1} f_{p,k}(t, x_2, x_3, \dots, x_n) dt + g_k(x_2, x_3, \dots, x_n)$$

form a chain of fundamental associated homogeneous functions of degree  $p+1$  and order  $k$ .

Naturally, any coordinate  $x_i$  can be used instead of the coordinate  $x_1$ .

**Proof.** According to Theorem 6, it is necessary and sufficient that relations (17) are fulfilled for the functions  $F_{p,k}(x_1, x_2, \dots, x_n)$ . This leads to the equation

$$\begin{aligned} 0 &= x_1 f_{p,k}(x_1, x_2, \dots, x_n) + \\ &+ \int_{a_k}^{x_1} \left( t \frac{\partial f_{p,k}}{\partial t} + x_2 \frac{\partial f_{p,k}}{\partial x_2} + \dots + x_n \frac{\partial f_{p,k}}{\partial x_n} \right) dt - \\ &- \int_{a_k}^{x_1} t \frac{\partial f_{p,k}}{\partial t} dt - (p+1) \int_{a_k}^{x_1} f_{p,k}(t, x_2, x_3, \dots) dt - \\ &- q \left( \int_{a_{k-1}}^{a_k} f_{p,k-1}(t, x_2, x_3, \dots) dt + \right. \end{aligned}$$

$$\begin{aligned} &\left. + \int_{a_k}^{x_1} f_{p,k-1}(t, x_2, x_3, \dots) dt \right) + x_2 \frac{\partial g_k}{\partial x_2} + x_3 \frac{\partial g_k}{\partial x_3} + \\ &+ \dots + x_n \frac{\partial g_k}{\partial x_n} - (p+1) g_k(x_2, x_3, \dots, x_n) - \\ &- q g_{k-1}(x_2, x_3, \dots, x_n) = \\ &= x_1 f_{p,k}(x_1, x_2, \dots, x_n) - \int_{a_k}^{x_1} \left( t \frac{\partial f_{p,k}}{\partial t} + f_{p,k} \right) dt - \\ &- q \int_{a_{k-1}}^{a_k} f_{p,k-1}(t, x_2, x_3, \dots, x_n) dt + \\ &+ x_2 \frac{\partial g_k}{\partial x_2} + \dots + x_n \frac{\partial g_k}{\partial x_n} - \\ &- (p+1) g_k(x_2, \dots, x_n) - \\ &- q g_{k-1}(x_2, \dots, x_n) = \\ &= x_2 \frac{\partial g_k}{\partial x_2} + x_3 \frac{\partial g_k}{\partial x_3} + \dots + x_n \frac{\partial g_k}{\partial x_n} - \\ &- (p+1) g_k - q g_{k-1} - \\ &- q \int_{a_{k-1}}^{a_k} f_{p,k-1}(t, x_2, x_3, \dots, x_n) dt + \\ &+ a_k f_{p,k}(a_k, x_2, x_3, \dots, x_n). \end{aligned}$$

The variable  $x_1$  is absent in the obtained equations. Moreover, the function  $g_{k-1}(x_2, x_3, \dots, x_n)$  is already known. The remaining task is to find the solution to the equation

$$\begin{aligned} &x_2 \frac{\partial g_k}{\partial x_2} + x_3 \frac{\partial g_k}{\partial x_3} + \dots + \\ &+ x_n \frac{\partial g_k}{\partial x_n} - (p+1) g_k \\ &= G_k(x_2, x_3, \dots, x_n), \end{aligned} \quad (18)$$

where the function  $G_k(x_2, x_3, \dots, x_n)$  is already known at the  $k^{\text{th}}$  step of integration:

$$\begin{aligned} G_k(x_2, x_3, \dots, x_n) &= q g_{k-1}(x_2, x_3, \dots, x_n) + \\ &+ q \int_{a_{k-1}}^{a_k} f_{p,k-1}(t, x_2, x_3, \dots, x_n) dt - \\ &- a_k f_{p,k}(a_k, x_2, x_3, \dots, x_n). \end{aligned}$$

It is convenient to use the following substitution to find this solution

$$\begin{aligned} &g_k(x_2, x_3, \dots, x_n) = \\ &= x_2^{p+1} h_k(x_2, x_3/x_2, x_4/x_2, \dots, x_n/x_2). \end{aligned}$$



Then Eq. (18) takes the form

$$\begin{aligned} x_2^{p+2} \partial h_k(x_2, t_3, t_4, \dots, t_n) / \partial x_2 = \\ = G_k(x_2, t_3 x_2, t_4 x_2, \dots, t_n x_2). \end{aligned}$$

A particular solution of this equation is found by transferring the multiplier  $x_2^{p+2}$  into the right-hand side and integrating the result with respect to the variable  $x_2$  with ‘frozen’ variables  $t_3, t_4, \dots, t_n$ . Furthermore, we need to add the general solution of homogeneous Eq. (18) with a zero right-hand side to the obtained particular solution of the inhomogeneous equation, that is, an Euler-homogeneous function of degree  $(p + 1)$  depending on the variables  $x_2, x_3, \dots, x_n$ .

Theorem 9 is proved.

As a result, we managed to not only prove that the required function  $g_k(x_2, x_3, \dots, x_n)$  exists but also to define its explicit quadratic form. The final solution is the sum of a particular case of the chain of functions  $g_k(x_2, x_3, \dots, x_n)$  expressed recursively in quadratic form in terms of the functions  $f_{p,k}(a_k, x_2, x_3, \dots, x_n)$ , and a random chain of fundamental associated homogeneous functions of degree  $(p + 1)$  and order  $k$  of the variables  $x_2, x_3, \dots, x_n$ , which can be given explicitly using Eqs. (10), (11), (14) or (15).

**Problem.** Suppose for all points of space  $R^n$ , except possibly the point  $x_1 = x_2 = \dots = x_n = 0$ , that the continuous differentiable functions  $g_k(x_1, x_2, \dots, x_n)$  satisfy the equalities

$$\begin{aligned} x_1 \partial g_k / \partial x_1 + x_2 \partial g_k / \partial x_2 + \dots + \\ + x_n \partial g_k / \partial x_n = p_k g_k + q_k g_{k-1}, \end{aligned} \quad (19)$$

where  $p_k, q_k$  are the given constants, and the functions  $g_k(x_1, x_2, \dots, x_n)$  with negative subscripts are taken to equal zero. What can we say about the form of the functions  $g_k(x_1, x_2, \dots, x_n)$ ?

If  $\forall k, p_k = p = \text{const}$ , and  $q_k = q = \text{const}$ , Euler’s criterion (17) provides an answer immediately: the functions  $g_k(x_1, x_2, \dots, x_n)$  are fundamental associated homogeneous functions  $f_{p,k}(x_1, x_2, \dots, x_n)$  of degree  $p$  and order  $k$ . In the general case, additional calculations are required. After substituting

$$\begin{aligned} g_k(x_1, x_2, \dots, x_n) = \\ = h_k(\ln x_1, x_2/x_1, x_3/x_1, \dots, x_n/x_1), \end{aligned}$$

the chain of conditions (19) is reduced to a system of ordinary linear differential equations with constant factors and a bidiagonal matrix of factors, where  $t = \ln x_1$  is a free variable, and

the variables  $t_2 = x_2/x_1, t_3 = x_3/x_1, \dots, t_n = x_n/x_1$  are ‘frozen’.

After solving the obtained system of differential equations and making the reverse transition to the variables  $x_1, x_2, \dots, x_n$ , we obtain the general form of the functions  $g_k(x_1, x_2, \dots, x_n)$ . At the same time, it should be borne in mind that the free constants obtained after integrating a system of ordinary linear differential equations with constant factors are in fact random functions depending on temporary ‘frozen’ variables  $t_2 = x_2/x_1, t_3 = x_3/x_1, \dots, t_n = x_n/x_1$ . Depending on what the constants  $p_k$  are equal to and how many of them turn out to be equal to each other, the structure of the solution can be quite complicated.

In a particular case, let us take a chain of relations (19), where all values of  $p_k$  equal the same number  $p$ , while  $\forall q_k \neq 0$ . Then, according to condition (17), the functions  $g_k(x_1, x_2, \dots, x_n)$ , scaled up by  $c_k$  times, turn out to be fundamental associated homogeneous functions  $f_{p,k}(x_1, x_2, \dots, x_n)$  described by the general equations (10) and (11) (or (14), or (15)), if the relations  $c_k q_k / c_{k-1} = q$  are fulfilled (where the value of the parameter  $q \neq 0$  is chosen arbitrarily). In other words, scaling factors  $c_k$  should be chosen in accordance with the recursive rule  $c_k = q c_{k-1} / q_k$ , where  $c_0 = 1$ , and the results coincide with a certain chain of fundamental associated homogeneous functions  $f_{p,k}(x_1, x_2, \dots, x_n)$  of degree  $p$  and order  $k$  up to the multipliers.

### Differentiation with respect to degree of homogeneity

An interesting technique allowing to generate new fundamental associated homogeneous functions is considered in [11, 12]. Specifically, suppose  $f_p(x_1, x_2, \dots, x_n)$  is a one-parameter family of Euler-homogeneous functions with the degree of homogeneity equal to  $p$ , where  $p$  is a continuously changing parameter.

Repeatedly differentiating the homogeneity relation

$$f_p(\lambda x_1, \lambda x_2, \dots, \lambda x_n) = \lambda^p f_p(x_1, x_2, \dots, x_n)$$

with respect to the parameter  $p$ , we obtain that the functions

$$f_{p,k}(x_1, x_2, \dots, x_n) = (1/k!) \partial^k f_p(x_1, x_2, \dots, x_n) / \partial p^k$$

satisfy functional relations (9), i.e., are a particular case of fundamental associated homogeneous functions.

The homogeneous function  $f_p(x_1, x_2, \dots, x_n)$  can be represented using Eqs. (3) and (4):

$$\begin{aligned} & \text{if } x_1 > 0, f_p(x_1, x_2, \dots, x_n) = \\ & = x_1^p h_p(x_2/x_1, x_3/x_1, \dots, x_n/x_1); \end{aligned} \quad (20)$$

$$\begin{aligned} & \text{if } x_1 < 0, f_p(x_1, x_2, \dots, x_n) = \\ & = (-x_1)^p g_p(x_2/x_1, x_3/x_1, \dots, x_n/x_1), \end{aligned} \quad (21)$$

where  $h_p(t_2, t_3, \dots, t_n)$ ,  $g_p(t_2, t_3, \dots, t_n)$  are functions of  $(n-1)$  variables independent of each other.

These functions are mapped one-to-one with respect to the given function  $f_p(x_1, x_2, \dots, x_n)$  according to the formulae

$$h_p(t_2, t_3, \dots, t_n) = f_p(+1, t_2, t_3, \dots, t_n),$$

$$g_p(t_2, t_3, \dots, t_n) = f_p(-1, -t_2, -t_3, \dots, -t_n),$$

and depend on the continuous parameter  $p$  as well.

Repeatedly differentiating expressions (20), (21) with respect to the parameter  $p$ , we obtain the universal formulae (10), (11) for fundamental associated homogeneous functions, if the new functions  $h_j(x_1, x_2, \dots, x_n)$  and  $g_j(x_1, x_2, \dots, x_n)$  are defined as

$$h_j(t_2, t_3, \dots, t_n) = (1/j!) \partial^j h_p(t_2, t_3, \dots, t_n) / \partial p^j,$$

$$g_j(t_2, t_3, \dots, t_n) = (1/j!) \partial^j g_p(t_2, t_3, \dots, t_n) / \partial p^j.$$

Eqs. (15) are obtained similarly by differentiating the function  $f_p(x_1, x_2, \dots, x_n)$  with respect to the parameter  $p$ . The function is written as

$$f_p(x_1, x_2, \dots, x_n) = r^p h_p(x_1/r, x_2/r, \dots, x_n/r),$$

where  $r = \sqrt{x_1^2 + x_2^2 + \dots + x_n^2}$ , and  $h_p(t_1, t_2, \dots, t_n)$  is a real function given on the surface of a unit hypersphere

$$t_1^2 + t_2^2 + \dots + t_n^2 = 1$$

and related to the function  $f_p(x_1, x_2, \dots, x_n)$  by

$$h_p(t_1, t_2, \dots, t_n) = f_p(t_1, t_2, \dots, t_n),$$

where  $t_1^2 + t_2^2 + \dots + t_n^2 = 1$ .

It follows from the obtained formulae that the process of differentiating the Euler-homogeneous functions with the degree of homogeneity equal to  $p$  with respect to the continuously changing parameter  $p$  does not generally lead to a loss of possible chains of fundamental associated homogeneous functions.

Importantly, if the functions  $f_p(x_1, x_2, \dots, x_n)$  are harmonic (or fulfil some other linear differential equation in partial derivatives with constant coefficients), then all the fundamental

associated homogeneous functions obtained by differentiating the initial function  $f_p(x_1, x_2, \dots, x_n)$  with respect to the parameter  $p$  are also harmonic.

## Conclusion

Analyzing mutually homogeneous functions which correspond to a matrix of functional equations with identical real eigenvalues, we obtained a refined class of associated homogeneous Gel'fand functions [11, 12]. The definitions and theorems formulated in the study allow to correctly describe this important class of functions and consider its properties in detail. In particular, Theorem 2 on fundamental associated homogeneous functions allows to safely consider the following generalizations

$$\begin{aligned} & f_{p,k}(x_1, x_2, \dots, x_n) = \\ & = (1/k!) R_p(x_1, x_2, \dots, x_n) \times \\ & \times (\ln S_q(x_1, x_2, \dots, x_n))^k \end{aligned}$$

and argue that such functions identically coincide with the given class of functions, while fully preserving their properties without producing any fundamentally new mathematical objects.

The mathematical constructions we have discussed may prove useful not only for theoretical studies but also for practical applications. The property of Euler homogeneity for scalar potentials of electric and magnetic fields [5–8] allows to synthesize efficient electron and ion-optical systems, presented, for example, in a series of works by Khursheed [27–43].

We hope that the obtained functional constructions generalizing the relation of Euler homogeneity can make it possible to transfer the principle of trajectory similarity, introduced by Golikov [5–8], to wider classes of electric and magnetic fields.

The calculations in this paper were carried out using the Wolfram Mathematica software [44].

## Acknowledgements

We wish to express our sincere gratitude to Anton Leonidovich Bulyanitsa, Doctor of Physical and Mathematical Sciences, Professor of Department of Higher Mathematics of Peter the Great St. Petersburg Polytechnic University, for active participation in discussions on the problem.

This study was partially supported by NIR 0074-2019-0009, part of State Task No. 075-01073-20-00 of the Ministry of Science and Higher Education of the Russian Federation.



## REFERENCES

1. **Berdnikov A.S., Gall L.N., Gall N.R., Solovyev K.V.**, Generalization of the Thomson formula for harmonic functions of a general type, *St. Petersburg Polytechnical State University Journal. Physics and Mathematics*. 12 (2) (2019) 32–48.
2. **Berdnikov A.S., Gall L.N., Gall N.R., Solovyev K.V.**, Generalization of the Thomson formula for homogeneous harmonic functions, *St. Petersburg Polytechnical State University Journal. Physics and Mathematics*. 12 (2) (2019) 49–62.
3. **Berdnikov A.S., Gall L.N., Gall N.R., Solovyev K.V.**, Donkin's differential operators for homogeneous harmonic functions, *St. Petersburg Polytechnical State University Journal. Physics and Mathematics*. 12 (3) (2019) 45–62.
4. **Berdnikov A.S., Gall L.N., Gall N.R., Solovyev K.V.**, Basic Donkin's differential operators for homogeneous harmonic functions, *St. Petersburg Polytechnical State University Journal. Physics and Mathematics*. 12 (3) (2019) 26–44.
5. **Golikov Yu.K., Krasnova N.K.**, *Teoriya sinteza elektrostatischeskikh energoanalizatorov* [Theory of designing of electrostatic energy analyzers], Saint-Petersburg Polytechnic University Publishing, Saint-Petersburg, 2010.
6. **Golikov Yu.K., Krasnova N.K.**, Application of electric fields uniform in the Euler sense in electron spectrography, *Technical Physics*. 56 (2) (2011), 164–170.
7. **Golikov Yu.K., Krasnova N.K.**, Generalized similarity principle of similarity in electron spectrography, *Prikladnaya fizika* (Applied Physics). (2) (2007) 5–11.
8. **Averin I.A., Berdnikov A.S., Gall N.R.**, The principle of similarity of trajectories for the motion of charged particles with different masses in electric and magnetic fields that are homogeneous in Euler terms, *Technical Physics Letters*. 43 (3) (2017) 156–158.
9. **Berdnikov A.S., Solovyev K.V., Krasnova N.K.**, Mutually homogeneous functions with finite-sized matrices, *St. Petersburg Polytechnical State University Journal. Physics and Mathematics*. 13 (1) (2020) 42–53.
10. **Fikhtengol'ts G.M.**, *The fundamentals of mathematical analysis*, Vol. 1, Pergamon Press, Oxford, New York, 1965.
11. **Gel'fand I.M., Shapiro Z.Ya.**, Generalized functions and their applications, *Uspekhi Mat. Nauk*. 10 (3) (1955) 3–70 (in Russian).
12. **Gel'fand I.M., Shilov G.E.**, *Generalized functions*, Vol. 1: Properties and Operations, AMS Chelsea Publishing, 1964.
13. **Ivanov V.K.**, On multiplication of generalized homogeneous functions of several variables, *Soviet mathematics – Doklady*. 237 (1) (1981) 29–33 (in Russian).
14. **Ivanov V.K.**, Asymptotic approximation to the product of generalized functions, *Soviet Mathematics (Izvestia VUZ. Matematika)*. 25 (1) (1981) 20–29.
15. **Estrada R., Kanwal R.P.**, *Asymptotic analysis. A distributional approach*, Birkhäuser, Boston, 1994.
16. **Estrada R., Kanwal R.P.**, *A distributional approach to asymptotic. Theory and applications*, Springer Science, New York, 2002.
17. **Albeverio S., Khrennikov A.Yu., Shelkovich V.M.**, Associated homogeneous p-adic distributions, *Doklady Mathematics*. 68 (3) (2003) 354–357.
18. **Albeverio S., Khrennikov A.Yu., Shelkovich V.M.**, Associated homogeneous p-adic distributions, *Journal of Mathematical Analysis and Applications*. 313 (1) (2006) 64–83.
19. **Ivanov V.K.**, *Selected scientific works. Mathematics*, Fizmatlit, Moscow, 2008 (in Russian).
20. **Khrennikov A.Yu., Shelkovich V.M.**, *Modern p-adic analysis and mathematical physics: Theory and applications*, Fizmatlit, Moscow, 2012 (in Russian).
21. **Shelkovich V.M.**, Associated and quasi-associated homogeneous distributions (generalized functions), *Journal of Mathematical Analysis and Applications*. 338 (1) (2008) 48–70.
22. **Albeverio S., Khrennikov A.Yu., Shelkovich V.M.**, *Theory of p-adic Distributions. Linear and Nonlinear Models*, Cambridge University Press, Cambridge, 2010.
23. **von Grudzinski O.**, *Quasi-homogeneous distributions*, North-Holland, Amsterdam, 1991.
24. **Miller K., Ross B.**, *An Introduction to the Fractional Calculus and Fractional Differential Equations*, Wiley, New York, 1993.
25. **Samko S., Kilbas A.A., Marichev O.**, *Fractional integrals and derivatives: theory and applications*, Taylor & Francis Books, 1993.
26. **Kilbas A.A., Srivastava H. M., Trujillo J.J.**, *Theory and applications of fractional differential equations*, Vol. 204, 1<sup>st</sup> Ed., Elsevier, Amsterdam, Netherlands, 2006.
27. **Khursheed A., Dinnis A.R., Smart P.D.**, *Micro-extraction fields to improve electron beam*



test measurements, *Microelectronic Engineering*. 14 (3–4) (1991) 197–205.

28. **Khursheed A.**, Multi-channel vs. conventional retarding field spectrometers for voltage contrast, *Microelectronic Engineering*. 16 (1–4) (1992) 43–50.

29. **Khursheed A., Phang J.C., Thong J.T.L.**, A portable scanning electron microscope column design based on the use of permanent magnets, *Scanning*. 20 (2) (1998) 87–91.

30. **Khursheed A.**, Magnetic axial field measurements on a high resolution miniature scanning electron microscope, *Review of Scientific Instruments*. 71 (4) (2000) 1712–1715.

31. **Khursheed A.**, A low voltage time of flight electron emission microscope, *Optik (Jena)*. 113 (11) (2002) 505–509.

32. **Khursheed A.**, Aberration characteristics of immersion lenses for LVSEM, *Ultramicroscopy*. 93 (3–4) (2002) 331–338.

33. **Khursheed A., Karupiah N., Osterberg M., Thong J.T.L.**, Add-on transmission attachments for the scanning electron microscope, *Review of Scientific Instruments*. 74 (1) (2003) 134–140.

34. **Khursheed A., Osterberg M.**, A spectroscopic scanning electron microscope design, *Scanning*. 26 (6) (2004) 296–306.

35. **Osterberg M., Khursheed A.**, Simulation of magnetic sector deflector aberration properties for low-energy electron microscopy, *Nuclear Instruments and Methods in Physics Research, Section A*. 555 (1–2) (2005) 20–30.

36. **Khursheed A., Osterberg M.**, Developments in the design of a spectroscopic scanning electron

microscope, *Nuclear Instruments and Methods in Physics Research, Section A*. 556 (2) (2006) 437–444.

37. **Luo T., Khursheed A.**, Imaging with surface sensitive backscattered electrons, *Journal of Vacuum Science and Technology B*. 25 (6) (2007) 2017–2019.

38. **Khursheed, A., Hoang, H.Q.**, A second-order focusing electrostatic toroidal electron spectrometer with 2 $\pi$  radian collection, *Ultramicroscopy*. 109 (1) (2008) 104–110.

39. **Khursheed A.**, Scanning electron microscope optics and spectrometers, World Scientific, Singapore, 2010.

40. **Hoang H.Q., Khursheed A.**, A radial mirror analyzer for scanning electron/ion microscopes, *Nuclear Instruments and Methods in Physics Research, Section A*. 635 (1) (2011) 64–68.

41. **Hoang H.Q., Osterberg M., Khursheed A.**, A high signal-to-noise ratio toroidal electron spectrometer for the SEM, *Ultramicroscopy*. 111 (8) (2011) 1093–1100.

42. **Khursheed A., Hoang H.Q., Srinivasan A.**, A wide-range Parallel Radial Mirror Analyzer for scanning electron/ion microscopes, *Journal of Electron Spectroscopy and Related Phenomena*. 184 (11–12) (2012) 525–532.

43. **Shao X., Srinivasan A., Ang W.K., Khursheed A.**, A high-brightness large-diameter graphene coated point cathode field emission electron source, *Nature Communications*. 9 (1) (2018) 1288.

44. Wolfram Mathematica, URL: <http://wolfram.com/mathematica/>

*Received 27.03.2020, accepted 17.04.2020.*

## THE AUTHORS

**BERDNIKOV Alexander S.**

*Institute for Analytical Instrumentation of the Russian Academy of Sciences*  
26 Rizhsky Ave., St. Petersburg, 190103, Russian Federation  
[asberd@yandex.ru](mailto:asberd@yandex.ru)

**SOLOVYEV Konstantin V.**

*Peter the Great St. Petersburg Polytechnic University*  
29 Politechnicheskaya St., St. Petersburg, 195251, Russian Federation  
[k-solovyevev@mail.ru](mailto:k-solovyevev@mail.ru)

**KRASNOVA Nadezhda K.**

*Peter the Great St. Petersburg Polytechnic University*  
29 Politechnicheskaya St., St. Petersburg, 195251, Russian Federation  
[n.k.krasnova@mail.ru](mailto:n.k.krasnova@mail.ru)





## СПИСОК ЛИТЕРАТУРЫ

1. Бердников А.С., Галль Л.Н., Галль Р.Н., Соловьев К.В. Обобщение формулы Томсона для гармонических функций общего вида // Научно-технические ведомости СПбГПУ. Физико-математические науки. 2019. Т. 12 № 2. С. 32–48.
2. Бердников А.С., Галль Л.Н., Галль Р.Н., Соловьев К.В. Обобщение формулы Томсона для гармонических однородных функций // Научно-технические ведомости СПбГПУ. Физико-математические науки. 2019. Т. 12. № 2. С. 49–62.
3. Бердников А.С., Галль Л.Н., Галль Н.Р., Соловьев К.В. Дифференциальные операторы Донкина для однородных гармонических функций // Научно-технические ведомости СПбГПУ. Физико-математические науки. 2019. Т. 12. № 3. С. 45–62.
4. Бердников А.С., Галль Л.Н., Галль Н.Р., Соловьев К.В. Базисные дифференциальные операторы Донкина для однородных гармонических функций // Научно-технические ведомости СПбГПУ. Физико-математические науки. 2019. Т. 12. № 3. С. 26–44.
5. Голиков Ю.К., Краснова Н.К. Теория синтеза электростатических энергоанализаторов. СПб.: Изд-во Политехнического ун-та, 2010. 409 с.
6. Голиков Ю.К., Краснова Н.К. Электрические поля, однородные по Эйлеру, для электронной спектроскопии // Журнал технической физики. 2011. Т. 81. № 2. С. 9–15.
7. Голиков Ю.К., Краснова Н.К. Обобщенный принцип подобия и его применение в электронной спектроскопии // Прикладная физика. 2007. № 2. С. 5–11.
8. Аверин И.А., Бердников А.С., Галль Н.Р. Принцип подобия траекторий при движении заряженных частиц с разными массами в однородных по Эйлеру электрических и магнитных полях // Письма в Журнал технической физики. 2017. Т. 3 № 43. С. 43–39.
9. Бердников А.С., Соловьев К.В., Краснова Н.К. Взаимно-однородные функции с матрицами конечного размера // Научно-технические ведомости СПбГПУ. Физико-математические науки. 2020. Т. 13. № 1. С. 42–53.
10. Фихтенгольц Г.М. Курс дифференциального и интегрального исчисления. Т. 1. М.: Физматлит, 2001. 616 с.
11. Гельфанд И.М., Шапиро З.Я. Однородные функции и их приложения // Успехи математических наук. 1955. Т. 10. Вып. 3. С. 3–70.
12. Гельфанд И.М., Шиллов Г.Е. Обобщенные функции и действия над ними. Серия «Обобщенные функции». Вып. 1. М.: ГИФМЛ, 1959. 470 с.
13. Иванов В.К. Об умножении обобщенных однородных функций нескольких переменных // Доклады АН СССР. 1981. Т. 1 № 237. С. 33–29.
14. Иванов В.К. Асимптотическая аппроксимация произведения обобщенных функций // Известия вузов. Сер. «Математика». 1. № 1981. С. 26–19.
15. Estrada R., Kanwal R.P. Asymptotic analysis: A distributional approach. Boston: Birkhduser, 1994. 253 p.
16. Estrada R., Kanwal R.P. A distributional approach to asymptotics: Theory and applications. New York: Springer Science, 2002. 454 p.
17. Албеверио С., Хренников А.Ю., Шелкович В.М. Присоединенные однородные р-адические распределения // Доклады РАН. 2003. Т. 393. № 3. С. 300–303.
18. Albeverio S., Khrennikov A.Yu., Shelkovich V.M. Associated homogeneous p-adic distributions // Journal of Mathematical Analysis and Applications. 2006. Vol. 313. No. 1. Pp. 64–83.
19. Иванов В.К. Избранные научные труды. Математика. М.: Физматлит, 2008. 553 с.
20. Хренников А.Ю., Шелкович В.М. Современный р-адический анализ и математическая физика: Теория и приложения. М.: Физматлит, 2012. 452 с.
21. Shelkovich V.M. Associated and quasi associated homogeneous distributions (generalized functions) // Journal of Mathematical Analysis and Applications. 2008. Vol. 338. No. 1. Pp. 48–70.
22. Albeverio S., Khrennikov A.Yu., Shelkovich V.M. Theory of p-adic distributions: Linear and nonlinear models. Cambridge: Cambridge University Press, 2010. 351 p.
23. von Grudzinski O. Quasihomogeneous distributions. Amsterdam, North-Holland, 1991. 469 p.
24. Miller K., Ross B. An Introduction to the Fractional Calculus and Fractional Differential Equations. New York, Wiley, 1993. 384 p.
25. Самко С.Г., Килбас А.А., Маричев О.И. Интегралы и производные дробного порядка и некоторые их приложения. Минск: Наука и техника, 1987. 687 с.

26. **Kilbas A.A., Srivastava H.M., Trujillo J.J.** Theory and applications of fractional differential equations. Vol. 204. 1<sup>st</sup> Ed. Amsterdam, Netherlands: Elsevier. 2006. 540 p.
27. **Khursheed A., Dinnis A.R., Smart P.D.** Micro-extraction fields to improve electron beam test measurements // Microelectronic Engineering. 1991. Vol. 14. No. 3–4. Pp. 197–205.
28. **Khursheed A.** Multi-channel vs. conventional retarding field spectrometers for voltage contrast // Microelectronic Engineering. 1992. Vol. 16. No. 1–4. Pp. 43–50.
29. **Khursheed A., Phang J.C., Thong J.T.L.** A portable scanning electron microscope column design based on the use of permanent magnets // Scanning. 1998. Vol. 20. No. 2. Pp. 87–91.
30. **Khursheed A.** Magnetic axial field measurements on a high resolution miniature scanning electron microscope // Review of Scientific Instruments. 2000. Vol. 71. No. 4. Pp. 1712–1715.
31. **Khursheed A.** A low voltage time of flight electron emission microscope // Optik (Jena). 2002. Vol. 113. No. 11. Pp. 505–509.
32. **Khursheed A.** Aberration characteristics of immersion lenses for LVSEM // Ultramicroscopy. 2002. Vol. 93. No. 3–4. Pp. 331–338.
33. **Khursheed A., Karuppiah N., Osterberg M., Thong J.T.L.** Add-on transmission attachments for the scanning electron microscope // Review of Scientific Instruments. 2003. Vol. 74. No. 1. Pp. 134–140.
34. **Khursheed A., Osterberg M.** A spectroscopic scanning electron microscope design // Scanning. 2004. Vol. 26. No. 6. Pp. 296–306.
35. **Osterberg M., Khursheed A.** Simulation of magnetic sector deflector aberration properties for low-energy electron microscopy // Nuclear Instruments and Methods in Physics Research, Section A. 2005. Vol. 555. No. 1–2. Pp. 20–30.
36. **Khursheed A., Osterberg M.** Developments in the design of a spectroscopic scanning electron microscope // Nuclear Instruments and Methods in Physics Research. Section A. 2006. Vol. 556. No. 2. Pp. 437–444.
37. **Luo T., Khursheed A.** Imaging with surface sensitive backscattered electrons // Journal of Vacuum Science and Technology B. 2007. Vol. 25. No. 6. Pp. 2017–2019.
38. **Khursheed A., Hoang H.Q.** A second-order focusing electrostatic toroidal electron spectrometer with  $2\pi$  radian collection // Ultramicroscopy. 2008. Vol. 109. No. 1. Pp. 104–110.
39. **Khursheed A.** Scanning electron microscope optics and spectrometers. Singapore: World Scientific, 2010. 403 p.
40. **Hoang H.Q., Khursheed A.** A radial mirror analyzer for scanning electron/ion microscopes // Nuclear Instruments and Methods in Physics Research. Section A. 2011. Vol. 635. No. 1. Pp. 64–68.
41. **Hoang H.Q., Osterberg M., Khursheed A.** A high signal-to-noise ratio toroidal electron spectrometer for the SEM // Ultramicroscopy. 2011. Vol. 111. No. 8. Pp. 1093–1100.
42. **Khursheed A., Hoang H.Q., Srinivasan A.** A wide-range parallel radial mirror analyzer for scanning electron/ion microscopes // Journal of Electron Spectroscopy and Related Phenomena. 2012. Vol. 184. No. 11–12. Pp. 525–532.
43. **Shao X., Srinivasan A., Ang W.K., Khursheed A.** A high-brightness large-diameter graphene coated point cathode field emission electron source // Nature Communications. 2018. Vol. 9. No. 1. P. 1288.
44. Wolfram Mathematica // URL: <http://wolfram.com/mathematica/>

*Статья поступила в редакцию 27.03.2020, принята к публикации 17.04.2020.*



## СВЕДЕНИЯ ОБ АВТОРАХ

**БЕРДНИКОВ Александр Сергеевич** — доктор физико-математических наук, ведущий научный сотрудник Института аналитического приборостроения Российской академии наук, Санкт-Петербург, Российская Федерация.

190103, Российская Федерация, г. Санкт-Петербург, Рижский пр., 26  
[asberd@yandex.ru](mailto:asberd@yandex.ru)

**СОЛОВЬЕВ Константин Вячеславович** — кандидат физико-математических наук, доцент Высшей инженерно-физической школы Санкт-Петербургского политехнического университета Петра Великого, младший научный сотрудник Института аналитического приборостроения РАН, Санкт-Петербург, Российская Федерация.

195251, Российская Федерация, г. Санкт-Петербург, Политехническая ул., 29  
[k-solovyev@mail.ru](mailto:k-solovyev@mail.ru)

**КРАСНОВА Надежда Константиновна** — доктор физико-математических наук, профессор Высшей инженерно-физической школы Санкт-Петербургского политехнического университета Петра Великого, Санкт-Петербург, Российская Федерация.

195251, Российская Федерация, г. Санкт-Петербург, Политехническая ул., 29  
[n.k.krasnova@mail.ru](mailto:n.k.krasnova@mail.ru)

DOI: 10.18721/JPM.13206

УДК 517.51; 517.28; 517.983; 537.213, 537.8

## GENERAL FORMULAE FOR CHAINS OF FUNDAMENTAL MUTUALLY HOMOGENEOUS FUNCTIONS WITH A COMMON PAIR OF COMPLEX CONJUGATE EIGENVALUES

*A.S. Berdnikov<sup>1</sup>, K.V. Solovyev<sup>2,1</sup>, N.K. Krasnova<sup>2</sup>*

<sup>1</sup> Institute for Analytical Instrumentation of the Russian Academy of Sciences,  
St. Petersburg, Russian Federation;

<sup>2</sup> Peter the Great St. Petersburg Polytechnic University, St. Petersburg, Russian Federation

This work continues our studies in properties of mutually homogeneous functions (MHFs), being a generalization of Euler homogeneous functions, which can be used in the synthesis of electric and magnetic fields of electron and ion-optical systems with special properties. MHFs corresponding to multiple pairs of complex conjugate eigenvalues of the matrix of basic functional equations have been considered in addition to MHF chains corresponding to multiple real eigenvalues of the matrix of basic functional relations. We deduced functional equations characterizing such functions and derived general formulae for the MHFs with complex conjugate multiple eigenvalues.

**Keywords:** functional equation, homogeneous function, associated homogeneous function, mutually homogeneous functions

**Citation:** Berdnikov A.S., Solovyev K.V., Krasnova N.K., General formulas for chains of fundamental mutually homogeneous functions with a common pair of complex conjugate eigenvalues, St. Petersburg Polytechnical State University Journal. Physics and Mathematics. 13 (2) (2020) 60–74. DOI: 10.18721/JPM.13206

This is an open access article under the CC BY-NC 4.0 license (<https://creativecommons.org/licenses/by-nc/4.0/>)

## ОБЩИЕ ФОРМУЛЫ ДЛЯ ЦЕПОЧЕК ФУНДАМЕНТАЛЬНЫХ ВЗАИМНО-ОДНОРОДНЫХ ФУНКЦИЙ С ОБЩЕЙ ПАРОЙ КОМПЛЕКСНО-СОПРЯЖЕННЫХ СОБСТВЕННЫХ ЧИСЕЛ

*А.С. Бердников<sup>1</sup>, К.В. Соловьев<sup>2,1</sup>, Н.К. Краснова<sup>2</sup>*

<sup>1</sup> Институт аналитического приборостроения Российской академии наук,  
Санкт-Петербург, Российская Федерация;

<sup>2</sup> Санкт-Петербургский политехнический университет Петра Великого,  
Санкт-Петербург, Российская Федерация

Данная работа продолжает изучение свойств взаимно-однородных функций (ВОФ), которые являются обобщением однородных по Эйлеру функций и могут использоваться при синтезе электрических и магнитных полей для электронно- и ионно-оптических систем со специальными свойствами. В дополнение к цепочкам ВОФ, соответствующим кратным вещественным собственным значениям матрицы базовых функциональных уравнений, рассматриваются ВОФ, соответствующие кратным парам комплексно-сопряженных собственных значений матрицы базовых функциональных уравнений. Выведены функциональные соотношения, характеризующие такие функции, получены общие формулы для ВОФ с комплексно-сопряженными кратными собственными значениями.

**Ключевые слова:** функциональное уравнение, однородная функция, присоединенная однородная функция, взаимно-однородные функции



**Ссылка при цитировании:** Бердников А.С., Соловьев К.В., Краснова Н.К. Общие формулы для цепочек фундаментальных взаимно-однородных функций с общей парой комплексно-сопряженных собственных чисел // Научно-технические ведомости СПбГПУ. Физико-математические науки. 2020. Т. 13. № 2. С. 72–88. DOI: 10.18721/JPM.13206

Статья открытого доступа, распространяемая по лицензии CC BY-NC 4.0 (<https://creativecommons.org/licenses/by-nc/4.0/>)

## Introduction

This paper continues a series of works [1–4] on the properties of homogeneous harmonic functions and their applications in synthesis of electric and magnetic fields for electron and ion-optical systems with special properties [5–8]. A system of fundamental mutually homogeneous functions constructed in this paper can be used to transfer the principle of trajectory similarity, introduced by Golikov, to new classes of electric and magnetic fields, and thus serve as a basis for synthesis of various electron and ion-optical systems, presented, for example, in Khursheed's studies [9–25].

The paper is a direct extension of [26, 27] and heavily relies on the results presented therein.

Consider the following functions

$$f_{p,k}^{(c)}(\mathbf{x}) = x_1^p ((q \ln x_1)^k / k!) \times \quad (1)$$

$$\times h(x_2/x_1, x_3/x_1, \dots, x_n/x_1) \cos(\omega \ln x_1),$$

$$f_{p,k}^{(s)}(\mathbf{x}) = x_1^p ((q \ln x_1)^k / k!) \times \quad (2)$$

$$\times h(x_2/x_1, x_3/x_1, \dots, x_n/x_1) \sin(\omega \ln x_1),$$

where  $\mathbf{x} = (x_1, x_2, \dots, x_n)$ ;  $p, q, \omega$  are real constants;  $k$  is an integer index ( $k = 0, 1, 2, \dots$ );  $h(t_2, t_3, \dots, t_n)$  is a certain function of  $(n - 1)$  variables; values of the variable  $x_1$  satisfy the condition  $x_1 > 0$ .

In fact, functions (1), (2) are the real and the imaginary part for the chains of fundamental mutually homogeneous functions with a common real eigenvalue from [27] when the degree of homogeneity  $p$  (multiple real eigenvalue of the matrix of mutually homogeneous functional equations) is replaced by a complex number  $p + i\omega$ . Since, generally speaking, the generator  $h(t_2, t_3, \dots, t_n)$  must also be considered in this case as a complex-valued function

$$h(t_2, t_3, \dots, t_n) + ig(t_2, t_3, \dots, t_n),$$

from a formal standpoint, Eqs. (1), (2) should be written as

$$f_{p,k}^{(c)}(\mathbf{x}) = x_1^p ((q \ln x_1)^k / k!) \times$$

$$\times h(x_2/x_1, x_3/x_1, \dots, x_n/x_1) \cos(\omega \ln x_1) -$$

$$- x_1^p ((q \ln x_1)^k / k!) \times$$

$$\times g(x_2/x_1, x_3/x_1, \dots, x_n/x_1) \sin(\omega \ln x_1);$$

$$f_{p,k}^{(s)}(\mathbf{x}) = x_1^p ((q \ln x_1)^k / k!) \times$$

$$h(x_2/x_1, x_3/x_1, \dots, x_n/x_1) \sin(\omega \ln x_1) +$$

$$+ x_1^p ((q \ln x_1)^k / k!) \times$$

$$\times g(x_2/x_1, x_3/x_1, \dots, x_n/x_1) \cos(\omega \ln x_1),$$

where expressions (1), (2) are a particular case corresponding to the choice  $g(t_2, t_3, \dots, t_n) = 0$ .

By virtue of this, the properties of the chains of fundamental mutually homogeneous functions with a common pair of complex conjugate eigenvalues closely resemble the properties of the chains of fundamental mutually homogeneous functions with a common real eigenvalue, considered in [27].

Given the functional relations

$$f_i(\lambda \mathbf{x}) = \sum a_{ij}(\lambda) f_j(\mathbf{x}), \quad (3)$$

where  $i, j = 1, 2, \dots, k$ , and functions  $a_{ij}(\lambda)$  are unknown in advance, in a particular case, when all eigenvalues of the matrix  $\|a_{ij}(\lambda)\|$  are pairs of complex conjugate values  $p \pm i\omega$  equal to each other, functions of the form (1), (2) can be regarded as the solutions to functional relations (3) [26].

Using direct substitution, we can confirm that functions (1), (2) satisfy the functional relations

$$f_{p,k}^{(c)}(\lambda \mathbf{x}) = \sum_{j=0,k} a_{k-j}(\lambda) f_{p,j}^{(c)}(\mathbf{x}) -$$

$$- \sum_{j=0,k} b_{k-j}(\lambda) f_{p,j}^{(s)}(\mathbf{x}); \quad (4)$$

$$f_{p,k}^{(s)}(\lambda \mathbf{x}) = \sum_{j=0,k} b_{k-j}(\lambda) f_{p,j}^{(c)}(\mathbf{x}) +$$

$$+ \sum_{j=0,k} a_{k-j}(\lambda) f_{p,j}^{(s)}(\mathbf{x}), \quad (5)$$

where the functions  $a_j(\lambda)$  and  $b_j(\lambda)$  are defined as

$$a_j(\lambda) = (1/j)! \lambda^p (q \ln \lambda)^j \cos(\omega \ln \lambda), \quad (6)$$



$$b_j(\lambda) = (1/j)! \lambda^p (q \ln \lambda)^j \sin(\omega \ln \lambda). \quad (7)$$

Introducing nondegenerate linear combinations of functions  $f_{p,k}^{(c)}(\mathbf{x})$  and  $f_{p,k}^{(s)}(\mathbf{x})$ , which can be written as

$$g_{p,k}^{(c)}(\mathbf{x}) = \alpha_k f_{p,k}^{(c)}(\mathbf{x}) - \beta_k f_{p,k}^{(s)}(\mathbf{x});$$

$$g_{p,k}^{(s)}(\mathbf{x}) = \gamma_k f_{p,k}^{(c)}(\mathbf{x}) + \delta_k f_{p,k}^{(s)}(\mathbf{x});$$

$$\alpha_k^2 + \beta_k^2 \neq 0, \gamma_k^2 + \delta_k^2 \neq 0,$$

$$\alpha_k \delta_k + \beta_k \gamma_k \neq 0,$$

the new functions  $g_{p,k}^{(c)}(\mathbf{x})$  and  $g_{p,k}^{(s)}(\mathbf{x})$  can be simplified to the following form

$$g_{p,k}^{(c)}(\mathbf{x}) = C_k x_1^p ((q \ln x_1)^k / k!) \times \\ \times h(x_2/x_1, x_3/x_1, \dots, x_n/x_1) \cos(\omega \ln x_1 + \varphi_k);$$

$$g_{p,k}^{(s)}(\mathbf{x}) = S_k x_1^p ((q \ln x_1)^k / k!) \times \\ \times h(x_2/x_1, x_3/x_1, \dots, x_n/x_1) \sin(\omega \ln x_1 + \psi_k);$$

$$C_k = \sqrt{\alpha_k^2 + \beta_k^2}, S_k = \sqrt{\gamma_k^2 + \delta_k^2};$$

$$\varphi = \arctg(\beta_k/\alpha_k), \psi_k = \arctg(\gamma_k/\delta_k),$$

$$C_k \neq 0, S_k \neq 0, \varphi_k \neq \psi_k \pm \pi/2.$$

It follows from conditions (4), (5) that functions  $g_{p,k}^{(c)}(\mathbf{x})$  and  $g_{p,k}^{(s)}(\mathbf{x})$  satisfy the functional relations

$$g_{p,k}^{(c)}(\lambda \mathbf{x}) = \sum_{j=0,k} c_{kj}(\lambda) g_{p,k}^{(c)}(\mathbf{x}) + \\ + \sum_{j=0,k} d_{kj}(\lambda) g_{p,k}^{(s)}(\mathbf{x});$$

$$g_{p,k}^{(s)}(\lambda \mathbf{x}) = \sum_{j=0,k} e_{kj}(\lambda) g_{p,k}^{(c)}(\mathbf{x}) + \\ + \sum_{j=0,k} s_{kj}(\lambda) g_{p,k}^{(s)}(\mathbf{x}),$$

where the functions  $c_{kj}(\lambda)$ ,  $d_{kj}(\lambda)$ ,  $e_{kj}(\lambda)$  and  $s_{kj}(\lambda)$  are defined as

$$c_{k,j}(\lambda) = \frac{\lambda^p (\ln \lambda)^{k-j}}{(k-j)!} \frac{C_k/C_j}{\cos(\phi_j - \psi_j)} \times \\ \times \cos(\omega \ln \lambda + (\phi_k - \psi_j)), \\ d_{k,j}(\lambda) = -\frac{\lambda^p (\ln \lambda)^{k-j}}{(k-j)!} \frac{C_k/S_j}{\cos(\phi_j - \psi_j)} \times \\ \times \sin(\omega \ln \lambda + (\phi_k - \psi_j)),$$

$$e_{k,j}(\lambda) = \frac{\lambda^p (\ln \lambda)^{k-j}}{(k-j)!} \frac{S_k/C_j}{\cos(\phi_j - \psi_j)} \times \\ \times \sin(\omega \ln \lambda + (\psi_k - \psi_j)), \\ s_{k,j}(\lambda) = \frac{\lambda^p (\ln \lambda)^{k-j}}{(k-j)!} \frac{S_k/S_j}{\cos(\phi_j - \psi_j)} \times \\ \times \cos(\omega \ln \lambda + (\psi_k - \phi_j)).$$

When a linear transformation satisfies the conditions

$$\text{at } \forall k \varphi_k = \psi_k = \varphi, C_k = S_k = C,$$

the new functions  $g_{p,k}^{(c)}(\mathbf{x})$  and  $g_{p,k}^{(s)}(\mathbf{x})$  satisfy functional relations (4), (5) with functions (6), (7).

The objectives of this paper consist in, firstly, developing general formulae for the functions  $f_{p,k}^{(c)}(\mathbf{x})$  and  $f_{p,k}^{(s)}(\mathbf{x})$  which satisfy functional equations (4), (5) with functions (6), (7), and, secondly, proving certain important theorems on the obtained class of mutually homogeneous functions.

#### Auxiliary formulae for positively Euler-homogeneous functions

The function  $f(\mathbf{x})$  is called positively Euler-homogeneous with a degree of homogeneity equal to  $p$  [28], if the condition

$$f(\lambda \mathbf{x}) = \lambda^p f(\mathbf{x}) \quad (8)$$

holds for every  $\forall \lambda > 0$ .

Universal formulae can be obtained for positively homogeneous functions which allow to represent them in a generalized form convenient for practical applications. The following expressions are typical examples, which will be useful later on.

If we substitute the values

$$\lambda = +1/x_1 \text{ and } -1/x_1$$

in condition (8), then after permutation of the right and the left-hand sides of the obtained equality, we obtain the following formula:

if  $x_1 > 0$ ,

$$f(\mathbf{x}) = x_1^p h(x_2/x_1, x_3/x_1, \dots, x_n/x_1); \quad (9)$$

if  $x_1 < 0$ ,

$$f(\mathbf{x}) = (-x_1)^p g(x_2/x_1, x_3/x_1, \dots, x_n/x_1), \quad (10)$$



where  $h(t_2, t_3, \dots, t_n)$  and  $g(t_2, t_3, \dots, t_n)$  are arbitrary functions of  $(n-1)$  variables, which, generally speaking, do not depend on each other and are related as follows to the function  $f(\mathbf{x})$ :

$$h(t_2, t_3, \dots, t_n) = f(+1, t_2, t_3, \dots, t_n),$$

$$g(t_2, t_3, \dots, t_n) = f(-1, -t_2, -t_3, \dots, -t_n).$$

The case  $x_1 = 0$  is not described by Eqs. (9), (10). However, the function  $f(0, x_2, x_3, \dots, x_n)$  is positively homogeneous as well, but depends on a smaller number of independent variables. Therefore, there is actually an entire hierarchy of equations of the form (9), (10) corresponding to a successively reduced list of independent variables  $x_{k+1}, x_{k+2}, \dots, x_n$ .

2. If we substitute values  $\lambda = 1/r$  in condition (8), where  $r = \sqrt{x_1^2 + x_2^2 + \dots + x_n^2}$ , we obtain the formula

$$f(\mathbf{x}) = r^p s(x_1/r, x_2/r, \dots, x_n/r), \quad (11)$$

where  $s(t_1, t_2, \dots, t_n)$  is an arbitrary function of  $n$  variables, given on a unit hypersphere

$$t_1^2 + t_2^2 + \dots + t_n^2 = 1,$$

which is related as follows to the function  $f(\mathbf{x})$ :

$$s(t_1, t_2, \dots, t_n) = f(t_1, t_2, \dots, t_n).$$

3. The domain  $\Omega$  contains a fixed positively homogeneous function  $\psi_p(\mathbf{x})$  of degree  $p$  which does not become zero in this domain, as well as fixed positively homogeneous functions  $\psi_2(\mathbf{x}), \psi_3(\mathbf{x}), \dots, \psi_n(\mathbf{x})$  of zero degree which are functionally independent, all of them having no singular points. We obtain in this domain  $\Omega$  a formula

$$f(\mathbf{x}) = \psi_p(\mathbf{x}) \chi(\psi_2(\mathbf{x}), \psi_3(\mathbf{x}), \dots, \psi_n(\mathbf{x})), \quad (12)$$

where  $\chi(t_2, t_3, \dots, t_n)$  is an arbitrary function of  $(n-1)$  variables.

As a result, Eqs. (9)–(11) turn out to be particular cases of Eq. (12).

Indeed, function  $\psi(\mathbf{x}) = f(\mathbf{x})/\psi_p(\mathbf{x})$  is well defined in domain  $\Omega$  and, as it is easy to prove, is a positively homogeneous function of zero degree.

The function  $\psi(\mathbf{x})$  cannot be functionally independent of functions

$$\psi_2(\mathbf{x}), \psi_3(\mathbf{x}), \dots, \psi_n(\mathbf{x}),$$

otherwise the variables  $x_1, x_2, \dots, x_n$  could be expressed in terms of functions

$$\psi(\mathbf{x}), \psi_2(\mathbf{x}), \dots, \psi_n(\mathbf{x}),$$

which are positively homogeneous of zero degree, and then any function of variables  $x_1, x_2, \dots, x_n$  would be a positively homogeneous function of zero degree, which is meaningless.

Therefore, this function can be represented as

$$\psi(\mathbf{x}) = \chi(\psi_2(\mathbf{x}), \psi_3(\mathbf{x}), \dots, \psi_n(\mathbf{x})).$$

After this, expression (12) is obtained for the function  $f(\mathbf{x})$ .

On the other hand, if the function  $f(\mathbf{x})$  has the form (12), it is positively Euler-homogeneous with the degree of homogeneity equal to  $p$ .

**Note.** Given a fixed choice of positive homogeneous functions

$$\psi_p(\mathbf{x}) \text{ and } \psi_2(\mathbf{x}), \psi_3(\mathbf{x}), \dots, \psi_n(\mathbf{x}),$$

the entire space  $R^n$  is partitioned into non-intersecting conic<sup>1</sup> domains  $\Omega_s$ , where the function  $\psi_p(\mathbf{x})$  does not become zero, the functions

$$\psi_2(\mathbf{x}), \psi_3(\mathbf{x}), \dots, \psi_n(\mathbf{x})$$

form an independent set of functions, and the given functions have no singular points.

Generally, while constructing parametrization (12), a specific function  $\chi_s(t_2, t_3, \dots, t_n)$  is used for each of the domains  $\Omega_s$ , which is completely unrelated to the functions  $\chi_s(t_2, t_3, \dots, t_n)$  used for other domains. Moreover, the boundaries between the domains  $\Omega_s$  are conic surfaces of a lesser dimension, with the function  $f(\mathbf{x})$  again behaving as a homogeneous function of degree  $p$  depending on a smaller number of variables along these surfaces. A separate method of parametrization depending on a smaller number of independent variables and using a new set of fixed functions has to be constructed for these boundaries. As a result, parametrization of positive homogeneous functions is partitioned into several independent branches, such a partition depends on the selected auxiliary functions

$$\psi_p(\mathbf{x}), \psi_2(\mathbf{x}), \psi_3(\mathbf{x}), \dots, \psi_n(\mathbf{x})$$

and does not reflect the internal structure of positively homogeneous functions parameterized using them.

A direct check shows that the functions given by Eqs. (9)–(12) indeed satisfy the homogeneity relation (8) for any selected functions involved in parametrization.

<sup>1</sup> The term ‘conic’ means that when point  $(x_1, x_2, \dots, x_n)$  belongs to a certain geometric object, then all points of the form  $(\lambda x_1, \lambda x_2, \dots, \lambda x_n)$  corresponding to arbitrary values of  $\lambda > 0$  also belong to this object.

### General equations for fundamental mutually homogeneous functions

**Definition.** A semi-infinite chain of pairs of functions  $f_{p,k}^{(c)}(\mathbf{x})$  and  $f_{p,k}^{(s)}(\mathbf{x})$ , where the index  $k = 0, 1, 2, \dots$ , and the functions themselves satisfy the functional relations

$$\begin{aligned} f_{p,k}^{(c)}(\lambda \mathbf{x}) &= \\ &= \sum_{j=0,k} \lambda^p ((q \ln \lambda)^{k-j} / (k-j)!) \times \\ &\quad \times f_{p,j}^{(c)}(\mathbf{x}) \cos(\omega \ln \lambda) - \end{aligned} \quad (13)$$

$$\begin{aligned} &- \sum_{j=0,k} \lambda^p ((q \ln \lambda)^{k-j} / (k-j)!) \times \\ &\quad \times f_{p,j}^{(s)}(\mathbf{x}) \sin(\omega \ln \lambda); \\ f_{p,k}^{(s)}(\lambda \mathbf{x}) &= \\ &= \sum_{j=0,k} \lambda^p ((q \ln \lambda)^{k-j} / (k-j)!) \times \\ &\quad \times f_{p,j}^{(c)}(\mathbf{x}) \sin(\omega \ln \lambda) + \end{aligned} \quad (14)$$

$$\begin{aligned} &+ \sum_{j=0,k} \lambda^p ((q \ln \lambda)^{k-j} / (k-j)!) \times \\ &\quad \times f_{p,j}^{(s)}(\mathbf{x}) \cos(\omega \ln \lambda) \end{aligned}$$

for any  $\lambda > 0$ , is called fundamental associated homogeneous functions of degree  $p$  and order  $k$  with the correlation factor  $\omega$ .

Conditions (13), (14) can be written in equivalent form by changing the order of summation:

$$\begin{aligned} f_{p,k}^{(c)}(\lambda \mathbf{x}) &= \\ &= \sum_{j=0,k} \lambda^p ((q \ln \lambda)^j / j!) \times \\ &\quad \times f_{p,k-j}^{(c)}(\mathbf{x}) \cos(\omega \ln \lambda) - \end{aligned} \quad (15)$$

$$\begin{aligned} &- \sum_{j=0,k} \lambda^p ((q \ln \lambda)^j / j!) \times \\ &\quad \times f_{p,k-j}^{(s)}(\mathbf{x}) \sin(\omega \ln \lambda); \end{aligned}$$

$$\begin{aligned} f_{p,k}^{(s)}(\lambda \mathbf{x}) &= \\ &= \sum_{j=0,k} \lambda^p ((q \ln \lambda)^j / j!) \times \\ &\quad \times f_{p,k-j}^{(c)}(\mathbf{x}) \sin(\omega \ln \lambda) + \end{aligned} \quad (16)$$

$$\begin{aligned} &+ \sum_{j=0,k} \lambda^p ((q \ln \lambda)^j / j!) \times \\ &\quad \times f_{p,k-j}^{(s)}(\mathbf{x}) \cos(\omega \ln \lambda). \end{aligned}$$

When  $\omega = 0$ , relations (13), (14) for functions  $f_{p,k}^{(c)}(\mathbf{x})$  and  $f_{p,k}^{(s)}(\mathbf{x})$  are decoupled and become independent of each other. In this case, a chain of functions  $f_{p,k}^{(c)}(\mathbf{x})$  and a chain of functions  $f_{p,k}^{(s)}(\mathbf{x})$  turn out to be chains of fundamental associated homogeneous functions of degree  $p$

and order  $k$ , independent of each other, which were considered in detail in paper [27].

The parameter  $q$  is responsible for normalizing fundamental mutually homogeneous functions and does not affect the rest of their properties. After substituting

$$f_{p,k}^{(c)}(\mathbf{x}) = q^j F_{p,j}^{(c)}(\mathbf{x}),$$

$$f_{p,k}^{(s)}(\mathbf{x}) = q^j F_{p,j}^{(s)}(\mathbf{x}),$$

the parameter  $q$  vanishes from functional relations (13), (14), and functions  $F_{p,j}^{(c)}(\mathbf{x})$  and  $F_{p,j}^{(s)}(\mathbf{x})$  take the meaning of normalized fundamental mutually homogeneous functions, corresponding to the choice  $q = 1$ .

We obtain for fundamental mutually homogeneous functions of zero degree the functional relations

$$\begin{aligned} f_{p,0}^{(c)}(\lambda \mathbf{x}) &= \lambda^p f_{p,0}^{(c)}(\mathbf{x}) \cos(\omega \ln \lambda) - \\ &- \lambda^p f_{p,0}^{(s)}(\mathbf{x}) \sin(\omega \ln \lambda); \end{aligned} \quad (17)$$

$$\begin{aligned} f_{p,0}^{(s)}(\lambda \mathbf{x}) &= \lambda^p f_{p,0}^{(c)}(\mathbf{x}) \sin(\omega \ln \lambda) + \\ &+ \lambda^p f_{p,0}^{(s)}(\mathbf{x}) \cos(\omega \ln \lambda). \end{aligned} \quad (18)$$

**Lemma 1.** Fundamental mutually homogeneous functions  $f_{p,0}^{(c)}(\mathbf{x})$  and  $f_{p,0}^{(s)}(\mathbf{x})$  of zero degree, satisfying functional relations (17) and (18) for  $\forall \lambda > 0$ , can be represented for  $x_1 > 0$  as

$$\begin{aligned} f_{p,0}^{(c)}(\lambda \mathbf{x}) &= \lambda^p f_{p,0}^{(c)}(\mathbf{x}) \cos(\omega \ln \lambda) - \\ &- \lambda^p f_{p,0}^{(s)}(\mathbf{x}) \sin(\omega \ln \lambda); f_{p,0}^{(c)}(\mathbf{x}) = \\ &= x_1^p h^{(c)}(x_2/x_1, x_3/x_1, \dots, x_n/x_1) \times \end{aligned} \quad (19)$$

$$\begin{aligned} &\quad \times \cos(\omega \ln x_1) - \\ &- x_1^p h^{(s)}(x_2/x_1, x_3/x_1, \dots, x_n/x_1) \times \\ &\quad \times \sin(\omega \ln x_1); \end{aligned}$$

$$\begin{aligned} f_{p,0}^{(s)}(\mathbf{x}) &= \\ &= x_1^p h^{(c)}(x_2/x_1, x_3/x_1, \dots, x_n/x_1) \times \\ &\quad \times \sin(\omega \ln x_1) + \end{aligned} \quad (20)$$

$$\begin{aligned} &+ x_1^p h^{(s)}(x_2/x_1, x_3/x_1, \dots, x_n/x_1) \times \\ &\quad \times \cos(\omega \ln x_1), \end{aligned}$$

where the functions  $h^{(c)}(t_2, t_3, \dots, t_n)$  and  $h^{(s)}(t_2, t_3, \dots, t_n)$  are arbitrary real functions of  $(n-1)$  variables which have a one-to-one correspondence with functions  $f_{p,0}^{(c)}(\mathbf{x})$  and  $f_{p,0}^{(s)}(\mathbf{x})$ , and represented for  $x_1 < 0$  as



$$\begin{aligned}
 f_{p,0}^{(c)}(\mathbf{x}) &= (-x_1)^p \times \\
 &\times g^{(c)}(x_2/x_1, x_3/x_1, \dots, x_n/x_1) \times \\
 &\times \cos(\omega \ln(-x_1)) - \\
 &- (-x_1)^p g^{(s)}(x_2/x_1, x_3/x_1, \dots, x_n/x_1) \times \\
 &\times \sin(\omega \ln(-x_1));
 \end{aligned} \quad (21)$$

$$\begin{aligned}
 f_{p,0}^{(s)}(\mathbf{x}) &= (-x_1)^p \times \\
 &\times g^{(c)}(x_2/x_1, x_3/x_1, \dots, x_n/x_1) \times \\
 &\times \sin(\omega \ln(-x_1)) + \\
 &+ (-x_1)^p g^{(s)}(x_2/x_1, x_3/x_1, \dots, x_n/x_1) \times \\
 &\times \cos(\omega \ln(-x_1)),
 \end{aligned} \quad (22)$$

where  $g^{(c)}(t_2, t_3, \dots, t_n)$  and  $g^{(s)}(t_2, t_3, \dots, t_n)$  are arbitrary real functions of  $(n-1)$  variables which have a one-to-one correspondence with functions  $f_{p,0}^{(c)}(\mathbf{x})$  and  $f_{p,0}^{(s)}(\mathbf{x})$ , and are selected independently of functions  $h^{(c)}(t_2, t_3, \dots, t_n)$  and  $h^{(s)}(t_2, t_3, \dots, t_n)$  used for  $x_1 > 0$ .

**Proof.** Let us substitute the value  $\lambda = 1/x_1$  in relations (17) and (18), assuming that  $x_1 > 0$ . As a result, we obtain the following linear equations for the functions  $f_{p,0}^{(c)}(\mathbf{x})$  and  $f_{p,0}^{(s)}(\mathbf{x})$ :

$$\begin{aligned}
 x_1^p f_{p,0}^{(c)}(1, x_2/x_1, x_3/x_1, \dots, x_n/x_1) &= \\
 &= f_{p,0}^{(c)}(\mathbf{x}) \cos(\omega \ln x_1) + \\
 &+ f_{p,0}^{(s)}(\mathbf{x}) \sin(\omega \ln \lambda); \\
 x_1^p f_{p,0}^{(s)}(1, x_2/x_1, x_3/x_1, \dots, x_n/x_1) &= \\
 &= f_{p,0}^{(c)}(\mathbf{x}) \sin(\omega \ln x_1) + \\
 &+ f_{p,0}^{(s)}(\mathbf{x}) \cos(\omega \ln \lambda).
 \end{aligned}$$

Let us add the notations:

$$h^{(c)}(t_2, t_3, \dots, t_n) = f_{p,0}^{(c)}(1, t_2, t_3, \dots, t_n),$$

$$h^{(s)}(t_2, t_3, \dots, t_n) = f_{p,0}^{(s)}(1, t_2, t_3, \dots, t_n).$$

Eqs. (19), (20) are obtained after that from the resulting system of linear equations.

Respectively, if  $x_1 < 0$ , after substituting  $\lambda = -1/x_1$  in Eqs. (17) and (18), we obtain Eqs. (21), (22), where the functions  $g^{(c)}(t_2, t_3, \dots, t_n)$  and  $g^{(s)}(t_2, t_3, \dots, t_n)$ , generally independent of the functions  $h^{(c)}(t_2, t_3, \dots, t_n)$  and  $h^{(s)}(t_2, t_3, \dots, t_n)$  used in Eqs. (19), (20), are given by the relations

$$g^{(c)}(t_2, t_3, \dots, t_n) = f_{p,0}^{(c)}(-1, -t_2, t_3, \dots, -t_n),$$

$$g^{(s)}(t_2, t_3, \dots, t_n) = f_{p,0}^{(s)}(-1, -t_2, \dots, -t_n).$$

Lemma 1 is proved.

If  $x_1 = 0$  and  $x_2 \neq 0$ , the problem of parametrization of functions  $f_{p,0}^{(c)}(\mathbf{x})$  and  $f_{p,0}^{(s)}(\mathbf{x})$  obeying the functional relations (17) and (18) but depending on a smaller number of independent variables is solved using the formulae similar to Eqs. (19), (20), (21), (22). The process is repeated until the list of variables  $x_1, x_2, \dots, x_n$  is exhausted.

**Lemma 2.** *Fundamental mutually homogeneous functions  $f_{p,0}^{(c)}(\mathbf{x})$  and  $f_{p,0}^{(s)}(\mathbf{x})$  of zero degree, which satisfy functional relations (17) and (18) for  $\forall \lambda > 0$ , can be represented as*

$$\begin{aligned}
 f_{p,0}^{(c)}(\mathbf{x}) &= r^p \times \\
 &\times h^{(c)}(x_1/r, x_2/r, \dots, x_n/r) \cos(\omega \ln r) - \\
 &- r^p h^{(s)}(x_1/r, x_2/r, \dots,
 \end{aligned} \quad (23)$$

$$x_n/r) \sin(\omega \ln r);$$

$$\begin{aligned}
 f_{p,0}^{(s)}(\mathbf{x}) &= r^p \times \\
 &\times h^{(c)}(x_1/r, x_2/r, \dots, x_n/r) \sin(\omega \ln r) + \\
 &+ r^p h^{(s)}(x_1/r, x_2/r, \dots, \\
 &x_n/r) \cos(\omega \ln r),
 \end{aligned} \quad (24)$$

where  $r = \sqrt{x_1^2 + \dots + x_n^2}$ , while  $h^{(c)}(t_1, t_2, \dots, t_n)$  and  $h^{(s)}(t_1, t_2, \dots, t_n)$  are arbitrary real functions of  $n$  variables given on a unit hypersphere

$$t_1^2 + t_2^2 + \dots + t_n^2 = 1,$$

which have a one-to-one correspondence with the functions  $f_{p,0}^{(c)}(\mathbf{x})$  and  $f_{p,0}^{(s)}(\mathbf{x})$ .

**Proof.** The reasoning is similar to the proof of Lemma 1, except for the multiplier  $\lambda > 0$  chosen as  $\lambda = 1/r$ . The functions

$$h^{(c)}(t_1, t_2, \dots, t_n) \text{ and } h^{(s)}(t_1, t_2, \dots, t_n),$$

given on a unit hypersphere

$$t_1^2 + t_2^2 + \dots + t_n^2 = 1,$$

are defined as

$$h^{(c)}(t_1, t_2, \dots, t_n) = f_{p,0}^{(c)}(t_1, t_2, \dots, t_n),$$

$$h^{(s)}(t_1, t_2, \dots, t_n) = f_{p,0}^{(s)}(t_1, t_2, \dots, t_n).$$

Lemma 2 is proved.

**Lemma 3.** *Suppose  $S_p(\mathbf{x})$  is a positively homogeneous function of degree  $p$ ,  $S_\omega(\mathbf{x})$  is a positively homogeneous function of degree  $\omega \neq 0$ , while  $\psi_2(\mathbf{x}), \psi_3(\mathbf{x}), \dots, \psi_n(\mathbf{x})$  are positively homogeneous functions of zero degree.*

Let us assume that these functions have no singular points in the domain  $\Omega$ , the function  $S_p$  does not become zero, the function  $S_\omega$  is strictly greater than zero, the functions  $\psi_2, \psi_3, \dots, \psi_n$  are functionally independent.

Then fundamental mutually homogeneous functions  $f_{p,0}^{(c)}(\mathbf{x})$  and  $f_{p,0}^{(s)}(\mathbf{x})$  of zero order which satisfy functional relations (17) and (18) for  $\forall \lambda > 0$  can be represented in domain  $\Omega$  as

$$\begin{aligned} f_{p,0}^{(c)}(\mathbf{x}) &= S_p(\mathbf{x}) \times \\ &\times h^{(c)}(\psi_2(\mathbf{x}), \psi_3(\mathbf{x}), \dots, \psi_n(\mathbf{x})) \times \\ &\times \cos(\omega \ln S_\omega(\mathbf{x})) - S_p(\mathbf{x}) \times \end{aligned} \quad (25)$$

$$\begin{aligned} &\times h^{(s)}(\psi_2(\mathbf{x}), \psi_3(\mathbf{x}), \dots, \psi_n(\mathbf{x})) \times \\ &\times \sin(\omega \ln S_\omega(\mathbf{x})); \\ f_{p,0}^{(s)}(\mathbf{x}) &= S_p(\mathbf{x}) \times \\ &\times h^{(c)}(\psi_2(\mathbf{x}), \psi_3(\mathbf{x}), \dots, \psi_n(\mathbf{x})) \times \\ &\times \sin(\omega \ln S_\omega(\mathbf{x})) + S_p(\mathbf{x}) \times \end{aligned} \quad (26)$$

$$\begin{aligned} &h^{(s)}(\psi_2(\mathbf{x}), \psi_3(\mathbf{x}), \dots, \psi_n(\mathbf{x})) \times \\ &\times \cos(\omega \ln S_\omega(\mathbf{x})), \end{aligned}$$

where  $h^{(c)}(t_2, t_3, \dots, t_n)$  and  $h^{(s)}(t_2, t_3, \dots, t_n)$  are arbitrary real functions of  $(n-1)$  variables which have a one-to-one correspondence with the functions  $f_{p,0}^{(c)}(\mathbf{x})$  and  $f_{p,0}^{(s)}(\mathbf{x})$ .

**Proof.** The functions

$$g^{(c)}(\mathbf{x}) = f_{p,0}^{(c)}(\mathbf{x})/S_p(\mathbf{x}),$$

$$g^{(s)}(\mathbf{x}) = f_{p,0}^{(s)}(\mathbf{x})/S_p(\mathbf{x})$$

are fundamental mutually homogeneous functions of zero order and zero degree satisfying the relations

$$g^{(c)}(\lambda \mathbf{x}) = g^{(c)}(\mathbf{x}) \cos(\omega \ln \lambda) -$$

$$g^{(s)}(\mathbf{x}) \sin(\omega \ln \lambda),$$

$$g^{(s)}(\lambda \mathbf{x}) = g^{(c)}(\mathbf{x}) \sin(\omega \ln \lambda) +$$

$$+ g^{(s)}(\mathbf{x}) \cos(\omega \ln \lambda).$$

Let us substitute the value  $\lambda = S_\omega(\mathbf{x})^{1/\omega}$  in this relation, which is well defined in the given domain and satisfies the condition  $\lambda > 0$ .

The functions

$$g^{(c)}(x_1/S_\omega(\mathbf{x})^{1/\omega}, x_2/S_\omega(\mathbf{x})^{1/\omega}, \dots, x_n/S_\omega(\mathbf{x})^{1/\omega}),$$

$$g^{(s)}(x_1/S_\omega(\mathbf{x})^{1/\omega}, x_2/S_\omega(\mathbf{x})^{1/\omega}, \dots, x_n/S_\omega(\mathbf{x})^{1/\omega})$$

are Euler-homogeneous of zero degree, therefore they can be written as

$$h^{(c)}(\psi_2(\mathbf{x}), \psi_3(\mathbf{x}), \dots, \psi_n(\mathbf{x}))$$

and, respectively,

$$h^{(s)}(\psi_2(\mathbf{x}), \psi_3(\mathbf{x}), \dots, \psi_n(\mathbf{x}))$$

(see Eq. (12)).

After this, using relations

$$h^{(c)}(\psi_2(\mathbf{x}), \psi_3(\mathbf{x}), \dots, \psi_n(\mathbf{x})) =$$

$$= g^{(c)}(\mathbf{x}) \cos(\ln S_\omega(\mathbf{x})) +$$

$$+ g^{(s)}(\mathbf{x}) \sin(\ln S_\omega(\mathbf{x}));$$

$$h^{(s)}(\psi_2(\mathbf{x}), \psi_3(\mathbf{x}), \dots, \psi_n(\mathbf{x})) =$$

$$= g^{(c)}(\mathbf{x}) \sin(\ln S_\omega(\mathbf{x})) +$$

$$+ g^{(s)}(\mathbf{x}) \cos(\ln S_\omega(\mathbf{x})),$$

we can express the functions  $g^{(c)}(\mathbf{x})$  and  $g^{(s)}(\mathbf{x})$ .

As a result, we obtain Eqs. (25), (26) for the functions  $f_{p,0}^{(c)}(\mathbf{x})$  and  $f_{p,0}^{(s)}(\mathbf{x})$ .

Lemma 3 is proved.

**Lemma 4.** Fundamental mutually homogeneous functions  $f_{p,0}^{(c)}(\mathbf{x})$  and  $f_{p,0}^{(s)}(\mathbf{x})$  of zero order, satisfying functional relations (17) and (18) for  $\forall \lambda > 0$ , can be represented in the form

$$f_{p,0}^{(c)}(\mathbf{x}) = R_p(\mathbf{x}) \cos(\ln |\Phi_\omega(\mathbf{x})|); \quad (27)$$

$$f_{p,0}^{(s)}(\mathbf{x}) = R_p(\mathbf{x}) \sin(\ln |\Phi_\omega(\mathbf{x})|), \quad (28)$$

where  $R_p(\mathbf{x})$  is an arbitrary positively homogeneous function of degree  $p$ , while  $\Phi_\omega(\mathbf{x})$  is an arbitrary positively homogeneous function of degree  $\omega$ , which have a one-to-one correspondence with the functions  $f_{p,0}^{(c)}(\mathbf{x})$  and  $f_{p,0}^{(s)}(\mathbf{x})$ .

**Proof.** Let us use Lemma 3, where  $\Omega = R^n$  and the following positively homogeneous functions are chosen:

$$S_p(\mathbf{x}) = r^p, S_\omega(\mathbf{x}) = r^\omega,$$

$$\psi_2(\mathbf{x}) = x_2/r, \psi_3(\mathbf{x}) = x_3/r, \dots,$$

$$\psi_n(\mathbf{x}) = x_n/r, r = \sqrt{x_1^2 + x_2^2 + \dots + x_n^2},$$

which satisfy the conditions of the lemma in the entire space  $R^n$ , except for the origin of coordinates.

The functions  $h^{(c)}(\psi_2, \psi_3, \dots, \psi_n)$  and  $h^{(s)}(t_2, t_3, \dots, t_n)$ , included in Eqs. (25), (26), can be represented as





$$h^{(c)}(\psi_2, \psi_3, \dots, \psi_n) =$$

$$= H(\psi_2, \psi_3, \dots, \psi_n) \cos(G(\psi_2, \psi_3, \dots, \psi_n));$$

$$h^{(s)}(\psi_2, \psi_3, \dots, \psi_n) =$$

$$= H(\psi_2, \psi_3, \dots, \psi_n) \sin(G(\psi_2, \psi_3, \dots, \psi_n)),$$

where  $H(\psi_2, \psi_3, \dots, \psi_n)$  and  $G(\psi_2, \psi_3, \dots, \psi_n)$  are arbitrary functions of  $(n-1)$  variables.

According to Eq. (12), an arbitrary positively homogeneous function  $R_p(\mathbf{x})$  of degree  $p$  can be represented as

$$R_p(\mathbf{x}) = S_p(\mathbf{x}) \times$$

$$\times H(\psi_2(\mathbf{x}), \psi_3(\mathbf{x}), \dots, \psi_n(\mathbf{x})),$$

while an arbitrary positively homogeneous function  $\Phi_\omega(\mathbf{x})$  of degree  $\omega$  can be represented as

$$\Phi_\omega(\mathbf{x}) = \pm S_\omega(\mathbf{x}) \times$$

$$\times \exp(G(\psi_2(\mathbf{x}), \psi_3(\mathbf{x}), \dots, \psi_n(\mathbf{x}))),$$

where  $G(\mathbf{x}) = \ln(|\Phi_\omega(\mathbf{x})|/S_\omega(\mathbf{x}))$  is a positively homogeneous function of zero degree, and the sign is chosen in accordance with the signs of the functions  $\Phi_\omega(\mathbf{x})$ . Here, we should take into account that the positively homogeneous function  $\Phi_\omega(\mathbf{x})$  preserves the same sign at all points of the form  $\lambda\mathbf{x}$ .

Eqs. (25), (26) take the form (27), (28) after the given substitutions.

Lemma 4 is proved.

**Theorem.** A chain of fundamental mutually homogeneous functions  $f_{p,k}^{(c)}(\mathbf{x})$  and  $f_{p,k}^{(s)}(\mathbf{x})$ , obeying functional relations (13) and (14) for  $\forall \lambda > 0$ , at all points where the function  $S_q(\mathbf{x})$  is not equal to zero, can be expressed in the form

$$f_{p,k}^{(c)}(\mathbf{x}) = \sum_{j=0,k} ((\ln |S_q(\mathbf{x})|)^{k-j}/(k-j)!) \times$$

$$\times R_p^{(j)}(\mathbf{x}) \cos(\ln Q_\omega^{(j)}(\mathbf{x})); \quad (29)$$

$$f_{p,k}^{(s)}(\mathbf{x}) = \sum_{j=0,k} ((\ln |S_q(\mathbf{x})|)^{k-j}/(k-j)!) \times$$

$$\times R_p^{(j)}(\mathbf{x}) \sin(\ln Q_\omega^{(j)}(\mathbf{x})), \quad (30)$$

where  $R_p^{(j)}(\mathbf{x})$  are arbitrary homogeneous functions of degree  $p$ ;  $Q_\omega^{(j)}(\mathbf{x})$  are arbitrary homogeneous functions of degree  $\omega \neq 0$  taking positive values;  $S_q(\mathbf{x})$  is a fixed homogeneous function, nonzero at any point, of degree  $q \neq 0$ .

There is a one-to-one correspondence between the functions  $f_{p,k}^{(c)}(\mathbf{x})$ ,  $f_{p,k}^{(s)}(\mathbf{x})$  and the functions  $R_p^{(j)}(\mathbf{x})$ ,  $Q_\omega^{(j)}(\mathbf{x})$ , provided that the function  $S_q(\mathbf{x})$  is fixed.

**Proof.** If  $k = 0$ , the validity of Eqs. (29), (30) is established by Lemma 4 and Eqs. (27), (28). Employing the method of induction, we assume the following: let conditions (29), (30) hold true, when  $k = 0, 1, \dots, m-1$ . Let us substitute

$$f_{p,m}^{(c)}(\mathbf{x}) = g_c(\mathbf{x}) + \sum_{k=1,m} ((\ln |S_q(\mathbf{x})|)^k/k!) \times$$

$$\times R_p^{(m-k)}(\mathbf{x}) \cos(\ln Q_\omega^{(m-k)}(\mathbf{x}));$$

$$f_{p,m}^{(s)}(\mathbf{x}) = g_s(\mathbf{x}) + \sum_{k=1,m} ((\ln |S_q(\mathbf{x})|)^k/k!) \times$$

$$\times R_p^{(m-k)}(\mathbf{x}) \sin(\ln Q_\omega^{(m-k)}(\mathbf{x})),$$

where  $g_c(\mathbf{x})$  and  $g_s(\mathbf{x})$  are arbitrary functions for the time being, while the functions  $R_p^{(j)}(\mathbf{x})$  and  $Q_\omega^{(j)}(\mathbf{x})$  are obtained in the previous steps of the proof.

Let us substitute these expressions together with Eqs. (29), (30) for  $k = 0, 1, \dots, m-1$  in Eqs. (13), (14) for  $k = m$ , which can be now written as

$$0 = f_{p,m}^{(c)}(\lambda\mathbf{x}) - \lambda^p \cos(\omega \ln \lambda) (f_{p,m}^{(c)}(\mathbf{x}) +$$

$$+ \sum_{k=1,m} ((q \ln \lambda)^k/k!) f_{p,m-k}^{(c)}(\mathbf{x})) +$$

$$+ \lambda^p \sin(\omega \ln \lambda) (f_{p,m}^{(s)}(\mathbf{x}) +$$

$$+ \sum_{k=1,m} ((q \ln \lambda)^k/k!) f_{p,m-k}^{(s)}(\mathbf{x}));$$

$$0 = f_{p,m}^{(s)}(\lambda\mathbf{x}) - \lambda^p \sin(\omega \ln \lambda) (f_{p,m}^{(c)}(\mathbf{x}) +$$

$$+ \sum_{k=1,m} ((q \ln \lambda)^k/k!) f_{p,m-k}^{(c)}(\mathbf{x})) -$$

$$- \lambda^p \cos(\omega \ln \lambda) (f_{p,m}^{(s)}(\mathbf{x}) +$$

$$+ \sum_{k=1,m} ((q \ln \lambda)^k/k!) f_{p,m-k}^{(s)}(\mathbf{x})).$$

We need to find such functions  $g_c(\mathbf{x})$  and  $g_s(\mathbf{x})$ , for which these equations hold. After rather cumbersome simplification, the equations are converted to the following form:

$$g_c(\lambda\mathbf{x}) = g_c(\mathbf{x}) \lambda^p \cos(\omega \ln \lambda) -$$

$$- g_s(\mathbf{x}) \lambda^p \sin(\omega \ln \lambda);$$

$$g_s(\lambda\mathbf{x}) = g_c(\mathbf{x}) \lambda^p \sin(\omega \ln \lambda) +$$

$$+ g_s(\mathbf{x}) \lambda^p \cos(\omega \ln \lambda).$$

According to Lemma 4, there are such functions  $R_p^{(m)}(\mathbf{x})$  and  $Q_\omega^{(m)}(\mathbf{x})$  satisfying the conditions of the theorem, that the following equalities hold true:

$$g_c(\mathbf{x}) = R_p^{(m)}(\mathbf{x}) \cos(\ln Q_\omega^{(m)}(\mathbf{x}));$$

$$g_s(\mathbf{x}) = R_p^{(m)}(\mathbf{x}) \sin(\ln Q_\omega^{(m)}(\mathbf{x})).$$

Respectively, Eq. (21) also holds true for  $k = m$ , which means for any  $k = 0, 1, 2, \dots$  as well.

The theorem is proved.

*Note.* A set of points for which  $S_q(\mathbf{x}) = 0$  comprises a conic surface of a smaller dimension, along which the functions  $f_{p,k}^{(c)}(\mathbf{x})$  and  $f_{p,k}^{(s)}(\mathbf{x})$  are again fundamental mutually homogeneous functions but of a smaller number of independent variables. Therefore, parametrization of the form (29), (30) is again applicable for the boundaries separating the conic domains  $S_q(\mathbf{x}) \neq 0$ , but with different functions  $S_q$  and with a smaller number of variables involved, etc.

**Corollary 1.** A chain of fundamental associated homogeneous functions  $f_{p,k}^{(c)}(\mathbf{x})$  and  $f_{p,k}^{(s)}(\mathbf{x})$ , which obeys functional relations (13) and (14) for  $\forall \lambda > 0$ , can be expressed as follows, if  $x_1 > 0$ :

$$\begin{aligned} f_{p,k}^{(c)}(\mathbf{x}) = & \sum_{j=0,k} x_1^p ((q \ln x_1)^{k-j} / (k-j)!) \times \\ & \times h_j^{(c)}(x_2/x_1, x_3/x_1, \dots, x_n/x_1) \cos(\omega \ln x_1) - \\ & - \sum_{j=0,k} x_1^p ((q \ln x_1)^{k-j} / (k-j)!) \times \end{aligned} \quad (31)$$

$$\begin{aligned} & \times h_j^{(s)}(x_2/x_1, x_3/x_1, \dots, x_n/x_1) \sin(\omega \ln x_1); \\ f_{p,k}^{(s)}(\mathbf{x}) = & \sum_{j=0,k} x_1^p ((q \ln x_1)^{k-j} / (k-j)!) \times \\ & \times h_j^{(c)}(x_2/x_1, x_3/x_1, \dots, x_n/x_1) \sin(\omega \ln x_1) + \\ & + \sum_{j=0,k} x_1^p ((q \ln x_1)^{k-j} / (k-j)!) \times \end{aligned} \quad (32)$$

where  $h_j^{(c)}(t_2, t_3, \dots, t_n)$  and  $h_j^{(s)}(t_2, t_3, \dots, t_n)$  are arbitrary real functions of  $(n - 1)$  variables, which have a one-to-one correspondence with the functions  $f_{p,k}^{(c)}(\mathbf{x})$  and  $f_{p,k}^{(s)}(\mathbf{x})$ .

By substituting  $x_1 \rightarrow -x_1$  in Eqs. (31), (32) we obtain the formulae for the case  $x_1 < 0$ :

$$\begin{aligned} f_{p,k}^{(c)}(\mathbf{x}) = & \sum_{j=0,k} (-x_1)^p ((q \ln(-x_1))^{k-j} / (k-j)!) \times \\ & \times g_j^{(c)}(x_2/x_1, x_3/x_1, \dots, x_n/x_1) \cos(\omega \ln(-x_1)) - \\ & - \sum_{j=0,k} (-x_1)^p ((q \ln(-x_1))^{k-j} / (k-j)!) \times \end{aligned} \quad (33)$$

$$\begin{aligned} & \times g_j^{(s)}(x_2/x_1, x_3/x_1, \dots, x_n/x_1) \sin(\omega \ln(-x_1)); \\ f_{p,k}^{(s)}(\mathbf{x}) = & \sum_{j=0,k} (-x_1)^p ((q \ln(-x_1))^{k-j} / (k-j)!) \times \\ & \times g_j^{(c)}(x_2/x_1, x_3/x_1, \dots, x_n/x_1) \sin(\omega \ln(-x_1)) + \\ & + \sum_{j=0,k} (-x_1)^p ((q \ln(-x_1))^{k-j} / (k-j)!) \times \end{aligned} \quad (34)$$

$$\times g_j^{(s)}(x_2/x_1, x_3/x_1, \dots, x_n/x_1) \cos(\omega \ln(-x_1)),$$

where  $g_j^{(c)}(t_2, t_3, \dots, t_n)$  and  $g_j^{(s)}(t_2, t_3, \dots, t_n)$  are arbitrary real functions of  $(n - 1)$  variables, with a one-to-one correspondence with the functions  $f_{p,k}^{(c)}(\mathbf{x})$  and  $f_{p,k}^{(s)}(\mathbf{x})$ , while the functions  $g_j^{(c)}(t_2, t_3, \dots, t_n)$  and  $g_j^{(s)}(t_2, t_3, \dots, t_n)$  are selected independently of the functions  $h_j^{(c)}(t_2, t_3, \dots, t_n)$  and  $h_j^{(s)}(t_2, t_3, \dots, t_n)$ , used in the case  $x_1 > 0$ .

*Proof.* Let us confine ourselves to proving Corollary 1 for the condition  $x_1 > 0$ , as the case  $x_1 < 0$  is obtained from calculations for the case  $x_1 > 0$  after substituting  $x_1 = -x_1$ , with which relations (29), (30) preserve their form. We apply the proved theorem with the function  $S(\mathbf{x}) = x_1^q$ , where the functions  $R_p^{(q)}(\mathbf{x})$  and  $Q_\omega^{(q)}(\mathbf{x})$  are represented in the domain  $x_1 > 0$  in accordance with Eqs. (9) in the following form:

$$R_p^{(q)}(\mathbf{x}) = x_1^p H_j(x_2/x_1, x_3/x_1, \dots, x_n/x_1),$$

$$Q_\omega^{(q)}(\mathbf{x}) = x_1^\omega G_j(x_2/x_1, x_3/x_1, \dots, x_n/x_1).$$

After substitution and transforming Eqs. (29), (30) for the new functions

$$h_j^{(c)}(t_2, t_3, \dots, t_n) =$$

$$= H_j(t_2, t_3, \dots, t_n) \cos(\ln G_j(t_2, t_3, \dots, t_n));$$

$$h_j^{(s)}(t_2, t_3, \dots, t_n) =$$

$$= H_j(t_2, t_3, \dots, t_n) \sin(\ln G_j(t_2, t_3, \dots, t_n)),$$

we obtain Eqs. (31), (32).

Because the functions

$$H_j(t_2, t_3, \dots, t_n) \text{ and } G_j(t_2, t_3, \dots, t_n)$$

are arbitrary, then the functions

$$h_j^{(c)}(t_2, t_3, \dots, t_n), h_j^{(s)}(t_2, t_3, \dots, t_n)$$

are arbitrary as well.

This proves Corollary 1.

*Note to Corollary 1.* When  $x_1 = 0$  and  $x_2 \neq 0$ , the problem of parametrization of functions  $f_{p,k}^{(c)}(\mathbf{x})$  and  $f_{p,k}^{(s)}(\mathbf{x})$ , which obey functional relations (13) and (14) but depend on a smaller number of independent variables, is solved using formulae similar to Eqs. (31), (32), (33), (34). The process is repeated recursively, until the list of nonzero variables  $x_1, x_2, \dots, x_n$  is exhausted.

**Corollary 2.** A chain of fundamental associated homogeneous functions  $f_{p,k}^{(c)}(\mathbf{x})$  and  $f_{p,k}^{(s)}(\mathbf{x})$ , which obeys functional relations (13) and (14) for  $\forall \lambda > 0$ , can be represented as

$$f_{p,k}^{(c)}(\mathbf{x}) = \sum_{j=0,k} r^p ((q \ln r)^{k-j} / (k-j)!) \times \quad (35)$$

$$\times h_j^{(c)}(x_1/r, x_2/r, \dots, x_n/r) \cos(\omega \ln r) -$$



$$\begin{aligned}
 & - \sum_{j=0,k} r^p ((q \ln r)^{k-j} / (k-j)!) \times \\
 & \times h_j^{(s)}(x_1/r, x_2/r, \dots, x_n/r) \sin(\omega \ln r);
 \end{aligned} \quad (35)$$

$$\begin{aligned}
 f_{p,k}^{(s)}(\mathbf{x}) &= \sum_{j=0,k} r^p ((q \ln r)^{k-j} / (k-j)!) \times \\
 & \times h_j^{(c)}(x_1/r, x_2/r, \dots, x_n/r) \sin(\omega \ln r) + \\
 & + \sum_{j=0,k} r^p ((q \ln r)^{k-j} / (k-j)!) \times \\
 & \times h_j^{(s)}(x_1/r, x_2/r, \dots, x_n/r) \cos(\omega \ln r),
 \end{aligned} \quad (36)$$

where  $r = |\mathbf{x}| = \sqrt{x_1^2 + x_2^2 + \dots + x_n^2}$ , and

$$h_j^{(c)}(t_1, t_2, \dots, t_n) \text{ and } h_j^{(s)}(t_1, t_2, \dots, t_n)$$

are arbitrary real functions given on the surface of a unit hypersphere

$$t_1^2 + t_2^2 + \dots + t_n^2 = 1$$

and which have a one-to-one correspondence with functions  $f_{p,k}^{(c)}(\mathbf{x})$  and  $f_{p,k}^{(s)}(\mathbf{x})$ .

**Proof.** We use the same procedure as for proving Corollary 2, where  $S(\mathbf{x}) = r^q$ , and Eqs. (11) are applied for functions  $R_p^{(j)}(\mathbf{x})$  and  $Q_\omega^{(j)}(\mathbf{x})$ .

Corollary 2 is proved.

**Corollary 3.** Suppose  $\psi_p(\mathbf{x})$  is a positively homogeneous function of degree  $p$ ,  $\psi_q(\mathbf{x})$  is a positively homogeneous function of degree  $q \neq 0$ ,  $\psi_\omega(\mathbf{x})$  is a positively homogeneous function of degree  $\omega \neq 0$ , a  $\psi_2(\mathbf{x}), \psi_3(\mathbf{x}), \dots, \psi_n(\mathbf{x})$  is a positively homogeneous function of zero degree.

Assume these functions have no singular points or discontinuities in the domain  $\Omega$ , the function  $\psi_p$  does not become zero, the functions  $\psi_q$  and  $\psi_\omega$  are strictly positive<sup>2</sup>, the functions  $\psi_2, \psi_3, \dots, \psi_n$  are functionally independent.

Then fundamental mutually homogeneous functions  $f_{p,k}^{(c)}(\mathbf{x})$  and  $f_{p,k}^{(s)}(\mathbf{x})$ , which obey functional relations (13) and (14) for  $\forall \lambda > 0$ , can be mapped one-to-one in the domain  $\Omega$  as

$$\begin{aligned}
 f_{p,k}^{(c)}(\mathbf{x}) &= \sum_{j=0,k} \psi_p(\mathbf{x}) (\ln \psi_q(\mathbf{x}))^{k-j} / (k-j)! \times \\
 & \times \cos(\ln \psi_\omega(\mathbf{x})) h_j^{(c)}(\psi_2(\mathbf{x}), \psi_3(\mathbf{x}), \dots, \psi_n(\mathbf{x})) - \\
 & - \sum_{j=0,k} \psi_p(\mathbf{x}) (\ln \psi_q(\mathbf{x}))^{k-j} / (k-j)! \times
 \end{aligned} \quad (37)$$

$$\begin{aligned}
 & \times \sin(\ln \psi_\omega(\mathbf{x})) h_j^{(s)}(\psi_2(\mathbf{x}), \psi_3(\mathbf{x}), \dots, \psi_n(\mathbf{x})); \\
 f_{p,k}^{(s)}(\mathbf{x}) &= \sum_{j=0,k} \psi_p(\mathbf{x}) (\ln \psi_q(\mathbf{x}))^{k-j} / (k-j)! \times \\
 & \times \sin(\ln \psi_\omega(\mathbf{x})) h_j^{(c)}(\psi_2(\mathbf{x}), \psi_3(\mathbf{x}), \dots, \psi_n(\mathbf{x})) + \\
 & + \sum_{j=0,k} \psi_p(\mathbf{x}) (\ln \psi_q(\mathbf{x}))^{k-j} / (k-j)! \times \\
 & \times \cos(\ln \psi_\omega(\mathbf{x})) h_j^{(s)}(\psi_2(\mathbf{x}), \psi_3(\mathbf{x}), \dots, \psi_n(\mathbf{x})),
 \end{aligned} \quad (38)$$

where  $h_j^{(c)}(t_2, t_3, \dots, t_n)$  and  $h_j^{(s)}(t_2, t_3, \dots, t_n)$  are arbitrary real functions of  $(n-1)$  variables, with a one-to-one correspondence with the functions  $f_{p,k}^{(c)}(\mathbf{x})$  and  $f_{p,k}^{(s)}(\mathbf{x})$ .

**Proof.** The same scheme is used for the proof as in Corollary 1, where  $S(\mathbf{x}) = \psi_q(\mathbf{x})$ , and Eqs. (12) are applied for the functions  $R_p^{(j)}(\mathbf{x})$  and  $Q_\omega^{(j)}(\mathbf{x})$ .

Corollary 3 is proved.

**Note to Corollary 3.** Using Eqs. (37), (38), the entire space  $R^n$  is partitioned into non-intersecting conic domains  $\Omega_s$ , where the functions  $\psi_p(\mathbf{x})$ ,  $\psi_q(\mathbf{x})$  and  $\psi_\omega(\mathbf{x})$ , selected in a fixed manner, do not become zero, the functions

$$\psi_2(\mathbf{x}), \psi_3(\mathbf{x}), \dots, \psi_n(\mathbf{x})$$

form a functionally independent set of functions, and the given functions have no singular points or discontinuities. Generally speaking, constructing parametrization (37), (38), we use for each of the domains  $\Omega_s$  a specific set of functions

$$h_j^{(c)}(t_2, t_3, \dots, t_n) \text{ and } h_j^{(s)}(t_2, t_3, \dots, t_n),$$

which is completely unrelated to the functions

$$h_j^{(c)}(t_2, t_3, \dots, t_n) \text{ and } h_j^{(s)}(t_2, t_3, \dots, t_n),$$

used for other domains.

As a result, parametrization of fundamental associated homogeneous functions  $f_{p,k}^{(c)}(\mathbf{x})$  and  $f_{p,k}^{(s)}(\mathbf{x})$  is partitioned into several independent branches, and such a partition depends on the selected auxiliary functions  $\psi_p(\mathbf{x})$ ,  $\psi_q(\mathbf{x})$  and  $\psi_\omega(\mathbf{x})$ , and, to a lesser degree, on the functions

$$\psi_2(\mathbf{x}), \psi_3(\mathbf{x}), \dots, \psi_n(\mathbf{x}),$$

and due to this does not reflect the internal structure of the chain of functions parameterized.

A linear combination of functions with constant factors comprised from several chains of fundamental mutually homogeneous functions of degree  $p$  is a chain of fundamental mutually homogeneous functions of degree  $p$  as well. Besides, if  $f_{p,k}^{(c)}(\mathbf{x})$  and  $f_{p,k}^{(s)}(\mathbf{x})$  are a chain of fundamental mutually homogeneous functions of degree  $p$ , then the new chain of functions

$$g_{p,k}^{(c)}(\mathbf{x}) = f_{p,k-1}^{(c)}(\mathbf{x}) \text{ and } g_{p,k}^{(s)}(\mathbf{x}) = f_{p,k-1}^{(s)}(\mathbf{x}),$$

obtained by shifting the index  $k \rightarrow k-1$  and supplemented by leading zeros  $g_{p,0}^{(c)}(\mathbf{x}) = 0$  and  $g_{p,0}^{(s)}(\mathbf{x}) = 0$ , is also a chain of fundamental mutually homogeneous functions of degree  $p$ .

The resulting Eqs. (29)–(38) illustrate the validity of Gel'fand's hypothesis that chains

<sup>2</sup> Absolute values are used for negative functions.

of general form are obtained from the main chains with a nonzero first term using a linear combination with constant factors comprised of main and derived chains, which in turn result from the main chains by shifting the index  $k$  and supplementing the chain with leading zeros. At the same time, unlike composite chains, all terms of the main chain of functions are reconstructed with a one-to-one correspondence by its first element in accordance with a certain rule.

The accurate formulation of this rule reflects the researcher's subjective preferences and can widely vary. Generally speaking, the main chain is a fairly vague notion, as selecting a different method for function parametrization makes previously main chains composite, and conversely, some previously composite chains become main ones.

As follows from Eq. (21), fundamental associated homogeneous functions are in fact linear combinations with constant factors generated by the main chains of functions expressed as

$$(1/k!) (\ln |S_q(\mathbf{x})|)^k R_p(\mathbf{x}) \cos(\ln |S_\omega(\mathbf{x})|),$$

$$(1/k!) (\ln |S_q(\mathbf{x})|)^k R_p(\mathbf{x}) \sin(\ln |S_\omega(\mathbf{x})|),$$

where  $R_p(\mathbf{x})$  are arbitrary positively homogeneous functions of degree  $p$ ,  $S_\omega(\mathbf{x})$  are arbitrary positively homogeneous functions of degree  $\omega$ , and  $S_q(\mathbf{x})$  are fixed positively homogeneous functions of degree  $q$ . The situation does not change and we can obtain no new functions, if we allow for functions  $S_q(\mathbf{x})$  to be arbitrary positively homogeneous functions of degree  $q$  (although distinguishing main chains from composite ones becomes exceptionally challenging with this approach).

### Preliminary conclusions

Analyzing mutually homogeneous functions which correspond to a matrix of functional equations with identical real eigenvalues, we obtained a class of functions which are a generalization of associated homogeneous Gel'fand functions [29, 30]. The definitions and theorems formulated in the study allow to define this important class of functions

well and consider its properties in detail. In particular, the theorem on fundamental mutually homogeneous functions allows to safely introduce the functions of the form

$$\begin{aligned} f_{p,k}^{(c)}(\mathbf{x}) &= (1/k!) \times \\ &\times (\ln S_q(\mathbf{x}))^k R_p(\mathbf{x}) \cos(\ln \Phi_\omega(\mathbf{x})); \\ f_{p,k}^{(s)}(\mathbf{x}) &= (1/k!) \times \\ &\times (\ln S_q(\mathbf{x}))^k R_p(\mathbf{x}) \sin(\ln \Phi_\omega(\mathbf{x})), \end{aligned}$$

as well as their linear combinations with constants factors (possibly, with a preliminary shift of index  $k$  and supplement of the function chain with leading zeros),

where  $R_p(\mathbf{x})$  is a positively Euler-homogeneous function of degree  $p$ ;  $S_q(\mathbf{x})$  is a positively Euler-homogeneous function of degree  $q$ , taking positive values;  $\Phi_\omega(\mathbf{x})$  is a positively Euler-homogeneous function of degree  $\omega$ , taking positive values.

These functions identically coincide with the given class of fundamental mutually homogeneous functions, while fully retaining their properties without producing fundamentally new mathematical objects.

We intend to continue the analysis of differential and integral properties of chains of fundamental mutually homogeneous functions as a new functional class of real variable functions in subsequent publications.

The calculations in this paper were carried out using the Wolfram Mathematica software [31].

### Acknowledgements

We wish to express our sincere gratitude to Anton Leonidovich Bulyanitsa, Doctor of Physical and Mathematical Sciences, Professor of Department of Higher Mathematics of Peter the Great St. Petersburg Polytechnic University, for active participation in discussions on the problem.

This study was partially supported by NIR 0074-2019-0009, part of State Task No. 075-01073-20-00 of the Ministry of Science and Higher Education of the Russian Federation.





## REFERENCES

1. **Berdnikov A.S., Gall L.N., Gall N.R., Solovyev K.V.**, Generalization of the Thomson formula for harmonic functions of a general type, *St. Petersburg Polytechnical State University Journal. Physics and Mathematics*. 12 (2) (2019) 32–48.
2. **Berdnikov A.S., Gall L.N., Gall N.R., Solovyev K.V.**, Generalization of the Thomson formula for homogeneous harmonic functions, *St. Petersburg Polytechnical State University Journal. Physics and Mathematics*. 12 (2) (2019) 49–62.
3. **Berdnikov A.S., Gall L.N., Gall N.R., Solovyev K.V.**, Donkin's differential operators for homogeneous harmonic functions, *St. Petersburg Polytechnical State University Journal. Physics and Mathematics*. 12 (3) (2019) 45–62.
4. **Berdnikov A.S., Gall L.N., Gall N.R., Solovyev K.V.**, Basic Donkin's differential operators for homogeneous harmonic functions, *St. Petersburg Polytechnical State University Journal. Physics and Mathematics*. 12 (3) (2019) 26–44.
5. **Golikov Yu.K., Krasnova N.K.**, *Teoriya synteza elektrostatocheskikh energoanalizatorov [Theory of designing of electrostatic energy analyzers]*, Saint-Petersburg Polytechnic University Publishing, Saint-Petersburg, 2010.
6. **Golikov Yu.K., Krasnova N.K.**, Application of electric fields uniform in the Euler sense in electron spectrography, *Technical Physics*. 56 (2) (2011) 164–170.
7. **Golikov Yu.K., Krasnova N.K.**, Generalized similarity principle of similarity in electron spectrography, *Prikladnaya fizika (Applied Physics)*. (2) (2007) 5–11.
8. **Averin I.A., Berdnikov A.S., Gall N.R.**, The principle of similarity of trajectories for the motion of charged particles with different masses in electric and magnetic fields that are homogeneous in Euler terms, *Technical Physics Letters*. 43 (2) (2017) 156–158.
9. **Khursheed A., Dinnis A.R., Smart P.D.**, Micro-extraction fields to improve electron beam test measurements, *Microelectronic Engineering*. 14 (3–4) (1991) 197–205.
10. **Khursheed A.**, Multi-channel vs. conventional retarding field spectrometers for voltage contrast, *Microelectronic Engineering*. 16 (1–4) (1992) 43–50.
11. **Khursheed A., Phang J.C., Thong J.T.L.**, A portable scanning electron microscope column design based on the use of permanent magnets, *Scanning*. 20 (2) (1998) 87–91.
12. **Khursheed A.**, Magnetic axial field measurements on a high resolution miniature scanning electron microscope, *Review of Scientific Instruments*. 71 (4) (2000) 1712–1715.
13. **Khursheed A.**, A low voltage time of flight electron emission microscope, *Optik (Jena)*. 113 (11) (2002) 505–509.
14. **Khursheed A.**, Aberration characteristics of immersion lenses for LVSEM, *Ultramicroscopy*. 93 (3–4) (2002) 331–338.
15. **Khursheed A., Karupiah N., Osterberg M., Thong J.T.L.**, Add-on transmission attachments for the scanning electron microscope, *Review of Scientific Instruments*. 74 (1) (2003) 134–140.
16. **Khursheed A., Osterberg M.**, A spectroscopic scanning electron microscope design, *Scanning*. 26 (6) (2004) 296–306.
17. **Osterberg M., Khursheed A.**, Simulation of magnetic sector deflector aberration properties for low-energy electron microscopy, *Nuclear Instruments and Methods in Physics Research, Section A*. 555 (1–2) (2005) 20–30.
18. **Khursheed A., Osterberg M.**, Developments in the design of a spectroscopic scanning electron microscope, *Nuclear Instruments and Methods in Physics Research, Section A*. 556 (2) (2006) 437–444.
19. **Luo T., Khursheed A.**, Imaging with surface sensitive backscattered electrons, *Journal of Vacuum Science and Technology B*. 25 (6) (2007) 2017–2019.
20. **Khursheed A., Hoang H.Q.**, A second-order focusing electrostatic toroidal electron spectrometer with  $2\pi$  radian collection, *Ultramicroscopy*. 109 (1) (2008) 104–110.
21. **Khursheed A.**, *Scanning electron microscope optics and spectrometers*. World Scientific, Singapore, 2010.
22. **Hoang H.Q., Khursheed A.**, A radial mirror analyzer for scanning electron/ion microscopes, *Nuclear Instruments and Methods in Physics Research, Section A*. 635 (1) (2011) 64–68.
23. **Hoang H.Q., Osterberg M., Khursheed A.**, A high signal-to-noise ratio toroidal electron spectrometer for the SEM, *Ultramicroscopy*. 111 (8) (2011) 1093–1100.
24. **Khursheed A., Hoang H.Q., Srinivasan A.**, A wide-range parallel radial mirror analyzer for scanning electron/ion microscopes, *Journal of Electron Spectroscopy and Related Phenomena*. 184 (11–12) (2012) 525–532.
25. **Shao X., Srinivasan A., Ang W.K., Khursheed A.**, A high-brightness large-diameter graphene coated point cathode field emission



electron source, Nature Communications. 9 (1) (2018) 1288.

26. **Berdnikov A.S., Solovyev K.V., Krasnova N.K.**, Mutually homogeneous functions with finite-sized matrices, St. Petersburg Polytechnical State University Journal. Physics and Mathematics. 13 (1) (2020) 42–53.

27. **Berdnikov A.S., Solovyev K.V., Krasnova N.K.**, Chains of fundamental mutually homogeneous functions with a common real eigenvalue, St. Petersburg Polytechnical State University Journal. Physics and Mathematics.

13 (2) (2020) 53–71.

28. **Fikhtengol'ts G.M.**, The fundamentals of mathematical analysis, Vol. 1, Pergamon Press, Oxford, New York, 1965.

29. **Gel'fand I.M., Shapiro Z.Ya.**, Generalized functions and their applications, Uspekhi Mat. Nauk. 10 (3) (1955) 3–70 (in Russian).

30. **Gel'fand I.M., Shilov G.E.**, Generalized functions, Vol. 1: Properties and operations, AMS Chelsea Publishing, 1964.

31. Wolfram Mathematica, URL : <http://wolfram.com/mathematica/>

*Received 27.03.2020, accepted 17.04.2020.*

## THE AUTHORS

**BERDNIKOV Alexander S.**

*Institute for Analytical Instrumentation of the Russian Academy of Sciences*  
26 Rizhsky Ave., St. Petersburg, 190103, Russian Federation  
[asberd@yandex.ru](mailto:asberd@yandex.ru)

**SOLOVYEV Konstantin V.**

*Peter the Great St. Petersburg Polytechnic University*  
29 Politechnicheskaya St., St. Petersburg, 195251, Russian Federation  
[k-solovyev@mail.ru](mailto:k-solovyev@mail.ru)

**KRASNOVA Nadezhda K.**

*Peter the Great St. Petersburg Polytechnic University*  
29 Politechnicheskaya St., St. Petersburg, 195251, Russian Federation  
[n.k.krasnova@mail.ru](mailto:n.k.krasnova@mail.ru)

## СПИСОК ЛИТЕРАТУРЫ

1. **Бердников А.С., Галль Л.Н., Галль Р.Н., Соловьев К.В.** Обобщение формулы Томсона для гармонических функций общего вида // Научно-технические ведомости СПбГПУ. Физико-математические науки. 2019. Т. 12 № 2. С. 32–48.

2. **Бердников А.С., Галль Л.Н., Галль Р.Н., Соловьев К.В.** Обобщение формулы Томсона для гармонических однородных функций // Научно-технические ведомости СПбГПУ. Физико-математические науки. 2019. Т. 12. № 2. С. 49–62.

3. **Бердников А.С., Галль Л.Н., Галль Н.Р., Соловьев К.В.** Дифференциальные операторы Донкина для однородных гармонических функций // Научно-технические ведомости СПбГПУ. Физико-математические науки. 2019. Т. 12. № 3. С. 45–62.

4. **Бердников А.С., Галль Л.Н., Галль Н.Р., Соловьев К.В.** Базисные дифференциальные операторы Донкина для однородных гармонических функций //

Научно-технические ведомости СПбГПУ. Физико-математические науки. 2019. Т. 12. № 3. С. 26–44.

5. **Голиков Ю.К., Краснова Н.К.** Теория синтеза электростатических энергоанализаторов. СПб.: Изд-во Политехнического ун-та, 2010. 409 с.

6. **Голиков Ю.К., Краснова Н.К.** Электрические поля, однородные по Эйлеру, для электронной спектрографии // Журнал технической физики. 2011. Т. 81. № 2. С. 9–15.

7. **Голиков Ю.К., Краснова Н.К.** Обобщенный принцип подобия и его применение в электронной спектрографии // Прикладная физика. 2007. № 2. С. 5–11.

8. **Аверин И.А., Бердников А.С., Галль Н.Р.** Принцип подобия траекторий при движении заряженных частиц с разными массами в однородных по Эйлеру электрических и магнитных полях // Письма в Журнал технической физики. 2017. Т. 43. № 3. С. 39–43.



9. **Khursheed A., Dinnis A.R., Smart P.D.** Micro-extraction fields to improve electron beam test measurements // *Microelectronic Engineering*. 1991. Vol. 14. No. 3–4. Pp. 197–205.
10. **Khursheed A.** Multi-channel vs. conventional retarding field spectrometers for voltage contrast // *Microelectronic Engineering*. 1992. Vol. 16. No. 1–4. Pp. 43–50.
11. **Khursheed A., Phang J.C., Thong J.T.L.** A portable scanning electron microscope column design based on the use of permanent magnets // *Scanning*. 1998. Vol. 20. No. 2. Pp. 87–91.
12. **Khursheed A.** Magnetic axial field measurements on a high resolution miniature scanning electron microscope // *Review of Scientific Instruments*. 2000. Vol. 71. No. 4. Pp. 1712–1715.
13. **Khursheed A.** A low voltage time of flight electron emission microscope // *Optik (Jena)*. 2002. Vol. 113. No. 11. Pp. 505–509.
14. **Khursheed A.** Aberration characteristics of immersion lenses for LVSEM // *Ultramicroscopy*. 2002. Vol. 93. No. 3–4. Pp. 331–338.
15. **Khursheed A., Karupiah N., Osterberg M., Thong J.T.L.** Add-on transmission attachments for the scanning electron microscope // *Review of Scientific Instruments*. 2003. Vol. 74. No. 1. Pp. 134–140.
16. **Khursheed A., Osterberg M.** A spectroscopic scanning electron microscope design // *Scanning*. 2004. Vol. 26. No. 6. Pp. 296–306.
17. **Osterberg M., Khursheed A.** Simulation of magnetic sector deflector aberration properties for low-energy electron microscopy // *Nuclear Instruments and Methods in Physics Research, Section A*. 2005. Vol. 555. No. 1–2. Pp. 20–30.
18. **Khursheed A., Osterberg M.** Developments in the design of a spectroscopic scanning electron microscope // *Nuclear Instruments and Methods in Physics Research, Section A*. 2006. Vol. 556. No. 2. Pp. 437–444.
19. **Luo T., Khursheed A.** Imaging with surface sensitive backscattered electrons // *Journal of Vacuum Science and Technology B*. 2007. Vol. 25. No. 6. Pp. 2017–2019.
20. **Khursheed, A., Hoang, H.Q.** A second-order focusing electrostatic toroidal electron spectrometer with  $2\pi$  radian collection // *Ultramicroscopy*. 2008. Vol. 109. No. 1. Pp. 104–110.
21. **Khursheed A.** Scanning electron microscope optics and spectrometers. Singapore: World Scientific, 2010. 403 p.
22. **Hoang H.Q., Khursheed A.** A radial mirror analyzer for scanning electron/ion microscopes // *Nuclear Instruments and Methods in Physics Research, Section A*. 2011. Vol. 635. No. 1. Pp. 64–68.
23. **Hoang H.Q., Osterberg M., Khursheed A.** A high signal-to-noise ratio toroidal electron spectrometer for the SEM // *Ultramicroscopy*. 2011. Vol. 111. No. 8. Pp. 1093–1100.
24. **Khursheed A., Hoang H.Q., Srinivasan A.** A wide-range parallel radial mirror analyzer for scanning electron/ion microscopes // *Journal of Electron Spectroscopy and Related Phenomena*. 2012. Vol. 184. No. 11–12. Pp. 525–532.
25. **Shao X., Srinivasan A., Ang W.K., Khursheed A.** A high-brightness large-diameter graphene coated point cathode field emission electron source // *Nature Communications*. 2018. Vol. 9. No. 1. P. 1288.
26. **Бердников А.С., Соловьев К.В., Краснова Н.К.** Взаимно-однородные функции с матрицами конечного размера // *Научно-технические ведомости СПбГПУ. Физико-математические науки*. 2020. Т. 13. № 1. С. 42–53.
27. **Бердников А.С., Соловьев К.В., Краснова Н.К.** Цепочки фундаментальных взаимно-однородных функций с общим вещественным собственным числом // *Научно-технические ведомости СПбГПУ. Физико-математические науки*. 2020. Т. 13. № 2. С. 53–71.
28. **Фихтенгольц Г.М.** Курс дифференциального и интегрального исчисления. Т. 1. М.: Физматлит, 2001. 616 с.
29. **Гельфанд И.М., Шапиро З.Я.** Однородные функции и их приложения // *Успехи математических наук*. 1955. Т. 10. Вып. 3. С. 3–70.
30. **Гельфанд И.М., Шилов Г.Е.** Обобщенные функции и действия над ними. Серия «Обобщенные функции». Вып. 1. М.: ГИФМЛ, 1959. 470 с.
31. Wolfram Mathematica // URL : <http://wolfram.com/mathematica/>

*Статья поступила в редакцию 27.03.2020, принята к публикации 17.04.2020.*

## СВЕДЕНИЯ ОБ АВТОРАХ

**БЕРДНИКОВ Александр Сергеевич** — доктор физико-математических наук, ведущий научный сотрудник Института аналитического приборостроения Российской академии наук, Санкт-Петербург, Российская Федерация.

190103, Российская Федерация, г. Санкт-Петербург, Рижский пр., 26  
[asberd@yandex.ru](mailto:asberd@yandex.ru)

**СОЛОВЬЕВ Константин Вячеславович** — кандидат физико-математических наук, доцент Высшей инженерно-физической школы Санкт-Петербургского политехнического университета Петра Великого, младший научный сотрудник Института аналитического приборостроения РАН, Санкт-Петербург, Российская Федерация.

195251, Российская Федерация, г. Санкт-Петербург, Политехническая ул., 29  
[k-solovyev@mail.ru](mailto:k-solovyev@mail.ru)

**КРАСНОВА Надежда Константиновна** — доктор физико-математических наук, профессор Высшей инженерно-физической школы Санкт-Петербургского политехнического университета Петра Великого, Санкт-Петербург, Российская Федерация.

195251, Российская Федерация, г. Санкт-Петербург, Политехническая ул., 29  
[n.k.krasnova@mail.ru](mailto:n.k.krasnova@mail.ru)

DOI: 10.18721/JPM.13207

УДК 621.384.663

## DEVICES FOR STEERING PARTICLE BEAMS IN THE ACCELERATORS BASED ON CRYSTALS CURVED BY SCRATCHING THE GROOVES ON THE SURFACE

*V.A. Maisheev, Yu.E. Sandomirskiy, M.Yu. Chesnokov,  
Yu.A. Chesnokov, A.A. Yanovich*

Institute for High Energy Physics named by A.A. Logunov  
of NRC "Kurchatov Institute", Protvino of Moscow region, Russian Federation

An interesting method of bending silicon crystal plates by scratching the grooves on the surface mechanically has been presented in the paper. This method appears to have considerable promise for both the U70 accelerator at the Institute for High Energy Physics and the devices at the Large Hadron Collider (LHC). Using the method mentioned above, specific devices were made: a crystalline undulator for 3 GeV positrons, short crystalline deflectors for extraction of 70 GeV proton beam from the U70 accelerator, and multistrip crystals for collimating the 6500 GeV proton beam into the LHC.

**Keywords:** Large Hadron Collider, beam collimation, crystal undulator, multistrip crystal

**Citation:** Maisheev V.A., Sandomirskiy Yu.E., Chesnokov M.Yu., Chesnokov Yu.A., Yanovich A.A., Devices for steering particle beams in the accelerators based on crystals curved by scratching the grooves on the surface, St. Petersburg Polytechnical State University Journal. Physics and Mathematics. 13 (2) (2020) 75–83. DOI: 10.18721/JPM.13207

This is an open access article under the CC BY-NC 4.0 license (<https://creativecommons.org/licenses/by-nc/4.0/>)

## ПРИБОРЫ ДЛЯ УПРАВЛЕНИЯ ПУЧКАМИ ЧАСТИЦ В УСКОРИТЕЛЯХ НА ОСНОВЕ КРИСТАЛЛОВ, ИЗОГНУТЫХ ПУТЕМ НАНЕСЕНИЯ КАНАВОК НА ПОВЕРХНОСТЬ

*В.А. Маишеев, Ю.Е. Сандомирский, М.Ю. Чесноков,  
Ю.А. Чесноков, А.А. Янович*

Институт физики высоких энергий имени А.А. Логанова  
НИЦ «Курчатовский институт»,  
г. Протвино Московской области, Российская Федерация

В статье описан интересный метод изгиба кристаллических пластин кремния с помощью нанесения механическим путем канавок на их поверхности. Метод перспективен для применения как в ускорителе U70 Института физики высоких энергий, так и в устройствах Большого адронного коллайдера (БАК). С использованием указанного метода созданы конкретные устройства: кристаллический ондулятор для пучка позитронов с энергией 3 ГэВ, короткие кристаллические дефлекторы для вывода пучка протонов с энергией 70 ГэВ из ускорителя U70, многополосковые кристаллы для коллимации пучка протонов в БАК при энергии 6500 ГэВ.

**Ключевые слова:** Большой адронный коллайдер, коллимация пучков, кристаллический ондулятор, многополосковые кристаллы

**Ссылка при цитировании:** Майшеев В.А., Сандомирский Ю.Е., Чесноков М.Ю., Чесноков Ю.А., Янович А.А. Приборы для управления пучками частиц в ускорителях на основе кристаллов, изогнутых путем нанесения канавок на поверхность // Научно-технические ведомости СПбГПУ. Физико-математические науки. 2020. Т. 13. № 2. С. 89–98. DOI: 10.18721/JPM.13207

Статья открытого доступа, распространяемая по лицензии CC BY-NC 4.0 (<https://creativecommons.org/licenses/by-nc/4.0/>)

## Introduction

The idea to use channeling in bent crystals to steer particle beams, first proposed by Tsyganov (Joint Institute for Nuclear Research, Dubna, Moscow Oblast) [1], was advanced and tested in many experiments (see [1–3] and references therein). The idea found the widest practical application at the U70 accelerator at the Institute for High Energy Physics (Protvino, Moscow Oblast), where crystals are used in regular sessions for extracting and steering the beams. Problems related to the physics of particle beam channeling were considered in [4, 5].

Our study introduces a method for bending crystals for subsequent use in accelerators. Notably, the efficiency of particle deflection by a bent crystal (for example, see book [4]) is described by the ratio of the critical angle of channeling  $\theta_c$  to beam divergence  $j$ , decreasing exponentially with crystal length  $L$ :

$$\text{Eff} \sim (\theta_c / j) \exp(-L / L_d),$$

where the characteristic parameter  $L_d$  called the dechanneling length increases linearly along with the particle energy; it amounts to 5 cm in silicon crystals for 100 GeV energy protons.

The critical angle of channeling (the Lindhard angle) is rather small:

$$\theta_c \approx (1/E)^{1/2} = 0.020\text{--}0.002 \text{ mrad}$$

for protons with the energies  $E$  ranging from 100 to 10 000 GeV, respectively.

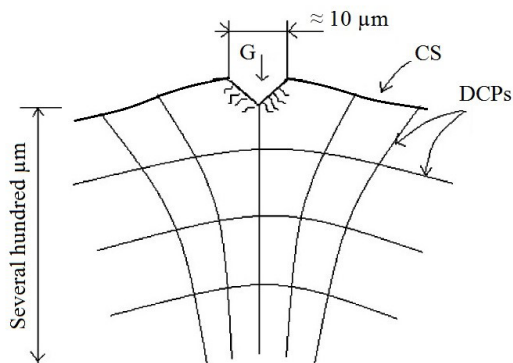


Fig. 1. Effect of deformation of crystal planes from microscratching of crystal surface: groove  $G$ , crystal surface  $CS$ , deformed crystal planes  $DCPs$

Because the angle is small, this beam steering method is not versatile but can be quite useful in some cases, especially for extraction of circulating beams and their splitting in particle channels where crystals act as miniature magnets.

The sizes of crystal plates (along the beam) range from 0.1 mm to 10 cm depending on the degree of bending and the type of problems solved. A commonly used bending method consists in applying the bending moment generated by a metal holder to the crystal [4, p. 85]. A method involving mechanical scratching of grooves on the surface of crystals was used in several cases for small bending angles.

## Basic principles of the groove scratching method

The Twyman effect, known in optics [6], is a phenomenon when small mechanical damage to the surface from microgrinding produces stresses causing the surface structure to bend, in some cases substantially. It is important that these deformations are smooth for channeling high energy particles. Experiments on particle deflection with crystals conducted at IHEP [4] revealed interesting phenomena in the end face of crystal, when the trajectories of channeled particles escaping the crystal are generated specifically depending on the microscratches present on the surface (i.e., the trajectories are sensitive to microscratches).

The explanation for the effect is that protons near, for instance, scratches are channeled in deformed layers of the crystal and move around these scratches. Reconstruction of deflection angles of the particles indicates that deformation of the crystal planes penetrates to substantial depths, up to a few hundred microns (Fig. 1). This effect was successfully applied to solving several acceleration problems for silicon crystals bent by periodic microgrooves scratched mechanically on the surface (using a diamond blade).

## Example applications of the method in accelerators

A method for creating a crystalline undulator, i.e., a periodically bent crystal, by mechanically scratching grooves on the faces of the crystal was first considered in



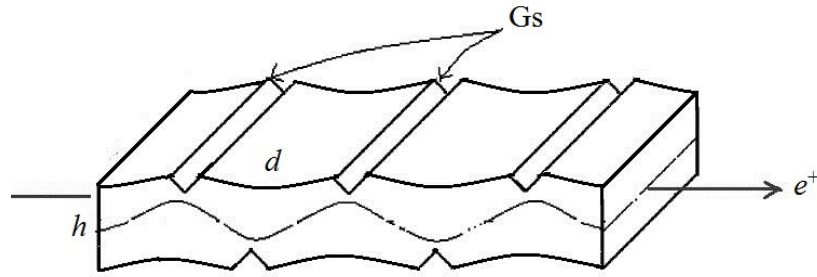


Fig. 2. Schematic representation of crystalline undulator: grooves are denoted as Gs,  $d$  is the groove period,  $h$  is the thickness of the crystal plate,  $e^+$  is the positron beam. The sinusoid corresponds to the bent crystal planes in the bulk of the crystal

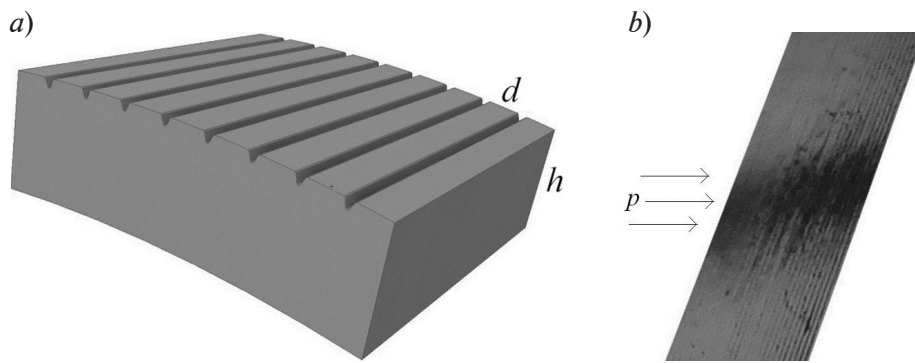


Fig. 3. Schematic representation of bent silicon crystal plate: smooth bending obtained by periodic scratching of grooves on the surface (a); plate fragment in the region of interaction with proton beam  $p$  (b)

[7]. An X-ray diffractometer was used to establish that the deformation amplitude of 40 E was reached in 10 periods with a 0.5 mm step, which is sufficient for generation of hard photons. The first experiment with such an undulator was carried out at the U70 accelerator with a 10 GeV positron beam [8]. Fig. 2 shows a scheme of the undulator with grooves developed at the IHEP.

The period  $d$  of bilateral groove scratching has to be no less than the thickness  $h$  of the crystal plate for the sinusoidal deformations to penetrate deep into the entire bulk of the crystal according to the Saint-Venant's principle, known from elasticity theory [9]. If the grooves are scratched with a small period, so that  $d \ll h$ , then the stresses become uniform at a depth approximately equal to  $d$ , producing a smooth bend in the crystal (Fig. 3,a).

The thickness of the layer with efficient channeling equals  $h - d$ . This method of crystal bending was first applied using a 70 GeV beam splitting station at the U70 accelerator [10]. The bending angle of a crystal 16 mm long and 0.5 thick amounted to 10 mrad. The experience with proton beams

with an intensity of  $10^{12}$  particle/( $\text{cm}^2 \cdot \text{s}^{-1}$ ), accumulated since 2009, indicates that the crystal preserves its bending and channeling properties, splitting the beam with the same efficiency. Fig. 3,b shows a fragment of the crystal after irradiation with protons (dose of  $5 \cdot 10^{19}$  particles).

Notably, the method of bending the crystal by scratching grooves on the surface is also applicable for production of crystal strips with a small bending angle (around 50  $\mu\text{rad}$ ), optimal for TeV energies. Such crystals were tested with a 400 GeV proton beam at the Super Proton Synchrotron (SPS) at the European Organization for Nuclear Research (CERN, Switzerland) via particle deflection by multiple volume reflection [11].

Fig. 4,b shows a photograph of the silicon crystal plate with periodic grooves serving as a deflector, prepared by the IHEP team for the experiment. Fig. 4,a shows a schematic for the deflector's operation during multiple volume reflection of particles. Deep grooves with a rough surface were made by a triangular cutter with diamond grit, providing sufficient curve bending of the strips produced on

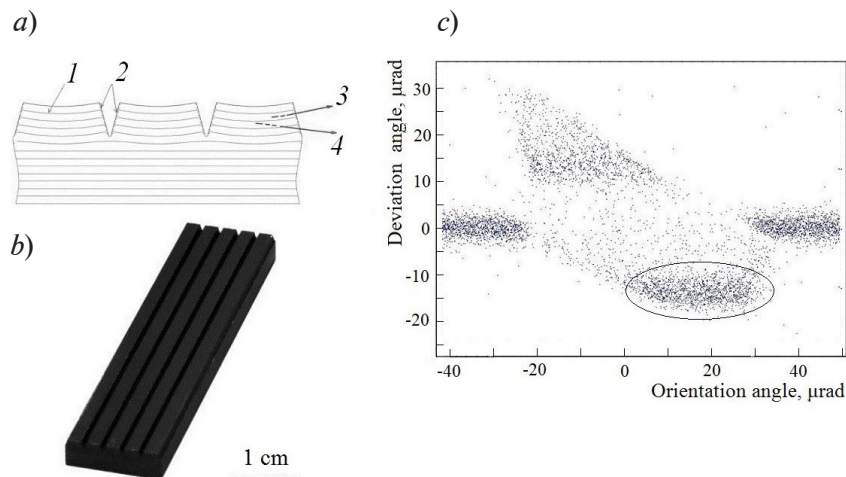


Fig. 4. Thick bent silicon multistrip crystal with periodic grooves scratched on the surface: operation sequence for multiple volume reflection (a); photograph of crystal (b); computational results for efficient 6.5 TeV proton deflection by multiple volume reflection in bent strips (c): Monte Carlo simulation and SCRAPER code were used. Fig. 4,a shows bent crystal planes (1); triangular grooves (2); tracks of particles deflected due to channeling (3) and multiply reflected by bent planes (4); the oval in Fig. 4,c marks the reflection region

the polished face of a thick silicon plate. The beam in the experiment described in [11] was deflected at an angle of  $50 \mu\text{rad}$  and agreed with the calculated value with an efficiency of about 90%.

Bending of separate strips and their mutual orientation was studied with the Kurchatov Synchrotron Radiation Source (Kurchatov Institute, Moscow) using a parallel X-ray beam [12]. Analysis of the results showed that this structure, i.e., a series of bent strips formed between large grooves on a thick plate, is aligned perfectly, fitting for collimation of 50 TeV proton beams at the Large Hadron Collider (LHC,

CERN) and even the Future Circular Collider (FCC, CERN), using multiple volume reflection of particles. The parameters of the crystal device can be easily adapted to this energy by varying the size of the grooves and the distance between them.

Fig. 4,c shows the calculated deflection angles of beam particles at 6.5 TeV depending on the orientation of the crystal plate in a form of two-dimensional density marked with dots. The calculations were performed using our SCRAPER software and the Monte Carlo method [14]. Evidently, the particles at the edges of the beam (on the right and left)

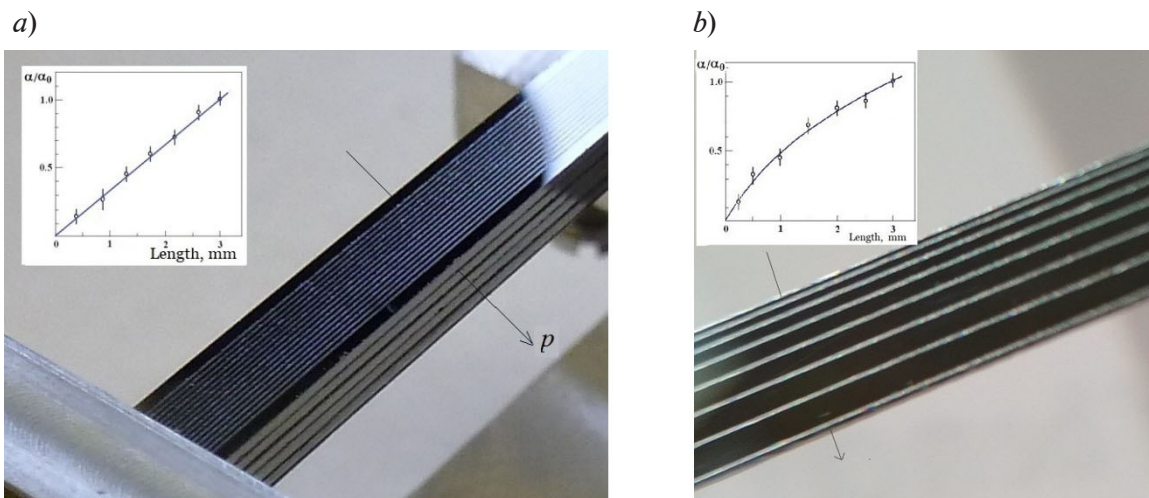


Fig. 5. General view of silicon crystals with periodically (a) and aperiodically (b) arranged grooves. The insets show distributions of the bending angle along the length of the crystals

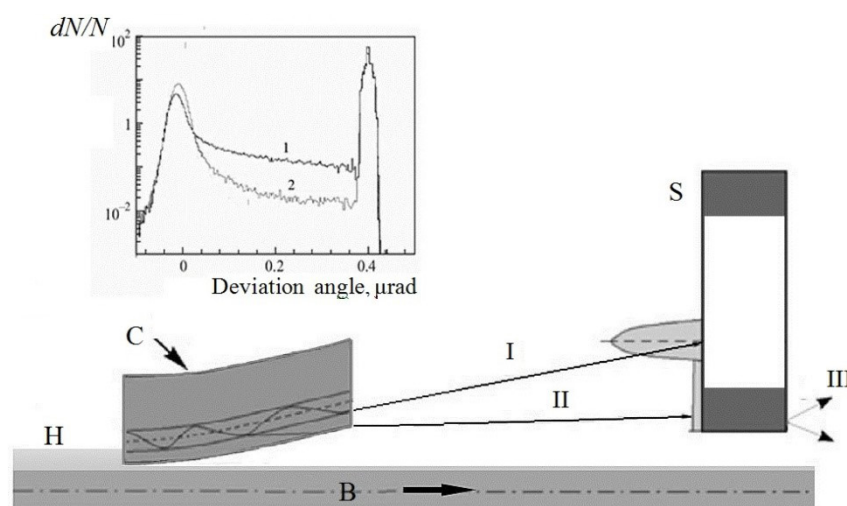


Fig. 6. Schematic layout for beam extraction by crystal (C): peak of channelled particles efficiently extracted (I); fraction of dechanneled particles (II); losses at the septum S (III);

H, B denote halo and beam, respectively.

The inset shows distributions of particles deflected by the crystals with constant (curve 1) and dropping (curve 2) curvature; computed using Monte Carlo method with our SCRAPER software [14]

are not deflected as they do not fall within the range of the strip bending angles. Almost the entire beam in the reflection region marked in the figure shifts down by an angle of  $15 \mu\text{rad}$  corresponding to multiple reflection on five crystal strips. According to our estimations, the calculated efficiency of beam deflection amounts to 92%.

#### Novel approaches introduced at the U70 accelerator using the proposed method of crystal bending

**Optimized beam extraction from the accelerator.** Beam extraction by short silicon crystals has been used at the U70 accelerator since 1998 [13]. The new bending method is aimed at increasing the efficiency of extraction by reducing the length of the crystals while preserving the required bending angle, since the surface grooves increase the crystal curvature. Moreover, if the grooves are arranged aperiodically, a bend with decreasing curvature can be achieved. This also suppresses particle dechanneling along the length of the crystal, which in turn reduces particle losses [14].

We prepared several samples of crystals bent by scratching grooves on the surface, including those with aperiodic scratching (Fig. 5). We conducted an optical test of the bend using a laser device (the technique is described in [4]). The insets in the figure show distributions of the bending angle along the length of the

crystals. Apparently, periodic grooves produce uniform bending, while aperiodic grooves result in a decreasing curvature. Fig. 5,a also shows that identical crystals are stacked to increase the transverse size of the crystal beam deflector, thus additionally improving its efficiency.

Fig. 6 shows a schematic layout for beam extraction with the improved crystals, illustrating how the beam extraction efficiency can be improved by reducing the share of dechanneled particles. The inset in Fig. 6 shows distributions of particles deflected by the crystals with constant (curve 1) and decreasing (curve 2) curvature calculated by the Monte Carlo method and our SCRAPER software [14]. It is apparent that decreasing curvature results in reducing the share of dechanneled particles by several times. Experiments aimed at improving the crystal extraction at U70 are planned as soon as the accelerator equipment is upgraded. The SCD19 crystal station uses a crystal 5 mm long with a bending angle of 2 mrad. The prepared crystals (see Fig. 5) allow to reduce their length down to 3 mm, which will increase the extraction efficiency from 70 up to 85%.

**Testing the crystal undulator with a 3 GeV positron beam.** The energy of photons generated by the undulator is proportional to the squared Lorentz factor of a  $\gamma$  particle and inversely proportional to the undulator period  $L$ . The period of a simple electromagnetic undulator reaches several centimeters. Thus,

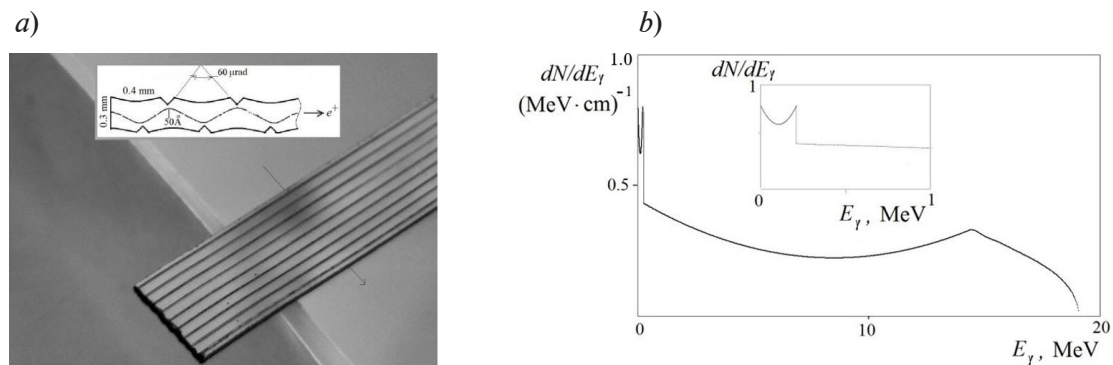


Fig. 7. Crystal undulator with 3 GeV positron beam: photograph and schematic cross section (inset) (a); calculated spectrum of photons obtained with the undulator and undulator peak around 0.23 MeV (inset) (b)

photons with the energies of several keV reach approximately 1 GeV in the beam of the electron accelerator. Consequently, crystal undulators with submillimeter periods are the subject of intense scrutiny because of the potential they hold for increasing photon energies.

The first data on radiation produced with a crystalline undulator were obtained for a 10 GeV positron beam at IHEP [8]. However, the majority of electron accelerators where crystalline undulators can be used operate at energies below 6 GeV. We prepared novel samples of crystal undulators (Fig. 7,a) optimized for positrons at lower energies achievable by the electron accelerators currently available. The first tests are planned to take place at IHEP's Crystal setup at the energy of 3 GeV. Given the achieved parameters, specifically, a period of 0.4 mm, an amplitude of 50 Å, and the number of periods equal to 9, we plan to obtain a photon peak at approximately 0.23 MeV with the undulator. Fig. 7,b shows the calculated photon spectrum obtained using the software described in [15]. This software implements an algorithm for simulating undulator radiation in the crystal taking into account rather strong radiation during positron channeling, proposed

in [16]. The undulator peak around 0.23 MeV is shown in detail in the inset to Fig. 7,b. The background radiation up to 20 MeV is due to channeling.

### Conclusion

The paper presents an interesting method for bending silicon crystal plates by mechanical scratching of grooves on the surface. This method has already been applied for a number of problems related to steering particle beams but we also propose vital improvements for potential applications in new problems described in the study. The method was used to construct novel devices: a crystal undulator for 3 GeV positrons, short crystal deflectors for extraction of 70 GeV proton beams at the U70 accelerator, and multistrip crystals for collimation of 6500 GeV proton beams at the LHC. The latter show promise for solving the global problem of beam collimation at future multi-TeV colliders.

The paper is sponsored by the Russian Foundation for Basic Research (grant No. 20-02-00045).

### REFERENCES

1. Elishev A.F., Filatova N.A., Golovatyuk V.M., et al., Steering of charged particle trajectories by a bent crystal, *Physics Letters. B.* 88 (3–4) (1979) 387–391.
2. Shiltsev V., Experience with crystals at Fermilab accelerators, *International Journal of Modern Physics. A.* 34 (2019) 1943007.
3. Scandale W., Taratin A.M., Channeling and volume reflection of high-energy charged particles in short bent crystals. *Crystal assisted collimation of the accelerator beam halo*, *Physics Reports.* 815 (25 June) (2019) 1–107.
4. Biryukov V.M., Chesnokov Yu.A., Kotov V.I., *Crystal channeling and its application at high-energy accelerators*, Springer, Berlin, Germany, 1997.
5. Chesnokov Yu.A., Afonin A.G., Baranov V.T., et al., Modern success in channeling study and applications at the U-70 accelerator of IHEP, *Nuovo Cimento, C.* 034 (4) (2011) 407–415.





6. Lambropoulos J.C., Xu S., Fang T., Golini D., Twyman effect mechanics in grinding and microgrinding, *Applied Optics*. 35 (28) (1996) 5704–5713.
7. Bellucci S., Bini S., Biryukov V.M., et al., Experimental study for the feasibility of a crystalline undulator, *Physical Review Letters*. 90 (3) (2003) 034801.
8. Baranov V.T., Bellucci S., Biryukov V.M., et al., First results of investigation of radiation from positrons in a crystalline undulator, *JETP Letters*, 82 (9) (2005) 562–564.
9. Timoshenko S.P., Goodier J.N., *Theory of elasticity*, McGraw-Hill, New-York, 1951.
10. Arkhipenko A.A., Afonin A.G., Baranov V.T., et al., Splitting of a 50-GeV proton beam by a slightly disturbing bent crystal, *Instruments and Experimental Techniques*. 52 (1 May) (2009) 155–158.
11. Scandale W., Arduini G., Butcher M., et al., Deflection of high energy protons by multiple volume reflections in a modified multi-strip silicon deflector, *Nucl. Instrum. Meth. B*. 338 (1 November) (2014) 108–111.
12. Kaloyan A.A., Tikhomirov S.A., Podurets K.M., et al., Study of the crystal device for deflecting high-energy proton beams using synchrotron radiation diffraction, *Crystallography Reports*. 62 (3) (2017) 370–373.
13. Afonin A.G., Maishev V.A., Troyanov E.F., et al., Proton beam extraction from the IHEP accelerator using short silicon crystals, *Phys. Part. Nucl.* 36 (1) (2005) 21–54.
14. Yazynin I.A., Maishev V.A., Chesnokov Yu.A., Use of a bent crystal with a decreasing curvature to increase the efficiency of the extraction and collimation of a beam in an accelerator, *JETP Letters*. 94 (3) (2011) 248–250.
15. Maishev V.A., Programma dlya rascheta ondulyatornogo spektra fotonov [Programm for calculation of undulator photon spectra] <http://phpc01.ihep.su/~laba/chesn/Simulation%20of%20photon%20spectrum%20in%20undulator/>.
16. Bellucci S., Maishev V.A., Calculations of intensity of radiation in crystal undulator, *Nuclear Instruments and Methods in Physics Research. B*. 252 (2) (2006) 339–346.

*Received 26.03.2020, accepted 21.04.2020.*

## THE AUTHORS

### **MAISHEEV Vladimir A.**

*Institute for High Energy Physics named by A.A. Logunov of NRC «Kurchatov Institute»*  
1, Nauki Sq., Protvino of Moscow Reg., 142281, Russian Federation  
[maishev@ihep.ru](mailto:maishev@ihep.ru)

### **SANDOMIRSKIY Yury E.**

*Institute for High Energy Physics named by A.A. Logunov of NRC «Kurchatov Institute»*  
1, Nauki Sq., Protvino of Moscow Reg., 142281, Russian Federation  
[Yury.Sandomirskiy@ihep.ru](mailto:Yury.Sandomirskiy@ihep.ru)

### **CHESNOKOV Mikhail Yu.**

*Institute for High Energy Physics named by A.A. Logunov of NRC «Kurchatov Institute»*  
1, Nauki Sq., Protvino of Moscow Reg., 142281, Russian Federation  
[Michail.Chesnokov@ihep.ru](mailto:Michail.Chesnokov@ihep.ru)

### **CHESNOKOV Yury A.**

*Institute for High Energy Physics named by A.A. Logunov of NRC «Kurchatov Institute»*  
1, Nauki Sq., Protvino of Moscow Reg., 142281, Russian Federation  
[chesnokov@ihep.ru](mailto:chesnokov@ihep.ru)

### **YANOVICH Andrey A.**

*Institute for High Energy Physics named by A.A. Logunov of NRC «Kurchatov Institute»*  
1, Nauki Sq., Protvino of Moscow Reg., 142281, Russian Federation  
[yanovich@ihep.ru](mailto:yanovich@ihep.ru)



## СПИСОК ЛИТЕРАТУРЫ

1. **Elishev A.F., Filatova N.A., Golovatyuk V.M., et al.** Steering of charged particle trajectories by a bent crystal // *Physics Letters. B.* 1979. Vol. 88. No. 3–4. Pp. 387–391.
2. **Shiltsev V.** Experience with crystals at Fermilab accelerators // *International Journal of Modern Physics. A.* 2019. Vol. 34. P. 1943007.
3. **Scandale W., Taratin A.M.** Channeling and volume reflection of high-energy charged particles in short bent crystals. Crystal assisted collimation of the accelerator beam halo // *Physics Reports.* 2019. Vol. 815. 25 June. Pp. 1–107.
4. **Biryukov V.M., Chesnokov Yu.A., Kotov V.I.** Crystal channeling and its application at high-energy accelerators. Berlin, Germany: Springer, 1997. 219 p.
5. **Chesnokov Yu.A., Afonin A.G., Baranov V.T., Britvich G.I., Chirkov P.N., Maisheev V.A., Terekhov V.I., Yazynin I.A.,** Modern success in channeling study and applications at the U-70 accelerator of IHEP // *Nuovo Cimento. C.* 2011. Vol. 034. No. 4. Pp. 407–415.
6. **Lambropoulos J.C., Xu S., Fang T., Golini D.** Twyman effect mechanics in grinding and microgrinding // *Applied Optics.* 1996. Vol. 35. No. 28. Pp. 5704–5713.
7. **Bellucci S., Bini S., Biryukov V.M., et al.** Experimental study for the feasibility of a crystalline undulator, *Physical Review Letters.* 2003. Vol. 90. No. 3. P. 034801.
8. **Баранов В.Т., Беллуччи С., Бирюков В.М. и др.** Первые результаты исследования излучения позитронов в кристаллическом ондуляторе // *Письма в Журнал экспериментальной и теоретической физики.* 2005. Т. 82. № 9. С. 638–641.
9. **Тимошенко С.П., Гудьер Дж.** Теория упругости. Пер. с англ. 2-е изд. М.: Наука. Гл. ред. физ.-мат. лит-ры, 1979. 560 с.
10. **Архипенко А.А., Афонин А.Г., Баранов В.Т. и др.** Деление пучка протонов с энергией 50 ГэВ слабовозмущающим изогнутым кристаллом // *Приборы и техника эксперимента.* 2009. № 2. С. 5–8.
11. **Scandale W., Arduini G., Butcher M., et al.,** Deflection of high energy protons by multiple volume reflections in a modified multi-strip silicon deflector// *Nuclear Instruments and Methods in Physics Research. B.* 2014. Vol. 338. 1 November. Pp. 108–111.
12. **Калоян А.А., Тихомиров С.А., Подурец К.М., Майшеев В.А., Сандомирский Ю.Е., Чесноков Ю.А.** Исследование кристаллического прибора для отклонения протонного пучка с помощью дифракции синхротронного излучения // *Кристаллография.* 2017. Т. 62. № 3. С. 370–373.
13. **Афонин А.Г., Майшеев В.А., Троянов Е.Ф. и др.,** Вывод протонного пучка из ускорителя ИФВЭ с помощью коротких кристаллов // *Физика элементарных частиц и атомного ядра.* 2005. Т. 36. № 1. С. 43–99.
14. **Язынин И.А., Майшеев В.А., Чесноков Ю.А.** Использование кристалла со спадающей кривизной для увеличения эффективности вывода пучка из ускорителя // *Письма в Журнал экспериментальной и теоретической физики.* 2011. Т. 94. № 3. С. 267–270.
15. **Майшеев В.А.** Программа для расчета ондуляторного спектра фотонов. <http://phpc01.ihep.su/~laba/chesn/Simulation%20of%20photon%20spectrum%20in%20undulator/>.
16. **Bellucci S., Maisheev V.A.** Calculations of intensity of radiation in crystal undulator // *Nuclear Instruments and Methods in Physics Research. B.* 2006. Vol. 252. No. 2. Pp. 339–346.

*Статья поступила в редакцию 26.03.2020, принята к публикации 21.04.2020.*



## СВЕДЕНИЯ ОБ АВТОРАХ

**МАИШЕЕВ** Владимир Александрович — кандидат физико-математических наук, ведущий научный сотрудник Института физики высоких энергий имени А.А. Логунова НИЦ «Курчатовский институт», г. Протвино Московской обл., Российская Федерация.

142281, Российская Федерация, г. Протвино Московской обл., пл. Науки, 1  
maisheev@ihep.ru

**САНДОМИРСКИЙ** Юрий Евгеньевич — инженер-технолог Института физики высоких энергий имени А.А. Логунова НИЦ «Курчатовский институт», г. Протвино Московской обл., Российская Федерация.

142281, Российская Федерация, г. Протвино Московской обл., пл. Науки, 1  
Yury.Sandomirskiy@ihep.ru

**ЧЕСНОКОВ** Михаил Юрьевич — инженер-исследователь Института физики высоких энергий имени А.А. Логунова НИЦ «Курчатовский институт», г. Протвино Московской обл., Российская Федерация.

142281, Российская Федерация, г. Протвино Московской обл., пл. Науки, 1  
Michail.Chesnokov@ihep.ru

**ЧЕСНОКОВ** Юрий Андреевич — доктор физико-математических наук, главный научный сотрудник Института физики высоких энергий имени А.А. Логунова НИЦ «Курчатовский институт», г. Протвино Московской обл., Российская Федерация.

142281, Российская Федерация, г. Протвино Московской обл., пл. Науки, 1  
chesnokov@ihep.ru

**ЯНОВИЧ** Андрей Антонович — научный сотрудник Института физики высоких энергий имени А.А. Логунова НИЦ «Курчатовский институт», г. Протвино Московской обл., Российская Федерация.

142281, Российская Федерация, г. Протвино Московской обл., пл. Науки, 1  
yanovich@ihep.ru

DOI: 10.18721/JPM.13208

УДК 621.455.4; 621.455.34

## AN ELECTRICALLY POWERED ION ACCELERATOR WITH CONTACT IONIZATION FOR PERSPECTIVE ELECTRICALLY POWERED THRUSTERS

*O.Yu. Tsybin<sup>1</sup>, S.B. Makarov<sup>1</sup>, D.B. Dyubo<sup>1</sup>, Yu.V. Kuleshov<sup>2</sup>,  
P.S. Goncharov<sup>2</sup>, V.V. Martynov<sup>2</sup>, N.A. Shunevich<sup>2</sup>*

<sup>1</sup> Peter the Great St. Petersburg Polytechnic University, St. Petersburg, Russian Federation;

<sup>2</sup> Military Space Academy named after A.F. Mozhaysky, St. Petersburg, Russian Federation

A number of characteristics of ionic and ion-plasma accelerators laboratory samples designed for electrically powered spacecraft propulsion have experimentally been studied. A large-sized vacuum chamber ( $2.4 \text{ m}^3$ ,  $10^3 \text{ Pa}$ ) made at the Military Space Academy named after A.F. Mozhaysky provided the necessary physical and technological processes, methods and means of measurement, parameters and operation modes of the ionic accelerators with contact ionization. The samples' design features, physical processes and operating parameters were theoretically analyzed, including the use of computer simulation. The implemented and tested measuring methods, technologies and ion-physical laboratory samples' characteristics were found to correspond to the tasks of developing the promising electrically powered spacecraft propulsion.

**Keywords:** vacuum chamber, computer simulation, ionization, ion accelerator, electrically powered spacecraft

**Citation:** Tsybin O.Y., Makarov S.B., Dyubo D.B., Kuleshov Yu.V., Goncharov P.S., Martynov V.V., Shunevich N.A., An electrically powered ion accelerator with contact ionization for perspective electrically powered thrusters, St. Petersburg Polytechnical State University Journal. Physics and Mathematics. 13 (2) (2020) 84–98. DOI: 10.18721/JPM.13208

This is an open access article under the CC BY-NC 4.0 license (<https://creativecommons.org/licenses/by-nc/4.0/>)

## ЭЛЕКТРОСТАТИЧЕСКИЙ ИОННЫЙ УСКОРИТЕЛЬ С КОНТАКТНОЙ ИОНИЗАЦИЕЙ ДЛЯ ПЕРСПЕКТИВНЫХ ЭЛЕКТРИЧЕСКИХ РАКЕТНЫХ ДВИГАТЕЛЕЙ

*О.Ю. Цыбин<sup>1</sup>, С.Б. Макаров<sup>1</sup>, Д.Б. Дюбо<sup>1</sup>, Ю.В. Кулешов<sup>2</sup>,  
П.С. Гончаров<sup>2</sup>, В.В. Мартынов<sup>2</sup>, Н.А. Шуневич<sup>2</sup>*

<sup>1</sup> Санкт-Петербургский политехнический университет Петра Великого,  
Санкт-Петербург, Российская Федерация;

<sup>2</sup> Военно-космическая академия имени А.Ф. Можайского,  
Санкт-Петербург, Российская Федерация

Выполнены экспериментальные измерения ряда характеристик лабораторных образцов ионных и ионно-плазменных ускорителей, предназначенных для электрических ракетных двигателей космических аппаратов. Крупногабаритная вакуумная камера ( $2,4 \text{ м}^3$ ,  $10^3 \text{ Па}$ ), созданная в Военно-космической академии им. А.Ф. Можайского, обеспечивала необходимые физико-технологические процессы, методы и средства измерений, параметры и режимы работы ионных ускорителей с контактной ионизацией. Особенности конструкции образцов, а также физические процессы с набором их рабочих параметров были проанализированы теоретически, в



том числе методом компьютерного моделирования. Установлено, что реализованные и тестируемые методы измерений, технологии и ионно-физические характеристики лабораторных образцов соответствуют задачам разработки перспективных электрических ракетных двигателей.

**Ключевые слова:** вакуумная камера, компьютерное моделирование, ионизация, ионный поток, ионный ускоритель

**Ссылка при цитировании:** Цыбин О.Ю., Макаров С.Б., Дюбо Д.Б., Кулешов Ю.В., Гончаров П.С., Мартынов В.В., Шуневич Н.А. Электростатический ионный ускоритель с контактной ионизацией для перспективных электрических ракетных двигателей // Научно-технические ведомости СПбГПУ. Физико-математические науки. 2020. Т. 13 2 №. С. 99–115. DOI: 10.18721/JPM.13208

Статья открытого доступа, распространяемая по лицензии CC BY-NC 4.0 (<https://creativecommons.org/licenses/by-nc/4.0/>)

### Introduction

Accelerated ion fluxes in vacuum are widely used in physical research, medicine, technologies for producing microchips and various materials, as well as in electric propulsion spacecraft [1–13]. There is a general call for systematized review of the physical problems related to electric propulsion systems (EPS) [2–6, 14–17]. It is difficult to improve the existing devices or develop new ones given the lack of comprehensive theory. A crucial task is to construct a new generation of EPS featuring alternative types of propellants, effective design and operation solutions, high reliability, extended service life, relative simplicity, and low cost.

Standard EPS are electromechanical vacuum systems where electromagnetic energy is converted to mechanical energy of propulsion. Momentum is generated using the following operating cycle: the propellant is transformed into an ionized gas/vapor phase, ions are accelerated in an electric field with subsequent neutralization of the charge of accelerated particles and free expansion of the neutralized beam into space. The main condition for generating the desired thrust is increasing the momentum of the mass accelerated in the beam, which means consuming greater amounts of propellant.

Reducing the consumption of propellant in EPS is based on obtaining high-velocity beams (50–100 km/s). The efficiency of EPS is 50% and higher, while the efficiency of chemical propulsion units does not exceed 35%. The mass of propellant on board a spacecraft amounts to 5–15% of the initial mass of the spacecraft in case of an EPS and 70% and higher in case of a chemical propulsion unit. The great advantages of the EPS are their large number of controlled firing cycles ( $10^6$ + times) and long service lives (10,000+ hours).

Modern EPS are largely represented by electrostatic thrusters, including ion thrusters with perforated electrodes (grids) and Hall-effect plasma thrusters. The latter group includes stationary plasma thrusters, thrusters with anode layer, end Hall thrusters, and multi-stage Hall thrusters [1–17].

Grid ion thrusters are characterized by the highest efficiency (60–80% and more), high specific impulse (2,000–10,000 s; determined as the ratio between the exhaust velocity of the beam ejected into space and the acceleration of gravity (about  $9.8 \text{ m/s}^2$ )) with the voltage difference in grids up to and exceeding 10 kV. Such thrusters consume propellant efficiently and have a long service life (up to 10–12 years of operation in space).

Hall thrusters have a simpler design and require fewer power sources compared with grid ion thrusters. Hall thrusters use a magnetic field to generate electron drift motion in the direction  $\vec{E} \times \vec{B}$  (transverse to the magnetic and electric vectors). Such motion of charged particles in vacuum can be attributed to the Wien filter (known since the end of the 19<sup>th</sup> century) with electron drift motion in vacuum in crossed fields rather than to the Hall effect (the classical Hall effect consists in voltage difference across a semiconductor placed in a magnetic field). The principles of the Wien filter were applied for the first time by Thompson in mass-analyzers in the early 20<sup>th</sup> century. Stationary plasma thrusters are typically referred to as Morozov's stationary plasma thrusters in Russian literature and practice, since it was Morozov who that a spatially-distributed electrostatic field could be obtained in plasma, which underlies the operation of such thrusters [2, 3].

However, the term *Hall thrusters* became widely accepted internationally. These units provide the most practically significant and reliable operating parameters, generate slightly

lower impulse but a higher thrust (compared with grid ion thrusters) at the same power. The typical parameters of Hall thrusters (manufactured by Experimental Design Bureau Fakel, Kaliningrad, Russia) in different configurations range within the power/thrust ratios of 13–19 W/mN at a power consumption of 200–2500 kW. Their specific impulse amounts to 1600–2500 s. The basic parameters of Russian-made thrusters are compared in Table 1 below.

Meteor, Kosmos-1066, Kanopus-V, BKA and several other spacecraft are equipped with SPT-50 Hall thrusters operating with xenon propellant.

The following can be added for comparison: the thrust to power ratio in such devices as solar sails, laser or photon propulsion systems is 3.33–6.67  $\mu\text{N/kW}$  for forward or reflected radiation, respectively.

According to the fundamental laws of physics, propulsion can be achieved in a device emitting an electromagnetic field (EMF). As the EMF is emitted, the thrust force exerts mechanical pressure on the antenna, which was predicted by Maxwell in 1873 and experimentally proved by Lebedev in 1899. It was also confirmed theoretically based on the Maxwell equations within the framework of classical electrodynamics for processes at the edge of a conductor.

The maximum pressure of an electromagnetic field on the antenna is as follows:

$$|F_{EMF}| \approx 2W/V_g,$$

where  $W$  is the power of radiation freely expanding in space;  $V_g$  is the group velocity of a wave (close to the speed of light); the coefficient 2 appears because the incident wave is reflected and emitted in the opposite direction.

To achieve noticeable accelerations with a force of approximately 1 N, significant wave power is required (approximately 150 MW).

An ion source is usually considered the most complex and critical element in the design of EPS [2, 3, 11–13, 16, 18]. The method and the characteristics of propellant ionization largely govern the required mechanical parameters. An ionizer should provide fuller ionization of the propellant so that the number of neutral particles entering the accelerating gap does not exceed 10–20% of the total number of particles exiting the ionizer. As a rule, the charges and masses of all ions should be the same, and the number of impurities should be minimal. Homogeneous processes should be maintained in the volume ionization chamber. Besides, the energy consumed by the ionizer and its mass should be minimal. The current density at the exit of the ionizer should correspond to the preset modes of the ion accelerator and the thruster as a whole.

Volume ionization by electrons is the main ionization method in stationary plasma thrusters and grid ion thrusters. The design of a volume ionizer should satisfy a certain set of requirements. In particular, in case of gas of propellant particles with the ionization cross-section  $\sigma$  and concentration  $n$ , the size  $L$  of the ionization chamber should exceed the ionization length  $\lambda$  of an electron track in gas ( $\lambda = 1/\sigma n$ ), i.e.,  $L > \lambda$ .

Along with these conditions, the device should have a long service life (about 10,000 h), during which fail-safe controlled switching and stable ionization should be ensured. In addition to ionization by electrons, methods of volume ionization in stationary plasma thrusters, grid ion thrusters, and prototype models of thrusters include discharge, plasma, laser, high-frequency ionization, etc. [2, 3, 14–16].

The high density of thrust in local surface areas is provided by field ionization with a strong local electric field near the cusps, e.g., with propellant in the form of liquid metal: mercury, magnesium, indium, cesium, zinc,

Table 1

Basic operating parameters of Hall thrusters

Parameter	Unit	Value		
		SPT-50	SPT-70	SPT-PPS
Thrust	mN	14.3	40	80
Specific impulse	s	860	1450	1600
Efficiency	%	26	44	48
Power	W	220	650	1350





gallium, etc., as well as electrospray capillary ionization where propellant particles are immersed in a colloidal solution. Using field ionizers with a multi-cusp surface in an ion thruster can generate a thrust of about 10 mN at a power consumption of about 300 W. Colloid thrusters provide an impulse of 2500 s and a thrust of 100  $\mu$ N with a thrust to power ratio of about 40 mN/kW. The volume of the ionization chamber in a colloid thruster is 0.3 dm<sup>3</sup>, and its efficiency may reach 50%. However, due to high concentration of energy damaging microscopic areas of the surface, these thrusters cannot compete with volume electron ionizers, especially in terms of durability.

Evidently, existing EPS use a wide variety of ionization methods, including ionization and accelerated motion of charged particles obtained from compressed gases (nitrogen, argon, xenon, krypton, etc.), liquid metals, as well as colloidal solutions of organic substances. It is believed that such volatile solids as iodine, teflon, etc., may have good prospects. Despite a large number of studies, many propellant materials have only been tested in laboratory setups. The EPS used in spacecraft mainly operate with xenon because it has several advantages: chemical inertness, sufficiently high atomic mass and ionization cross-section, acceptable ionization energy. However, due to its high cost and limited resources, it is expedient to replace xenon with an alternative propellant. Consequently, a novel design of an EPS has to be developed for such propellant.

In this regard, surface, or contact ionization distributed over the surface of a solid seems quite interesting [17–23]. Contact sources equipped with a surface ionizer where cesium vapor passed through a porous tungsten membrane were tested in electrostatic ion thrusters [2–6]. However, for reasons that are now clear, the experiments met only with limited success and were not continued.

Currently, with further advances made in the theory and technology of porous materials, a new stage in surface ionization studies appears to be more justified. The probability of electron tunneling and surface ionization in a porous material can be increased due to new materials and technologies, unsteady processes, increased energy of neutral particles and electrons in the material, and surface heterogeneity [12, 13, 16–23].

Extensive experimental studies should be conducted in ground laboratories to develop novel designs. Surface ionization combined

with implementing and monitoring a range of ion-plasma processes should play a major role.

Ground tests of spacecraft prototypes equipped with EPS are carried out in vacuum chambers with a large volume characterized by a high pumping speed. They include a VU-M chamber with a vacuum volume of 2.4 m<sup>3</sup> and a pressure of  $1 \cdot 10^{-3}$  Pa, designed at the Military Space Academy named after A.F. Mozhaysky [24, 25].

The chamber was used in a series of studies conducted by the team comprising staff members from the Military Space Academy named after A.F. Mozhaysky and Peter the Great St. Petersburg Polytechnic University. Parameters were measured, and theoretical analysis (including computer simulation) was carried out for physical processes, as well as for operating parameters of laboratory prototypes of ionic and ion-plasma accelerators for electric propulsion systems used in spacecraft. The vacuum chamber provides the necessary processes, measurement methods and tools, operating parameters and modes of ion accelerators.

This paper describes the prototypes, the main methods for testing them, the stages and characteristics of the analysis, and results of experimental and theoretical studies.

### Experimental methods and equipment

#### Characteristics of experimental prototypes.

The required parameters of the prototypes to be tested were obtained by computer simulation (primarily using the Computer Simulation Technology (CST) package) [26–30]. This approach allowed to obtain the size and shape of the electrodes as well as the current-voltage characteristics of the charged particle flux in the injector circuit and distributions of particle velocity and electric field with respect to the coordinates in the accelerator volume. Additionally, new physical and technological solutions were introduced, and an ion-mechanical algorithm was used to determine the thrust in different sections of the accelerator with varying operating modes [31–35]. The following parameters of the experimental prototypes were measured:

- electric voltage of ion acceleration,
- ion drift current in the accelerator,
- ionization coefficient of the vapor-gas flow injected,
- neutralization coefficient of the accelerated ion flux,
- beam pressure force.

Based on the obtained values, we determined the main performance characteristics of the ion thruster developed.

Fig. 1 shows a typical block diagram for the experimental prototype in the form of a single-stage linear DC accelerator and an electrical circuit of the measurements. The ionized gas flow of the propellant is injected into accelerating gap 4 via ionizer 1, where drift current 5 of accelerated ions is generated. Due to the Coulomb force, ions are attracted to the charges induced on grids I and II. This generates ion acceleration and thrust. The accelerated ions are neutralized in neutralizer 7; these particles no longer generate thrust after that and expand

into vacuum as beam 8. The power of source 10 is transferred to the ion flux in gap 4 and is then carried away in the form of a kinetic energy flux by a beam of neutral particles.

Fig. 2 shows a simplified schematic representation of the experimental prototype with ion trajectories in the accelerating gap, obtained using CST.

Fig. 3 shows a photograph of a simple two-electrode experimental prototype (corresponding to the scheme in Fig. 2) tested.

The tested device is based on surface or contact ionization in the module injecting the ion flux into the acceleration section. Ionization with positively or negatively charged

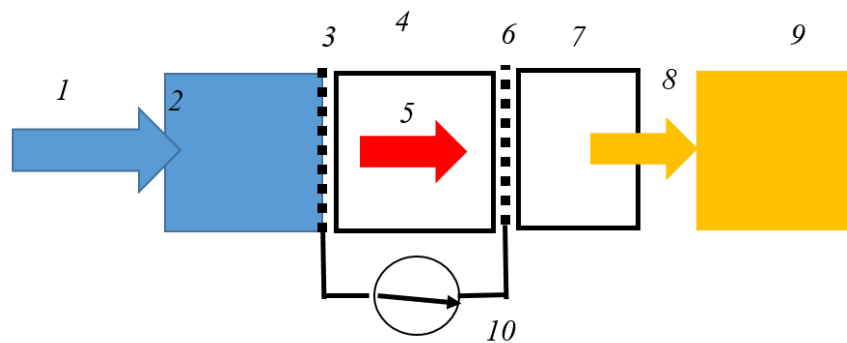


Fig. 1. Block diagram for experimental prototype and electric circuit for measurements (cation generation): gas flow of propellant 1; ionizer 2; electrodes 3, 6 generating the electric field; accelerating gap 4 and ion drift current 5 in the gap; neutralizer 7; beam 8 of neutral particles; beam impulse meter 9; EMF source 10

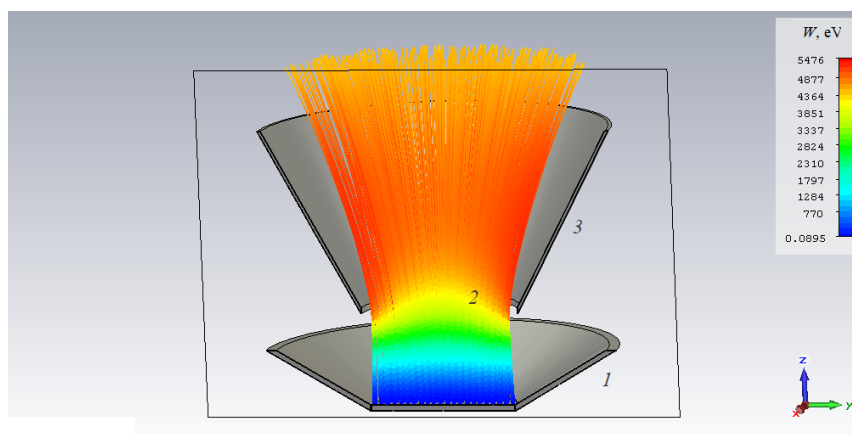


Fig. 2. Schematic representation of two-electrode prototype with ion trajectories in accelerating gap, obtained using the CST package (the black line marks the boundary of the computational domain): electrode 1 with ionizer distributing gas, ion-plasma flow 2, electrode 3 generating an electric field; the color scale reflects the energy spectrum of the plasma

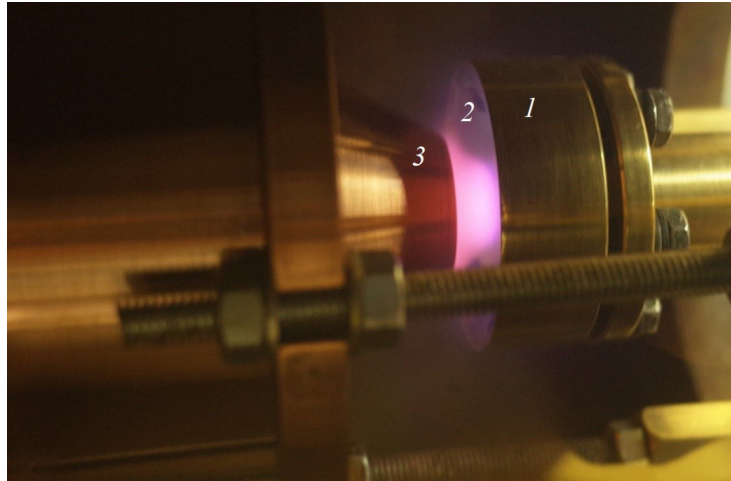


Fig. 3. Photograph of experimental prototype tested (see Fig. 2):  
electrode 1 with ionizer, ion-plasma flow 2, electrode 3 generating the electric field

particles generated occurs due to electron tunneling from a neutral particle to the surface or in the opposite direction. The experimental prototype used a structured microporous ionizer distributing gas with a flat electrically conductive surface (1 in Fig. 3), manufactured in accordance with the description given in [23]. Aside from efficient generation of ion flux and plasma, such a spatially developed surface made it possible to focus the ion flux in the electrostatic field of the accelerator. Electrodes 1 and 3 (Fig. 3) were made of copper. The diameter of the gas-distributing ionizer was 25 mm, the gap between the electrodes was varied in the range of 2–20 mm.

The measured parameters of the experimental prototype were compared with the results of computer simulation as well as with the known values typical for the best modern devices.

**Experimental vacuum chamber.** The experimental prototypes of electrostatic ion accelerators were tested in a large VU-M vacuum chamber, maintaining the necessary parameters of processes and operating modes, equipment and technologies were provided [22, 23].

The parameters of ion and ion-plasma processes, including the following quantities, were measured in the tests:

voltage at the gaps between the electrodes in the acceleration module;

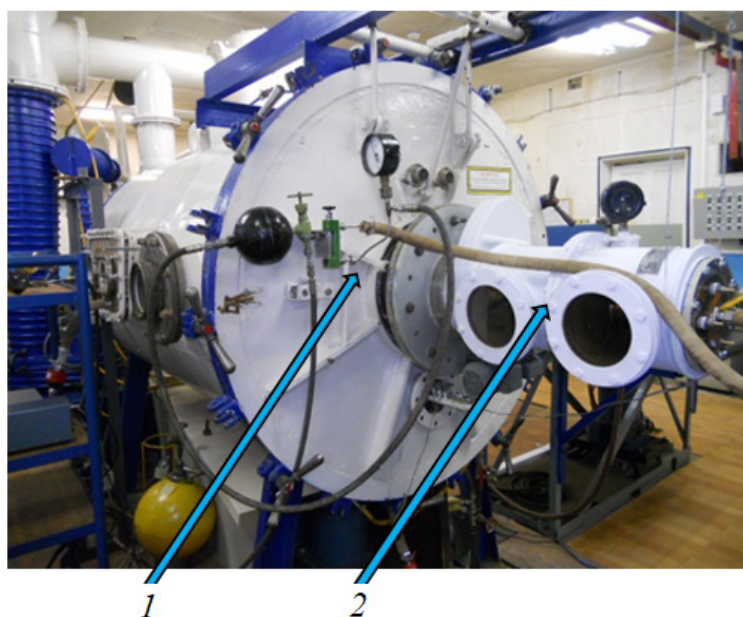


Fig. 4. Photograph of main VU-M vacuum chamber (1) with instrument module (2)

electric currents in the circuits of the accelerator electrode;

mass flow rate of propellant in the gas distributor channel;

characteristics of the radiation in the visible range;

mechanical thrust generated by the beam of particles.

The measurements were performed with continuous and pulsed high-voltage power supply. The measured parameters of the experimental prototype were compared with both theoretical and standard parameters of existing and newly proposed ion thrusters.

The experimental prototype was placed in the instrument module connected to the main VU-M vacuum chamber with a volume of 2.4 m<sup>3</sup> through a gate valve (a photograph of the chamber with the instrument module is shown in Fig. 4).

The instrument module was a cylindrical metal structure with a vacuum volume of approximately 0.03 m<sup>3</sup>. The gate valve was installed between the flange and the cylindrical body. Such a technical solution made it possible to quickly change experimental prototypes in case of depressurization and subsequent rapid

bypass pumping of the instrument module. Vacuum pressure was maintained in the main vacuum chamber. The instrument module had two transparent windows to record visible radiation, as well as an end flange for mounting the tested prototype, high-voltage leads, and a choke to supply propellant gases. The mechanical impulse of the beam was measured using a ballistic pendulum installed in the instrument module.

Fig. 5 shows a scheme of the VU-M vacuum chamber. The required vacuum pressure was maintained during the tests in the main chamber as well as in the instrument module upon propellant gas supply.

The vacuum pumping system and control equipment of the VU-M vacuum chamber included the following components:

two NVBM-5 oil-vapor booster pumps;

NVDM-400 oil-vapor diffusion pump;

TMN-500 turbomolecular pump;

piping system with shutoff valves and gates;

vacuum gauge heads;

backing-vacuum system, including mechanical pumps, a piping system with shutoff valves and gates, and vacuum gauge heads;

measuring equipment.

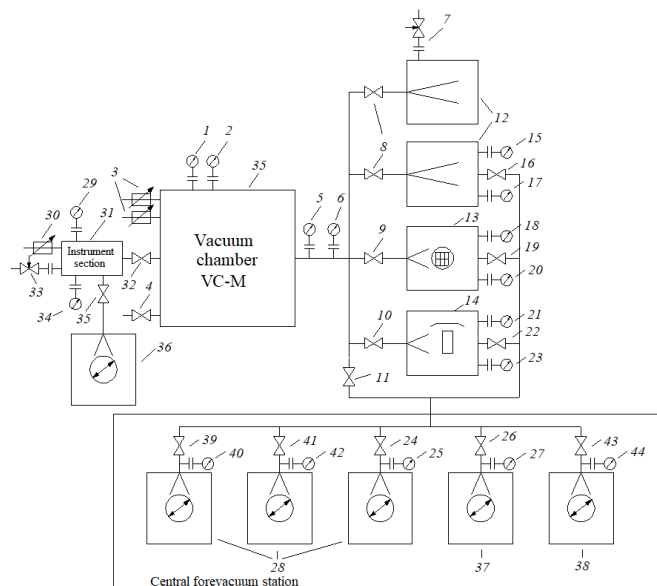


Fig. 5. Scheme of VU-M vacuum chamber:

PMT-2 thermocouple gauge heads 1, 5, 15, 18, 21, 25, 27, 29, 40, 42, 44;

PMI-2 ionization gauge heads 2, 6, 17, 20, 23, 34; lead-in wires 3, 30; leak valves 7, 33;

valves 4, 8–11, 16, 19, 22, 24, 26, 32, 35, 39, 41, 43; NVBM-5 high-vacuum oil-vapor booster pumps 12;

TMN-500 high-vacuum turbomolecular pump 13; NVDM-400 high-vacuum oil-vapor diffusion pump 14;

VN-6G backing-vacuum pumps 28 with oil seal; instrument module 31; VK-M vacuum chamber 35;

VN-461M backing-vacuum pump 36 with oil seal; VN-6Gm backing-vacuum pump 37 with oil seal;

VN-7 backing-vacuum pump with oil seal 38





The operation of the VU-M vacuum chamber is characterized by the following parameter values:

residual gas pressure (without propellant gas supply) no higher than  $10^{-3}$  Pa;

pressure upon propellant gas supply no higher than  $10^{-2}$  Pa;

pumping time (from atmospheric pressure to residual gas pressure below  $1 \cdot 10^{-3}$  Pa) no more than 4 h.

The total capacity of the high-vacuum pumps comprising the VU-M chamber was approximately  $18 \text{ m}^3/\text{s}$  at a pressure of  $10^{-1}$  Pa, meeting the condition for free passage of ions in the accelerating gaps between the electrodes at an operating pressure upon gas supply.

The mass flow rate of the gas supplied was measured and controlled using an RS-3A rotameter. The mass flow rates for different propellant gases used during the experiments (compressed air, helium, argon, etc.) were varied in the range of  $0.5\text{--}15 \text{ mg/s}$ . The upper limit for air was  $0.06 \text{ m}^3/\text{h}$ , the measurement error did not exceed  $\pm 4.0\%$  of that value.

The rotameter was calibrated by atmospheric air. The mass flow rates of propellant gases were found by recalculation by the following formula:

$$Q_{wm} = Q_{a.gr} \sqrt{\frac{\rho_{a.gr}}{\rho_{wm}}}, \quad (1)$$

where  $Q_{a.gr}$ ,  $\text{m}^3/\text{h}$ , is the air flow rate during calibration;  $\rho_{a.gr}$ ,  $\text{kg}/\text{m}^3$ , is the air density during calibration;  $\rho_{wm}$ ,  $\text{kg}/\text{m}^3$ , is the density of the propellant gas fed into the vacuum chamber.

The mass flow rate of propellant  $\rho$  at the inlet to the gas distributor was determined based on the following relation:

$$\dot{m} = \dot{m}_{wm} = Q_{wm} \rho_{wm} = Q_{a.gr} \sqrt{\rho_{a.gr} \rho_{wm}}. \quad (2)$$

Mass flow rate of the propellant and ion current in the injector circuit in the accelerating gap were measured simultaneously during the experiments, which made it possible to determine the ionization coefficient for propellant atoms in the gas flow using the following equation:

$$K_i(\dot{m}, I) = [(e\dot{m}/\mu I) - 1]^{-1}, \quad (3)$$

where  $\dot{m}$ ,  $\text{mg/s}$ , is the mass flow rate;  $I$ , A, is the ion current;  $\mu$ ,  $\text{mg}$ , is the ion mass;  $e$ , C, is the electron charge.

The ionization coefficient depends on the geometric and physical parameters of the experimental prototypes.

The approximate estimate of mechanical thrust is based on formally accounting for the mechanical impulse of the beam:

$$F_T(z=d) = \frac{dm}{dt} \cdot v = \sqrt{\frac{2\mu U_d}{q}} \cdot I,$$

where  $U_d$ , V, is the voltage;  $q$ , C, is the ion charge;  $v$ ,  $\text{m/s}$ , is the ion velocity at the exit from the gap,  $d$ , mm, is the gap width.

Since the expression does not account for elastic interactions of ions with neutrals, resonant charge exchange, radiation losses, and ion scattering in the acceleration module, it was used only for initial rough estimation.

The supply power of the stationary accelerator is converted to the power of ion drift motion in the gap, heat and radiation losses. The mechanical properties of the stationary ion thruster on the test bench correspond to the idle mode (in terms of power consumption) when the kinetic energy of the device amounts to zero.

## Results and discussion

When DC voltage in the range of  $0\text{--}5 \text{ kV}$  was supplied to the ion accelerator at zero propellant flow, no discharge phenomena (breakdowns) were observed, and the measured currents in the acceleration module circuits were close to zero.

With voltage switching and propellant gas supply, the ion accelerator was brought into operation almost with zero lag. The measured current in the injector circuit reached its maximum of approximately 1 A, and the value depended on the gas type, the voltage (up to 5 kV), and the velocity of the gas flow supplied. The switching threshold (the average value of electric intensity in the accelerating gap) was approximately  $250\text{--}500 \text{ V/cm}$  for different propellant gases. The focused flow was observed to glow brightly, which is typically due to charge and energy relaxation of the ion flux. The glow was uniformly distributed over the surface of the microporous injector and remained stable during continuous testing. In particular, visible radiation from the accelerating gap of the experimental prototype (Fig. 3) was obtained with dry atmospheric air supplied, accompanied by generation of negative ions. Similar results were obtained for different propellants and positive ions.

Figs. 6 and 7 present typical experimental characteristics and their extrapolating curves



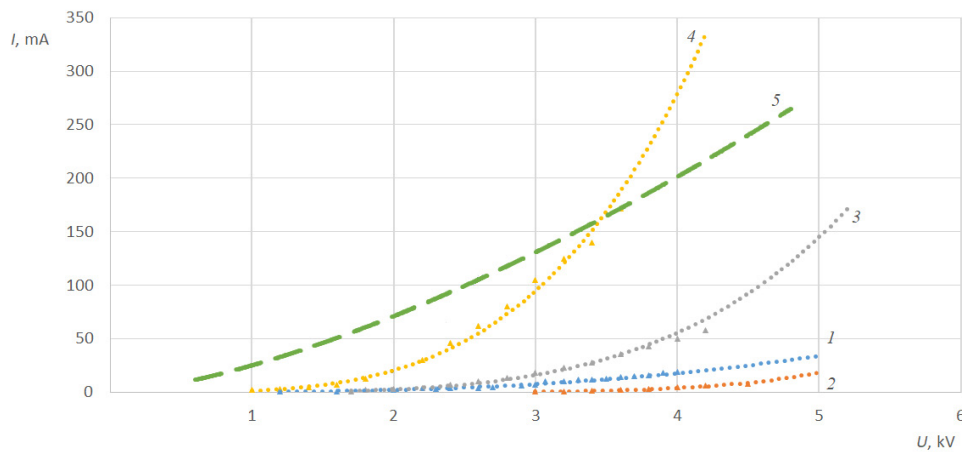


Fig. 6. Typical experimental current-voltage characteristics (points) of negative ion flux in injector circuit and their extrapolating curves (lines) for different propellants and mass flow rates  $\dot{m}$ :

air (1),  $\dot{m} = 8$  mg/s;  $\text{SF}_6$  gas,  $\dot{m} = 3, 6$  and  $9$  mg/s, respectively (2–4).

The curves are given for  $d = 16$  mm,  $h = 4$  mm (1–4); 5 is the theoretical curve obtained using the CST package for the conditions corresponding to dependence 4.

Extrapolating power-law relationships are summarized in Table 2.

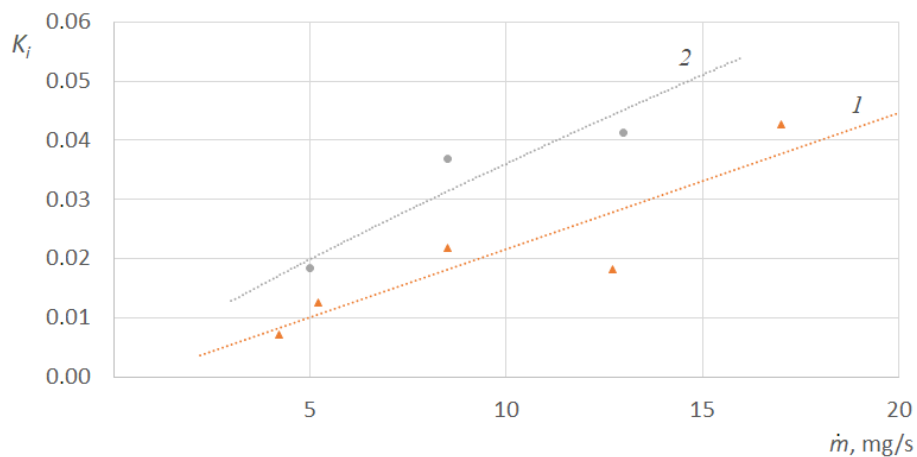


Fig. 7. Typical relationships between ionization coefficient and mass flow rate of propellant (see Eq. (3)) for two values of supplied voltage  $U$ , kV: 2.5 (1) and 3.0 (2);

The propellant is the  $\text{SF}_6$  gas,  $d = 12$  mm,  $h = 3$  mm

for ion current in the injector circuit depending on the DC voltage supplied at different mass flow rates of the propellant, and for ionization coefficient depending on the mass flow rate of the propellant mass. Data were obtained for two distances between the electrodes  $d$  and two thicknesses  $h$  of the microporous plate. To provide a comparison with experimental data, Fig. 6 shows curve 5, which is a theoretical dependence obtained with CST for the conditions corresponding to the experimental dependence 4. Extrapolating power-law dependences are summarized in Table 2.

According to the form of the extrapolating power-law dependences, the theoretical current-voltage characteristic 5 given in Fig. 6 for the computer model (see Fig. 2) corresponds to the kinetic ion model described by the Child–Langmuir law (three-halves-power law). However, the experimental curves obtained in a wide range of modes exhibited considerable differences and peculiarities in terms of the current increase. This indicates the influence of ion-plasma phenomena, including strong radiation effects, collisions, neutralization, and resonant charge exchange.



Table 2

**Extrapolating functions for current-voltage characteristics in Fig. 6**

Curve	$I(U)$ dependence
1	$I_1 = 0.3244U^{2.8949}$
2	$I_2 = 0.0004U^{6.7266}$
3	$I_3 = 0.1466U^{4.2848}$
4	$I_4 = 25.178U^{1.5000}$

Note. The given functions correspond to the data in Fig. 6 only.

Furthermore, the processes were of a general quasi-stationary nature and were not accompanied by any uncontrolled discharge phenomena. Typical relationships between the ionization coefficient and the propellant mass flow rate (Fig. 7), calculated on the basis of the experimental curves according to Eq. (3), correspond to an approximately linear increase of plasma generation effects in a wide range of parameters.

**Conclusion**

It has been established in the experiments that proper methods and means of measurement, values of process parameters, and operating conditions at a mass flow rate of different propellant gases (air, helium, argon, etc., in cation and anion generation

modes) within the range of 0.5–15 mg/s were ensured in the vacuum chamber.

Measurements and analysis of the characteristics of the experimental models of ion accelerators have also revealed that the calculated and experimental ion-physical characteristics of the tested prototypes correspond to the current tasks. The given prototypes have the following properties:

enhanced surface ionization;

ion and plasma ion bipolar modes;

uniform distribution of radiation and temperature over the developed surface of the injector;

ion injection with almost zero lag.

It has also been established that it is possible to use different propellant alternatives other than xenon.

We have found that the ion-physical characteristics of the laboratory prototypes with contact ionization implemented and tested can meet the requirements for developing promising electric propulsion units.

We assume that the developed unit with a novel physical and technological design and the given characteristics will be of interest for developing new promising equipment. In general, the experimental setup, its measuring and technological capabilities, as well as the designs of prototypes lay the foundations for further in-depth research and development of electric propulsion units.

**REFERENCES**

1. Plazmennyye i elektrostatische raketnyye dvigateli [Plasma and electrically powered spacecraft propulsion], Ed. by D.V. Razevig, Foreign Literature Publishing, Moscow, 1962.
2. Morozov A.I., Plazmennyye uskoriteli i ionnyye inzhektory [Plasma accelerators and ion injectors], Nauka, Moscow, 1984 (in Russian).
3. Morozov A.I., Fizicheskie osnovy kosmicheskikh elektrokektivnykh dvigatelej. T. 1. Elementy dinamiki potokov v ERD [Physical foundations of electrically powered spacecraft propulsion. Vol. 1: Elements of flow dynamics in EPSP], M.: Atomizdat, Moscow, 1978 (in Russian).
4. Grishin S.D., Leskov L.V., Kozlov N.P., Elektricheskie raketnyye dvigateli [Electrically powered spacecraft propulsion], Mashinostroenie, Moscow, 1975 (in Russian).
5. Favorskij O.N., Fishgojt V.V., Yantovskij E.I., Osnovy teorii kosmicheskikh elektrokektivnykh dvigatelej [Fundamentals of the theory of electrically powered spacecraft propulsion setups], Vysshaya Shkola, Moscow, 1978 (in Russian).
6. Gorshkov O.A., Muravlev V.A., Shagayda A.A., Khollovskiy i ionnyye plazmennyye dvigateli dlya kosmicheskikh apparatov [Hall and ion plasma thrusters for spacecrafts], Ed. by Koroteyev A.S., Mashinostroyeniye, Moscow, 2008 (in Russian).
7. Gusev Yu.G., Pilnikov A.V., The electric propulsion role and place within the Russian Space Program, Trudy MAI (Network scientific periodic publication) (60) (2012) 1–20. Access Mode: [www.mai.ru/science/trudy/](http://www.mai.ru/science/trudy/).
8. Gopanchuk V.V., Potapenko M.Yu., Hall effect thrusters for small-sized spacecrafts, IKBFU's Vestnik. (4) (2012) 60–67.
9. Aston G., High efficiency ion beam accelerator system, Review of Scientific

Instruments. 52 (9) (1981) 1325–1327.

10. **Hassan A., Elsaftawy A., Zakhary S.G.**, Analytical studies of the plasma extraction electrodes and ion beam formation, *Nuclear Instruments and Methods in Physics Research*, A. 586 (2) (2008) 148–152.

11. **Goebel D.M., Katz I.**, Fundamentals of electric propulsion ion and Hall thrusters, John Wiley & Sons, Hoboken, New Jersey, USA, 2008, Ch. 1, 6 and 7.

12. **Mazouffre S.**, Electric propulsion for satellites and spacecraft: established technologies and novel approaches, *Plasma Sources Sci. Technol.* 25 (3) (2016) 033002.

13. **Kaufman H.R.**, Technology of electron-bombardment ion thrusters, In the book: *Advances in electronics and electron physics*. Vol. 36. Ed. by L. Marton, Academic Press, New York (1975) 265–373.

14. **Charles C.**, Plasmas for spacecraft propulsion, *J. Phys. D: Applied Phys.* 42 (16) (2009) 163001.

15. **King J.G., Zacharias J.R.**, Some new applications and techniques of molecular beams, *Advances in electronics and electron physics*, Vol. 8, Ed. by L. Marton, Academic Press, New York (1956) 1–88.

16. **Kaminsky M.**, Atomic and ionic impact phenomena on metal surfaces, Springer Verlag, New York, 1965.

17. **Alton G.D.**, Characterization of a cesium surface ionization source with a porous tungsten ionizer. I, *Review of Scientific Instruments*. 59 (7) (1988) 1039–1044.

18. **Datz S., Taylor E.H.**, Ionization on platinum and tungsten surfaces. I. The alkali metals, *Journal of Chemical Physics*. 25 (3) (1956) 389–394.

19. **Dresser M.J.**, The Saha – Langmuir equation and its application, *Journal of Applied Physics*. 39 (1) (1968) 338–339.

20. **Zandberg E.Ya.**, Surface-ionization detection of particles (Review), *Technical Physics*. 40 (1995) 865–890.

21. **Zandberg E. Ya., Ionov N.I.**, Poverhnostnaya ionizaciya [Surface ionization], Nauka, Moscow, 1969 (in Russian).

22. **Blashenkov N.M., Lavrent'ev G.Ya.**, Surface-ionization field mass-spectrometry studies of nonequilibrium surface ionization, *Phys. Usp.* 50 (1) (2007) 53–78.

23. **Tsybin O.Yu., Tsybin Yu.O., Hakansson P.**, Laser or/and electron beam activated desorption of ions: a comparative study, In: *Desorption 2004, Papers of 10th International Conference*, Saint Petersburg (2004) 61.

24. **Goncharov P.S., Kuleshov Yu.V., Martynov V.V., et al.**, Vacuum equipment for fire tests of electric rocket engines, *Proceedings of the Military Space Academy Named after A.F. Mozhaisky*, St. Petersburg. (668) (2019) 216–223.

25. **Goncharov P.S., Martynov V.V., Pen'kov M.M., et al.**, Switching power supply for fire tests of electric rocket engines, *Proceedings of the Military Space Academy Named after A.F. Mozhaisky*, St. Petersburg. (668) (2019) 224–228.

26. **Kalentev O., Matyash K., Duras J., et al.**, Electrostatic ion thrusters – towards predictive modeling, *Contributions to Plasma Physics*. 54(2) (2014) 235–248.

27. **Lovtsov A.S., Kravchenko D.A.**, Kinetic simulation of plasma in ion thruster discharge chamber. Comparison with experimental data, *Procedia Engineering*. 185 (2017) 326–331.

28. **Peng X., Keefert D., Ruytent W.M.**, Plasma particle simulation of electrostatic ion thrusters, *Journal of Propulsion and Power*. 8 (2) (1992) 361–366.

29. **Kurushin A.** Basic course of design of microwave devices using CST Studio Suite, One-Book, Moscow, 2014.

30. **Kurushin A.A., Plastikov A.N.**, *Proyektirovaniye SVCh ustroystv v srede CST Microwave Studio [Design of microwave devices in CST Microwave Studio]*, MEI Press, 2011.

31. **Tsybin O.Y., Makarov S.B., Ostapenko O.N.**, Jet engine with electromagnetic field excitation of expendable solid-state material, *Acta Astronautica*. 129 (December) (2016) 211–213.

32. **Makarov S.B., Tsybin O.Yu.**, Ionic rocket engine of spacecraft, Pat. No. 2682962, Russian Federation, MPK H05H1/54 (2006.01); F03H1/00 (2006.01); B64G1/00 (2006.01); Federalnoe gosudarstvennoe avtonomnoe obrazovatelnoe uchrezhdenie vysshego obrazovaniya “Sankt-Peterburgskij Politehnicheskij Universitet Petra Velikogo” (FGAOUVO “SPbPU”) is a declarant and patentee. No. 2018121762, declar. 14. 06. 2018; publ. 25.03. 2019, Bull. No. 9, 17 p.

33. **Makarov S.B., Tsybin O.Yu.**, Diaphragm ion plasma thruster for spacecraft, Pat. No. 2709231, Russian Federation, MPK F03H 1/00 (2006.01); Federalnoe gosudarstvennoe avtonomnoe obrazovatelnoe uchrezhdenie vysshego obrazovaniya “Sankt-Peterburgskij Politehnicheskij Universitet Petra Velikogo” (FGAOUVO “SPbPU”). No. 2018142412, declar.



01.12.2018; publ. 17.12.2019. Bull. No. 35.

34. **Dyubo D.B., Tsybin O.Yu.**, Mekhanicheskie svoystva uskoritelya ionov dlya elektroraketnogo dvigatelya kosmicheskogo apparata [Mechanical properties of an ion accelerator for an electrically powered spacecraft propulsion of a spacecraft], In: Proceedings of the Science Conference with International Participation

“Nedelya nauki SPbPU [Scientific Week at SPbPU]”, November 18–23 (2019) 144–147.

35. **Dyubo D.B., Tsybin O.Yu.** The contact ionization ion accelerator for the electrically powered spacecraft propulsion: a computer model // St. Petersburg State Polytechnical University Journal. Physics and Mathematics. 2020. Vol. 13. No. 1. Pp. 78–91.

*Received 31.03.2020, accepted 18.05.2020.*

## THE AUTHORS

### **TSYBIN Oleg Yu.**

*Peter the Great St. Petersburg Polytechnic University*

29 Politechnicheskaya St., St. Petersburg, 195251, Russian Federation  
otsybin@rphf.spbstu.ru

### **MAKAROV Sergey B.**

*Peter the Great St. Petersburg Polytechnic University*

29 Politechnicheskaya St., St. Petersburg, 195251, Russian Federation  
makarov@cee.spbstu.ru

### **DYUBO Dmitry B.**

*Peter the Great St. Petersburg Polytechnic University*

29 Politechnicheskaya St., St. Petersburg, 195251, Russian Federation  
doobinator@rambler.ru

### **KULESHOV Yuri V.**

*Military Space Academy named after A.F. Mozhaysky*

13 Zhdanovskaya St., St. Petersburg, 197198, Russian Federation  
kuleshov\_y@email.ru

### **GONCHAROV Pavel S.**

*Military Space Academy named after A.F. Mozhaysky*

13 Zhdanovskaya St., St. Petersburg, 197198, Russian Federation  
goncharov\_p@email.ru

### **MARTYNOV Viktor V.**

*Military Space Academy named after A.F. Mozhaysky*

13 Zhdanovskaya St., St. Petersburg, 197198, Russian Federation  
martynov\_v@email.ru

### **SHUNEVICH Nikolay A.**

*Military Space Academy named after A.F. Mozhaysky*

13 Zhdanovskaya St., St. Petersburg, 197198, Russian Federation  
shunevich\_n@email.ru

## СПИСОК ЛИТЕРАТУРЫ

1. Плазменные и электростатические ракетные двигатели. Пер. с англ. Под ред. Д.В. Разевига. М.: Изд-во иностр. лит-ры, 1962, 170 с.
2. **Морозов А.И.** Плазменные ускорители и ионные инжекторы. М.: Наука, 1984. 269 с.
3. **Морозов А.И.** Физические основы космических электрореактивных двигателей. Т. 1. Элементы динамики потоков в ЭРД. М.: Атомиздат, 1978. 328 с.
4. **Гришин С.Д., Лесков Л.В., Козлов Н.П.** Электрические ракетные двигатели. М.: Машиностроение, 1975, 272 с.
5. **Фаворский О.Н., Фишгойт В.В., Янговский Е.И.** Основы теории космических электрореактивных двигательных установок. М.: Высшая школа, 1978. 384 с.
6. **Горшков О.А., Муравлев В.А., Шагайда А.А.** Холловские и ионные плазменные двигатели для космических аппаратов. Под ред. акад. РАН А.С. Коротеева М.: Машиностроение, 2008. 280 с.
7. **Гусев Ю.Г., Пильников А.В.** Роль и место электроракетных двигателей в Российской космической программе // Труды МАИ (электронный журнал). 2012. Вып. № 60. С. 1–20. Режим доступа: [www.mai.ru/science/trudy/](http://www.mai.ru/science/trudy/).
8. **Гопанчук В.В., Потапенко М.Ю.** Электрореактивные двигатели для малых космических аппаратов // Вестник Балтийского федерального университета им. И. Канта. 2012. Вып. 4. С. 60–67.
9. **Aston G.** High efficiency ion beam accelerator system // Review of Scientific Instruments. 1981. Vol. 52. No. 9. Pp. 1325–1327.
10. **Hassan A., Elsaftawy A., Zakhary S.G.** Analytical studies of the plasma extraction electrodes and ion beam formation // Nuclear Instruments and Methods in Physics Research. A. 2008. Vol. 586. No. 2. Pp. 148–152.
11. **Goebel D.M., Katz I.** Fundamentals of electric propulsion ion and Hall thrusters. Hoboken, New Jersey, USA: John Wiley & Sons, 2008. Ch. 1, 6 and 7.
12. **Mazouffre S.** Electric propulsion for satellites and spacecraft: established technologies and novel approaches // Plasma Sources Sci. Technol. 2016. Vol. 25. No. 3. P. 033002.
13. **Kaufman H.R.** Technology of electron-bombardment ion thrusters // Advances in Electronics and Electron Physics. Vol. 36. Ed. by L. Marton, New York: Academic Press, 1975. Pp. 265–373.
14. **Charles C.** Plasmas for spacecraft propulsion // J. Phys. D: Applied Phys. 2009. Vol. 42. No. 16. P. 163001.
15. **King J.G., Zacharias J.R.** Some new applications and techniques of molecular beams // Advances in electronics and electron physics. Vol. 8. Ed. by L. Marton. New York: Academic Press, 1956. Pp. 1–88.
16. **Kaminsky M.** Atomic and ionic impact phenomena on metal surfaces. New York: Springer Verlag, 1965. 402 p.
17. **Alton G.D.** Characterization of a cesium surface ionization source with a porous tungsten ionizer. I // Review of Scientific Instruments. 1988. Vol. 59. No. 7. Pp. 1039–1044.
18. **Datz S., Taylor E.H.** Ionization on platinum and tungsten surfaces. I. The alkali metals // Journal of Chemical Physics. 1956. Vol. 25. No. 3. Pp. 389–394.
19. **Dresser M.J.** The Saha – Langmuir equation and its application // Journal of Applied Physics. 1968. Vol. 39. No. 1. Pp. 338–339.
20. **Зандберг Э.Я.** Поверхностно-ионизационное детектирование частиц (Обзор) // Журнал технической физики. 1995. Т. 9 № .65. С. 38–1.
21. **Зандберг Э.Я., Ионов Н.И.** Поверхностная ионизация. М.: Наука, 1969. 432 с.
22. **Блашенко Н.М., Лаврентьев Г.Я.** Исследование неравновесной поверхностной ионизации методом полевой поверхностно-ионизационной масс-спектрометрии // Успехи физических наук. 2007. Т. 177. № 1. С. 59–85.
23. **Tsybin O.Yu., Tsybin Yu.O., Hakansson P.** Laser or/and electron beam activated desorption of ions: a comparative study // Desorption 2004. Papers of 10th International Conference. Saint Petersburg, 2004. P. 61.
24. **Гончаров П.С., Кулешов Ю.В., Мартынов В.В., Цыбин О.Ю., Шуневич Н.А.** Вакуумная установка для огневых испытаний электрических ракетных двигателей // Труды Военно-космической академии имени А.Ф. Можайского. 2019. Вып. 668. С. 216–223.
25. **Гончаров П.С., Мартынов В.В., Пеньков М.М., Скунтицкий В.М., Цыбин О.Ю., Шуневич Н.А.** Импульсный источник питания для проведения испытаний электрических ракетных двигателей // Труды Военно-космической академии имени А.Ф. Можайского. 2019. Вып. 668. С. 224–228.
26. **Kalentev O., Matyash K., Duras J., Lyskow K.F., Schneider R., Koch N., Schirra M.**





Electrostatic ion thrusters – towards predictive modeling// Contributions to Plasma Physics. 2014. Vol. 54. No. 2. Pp. 235–248.

27. **Lovtsov A.S., Kravchenko D.A.** Kinetic simulation of plasma in ion thruster discharge chamber. Comparison with experimental data // Procedia Engineering. 2017. Vol. 185. Pp. 326–331.

28. **Peng X., Keefert D., Ruysent W.M.** Plasma particle simulation of electrostatic ion thrusters// Journal of Propulsion and Power. 1992. Vol. 8. No. 2. Pp. 361–366.

29. **Kurushin A.** Basic course of design of microwave devices using CST Studio Suite. Moscow: One-Book, 2014. 433 p.

30. **Курушин А.А., Пластиков А.Н.** Проектирование СВЧ устройств в среде CST Microwave Studio. М.: Изд-во МЭИ, 155. 2011 с.

31. **Tsybin O.Y., Makarov S.B., Ostapenko O.N.** Jet engine with electromagnetic field excitation of expendable solid-state material // Acta Astronautica. 2016. Vol. 129. December. Pp. 211–213.

32. **Макаров С.Б., Цыбин О.Ю.** Ионный ракетный двигатель космического аппарата. Пат. № 2682962. Российская Федерация. МПК H05H1/54 (2006.01); F03H1/00 (2006.01); B64G1/00 (2006.01); заявитель и патентообладатель – Федеральное государственное автономное образовательное учреждение высшего

образования «Санкт-Петербургский политехнический университет Петра Великого» (ФГАОУВО «СПбПУ»). № 2018121762, заявл. 14. 06. 2018; опубл. 25.03. 2019. Бюлл. № 9. 17 с., с илл.

33. **Макаров С.Б., Цыбин О.Ю.** Мембранный ионно-плазменный ракетный двигатель космического аппарата. Пат. № 2709231. Российская Федерация. МПК F03H1/00 (2006.01); заявитель и патентообладатель – Федеральное государственное автономное образовательное учреждение высшего образования «Санкт-Петербургский политехнический университет Петра Великого» (ФГАОУВО «СПбПУ»). № 2018142412, заявл. 01.12.2018; опубл. 17.12.2019. Бюлл. № 35.

34. **Дюбо Д.Б., Цыбин О.Ю.** Механические свойства ускорителя ионов для электроракетного двигателя космического аппарата//Неделя науки СПбПУ. 18 – 23 ноября 2019. Материалы научной конференции с международным участием. СПб.: Изд-во Политехнического ун-та, 2019. С. 144–147.

35. **Дюбо Д.Б., Цыбин О.Ю.** Компьютерная модель ускорителя ионов с контактной ионизацией для электроракетных двигателей космических летательных аппаратов // Научно-технические ведомости СПбГПУ. Физико-математические науки. 2020. Т. 13. № 1. С. 78–91.

*Статья поступила в редакцию 31.03.2020, принята к публикации 18.05.2020.*

## СВЕДЕНИЯ ОБ АВТОРАХ

**ЦЫБИН Олег Юрьевич** – доктор физико-математических наук, профессор Высшей инженерно-физической школы Санкт-Петербургского политехнического университета Петра Великого, Санкт-Петербург, Российская Федерация.

195251 Российская Федерация, г. Санкт-Петербург, Политехническая ул., 29  
otsybin@rphf.spbstu.ru

**МАКАРОВ Сергей Борисович** – доктор технических наук, профессор Высшей школы прикладной физики и космических технологий Санкт-Петербургского политехнического университета Петра Великого, главный научный сотрудник научной лаборатории «Космические телекоммуникационные системы» того же университета, Санкт-Петербург, Российская Федерация.

195251, Российская Федерация, г. Санкт-Петербург, Политехническая ул., 29  
makarov@cee.spbstu.ru

**ДЮБО Дмитрий Борисович** – аспирант Высшей инженерно-физической школы Санкт-Петербургского политехнического университета Петра Великого, Санкт-Петербург, Российская Федерация.

195251, Российская Федерация, г. Санкт-Петербург, Политехническая ул., 29  
doobinator@rambler.ru

**КУЛЕШОВ Юрий Владимирович** — доктор технических наук, профессор, заместитель начальника Военно-космической академии имени А.Ф. Можайского по учебной и научной работе Военно-космической академии имени А.Ф. Можайского, Санкт-Петербург, Российская Федерация.  
197198, Российская Федерация, г. Санкт-Петербург, Ждановская ул., 13  
kuleshov\_y@email.ru

**ГОНЧАРОВ Павел Сергеевич** — кандидат технических наук, начальник 12-го отдела Военного института (научно-исследовательского) Военно-космической академии имени А.Ф. Можайского, Санкт-Петербург, Российская Федерация.  
197198, Российская Федерация, г. Санкт-Петербург, Ждановская ул., 13  
goncharov\_p@email.ru

**МАРТЫНОВ Виктор Васильевич** — старший научный сотрудник -121й лаборатории -12го отдела Военного института (научно-исследовательского) Военно-космической академии имени А.Ф. Можайского, Санкт-Петербург, Российская Федерация.  
197198, Российская Федерация, г. Санкт-Петербург, Ждановская ул., 13  
martynov\_v@email.ru

**ШУНЕВИЧ Николай Александрович** — кандидат технических наук, начальник лаборатории, старший научный сотрудник 122-й лаборатории 12-го отдела Военного института (научно-исследовательского) Военно-космической академии имени А.Ф. Можайского, Санкт-Петербург, Российская Федерация.  
197198, Российская Федерация, г. Санкт-Петербург, Ждановская ул., 13  
shunevich\_n@email.ru

DOI: 10.18721/JPM.13209

UDC 535.417; 535.317; 778.38

## IMAGING PROPERTIES OF COMPUTER-GENERATED HOLOGRAMS: THE PHASE DISTRIBUTION EFFECT IN THE OBJECTS' SPACE

*S.N. Koreshev, D.S. Smorodinov, M.A. Frolova, S.O. Starovoitov*

St. Petersburg National Research University of Information Technologies,  
Mechanics and Optics, St. Petersburg, Russian Federation

In the paper, the influence of phase distribution over the objects' space on resolution and depth of field of computer-generated holograms has been investigated. The study was carried out through mathematical simulation of real physical processes of synthesis and reconstruction of binary transparent holograms. The possibility of a significant increase (up to several times) in the resolution and depth of field of the reconstructed image because of using phase-shift masks was found. Moreover, this increase was achieved due to representation of the object wave in hologram synthesis as a superposition of object waves emanating light from two identical objects located at different, strictly fixed distances from the hologram synthesis plane.

**Keywords:** synthesized hologram, binarization, threshold processing, depth of field, phase mask

**Citation:** Koreshev S.N., Smorodinov D.S., Frolova M.A., Starovoitov S.O. Imaging properties of computer-generated holograms: the phase distribution effect in the object's space, St. Petersburg Polytechnical State University Journal. Physics and Mathematics. 13 (2) (2020) 99–107. DOI: 10.18721/JPM.13209

This is an open access article under the CC BY-NC 4.0 license (<https://creativecommons.org/licenses/by-nc/4.0/>)

## ВЛИЯНИЕ РАСПРЕДЕЛЕНИЯ ФАЗЫ В ПРОСТРАНСТВЕ ОБЪЕКТОВ НА ИЗОБРАЖАЮЩИЕ СВОЙСТВА СИНТЕЗИРОВАННЫХ ГОЛОГРАММ

*С.Н. Корешев, Д.С. Смородинов, М.А. Фролова, С.О. Старовойтов*

Санкт-Петербургский национальный исследовательский университет  
информационных технологий, механики и оптики,  
Санкт-Петербург, Российская Федерация

В работе изучено влияние распределения фазы в пространстве предметов на разрешающую способность и глубину резкости синтезированных голограмм. Исследование проведено методом математического моделирования реальных физических процессов синтеза и восстановления голограмм бинарных транспарантов. Установлена возможность существенного (в нескольких раз) увеличения разрешения и глубины резкости восстановленного изображения благодаря использованию при синтезе голограммы фазовых масок и представлению объектной волны в виде суперпозиции объектных волн, исходящих от двух одинаковых объектов, расположенных на различных, строго фиксированных расстояниях от плоскости синтеза голограммы.

**Ключевые слова:** синтезированная голограмма, бинаризация, пороговая обработка, глубина резкости, фазовая маска

**Ссылка при цитировании:** Корешев С.Н., Смородинов Д.С., Фролова М.А., Старовойтов С.О. Влияние распределения фазы в пространстве объектов на изображающие свойства синтезированных голограмм // Научно-технические ведомости СПбГПУ. Физико-математические науки. 2020. Т. 13. № 2. С. 116–125. DOI: 10.18721/JPM.13209

Эта статья открытого доступа, распространяемая по лицензии CC BY-NC 4.0 (<https://creativecommons.org/licenses/by-nc/4.0/>)

### Introduction

Holography is widely used in electronics, microtechnology and other spheres. In addition to well-known holographic methods of protection against counterfeiting of goods, holographic diffraction gratings, complex wave front shapers, sights, three-dimensional projection, and other holographic technologies can be applied in photolithography.

The advances of holography in projection photolithography is primarily due to the possibility of simultaneous aberration-free reconstruction of large-sized real images, including images of binary two-dimensional transparencies, namely, photomasks [1 – 3]. The application of holograms in projection photolithography makes it possible to avoid the usage of sophisticated optical systems, complex in design due to strict requirements for quality of the images formed using a photolithographic lens. In particular, the current tendency of size reduction of electronic devices leads to gradual increase in resolution of optical systems. This is usually achieved by reducing the operating wavelength, which in turn leads to a reduction in the size of the aberration-free area of an image.

Particularly noteworthy is the possibility of using images of photolithographic objects of computer-generated Fresnel holograms as projectors, which are a set of discrete pixel-cells with different phase and intensity values and can be easily calculated using modern computers and displayed on physical media. The methods of hologram synthesis for extreme ultraviolet, as well specific requirements for synthesis scheme parameters that would allow to reconstruct a high-quality image were presented earlier [4–6].

Imaging properties of the computer-generated holograms in some cases differ from the properties of analog holograms and have their own characteristics. These features are well studied and exist primarily due to the discrete structure of the hologram and image [7–11].

This paper presents our findings of the phase distribution effect in the objects' space during synthesis of the Fresnel holograms on its resolution and depth of field of the image formed using these holograms. Real physical

processes of synthesis and reconstruction of reflection holograms have been mathematically simulated.

The discrete object-transparency is usually presented as a set of coherent point sources with each source emanating light uniformly in all directions. In this case, the ratio between the values of the amplitude at two selected points on the hologram registration plane is determined by the ratio of the areas of the spheres on which the points are located (Fig. 1). Thus, if the amplitude located at a point on the normal and restored from the source to the hologram plane is taken as a unit, it becomes possible to determine the amplitude at any point on the plane.

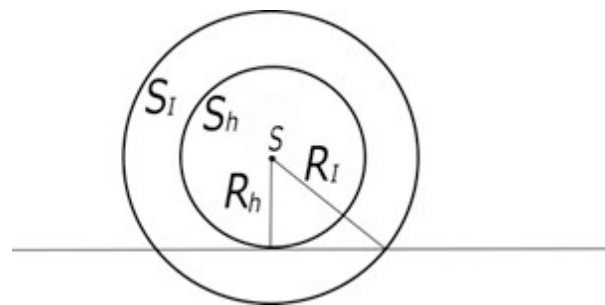


Fig. 1. Distribution of amplitude from a point source ( $s$ ) emanating light over the hologram registration plane (a straight line);

$R_l$ ,  $R_h$  are the spherical radii of light rays;

$S_l$ ,  $S_h$  are the spherical areas

Furthermore, since all the point sources making up the object are coherent, the phase shift from the source to the point on the hologram also depends solely on the radius of the sphere  $R_l$  and the wavelength  $\lambda$ :

$$\varphi_l = \frac{2\pi R_l}{\lambda} + \varphi_0, \quad (1)$$

where  $\varphi_0$  is the initial value of the light source phase.

The final value of the amplitude at each point on the hologram plane is defined as the vector sum of the amplitudes from all points of the object, taking into account distances between the point of the object and the



point on the hologram. At the same time, the structure of the hologram and the image formed are significantly influenced by initial phase distributions during hologram synthesis in the object space.

**The phase distribution effect in the object's space on the resolution of computer-generated Fresnel holograms-projectors**

The phenomenon of the overlap between diffraction maxima from closely spaced elements of the object which leads to resolution lowering is called proximity effect. To correct it, it is proposed to apply a method like the one used in traditional projection photolithography: the installation of phase-shifting masks in the object space, which makes phase difference between wave fronts that form images of neighboring elements of the object structure equal  $\pi$  [12]. Since the synthesis of holograms is performed in virtual space, this could be achieved through the correction of the mathematical model of the photomask, i. e., the introduction of the necessary phase modulation in its transmission function.

Let us find out the applicability limits of the proximity effect compensation method, i.e. conditions under which the elements of the structure of the photomask can be considered neighboring, so that the method under consideration would have a positive effect on the quality of the reconstructed image. This could be done either by diffraction integral calculation, or experimentally, for example, by using mathematical simulation. It was carried out in a software package for synthesis and digital reconstruction of Fresnel holograms [4]. The research included a series of numerical experiments of synthesis and digital reconstruction of the phase-relief reflective Fresnel hologram of a flat object: two slits located closely in a non-transparent screen. It was assumed that the effectiveness of the method for correcting the proximity effect should depend on the distance between the slits.

The parameters for the hologram synthesis scheme were selected based on the requirements described in Refs. [5, 6]. Thus, laser wavelength  $\lambda$  was 13.5 nm; the pixel size of the object and the hologram  $d_d$  was  $20 \times 20$  nm<sup>2</sup>. The characteristic size of the minimum element of objects' structure was 80 nm. The pixel size of the object was chosen to satisfy the requirements of the Rayleigh criterion [5]. The angle of the parallel reference beam incidence was chosen equal to  $14.7^\circ$  in all experiments, and the distance between the plane of the

object and the plane of hologram registration was  $R_h = 20345$  nm.

The influence of proximity effect on image quality for different distances between the structural elements of the object was studied by synthesizing and digitally reconstructing the holograms of two slits of  $4 \times 40$  pixels, i.e.,  $80 \times 800$  nm each. The resulting numerically reconstructed images are shown in Fig. 2. According to the Rayleigh criterion, two point-sources (in this experiment, narrow slits could be considered as point sources) are completely resolved if the diffraction maximum of one of them is superimposed on the diffraction minimum of the other. Therefore, experiments should be carried out only for those distances between slits that are smaller than Rayleigh resolution criterion for coherent radiation, which is equal to 57 nm for the slits under study.

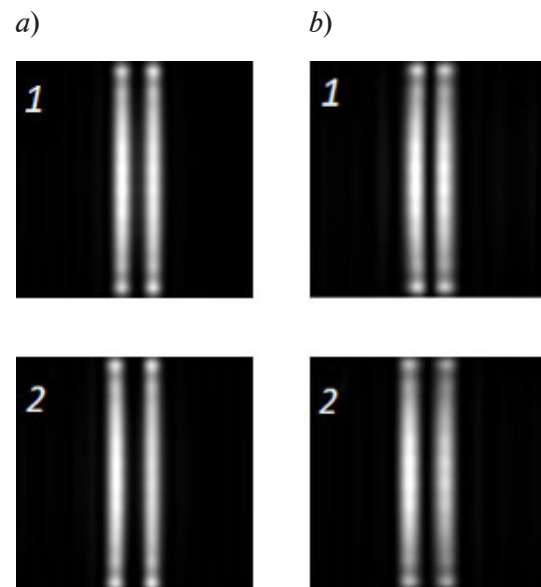


Fig. 2. Reconstructed images obtained with in-phase (a) and out-of-phase (b) radiation for two distances (nm) between segments: 20 (1) and 40 (2)

Thus, the distances between the slits in the experiments ranged from 1 to 2 pixels, i.e. from 20 to 40 nm. Two holograms were synthesized for each of the indicated distances between the slits – one for the case when all the radiation incident on the object was in phase, the other for the case when the beams incident on slits were out of phase. Thus, four holograms were synthesized, and the corresponding images were numerically reconstructed.

To assess the quality of the reconstructed images, we used a method based on comparing the number of threshold processing levels, which



imitates photoresist response to actinic radiation exposure. Since the pixels of reconstructed images are encoded using 8 bits, the total number of possible threshold processing levels (intensity gradations) is 256, from 0 (black) to 255 (white), in accordance with so called "gray scale" [13]. So, the greater the number of threshold processing levels (gradations) at which the intensity distribution on the image is identical to intensity distribution on the object, the higher the quality of reconstructed image. The eligibility of using this criterion is explained by the threshold properties of photoresists. The larger the number of acceptable threshold levels for the reconstructed image, the larger the range of exposure doses is permissible in the photolithographic process.

Images reconstructed using holograms recorded with all incident radiation being in phase, corresponded to the original objects in the interval of zero gradations of threshold processing at a distance between slits of 20 nm and 12 gradations at 40 nm. With waves incident on slits being out of phase, the image corresponded to the original object in the range of 14 gradations with a distance between slits of 20 nm and 17 gradations at 40 nm. Thus, in the case of the smallest possible distance between the slits (20 nm), the use of phase masks makes the slits resolvable, while if the distance between the slits is 40 nm, its quality is almost the same regardless of using the phase masks.

Thus, numerical experiments have shown that the application of the phase correction method for the proximity effect allows one to successfully resolve structural elements of the object that are at the minimum possible (equal to the size of the object's pixel) distance between them.

#### **The phase distribution effect in the object's space on the depth of field of the computer-generated Fresnel holograms**

The image is considered to be sharp within the limits of such a displacement of the observation plane, at which the diameter of a point object image represented as a geometric point does not exceed the Airy disc diameter. The expression that allows the depth of field of the optical system to be determined in accordance with this criterion is presented as [14]:

$$|b| = \pm \frac{\tilde{e}n}{2A^2}, \quad (2)$$

where  $A$  is the system numerical aperture,  $\lambda$  is the wavelength of the laser used,  $n$  is a refractive index of a medium, equals 1 for air.

Thus, the numerical aperture of the radiation diffracted on the smallest element of the object structure, a pixel with the size  $a_p$ , is described as follows:

$$A = n \sin \alpha = \frac{\lambda}{a_t}, \quad (3)$$

where  $\alpha$  is the aperture angle of the diffracted radiation.

From Eqs. (2) and (3), the only parameters affecting the depth of field are the operating wavelength  $\lambda$  and the size of one pixel  $a_p$ . Currently, various methods are known to further increase the depth of field of images. In particular, there are methods based on phase-shift masks [15], modifications of optical devices [16], special digital processing of images at the stage of their registration [17].

However, not all these methods are suitable for photolithography. The best results in this case can be obtained by the method based on representation of an object wave during the hologram synthesis as a superposition of several object waves generated by the same object, a photomask, located at different distances from the hologram [18].

In this case, the increase in the depth of field of the reconstructed image is due to the fact that the hologram restores not one, but several images with a small offset, not exceeding the depth of field. Since the objects used are flat, the sequence of such images will be perceived as a single image with an increased depth-of-field.

Practical implementation of the hologram synthesis mentioned above requires representation of the object beam as a superposition of two or more object waves generated by the same objects. Such an operation would require a very precise installation of objects during the physical registration of the hologram, inversely to holograms synthesized in virtual space. The distance between flat objects leads to a certain phase difference between the object waves, which obviously affects the recorded hologram structure, the final intensity distribution in the reconstructed image and, accordingly, and the depth of field. In this case, the reconstructed image has the best quality when the object beams are fully in-phase.

If the object and the reconstructed image are in-phase, as proposed above, then the reconstructed images has a constant phase difference in each plane of the image space. If the wavelength is considered as a constant, then the only factor affecting the phase difference



between the object waves is the distance between the planes of the objects.

These data are almost completely consistent with the results of phase distribution in the reconstructed image [18]. It should be noted that for small distance values  $\Delta$  between objects, the main factor affecting phase distribution in the hologram synthesis plane is the point position on the hologram relative to its axis. At the same time, as the  $\Delta$  value increases, the influence of the point position gradually decreases and the distance between light sources becomes the main factor affecting the phase difference.

Another equally significant factor is discretization. Theoretically, the value of the complex amplitude calculated at a particular point is actually set for the entire pixel due to the limited size of discrete cells of the hologram plane, calculated with Eq. (3). This leads to uncertainty and, as a consequence, to an increase in difference between the recorded values of the phase and the complex amplitude and the real value, as it shifts from the center of the pixel to its boundaries. Note that an offset of one spatial period leads to a phase shift of the reconstructed image of  $2\pi$  [11]. A sharp change in the phase and amplitude values occurs at the boundaries of adjacent pixels.

The relationship of distance between the object planes and the quality of the reconstructed image was demonstrated experimentally with the above mentioned software package. Experimental evaluation included the synthesis of half-tone Fresnel holograms of the test object called "corners". The object is shown in Fig. 3, *a*.

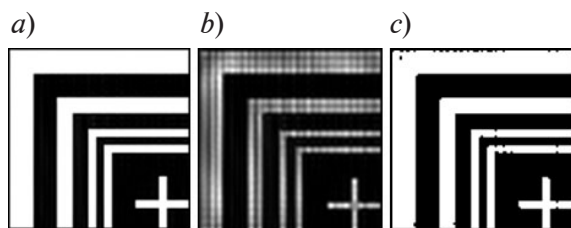


Fig. 3. The original image of the test object (*a*) and the image reconstructed using a synthesized hologram: before (*b*) and after (*c*) threshold processing

The test object was characterized by cross-lines of  $1 \times 7$  pixels. Two corners closest to the cross were made up of 1 pixel-thick segments, the distance between them equaled 1 pixel. This was followed by a gap of 2 pixels

in width, and a third corner with 2 pixels in width. The width of the fourth corner was 3 pixels. The total size of the object was  $23 \times 23$  pixels.

The synthesis parameters were chosen in accordance with the conditions defined in [11] and generally coincided with the parameters used in the previous experiment. That is, the size of the minimum element of the object was  $80 \times 80$  nm, the pixel size of the object planes and holograms  $d_d$  was  $20 \times 20$  nm, and the wavelength  $\lambda$  was 13.5 nm. Under such conditions, the angle of incidence of the reference beam  $\alpha$  was  $14.67^\circ$ , and the distance between the hologram and the plane of the nearest object was at least 20345 nm. Since the structure of the object is rather complex,  $R_h$  value was doubled to 40690 nm. The distance was increased two times to avoid overlapping of restored orders of diffraction. This step is needed to address the problem of interference which starts to influence the quality of the image when high resolution is applied [5]. The depth of field of the reconstructed image at the parameters specified above were  $b = \pm 237$  nm, according to Eq. (3).

The second plane of the object was placed a little farther from the hologram at some distance  $\Delta$  relative to the first, with this distance changing during the experiment.

The reconstructed image quality estimate was carried out using the method based on comparing the number of threshold processing levels described above. The only difference was that due to the high resolution on the reconstructed image, it was considered identical to the object not only when their intensity distributions were the same, but also when the difference between their intensity distributions did not exceed 15 %.

Fig. 4 shows dependence between the allowable levels of threshold image processing obtained in the plane of the best installation at a distance  $R_h$  related to the maximum number of gradations achieved with the above described hologram synthesis and reconstruction, and the distance  $\Delta$  between the planes of two objects.

As long as the  $\Delta$  value remains sufficiently small (within several wavelengths), the image quality as a whole is not strongly dependent on  $\Delta$ . The exceptions are the individual maxima corresponding to the object images with higher quality, characteristic of the distances, at which the registered object waves are in phase in the

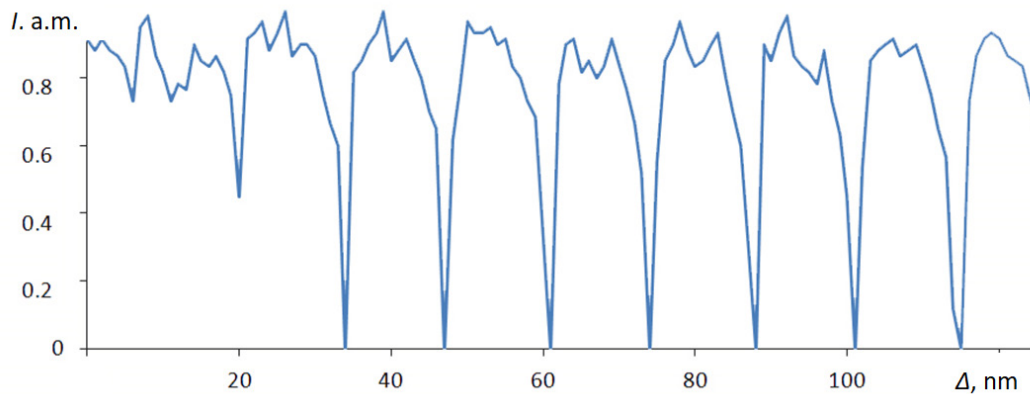


Fig. 4. Graph of the quality of the image of the test object obtained in the plane of the best installation vs the distance  $\Delta$  between the planes of the objects during the synthesis

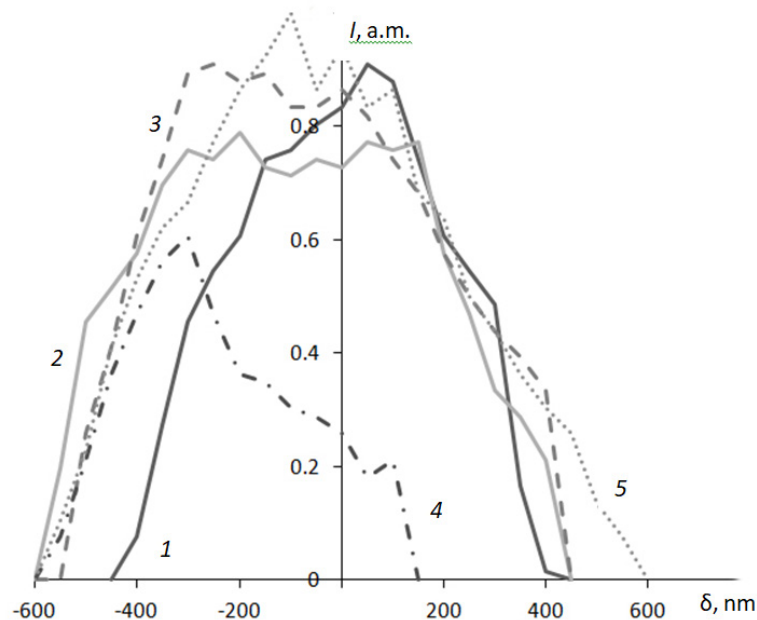


Fig. 5. Graphs of the quality of the test object's image reconstructed vs. defocus  $\delta$  for different  $\Delta$  values, nm:  $\Delta = 0$ , i.e., without installing the second plane (1),  $\Delta = 4$  (2), 21 (3), 194 (4), 199 (5);  $\Delta$  is the distance between the planes of the objects during the synthesis

synthesis process. Thus, the minima on the chart correspond to the distances at which the object waves are out of phase.

As  $\Delta$  increases, the values of the minima approach zero: the influence of the aperture can no longer compensate for the violation of in-phase. As a result, restoration of a high-quality image using such holograms becomes almost impossible. At the same time, the in-phase recording of object waves in absence of the aperture influence can significantly improve the image quality. The "phase uncertainty in hologram synthesis" described above leads to

abrupt transitions between adjacent minimum and maximum due to abrupt changes in phase values.

At large distances  $\Delta$ , close to  $b$ , the influence of the hologram aperture practically disappears: the image quality is, on the average, noticeably lower, except for individual maxima arising from the in-phase recording due to the influence of discretization.

The distance between the adjacent maxima corresponds to the working wavelength  $\lambda$ ; thus, checking a series of values when shifting within



the wavelength, allows to accurately determine the position of the maximum.

To directly estimate the depth of field of the reconstructed images using holograms synthesized at given  $\Delta$  values, a series of images was reconstructed at distances  $\delta$  different from the distance  $R_h$  by values from  $-1000$  to  $+1000$  nm with a step of 50 nm. The results of the study of image quality in gradations, normalized by their maximum number, are shown in Fig. 5.

Thus, it was established that the addition of a second object plane, provided that the phase of the object waves coincides, made it possible to increase not only the depth of field, but also the overall image quality (maximum number of gradations). The best quality of the reconstructed images was achieved by installing the second plane of the object at distances close to the  $b$  value of the limiting depth of field, in this case the depth of field of the image increases by 2 times.

### Summary

In this paper, the influence of phase distribution in the object's space on the quality of the images reconstructed from computer-generated Fresnel holograms has been studied. The main features of image formation were considered and the factors affecting their resolution and depth of field were identified. It was established that modifications of the structure of the digital hologram, inaccessible to holograms recorded by traditional methods, could significantly improve the image quality. In particular, the use of phase correction of the proximity effect allows to resolve features being as close as one pixel to each other. Installation of the second object plane in addition to the original one made it possible to increase the depth of field up to 1.5 – 2.0 times depending on the distance between planes.

The results obtained can be used for recording and reconstruction of holograms in real physical space.

### REFERENCES

1. Cube F., Gray S., Struchen D., et al., Holographic microlithography, *Optical Engineering*. 34 (9) (1995) 2724 – 2730.
2. Maiden A., McWilliam R., Purvis A., et al., Nonplanar photolithography with computer-generated holograms, *Optics Letters*. 30 (11) (2005) 1300 – 1302.
3. Bay C., Hübner N., Freeman J., Wilkinson T., Maskless photolithography via holographic optical projection, *Optics Letters*. 35 (13) (2010) 2230–2232.
4. Koreshev S.N., Nikanorov O.V., Gromov A.D., Method of synthesizing hologram projectors based on breaking down the structure of an object into typical elements, and a software package for implementing it, *Journal of Optical Technology*. 79 (12) (2012) 769–774.
5. Koreshev S.N., Nikanorov O.V., Smorodinov D.S., Gromov A.D., How the method of representing an object affects the imaging properties of synthesized holograms, *Journal of Optical Technology*. 82 (4) (2015) 246–251.
6. Koreshev S.N., Smorodinov D.S., Nikanorov O.V., Influence of the discreteness of synthetic and digital holograms on their imaging properties, *Computer Optics*. 40 (6) (2016) 793–801.
7. Collier R.J., Burckhardt C.B., Lin L.H., *Optical holography*, Academic Press, New York – London, 1971.
8. Levenson M.D., Johnson K.M., Hanchett V.C., Chiang K., Projection photolithography by wave-front conjugation, *Journal of the Optical Society of America*. 71 (6) (1981) 737–743.
9. Martinez-Leon L., Clemente P., Mori Y., et al., Single-pixel digital holography with phase-encoded illumination, *Optics Express*. 25 (5) (2017) 4975–4984.
10. Zhang Y., Lu Q., Ge B., Elimination of zero-order diffraction in digital off-axis holography, *Optics communications*. 240 (4–6) (2004) 261–267.
11. Koreshev S.N., Nikanorov O.V., Smorodinov D.S., Imaging properties of discrete holograms. I. How the discreteness of a hologram affects image reconstruction, *Journal of Optical Technology*. 81 (3) (2014) 123–127.
12. Moreau W.M., *Semiconductor lithography. Principles, practices, and materials*, Plenum Press, New York, 1988.
13. Johnson S., *Stephen Johnson on digital photography*, O'Reilly Media Incorp., USA, Sebastopol, 2006.
14. Tsukanova G.I., Karpova G.V., Bagdasarova O.V., et al., *Prikladnaya optika, Chast 2 [Applied optics, part 2]*, Saint Petersburg State University of Information Technologies, Mechanics and Optics, Saint Petersburg, 2003 (in Russian).
15. Castro A., Ojeda-Castaceda J., Asymmetric phase masks for extended depth of field, *Applied*

Optics. 43 (17) (2004) 3474–3479.

16. **Shain W.J., Vickers N.A., Goldberg B.B., et al.**, Extended depth-of-field microscopy with a highspeed deformable mirror, *Optics Letters*. 42 (5) (2017) 995–998.

17. **Basov I.V., Krasnobaev A.A.**, Methods of increasing the depth of field of optical-digital image recorders, *Preprints of Keldysh Institute of*

*Applied Mathematics*, Moscow, 2010, No. 37 (in Russian).

18. **Koreshev S.N., Smorodinov D.S., Nikanorov O.V., Frolova M.A.**, Distribution of the complex amplitude and intensity in a 3D scattering pattern formed by the optical system for an on-axis point object, *Computer Optics*. 2018, 42 (3) (2018) 377–384.

*Received 12.02.2020, accepted 19.05.2020.*

## THE AUTHORS

**KORESHEV Sergey N.**

*St. Petersburg National Research University of Information Technologies, Mechanics and Optics*  
49 Kronverkskiy Ave., St. Petersburg, 197101, Russian Federation  
koreshev@list.ru

**SMORODINOV Denis S.**

*St. Petersburg National Research University of Information Technologies, Mechanics and Optics*  
49 Kronverkskiy Ave., St. Petersburg, 197101, Russian Federation  
smorodinov.denis@gmail.com

**FROLOVA MARINA A.**

*St. Petersburg National Research University of Information Technologies, Mechanics and Optics*  
49 Kronverkskiy Ave., St. Petersburg, 197101, Russian Federation  
marrain6@yandex.ru

**STAROVOITOV Sergei O.**

*St. Petersburg National Research University of Information Technologies, Mechanics and Optics*  
49 Kronverkskiy Ave., St. Petersburg, 197101, Russian Federation  
s.starovoitov95@gmail.com

## СПИСОК ЛИТЕРАТУРЫ

1. **Cube F., Gray S., Struchen D., Tisserand J., Malfroy S., Darbellay Y.** Holographic microlithography // *Optical Engineering*. 1995. Vol. 34. No. 9. Pp. 2724–2730.

2. **Maiden A, McWilliam R, Purvis A, Johnson S., Williams G.L., Seed N.L., Ivey P.A.** Nonplanar photolithography with computer-generated holograms // *Optics Letters*. 2005. Vol. 30. No. 11. Pp. 1300–1302.

3. **Bay C, Hübner N., Freeman J., Wilkinson T.** Maskless photolithography via holographic optical projection // *Optics Letters*. 2010. Vol. 35. No. 13. Pp. 2230–2232.

4. **Корешев С.Н., Никаноров О.В., Громов А.Д.** Метод синтеза голограмм-проекторов, основанный на разбиении структуры объекта на типовые элементы, и программный комплекс для его реализации // *Оптический журнал*. 2012. Т. 79. № 12. С. 30–37.

5. **Корешев С.Н., Смородинов Д.С., Никаноров О.В., Громов А.Д.** Влияние

способа представления объекта на изображающие свойства синтезированных голограмм // *Оптический журнал*. 2015. Т. 82. № 4. С. 66–73.

6. **Корешев С.Н., Смородинов Д.С., Никаноров О.В.** Влияние дискретности синтезированных и цифровых голограмм на их изображающие свойства // *Компьютерная оптика*. 2016. Т. 40. № 6. С. 793–801.

7. **Collier R.J., Burckhardt C.B., Lin L.H.** *Optical holography*. New York – London: Academic Press, 1971.

8. **Levenson M.D., Johnson K.M., Hanchett V.C., Chiang K.** Projection photolithography by wave-front conjugation // *Journal of the Optical Society of America*. 1981. Vol. 71. No. 6. Pp. 737–743.

9. **Martinez-Leon L., Clemente P., Mori Y., Climent V., Lancis J., Tajahuerce E.** Single-pixel digital holography with phase-encoded illumination // *Optics Express*. 2017. Vol. 25. No. 5. Pp. 4975–4984.





10. Zhang Y., Lu Q., Ge B. Elimination of zero-order diffraction in digital off-axis holography // Optics communications. 2004. Vol. 240. No. 4–6. Pp. 261–267.
11. Корешев С.Н., Никаноров О.В., Смородинов Д.С. Изображающие свойства дискретных голограмм. I. Влияние дискретности голограмм на восстановленное изображение // Оптический журнал. 2014. Т. 81. № 3. С. 14–19.
12. Moreau W.M. Semiconductor lithography. Principles, practices, and materials. New York: Plenum Press, 1988. 919 p.
13. Johnson S. Stephen Johnson on digital photography. USA, Sebastopol: O'Reilly Media Incorp., 2006. 305 p.
14. Цуканова Г.И., Карпова Г.В., Багдасарова О.В. Прикладная оптика. Ч. 2. СПб.: Университет ИТМО, 2014. 83 с.
15. Castro A., Ojeda-Castaceda J. Asymmetric phase masks for extended depth of field // Applied Optics. 2004. Vol. 43. No. 17. Pp. 3474–3479.
16. Shain W.J., Vickers N.A., Goldberg B.B., Bifano T., Mertz J. Extended depth-of-field microscopy with a highspeed deformable mirror // Optics Letters. 2017. Vol. 42. No. 5. Pp. 995–998.
17. Басов И.В., Краснобаев А.А. Методы увеличения глубины резкости оптико-цифровых регистраторов изображения. *Препринты ИПМ им. М.В. Келдыша*. М., 2010. Вып. 37. 32 с.
18. Корешев С.Н., Смородинов Д.С., Никаноров О.В., Фролова М.А. Распределение комплексной амплитуды и интенсивности в трехмерной фигуре рассеяния, формируемой оптической системой при осевом расположении точечного объекта // Компьютерная оптика. 2018. Т. 42. № 3. С. 377–384.

*Статья поступила в редакцию 12.02.2020, принята к публикации 19.05.2020.*

## СВЕДЕНИЯ ОБ АВТОРАХ

**КОРЕШЕВ** Сергей Николаевич — доктор технических наук, профессор кафедры прикладной и компьютерной оптики Санкт-Петербургского университета информационных технологий, механики и оптики, Санкт-Петербург, Российская Федерация.

197101, Российская Федерация, г. Санкт-Петербург, Кронверкский пр., 49.  
koreshev@list.ru

**СМОРОДИНОВ** Денис Сергеевич — кандидат технических наук, инженер кафедры прикладной и компьютерной оптики Санкт-Петербургского университета информационных технологий, механики и оптики, Санкт-Петербург, Российская Федерация.

197101, Российская Федерация, г. Санкт-Петербург, Кронверкский пр., 49.  
smorodinov.denis@gmail.com

**ФРОЛОВА** Марина Алексеевна — аспирантка кафедры прикладной и компьютерной оптики Санкт-Петербургского университета информационных технологий, механики и оптики, Санкт-Петербург, Российская Федерация.

197101, Российская Федерация, г. Санкт-Петербург, Кронверкский пр., 49.  
marrain6@yandex.ru

**СТАРОВОЙТОВ** Сергей Олегович — аспирант кафедры прикладной и компьютерной оптики Санкт-Петербургского университета информационных технологий, механики и оптики, Санкт-Петербург, Российская Федерация.

197101, Российская Федерация, г. Санкт-Петербург, Кронверкский пр., 49.  
s.starovoitov95@gmail.com

DOI: 10.18721/JPM.13210  
УДК 535.3, 535-15, 535.417

## THE FIBER-OPTIC INTERFEROMETRIC SCHEMES WITH MULTIPLEXED SENSITIVE ELEMENTS: AN ANALYSIS OF OUTPUT OPTICAL POWER LEVEL

*A.O. Kostromitin<sup>1,2</sup>, L.B. Liokumovich<sup>2</sup>, P.V. Skliarov<sup>1,2</sup>, O.I. Kotov<sup>2</sup>*

<sup>1</sup> Concern CSRI "Elektropribor", St. Petersburg, Russian Federation;

<sup>2</sup> Peter the Great St. Petersburg Polytechnic University, St. Petersburg, Russian Federation

A concept for calculation of element parameters and analyzing the output power in the fiber-optic interferometric schemes with time-division multiplexing of the sensitive elements (TDM) has been put forward in the paper. The calculation procedure of element parameters allows ensuring the equality of the optical power from all multiplexed sensitive elements, as well as evaluating the effect of deviation of the optical scheme parameters from the calculated ones. Using two optical schemes as an example, the implementation of this calculation concept, the sequence of obtaining mathematical expressions, and examples of calculation results were presented. The proposed calculation method could be successfully applied in the design of interferometric meters with multiplexing of fiber-optic sensitive elements.

**Keywords:** fiber-optic sensor, fiber-optic splitter, optical power, optical loss, time-division multiplexing

**Citation:** Kostromitin A.O., Liokumovich L.B., Skliarov P.V., Kotov O.I., The fiber-optic interferometric schemes with multiplexed sensitive elements: an analysis of output optical power level, St. Petersburg Polytechnical State University Journal. Physics and Mathematics. 13 (2) (2020) 108–120. DOI: 10.18721/JPM.13210

This is an open access article under the CC BY-NC 4.0 license (<https://creativecommons.org/licenses/by-nc/4.0/>)

## АНАЛИЗ ВЫХОДНОЙ МОЩНОСТИ ОПТОВОЛОКОННЫХ ИНТЕРФЕРОМЕТРИЧЕСКИХ СХЕМ С МУЛЬТИПЛЕКСИРОВАННЫМИ ЧУВСТВИТЕЛЬНЫМИ ЭЛЕМЕНТАМИ

*А.О. Костромитин<sup>1,2</sup>, Л.Б. Ликумович<sup>2</sup>, Ф.В. Скляров<sup>1,2</sup>, О.И. Котов<sup>2</sup>*

<sup>1</sup> АО «Концерн «ЦНИИ "Электрон"», Санкт-Петербург, Российская Федерация;

<sup>2</sup> Санкт-Петербургский политехнический университет Петра Великого,  
Санкт-Петербург, Российская Федерация

В статье предложена идеология расчета параметров элементов и анализа выходной мощности в волоконно-оптических интерферометрических схемах с мультиплексированием чувствительных элементов по времени (TDM). Метод расчета параметров элементов позволяет обеспечивать равенство оптической мощности от всех мультиплексированных чувствительных элементов, а также оценивать влияние отклонения параметров оптической схемы от расчетных. На примере двух оптических схем показана реализация такой идеологии расчета, последовательность получения математических выражений и примеры расчетных результатов. Описанный метод расчета предлагается применять при проектировании интерферометрических измерителей с мультиплексированием волоконно-оптических чувствительных элементов.



**Ключевые слова:** волоконно-оптический датчик, волоконно-оптический разветвитель, оптическая мощность, потери оптической мощности

**Ссылка при цитировании:** Костромитин А.О., Лиокумович Л.Б., Скляр Ф.В., Котов О.И. Анализ выходной мощности оптоволоконных интерферометрических схем с мультиплексированными чувствительными элементами // Научно-технические ведомости СПбГПУ. Физико-математические науки. 2020. Т 2. № 13. С. 108–120. DOI: 10.18721/JPM.13210

Статья открытого доступа, распространяемая по лицензии CC BY-NC 4.0 (<https://creativecommons.org/licenses/by-nc/4.0/>)

## Introduction

Major advances are currently made in developing fiber-optic interferometric sensors and introducing them to measure different physical quantities [1]. Multiplexing a large number of fiber-optic sensitive elements (SE) in a single fiber-optic cable allows to create efficient quasi-distributed interferometric measuring systems, including long-distance ones. These technologies hold potential, for example, for constructing towed hydrophone arrays for seismic surveys of mineral resources in the shelf [2, 3], as well as many other similar systems.

There are several approaches to multiplexing in fiber-optic interferometric measuring devices separating signals from different SE: time-division multiplexing (TDM), frequency-division multiplexing (FDM), wavelength-division multiplexing (WDM), code-division multiplexing (CDM) or polarization-division multiplexing (PDM) [4]. The TDM technology, providing the maximum number of multiplexed elements using a single laser and photoreceiver, is the most widespread approach [5]. A TDM/WDM combination is often proposed, even though the TDM remains the primary technology in this case, while WDM technologies are used for secondary multiplexing of SE arrays separated in time, which allows reducing the number of fiber cables used [6].

An important issue related to installing fiber-optic systems with TDM is selecting reasonable parameters for the optical scheme elements providing multiplexing, estimating and optimizing the key parameters values of interference signals, such as relative level of interference signals and its difference for different SE, signal-to-noise ratio, contrast, etc.

However, studies considering fiber-optic multiplexing schemes for interferometric measuring devices practically never provide clear accounts of the procedures for calculating and estimating the parameters of such schemes in terms of methods for reasonably choosing optimal beam-splitting elements. While expressions

for such calculations are occasionally presented [7, 8], they are usually obtained with many simplifications. It is often proposed to neglect the losses of optical power in the elements, or to approximate a large number of multiplexed SE [8], although systems with 4, 8 and 16 elements in one fiber-optic cable are often used in practice [9, 10].

Most studies give estimates for phase resolution depending on the number of sensitive elements  $N$ , i.e., the calculations rely on certain methods of auxiliary modulation and processing of interference signal [8, 9].

This paper presents a procedure for energy calculation of the parameters of the fiber-optic part, independent of the operating principles, considering two standard fiber-optic interferometric schemes with SE multiplexing. Formulated in this manner, the procedure can be applied for schemes with different types of auxiliary signal modulation and processing. The proposed approaches to calculations allow to take into account the influence of deviations from parameter values of passive fiber-optic elements on parameter values of interference signals formed in schemes from multiplexed SE.

## Problem statement

Time-division multiplexing implies that short optical pulses with high duty cycle and optical power  $P_{in}$  are fed from a laser source to the input of an optical scheme with an array of  $N$  sensitive elements. The fiber optic scheme contains beam-splitting elements (splitters or semi-transparent reflectors) and should be constructed so that every input pulse passes through different paths and different combinations of SE, forming a sequence of  $N+1$  output pulses with the power  $p_n$  ( $n$  is the number of an output pulse changing from 0 to  $N$ ), delayed in time relative to each other. Most of the practical schemes (including those considered below) are organized so that every subsequent output pulse passes through one more SE than the previous one. The difference in the delay between the output pulses relative to each

other is due to the difference in optical paths  $\Delta L$  which the input pulse passes to form output pulses. These differences must be identical. The so-called compensated interferometer (CI) with the optical path difference also equal to  $\Delta L$  is used to generate interferometric signal. When output pulses pass through the CI, they are split and combined in pairs with a shift by one pulse. As a result, a new sequence of  $N+2$  pulses with the powers  $P_m$  (it is convenient to number them from 0 to  $N+1$ ), where each initial output impulse is combined with the previous one, is generated at the CI output and is subsequently transmitted to the photodetector. Each pulse  $P_m$  is a result of interference of the pulses  $p_n$  and  $p_{n-1}$ . The only exceptions are the first and the last pulses,  $P_{0n}$  and  $P_{r(N+1)}$ , which are not combined with the previous and the subsequent pulse while passing through the CI due to lack thereof. Impacts on the  $n^{\text{th}}$  fiber SE change the phase delay  $\Delta\phi_n$  of light emission passing through this SE. For this reason, the interference of the pulses  $p_n$  and  $p_{n-1}$  is related to  $\Delta\phi_n$ , as the pulse  $p_{n-1}$  passed through SE from the first to the  $(n-1)^{\text{th}}$ , and pulse  $p_n$  passed through the SE from the first to the  $n^{\text{th}}$ . Given that  $P_m$  is defined by the interference of two output pulses, they have the form

$$P_{rn}(t) = C\{P_{0n} + P_{mn} \cdot \cos[\Delta\phi_n(t)]\}, \quad (1)$$

where  $P_{0n} = p_n + p_{n-1}$  is the constant component;  $P_{mn} = 2(p_n p_{n-1})^{1/2}$  is the amplitude of the interference component.

The argument of the interference signal  $\Delta\phi_n$  contains target oscillations of the phase delay of the  $n^{\text{th}}$  SE, related to measured impacts, and can be determined during subsequent processing. The coefficient  $C$  is related to losses during passage through the CI, and ideally,  $C = 1/2$ . Notably, CI can be located at the input of a fiber optic scheme as well. In this case, the details differ for the pulses passing through the scheme, but interference signals taking the form (1) are also generated as a result.

Comprehensive analysis of fiber-optic interferometric schemes with SE multiplexing should consider different systems of relations including different types of parameters for the optic scheme elements, characteristics of other elements of the system and interrogation pulses. In terms of energy relations, one of the key problems is selecting the elements that provide optimal parameter values of interference signals  $P_{0n}$  and  $P_{mn}$ . The set of values of  $P_{0n}$  and  $P_{mn}$  plays an essential role in organizing correct

signal recording, estimating the signal-to-noise ratio achieved, and, consequently, resolution of a system.

An important result of energy calculation from the standpoint of scheme design is finding the required ratios for light beam splitting in the splitting elements of a fiber-optic scheme. Depending on the elements used in the scheme, these parameters include the splitting ratios of fiber-optic splitters or the reflection coefficients of semi-transparent reflectors.

If identical splitting elements are used, inevitably, the values of  $p_n$  and  $P_m$  greatly depend on  $n$ , and the problem of choosing optimal splitting ratios necessitates complex analysis of the criteria of optimality. A more attractive option in terms of the achieved effect and, at the same time, a simpler one in terms of the criteria of optimality entails choosing the splitting elements provided that all  $p_n$  are equal:

$$p_0 = p_1 = \dots = p_n = \dots = p_N = P_0. \quad (2)$$

In this case,  $P_{0n} = P_{mn} = 2P_0$ , the contrast of all interference signals equals unity (if polarization matching is ensured).

The scheme constructed in this study satisfies this condition specifically. At the same time, the normalized power level of pulses serves as an important indicator:

$$p_{norm} = P_0/P_{in}; \quad (3)$$

this indicator makes it convenient to compare the “energy efficiency” achieved in different schemes and at different values of  $N$ .

Generally, if condition (2) is fulfilled, it is evident that the higher the value of  $p_{norm}$ , the less influence different noises and fluctuations have on the output signals of a measuring device.

Clearly, a special set of splitting ratios for splitters or reflectors has to be used to satisfy condition (2), but since modern technologies allow to produce these elements with virtually arbitrary parameters, this approach to constructing optimal schemes based on criterion (2) can be put into practice. However, it is essential for designing such schemes that not only the optimal splitting ratios of the elements are found but various additional aspects can be analyzed in detail, including the influence of other parameters of splitting elements, their fluctuations and other factors on the parameters of interference signals, all of which must be taken into account at the stage of design.





### General principles of the calculation procedure

Considering the calculation procedure, let us review different groups of parameters characterizing the scheme elements, which are used in analysis and calculations. First of all, these are transmittances (with respect to power) in fiber sections connecting the scheme elements including those in SE. These transmittances differ from unity due to optical power losses in the fiber-optic cable and additional conditions (fiber sections can be wound into a coil, contain connections, etc.). The transmittances defined initially are assumed to be given and are not supposed to be found in the calculations. The transmittances can actually be either identical or different for different SE but are regarded as known parameters.

Another type of parameters are the splitting ratios of optical power in splitters and semi-transparent reflectors (typically fiber Bragg gratings) if the schemes use the first or the second type of elements as optical power splitters. Optimal splitting ratios should be selected on the calculation procedure that satisfies condition (2).

We should note that splitters or fiber-optic Bragg gratings also incur internal losses which, strictly speaking, should be also taken into account in the calculations. In general, the losses of splitting elements may depend on splitting ratios and transmission coefficients. This can be included in the calculations if the dependence is known. To represent the specific results obtained in a clear and simple manner, the analysis below includes a case when these losses have fixed values, and are regarded as a known parameter.

Calculating optimal splitting ratios of splitters or reflectors, it is of course possible and feasible to take into account only regular components of transmittances in the fiber sections known in advance and losses in the splitting elements. However, the calculation procedure as a whole should provide a possibility to analyze the influence of potential deviations of the calculated and initially given parameters of the elements from the actual ones. These phenomena can be caused by both regular deviations from reference values and by fluctuations of parameters during operation. The changes may occur, for example, due to aging, unstable temperature and polarization of optical emission.

The procedure for energy calculation and analysis of fiber optic elements of the scheme involves obtaining and applying two systems of relations:

*firstly*, the equations of multiplicative structure for calculating the values of  $p_n$  taking into account all key parameters characterizing the elements of the fiber optical scheme;

*secondly*, recurrence relations connecting the selected parameters of splitting elements of adjacent links in the scheme and allowing to calculate the splitting ratios of all splitting elements taking into account certain conditions for boundary elements.

The first system of relations is formulated by considering a light pulse related to the  $n^{\text{th}}$  splitting element passing from the input to the output.

The second system of relations requires considering the condition for power balance  $p_{n-1} = p_n = P_0$  and solving the balance equation with respect to the splitting element parameter.

Regarding the choice of schemes discuss further in this paper, we should note that different types of optical schemes with TDM can be divided into two types: reflective schemes or passage schemes.

In case of the reflective scheme, a scanning pulse passes through the scheme from the first to the  $n^{\text{th}}$  SE, then travels in the opposite direction and is fed as an  $n^{\text{th}}$  output pulse into the same part of the scheme (or directly to the same fiber-optic line) as the input pulse, but in the reverse direction. In this case, the scheme requires mirrors (the so-called Faraday mirrors are often used to suppress polarization fading).

In case of the passage scheme, an input pulse is fed from one end of the scheme and then, passing from the first to the  $n^{\text{th}}$  SE, forms an  $n^{\text{th}}$  output pulse at the opposite end of the scheme. It is typically assumed for the schemes considered below that the decrease of  $p_{\text{norm}}$  with the growth in  $N$  is described by  $\sim 1/N^2$  provided there are no losses [9].

There are different types of schemes where the decrease is described by  $1/N$ , but they may contain multiple passes through the SE and aliasing of different pulses, as well as crosstalk [8]. The schemes with crosstalk have their own peculiarities, but they are not considered in this paper.

### Analysis of the power of output pulses in a reflective-type scheme

Let us consider a standard scheme of the reflective type (Fig. 1). The scheme includes  $N$  coils of sensitive elements (SE) numbered  $n = 1, 2, \dots, N$ , as well as  $(N+1)$  Ysplitters (Y) and mirrors (M) numbered  $n = 0, 1, 2, \dots, N$ .

It seems helpful to introduce the direct ( $K_d$ ) and cross ( $K_c$ ) gains of the splitter, the gain  $K_f$  of



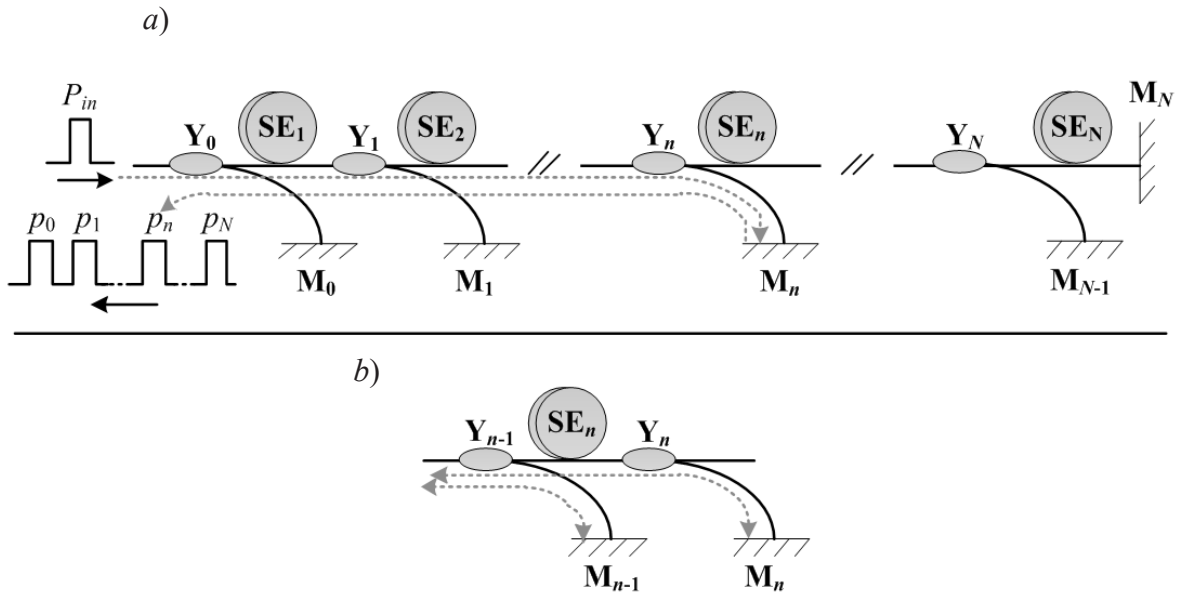


Fig. 1. Reflective scheme and generation of output pulses (a),  $n^{\text{th}}$  link of scheme (b): sensitive elements  $SE_i$ ; mirrors  $M_i$ ; splitters  $Y_i$ ; input pulse  $P_{in}$ ; output pulses  $p_i$

a fiber section with the sensitive element, gain  $K_f$  of a service fiber section between the splitter and the mirror, the reflection coefficient  $R$  (ideally,  $R = 1$ , however, the actual reflection coefficient may be less than unity) as the key parameters of the scheme. If the scheme contains connections, the losses in them should be taken into account in the fiber section gains  $K_{sf}$  and  $K_r$ . The gains  $K_d$  and  $K_c$  are rigidly bound to the splitting ratio  $D$  and the parameter of internal losses of the splitter  $\alpha$ , as described in Appendix 1.

Considering the path of an input pulse from the  $n^{\text{th}}$  mirror and back (see Fig. 1), it is easy to formulate multiplicative equations for  $p_n$ :

$$p_n = P_n K_{fn}^2 K_{cn}^2 R_n \cdot \prod_{q=1}^n (K_{d(q-1)}^2 K_{sfq}^2). \quad (4)$$

Eq. (4) implies that if the upper limit of the product is less than its lower limit, which occurs at  $n = 0$ , then the product equals unity. Furthermore, the case when  $n = N$ , related to the difference of the final link in the scheme from others, is different because there is no need to direct the optical power further for the last  $N^{\text{th}}$  SE, and it is not practical to use a splitter between the  $N^{\text{th}}$  SE and the  $N^{\text{th}}$  mirror. However, expression (4) is relevant for all  $n$ , if the presence of formal coefficients  $K_{cN} = K_{fN} = 1$  is taken by definition. In practice, it can be often assumed that all SE are equivalent and  $K_{sf}$  does not depend on  $n$ . Then this parameter can be excluded from the product in Eq. (4) and the multiplier  $(K_{sf})^{2n}$  can be used.

Analyzing one link of the scheme and comparing the difference in the paths of the  $(n-1)^{\text{th}}$  and  $n^{\text{th}}$  pulse (see Fig. 1, b) we can obtain an equation corresponding to the balance  $p_{n-1} = p_n$ . For the given scheme (if the definition  $K_{cN} = K_{fN} = 1$  is preserved), this equation has the form

$$K_{c(n-1)}^2 K_{f(n-1)}^2 R_{n-1} = K_{d(n-1)}^2 K_{cn}^2 K_{sfn}^2 K_{fn}^2 R_{n-1}. \quad (5)$$

The recurrence relation for the parameters of the splitters is obtained by taking into account the connection between  $K_d$  and  $K_c$ . In view of the explanations in Appendix 1, we can use a model of splitter parameters that has the form

$$K_d = (1 - \alpha_{el}) \cdot D / (1 + D) \quad (6)$$

and  $K_c = (1 - \alpha_{el}) / (1 + D),$

then Eq. (6) is transformed directly transforms to the recurrence form:

$$D_{n-1} = A_n (1 + D_n), \quad (7)$$

based on the assumption that the parameter of excess splitter losses  $\alpha_{el}$  does not depend on  $D$  and is the same for any  $n$ , introducing a constant

$$A_n = K_{f(n-1)} \sqrt{R_{n-1}} \times [(1 - \alpha_{el}) K_{sfn} K_{fn} \sqrt{R_n}]^{-1}. \quad (8)$$



It is commonly acceptable for calculations of practical schemes to assume the gains  $K_{sf}$ ,  $K_f$  and the coefficient  $R$  to be identical for all  $n$ . In this case, the calculation of optimal values of  $D_n$  does not depend on the values of  $K_f$  and  $R$ , while the constant  $A_n$  does not depend on  $n$  and is simplified:

$$A = 1/[(1 - \alpha_{el})K_{sf}] \quad (9)$$

(here the calculations of the optimal values of  $D_n$  are affected by the excess losses of the splitters and the SE).

If it is acceptable to neglect the excess losses of the splitters and the SE, it can be assumed that  $\alpha_{el} = 0$ .

To use Eq. (7), we need to define the initial condition for recursive calculation of optimal values of  $D_n$ . For this scheme, this condition is a direct result of the absence of a splitter with the number  $N$ . A different connection of the last SE would definitely impair the obtained values of  $p_0$  and  $P_{norm}$ . At the same time, considering the final link which contains the last SE provides a condition of power balance (5), if  $K_{cn} = K_{sfN} = 1$  is substituted in the right-hand side. Then, taking into account Eqs. (6) for the  $(N-1)^{th}$  splitter leads to a simple relation:

$$D_{(N-1)} = \frac{K_{f(N-1)}}{K_{sfN}} \sqrt{\frac{R_{N-1}}{R_N}}, \quad (10)$$

which corresponds to the recurrent expression (7), excluding the parameters  $K_{cn}$ ,  $K_{fn}$  and  $\alpha_{el}$  from Eq. (8) for determining the constant  $A_n$ .

Evidently, expression (10) gives  $D_{N-1} \cdot 1$  for small losses in the elements, when the gains

$K_{f(n-1)}$  and  $K_{sfN}$  and the coefficients  $R_{N-1}$  and  $R_N$  approach unity, which is a logical result for the balance of such a link with splitting close to a 50:50 splitter, regardless of the losses in the splitter.

Furthermore, recurrent expression (7) can be used to successively obtain values for the rest of the splitters numbered from  $n = N - 2$  to  $n = 0$ , forming a set of values  $\{D\}$ , and then recalculating the values of  $\{D\}$  into sets of values  $\{K_d\}$  and  $\{K_c\}$  for all splitters based on Eq. (6) and a given  $\alpha_{el}$ .

Substituting sets of values  $\{K_d\}$  and  $\{K_c\}$  in expressions (4), we obtain the same value of  $p_0$  because of the method by which these sets of values were obtained; moreover, this value of  $p_0$  is the largest possible for any  $n$  with the given parameters used in the calculation.

However, an important result of the calculation is the actual value for the level of  $p_{norm}$ , as well a possibility to analyze its dependence on  $N$  and other parameters used in the calculation.

The calculated sets of values  $\{D\}$ ,  $\{K_d\}$ ,  $\{K_c\}$  for the splitters are given in Appendix 2 for  $N = 8$  and

$$\alpha_{el[dB]} = \alpha_{sf[dB]} = 0.10 \text{ dB},$$

$$\alpha_{f[dB]} = 0.05 \text{ dB and } R = 0.99,$$

where it is taken that

$$\alpha_{sf[dB]} = -10\lg(K_{sf}),$$

$$\alpha_{f[dB]} = -10\lg(K_f),$$

$$\alpha_{el[dB]} = -10\lg(1 - \alpha_{el}).$$

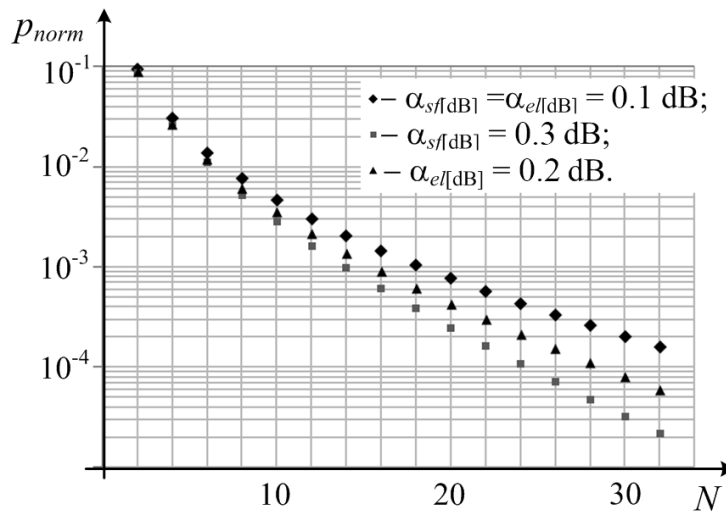


Fig. 2. Example of reflective-type scheme. Normalized power level of pulses depending on the number of sensitive elements (SE) for different values of losses  $\alpha_{sf}$  and  $\alpha_{el}$

These values of the splitting ratios are important for practical implementation of this scheme, as they have to be known in order to install the appropriate splitters. However, the examples shown in Fig. 2 for  $p_{norm}$  depending on  $N$  for the same set of parameters, as well as for cases when either of the parameters  $\alpha_{sf}$  or  $\alpha_{el}$  have different values are more important for analysis of energy efficiency of the scheme.

An example of the dependences in Fig. 2 shows the achieved levels of relative power for the schemes with the given parameters and with optimal splitting ratios chosen for the splitters, the exponential form of the dependences  $p_{norm}(N)$ , indicating that it is possible to study the influence of other parameters of the scheme elements on the achieved level of  $p_{norm}$ .

Importantly, the given systems of expressions allow not only to analyze the influence of scheme element parameters on the achievable level of  $p_{norm}$ , but also take into account and study the influence of deviations of actual parameters from ideal ones for the values of  $p_n$ . If the ratios  $D$  are given as  $(1-d)/d$  with the accuracy in selecting  $d$  ranging, for example, to 1 or 2% in production of real splitters, the set of optimal values  $\{D\}$  value set obtained by a recurrent procedure can then be rounded up. Next, we can substitute the rounded values in expressions (4) and, calculating  $p_{0n}$ , estimate their variance and deviation from the calculations without the round-off.

Similarly, we can take into account the influence of both fixed and random deviations of element parameters from the initially calculated ones.

The first case concerns precision measurements of the parameters of an actual set of splitters produced for the scheme, which are then used in calculations.

The second case implies that the element parameters may fluctuate during operation. Then, after the initial calculations of optimal sets  $\{D\}$  for the splitters using regular parts of  $\alpha_{el}$ ,  $K_p$ ,  $K_{sf}$  and  $R$ , the parameters containing, aside from the regular component, random additions are substituted in Eq. (4) at the second stage of the calculations. Then the calculations will give a set of values of  $p_n$  with random deviations with respect to the estimate obtained for  $p_0$  in the calculations with regular parameters.

Those are important aspects of the proposed calculation procedure, although considering specific examples is outside the scope of this study.

### Analysis of the power of output pulses in a passage-type scheme

Let us consider a standard scheme of the passage type (Fig. 3). The scheme includes pairs of Y-splitters in the “upper” and the “lower” lines. The sequence of output pulses is formed by means of the  $n^{\text{th}}$  pulse passing a part of the path through the “upper” line, splitting into the lower part through the  $n^{\text{th}}$  couple of splitters and then propagating towards the output through the “lower” line. We can confirm that both of the  $n^{\text{th}}$  splitters must have the same splitting ratios within the scope of the given problem. The situations differ for  $n = 0$  and  $n = N$ , when a pulse passes to the “lower” line only through the zero or only through the  $N^{\text{th}}$  splitter which have no pair.

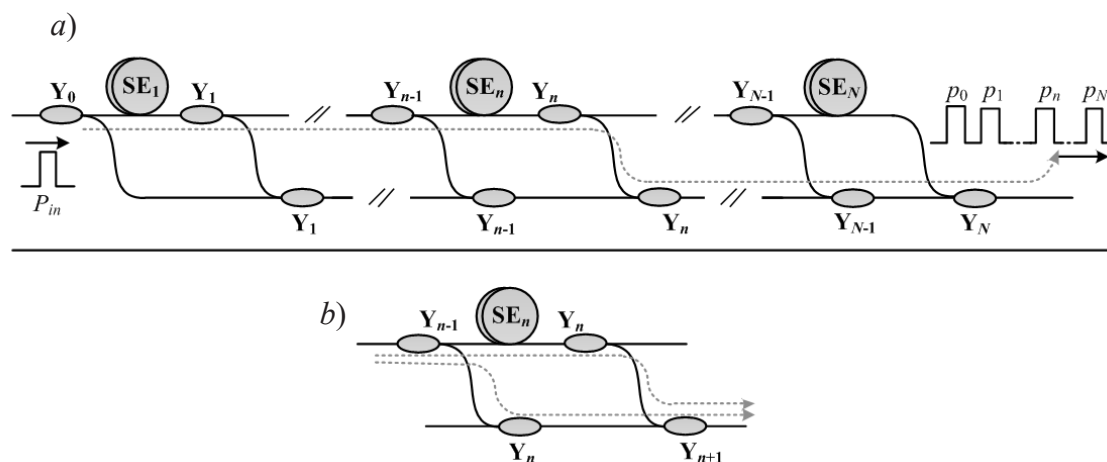


Fig. 3. Passage-type scheme and generation of output pulses (a),  $n^{\text{th}}$  link in given scheme (b); the notations are the same as in Fig. 1



We also need to take into account the transmittance of fiber sections:  $K_{sf_n}$  for a fiber section with the  $n^{\text{th}}$  sensitive element;  $K_{fn}$  for service fiber sections connecting the  $(n-1)^{\text{th}}$  and the  $n^{\text{th}}$  splitters in the “lower” line;  $K'$  for “vertical” sections between a pair of the  $n^{\text{th}}$  splitters. The difference in optical paths  $DL$  is formed by the difference in the lengths of fiber sections between adjacent splitters in the “upper” and in the “lower” lines (the fiber in the SE is typically larger than the service section of the “lower” line). The scheme could be constructed symmetrically, with the SE located in the “lower” line but the principles of operation and calculation would remain the same.

Considering the path travelled in the scheme by the  $n^{\text{th}}$  pulse, it is easy to compose multiplicative equations to find  $p_n$ . As the structures of the first and the last links differ from the structure of the central links, the expressions are different for  $n=0$  and  $n=N$ :

$$\begin{aligned} p_0 &= P_{in} K_{f0} K_{c0} K_{d1} \cdot \prod_{q=1}^N K_{dq} K_{fq} \\ &\text{for } n = 0; \\ p_n &= P_{in} K_{fq} K_{cn}^2 \cdot \prod_{q=1}^n K_{d(q-1)} K_{sfq} \cdot \prod_{q=n+1}^N K_{dq} K_{fq} \\ &\text{for } n = 1, \dots, (N-1); \\ p_N &= P_{in} K_{cN} \cdot \prod_{q=1}^N K_{d(q-1)} K_{sfq} \\ &\text{for } n = N. \end{aligned} \quad (11)$$

Equations for the power balance of adjacent pulses for the first and the last links also differ from the equation for the central links and, as follows from the difference in the paths of the  $(n-1)^{\text{th}}$  and the  $n^{\text{th}}$  output pulses (Fig. 3,b), take the following forms for these three case

$$\begin{aligned} K_{c0} K_{d1} K_{f1} &= K_{d0} K_{c1}^2 K_{sf1} K'_{f1} \\ &\text{for } n = 1; \\ K_{c(n-1)}^2 K_{dn} K'_{f(n-1)} K_{fn} &= K_{d(n-1)} K_{cn}^2 K_{sf1} K'_{fn} \\ &\text{for } n = 2, \dots, (N-1); \\ K_{c(N-1)}^2 K_{dN} K'_{f(N-1)} K_{f(N-1)} &= K_{cN} K_{d(N-1)} K_{sfN} \\ &\text{for } n = N; \end{aligned} \quad (12)$$

where  $n$  corresponds to the link covering the  $n^{\text{th}}$  SE.

Notably, Eqs. (11) imply equal ratios for the  $n^{\text{th}}$  splitter in the “upper” and the “lower” lines.

Based on Eq. (12), we can obtain recurrence relations connecting the splitter parameters. In view of model (6), we can obtain an equation for the first link (for  $n=0$ ) from Eq. (12), which has the following form:

$$D_1^2 + D_1 - A_0 D_0 = 0, \quad (13)$$

where we introduce a constant

$$A_0 = (1 - \alpha_{el}) K_{sf1} K'_{f1} / K_{f0}. \quad (14)$$

The solution to this quadratic equation (only one of the two roots is positive and acceptable) has the form

$$D_1 = 0.5 [(4D_0 A_0 + 1)^{1/2} - 1]. \quad (15)$$

Using model (6) and Eq. (12), we obtain a relation for the subsequent links (except the last one):

$$D_n^2 + D_n - A_n [(D_{n-1})^2 + D_{n-1}] = 0, \quad (16)$$

introducing a constant

$$A_n = K_{sf1} K'_{fn} / (K'_{f(n-1)} K_{fn}). \quad (17)$$

The solution to this equation provides a recurrence relation taking the form

$$\begin{aligned} D_n &= 0.5 \{ [4((D_{n-1})^2 + \\ &+ D_{n-1}) A_n + 1]^{1/2} - 1 \}. \end{aligned} \quad (18)$$

And, finally, the equation for the last link ( $n = N$ ) follows from model (6) and Eq. (12):

$$(D_{N-1})^2 + D_{N-1} = A_N D_N, \quad (19)$$

introducing a constant

$$A_N = (1 - \alpha_{el}) K_{f(N-1)} K'_{f(N-1)} / K_{sfN}. \quad (20)$$

In this case, we need to determine  $D_N$ , so the solution takes the form

$$D_N = [(D_{N-1})^2 + D_{N-1}] / A_N. \quad (21)$$

We should note that we formulated the expressions for the passage scheme assuming that  $N > 2$ . The case  $N = 2$  has to be considered separately to obtain the corresponding expressions but because it has little practical value, it was not included in this study.

If we give a certain value for  $D_0$ , then, based on Eqs. (15), (18), (21), we can derive the

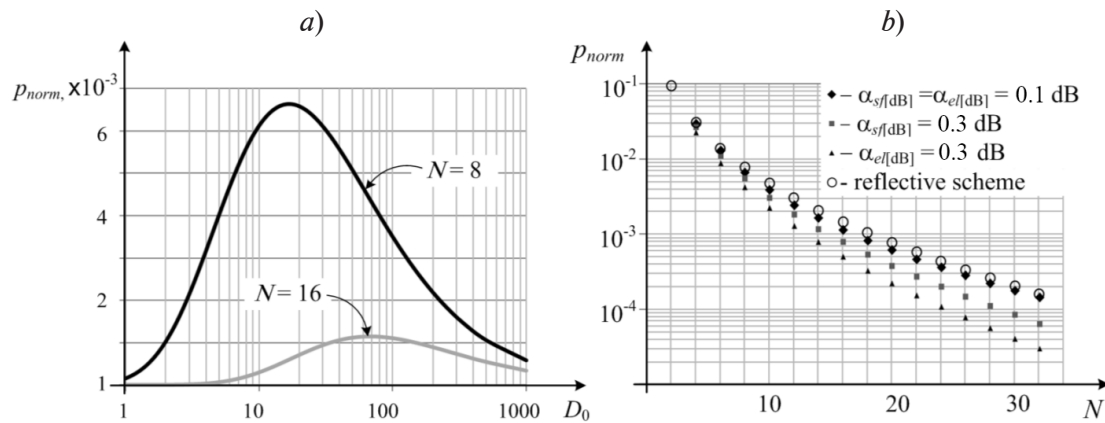


Fig. 4. Example of passage-type scheme. Calculated normalized power level of pulses  $p_{norm}$  depending on splitting ratio of first splitter for two values of  $N$  (a) and on number of sensitive elements  $N$  for two different values of losses in SE and in splitters.

Dependence of  $p_{norm}$  for the reflective scheme is shown for comparison (b)

values of  $D_n$  for all the remaining splitters, i.e., a complete set  $\{D\}$ . Clearly, if we recalculate the set  $\{D\}$  into the sets  $\{K_d\}$  and  $\{K_c\}$ , and then calculate  $p_n$  based on Eq. (10), condition (2) is satisfied, and we obtain a certain value of  $p_{norm}$ , which does not depend on  $n$ . However, this value does depend on the initial choice of  $D_0$ .

Thus, the condition for obtaining the maximum value of  $p_{norm}$  in this scheme is the choice of the optimal value of  $D_0$ . A direct and simple approach to solving this problem consists in enumerating the values of  $D_0$  and choosing an optimal value  $D_{opt}$  of such a value of  $D_0$  for which  $p_{norm}$  reaches the greatest level. Evidently, a specific value of  $D_{opt}$ , as well as maximum achieved by  $p_{norm}$ , obviously depends on  $N$  and on the values of other parameters used in the calculations.

Let us provide examples of the calculations, where, as before, we assume for simplicity that  $K_r, K'_f$  and  $K_{sf}$  do not depend on  $n$ . Fig. 4,a shows examples of dependences of  $p_{norm}$  on  $D_0$  with  $\alpha_{el}[dB] = \alpha_{sf}[dB] = 0.1$  dB and  $\alpha_{sf}[dB] = \alpha'_{sf}[dB] = 0.05$  dB for the cases when  $N = 8$  and  $N = 16$ . In the first case, it follows from the calculation that  $D_{opt} = 16.86$ , providing  $p_{norm} = 6.63 \cdot 10^{-3}$ . In the second case,  $D_{opt} = 62.67$ , providing  $p_{norm} = 1.15 \cdot 10^{-3}$ .

Calculated sets of value for  $\{D\}$ ,  $\{K_c\}$  and  $\{K_d\}$  are also given in Appendix 2 for  $N = 8$ , which can be used for practical applications of the scheme with these initial data.

From the standpoint of energy analysis, this scheme provides a good illustration of the dependences of  $p_{norm}$  on  $N$  (shown in Fig 4,b), obtained selecting  $D_0 = D_{opt}$  for each  $N$ . As before, aside from calculation of the dependences with the above parameters of losses, two additional

curves are given for the cases when the parameter  $\alpha_{fs}$  and  $\alpha_{el}$  have different values. To compare this scheme with the reflective one, Fig. 4 shows a dependence obtained earlier for the main sets of parameters.

Comparing the calculation results in Figs. 2 and 4, we can see that the levels achieved by  $p_{norm}$  with the optimal choice of the splitting ratios of the splitters are almost the same for both schemes given equal losses in the SE, with a small advantage in case of the reflective scheme (increasing with greater values of  $N$ ). This is an expected result because, despite the different configurations of the schemes, a pulse passes through an equal number of splitters forwards, the same number of branches and sections of SE in both of them.

Each link of the second scheme contains an additional connecting section but the first scheme includes losses due to reflection from the mirror (the second scheme can be improved slightly in terms of power by changing the ratio of losses in these elements).

Fig. 4,b also shows that the dependence on  $N$  has an exponential behavior of  $p_{norm}(N) \sim N^{-q}$ , and the value of  $q$  is close to 2 if the losses decrease but increases if the losses increase. For the given dependences,  $q$  has values in the range of 2.5–3.3. We should note here that approximation yields different results and better accuracy if limited ranges of  $N$  are analyzed. For example, the values of the parameter for the curves in Figs. 2 and 4 lie between 2.4 and 2.8 in the range  $4 \leq N \leq 16$ , and between 2.8 and 3.7 in the range  $10 \leq N \leq 32$ .

However, it was not our intention to carry out comprehensive studies of such patterns as





we focused instead on the procedure for correct calculation of this kind of dependences and the expressions required for this purpose. At the same time, correct calculation implies that the optimal choice of parameters is provided for the splitters.

Similarly to the reflective scheme, the principle proposed for the calculations of the passage scheme allows (except for the choice of the optimal system of splitters and estimation of the  $p_{norm}$  value) to analyze the influence of various additional factors: limitations in the accuracy with which the splitters can be made, random fluctuations of the element parameters, etc. However, we should also consider the fact that multiplicative expressions (11) restrict such analysis, assuming equal parameters in the pairs of splitters in the “upper” and the “lower” lines. Eqs. (11) are simplified because of this, and, most importantly, we can obtain a simple recursive expression (18) that is easy to interpret. To analyze the influence of the rounded splitting ratios, regular or random deviations of these ratios and similar factors, we need to use multiplicative equations of the following form:

$$\begin{aligned}
 p_0 &= P_{in} K_{f0} K_{c0} K_{d1} \cdot \prod_{q=1}^N k_{dq} K_{fq} \\
 &\text{for } n = 0; \\
 p_n &= P_{in} K'_{fq} K_{cn} k_{cn} \cdot \prod_{q=1}^n K_{d(q-1)} K_{sfq} \cdot \prod_{q=n+1}^N k_{dq} K_{fq} \\
 &\text{for } n = 1, \dots, (N-1); \\
 p_N &= P_{in} k_{cN} \cdot \prod_{q=1}^N K_{d(q-1)} K_{sfq} \\
 &\text{for } n = N,
 \end{aligned} \tag{22}$$

where the gains  $K_{dn}$ ,  $K_{cn}$  of the splitters on the “upper” line are separate from the gains  $k_{dn}$ ,  $k_{cn}$  of the splitters on the “lower” line.

### Conclusion

We have proposed a procedure for calculating the parameters of elements in optical schemes with multiplexed fiber optic sensors, allowing to optimize the scheme in terms of achieving the maximum level and contrast of the generated interference signals, taking into account the optical power losses in splitting elements as well as in fiber sections and mirrors included in the fiber optic scheme.

The procedure for obtaining expressions for calculating the element parameters is described for two optical schemes.

We have given examples of the calculations of the element parameters in the scheme under consideration for  $N = 8$  sensitive elements and the dependences of the normalized power level of an optical pulse at the output of the schemes on the number  $N$  for certain sets of element parameters.

The principles proposed for organizing the calculations allow not only to calculate the optimal splitting ratios of the scheme splitters and the power achieved by the output pulses but also to analyze the influence from varying the parameters of individual elements of the optical scheme (including random ones) on the characteristics of the system as a whole.

The calculated expressions formulated for the given schemes illustrate how similar calculations can be organized for other configurations of similar schemes.

The methods and results presented can be applied in design of fiber-optic interferometers based on multiplexing of sensitive elements.

### Appendix 1

#### Parameters of Y-splitter

A Y-splitter has three terminals and is formally described by nine power gains  $K_{ij}$ . In view of symmetry, which is easy to achieve in practice,  $K_{ij} = K_{ji}$ . Let us choose numbering so that when light is submitted to the first terminal, it is then transmitted to the second and the third terminals. Then, due to directivity,  $K_{23} = 0$ , and the coefficients of reflection from the splitter,  $K_{ii} = 0$ , are small as well (in reality these coefficients correspond to attenuations by several tens of dB). Then two coefficients are significant:  $K_{12}$  and  $K_{13}$ . Assuming  $K_{12} \geq K_{13}$  (the connection between terminals 1 and 2 is direct, and  $K_{12} = K_d$ , while terminals 1 and 3 are cross-connected, and  $K_{13} = K_c$ ), the key parameter of the splitter, its splitting ratio, is given by the relation  $D = K_{12}/K_{13}$  ( $D > 1$ ). If  $K_{23}$ ,  $K_{ii} \ll K_{13}$ , then based on the condition imposed for the power balance,  $K_{12} + K_{13} = 1$ . However, taking into account the internal (excess) losses of optical power,  $K_{12} + K_{13} = 1 - \alpha_{el}$  for an actual splitter (where  $\alpha_{el}$  is a small parameter characterizing the losses). The last equality from the definition of  $D$  gives

$$K_{12} = K_d = (1 - \alpha_{el})D/(D+1);$$

$$K_{13} = K_c = (1 - \alpha_{el})/(D+1),$$

introduced as expression (4).

Table

Calculated parameters  $\{D\}$ ,  $\{K_c\}$  and  $\{K_d\}$   
for reflective and passage schemes  
with optical power losses given in scheme elements

$n$	Reflective scheme			Passage scheme		
	$D$	$K_d$	$K_c$	$D$	$K_d$	$K_c$
0	9.848	0.887	0.09	16.857	0.923	0.055
1	8.405	0.873	0.104	3.543	0.762	0.215
2	7.026	0.855	0.122	3.520	0.761	0.216
3	5.71	0.832	0.146	3.498	0.76	0.217
4	4.453	0.798	0.179	3.475	0.759	0.218
5	3.253	0.747	0.23	3.453	0.758	0.219
6	2.106	0.663	0.315	3.43	0.757	0.221
7	1.012	0.491	0.486	3.408	0.756	0.222
8	—	—	—	15.374	0.918	0.06

Notations:  $n$  is the number of the Y-splitter.

Giving the parameters  $D$  and  $\alpha_{el}$  rather than  $K_{12}$  and  $K_{13}$  is often clearer and more wide-spread for real splitters ( $\alpha_{el[dB]} = 10 \cdot \lg(1 - \alpha_{el})$  is usually taken).

#### Appendix 2

##### Examples of calculating the parameters $\{D\}$ , $\{K_c\}$ and $\{K_d\}$

The summary Table below presents the calculation results for the splitting ratios  $D$  and gains  $K_d$ ,  $K_c$  for the schemes described in case

$N = 8$ ,  $\alpha_{el} = 0.977$ ,  $K_{sf} = 0.977$ ,  $K_f = 0.989$ , and  $R = 0.99$  for the reflective scheme and  $K'_f = 0.989$  for the passage scheme (the given ratios and gains correspond to the levels  $\alpha_{el[dB]} = \alpha_{sf[dB]} = 0.1$ ,  $\alpha_{f[dB]} = \alpha'_{f[dB]} = 0.05$ ).

While the values listed in the Table are not particularly illustrative or interesting for the considered dependences of  $p_{norm}$  on  $N$  and other parameters of similar characteristics, splitters with the calculated set of parameters  $\{K_c\}$  and  $\{K_d\}$  should be chosen for practical implementations of the optimal scheme satisfying condition (2).

## REFERENCES

1. Measures R.M., Structural monitoring with fiber optic technology, Academic Press, Cambridge, Massachusetts, USA, 2001.
2. Langhammer J., Eriksrud M., Berg C., Nakstad H., Fiber optic permanent seismic system for increased hydrocarbon recovery, In: Proceedings of the 11th International Congress of the Brazilian Geophysical Society, European Association of Geoscientists & Engineers, Salvador, Brasil, 24–28 Aug 2009, cp-195-00408.
3. Plotnikov M.Y., Lavrov V.S., Dmitraschenko P.Y., et al., Thin cable fiber-optic hydrophone array for passive acoustic surveillance applications, IEEE Sensors Journal. 19 (9) (2019) 3376–3382.
4. Kersey A.D., et al., Multiplexed interferometric fiber sensors, 7th Optical Fibre Sensors Conference, The Institution of Radio and Electronics Engineers Australia (1990) 313–319.
5. Akkaya O.C., Digonnet M.J.F., Kino G.S., Solgaard O., Time-division-multiplexed interferometric sensor arrays, Journal of Lightwave Technology. 31 (16) (2013) 2701–2708.
6. Liao Y., Austin E., Nash P.J., et al., Highly scalable amplified hybrid TDM/DWDM array architecture for interferometric fiber-optic sensor systems, Journal of Lightwave Technology. 31 (6) (2013) 882–888.
7. Kersey A.D., Dandridge A., Dorsey K.L., Transmissive serial interferometric fiber sensor



array, *Journal of Lightwave Technology*. 7 (5) (1989) 846–854.

8. **Brooks J., Moslehi B., Kim B., Shaw H.**, Time-domain addressing of remote fiber-optic interferometric sensor arrays, *Journal of Lightwave Technology*. 5 (7) (1987) 1014–1023.

9. **Lijuan Gu, Xiangge He, Duo Yi, et al.**, Common-mode noise suppression technique in

interferometric fiber-optic sensors, *Journal of Lightwave Technology*. 37 (21) (2019) 5619–5627.

10. **Yoshida M., Hirayama Y., Takahara A.**, Real-time displacement measurement system using phase-shifted optical pulse interferometry: Application to a seismic observation system, *Japanese Journal of Applied Physics*. 55 (2) (2016) 022701.

*Received 16.04.2020, accepted 25.04.2020.*

## THE AUTHORS

**KOSTROMITIN Aleksey O.**

*Concern CSRI “Elektropribor”;*

*Peter the Great St. Petersburg Polytechnic University*

30 Malaya Posadskaya St., St. Petersburg, 197046, Russian Federation

kostromitin.aleksei@yandex.ru

**LIOKUMOVICH Leonid B.**

*Peter the Great St. Petersburg Polytechnic University*

29 Politechnicheskaya St., St. Petersburg, 195251, Russian Federation

leonid@spbstu.ru

**SKLIAROV Philipp V.**

*Concern CSRI “Elektropribor”;*

*Peter the Great St. Petersburg Polytechnic University*

30 Malaya Posadskaya St., St. Petersburg, 197046, Russian Federation

sklyarov.fil@gmail.com

**KOTOV Oleg I.**

*Peter the Great St. Petersburg Polytechnic University*

29 Politechnicheskaya St., St. Petersburg, 195251, Russian Federation

kotov@rphf.spbstu.ru

## СПИСОК ЛИТЕРАТУРЫ

1. **Measures R.M.** Structural monitoring with fiber optic technology. Cambridge, Massachusetts, USA: Academic Press, 2001. 716 p.

2. **Langhammer J., Eriksrud M., Berg C., Nakstad H.** Fiber optic permanent seismic system for increased hydrocarbon recovery // *Proceedings of the 11th International Congress of the Brazilian Geophysical Society, European Association of Geoscientists & Engineers, Salvador, Brasil, 24–28 August, 2009.* cp-195-00408.

3. **Plotnikov M.Y., Lavrov V.S., Dmitraschenko P.Y., Kulikov A.V., Meshkovskiy I.K.** Thin cable fiber-optic hydrophone array for passive acoustic surveillance applications // *IEEE Sensors Journal*. 2019. Vol. 19. No. 9. Pp. 3376–3382.

4. **Kersey A.D., et al.** Multiplexed

interferometric fiber sensors // *7th Optical Fibre Sensors Conference. The Institution of Radio and Electronics Engineers Australia, 1990.* Pp. 313–319.

5. **Akkaya O.C., Digonnet M.J.F., Kino G.S., Solgaard O.** Time-division-multiplexed interferometric sensor arrays // *Journal of Lightwave Technology*. 2013. Vol. 31. No. 16. Pp. 2701–2708.

6. **Liao Y., Austin E., Nash P.J., Kingsley S.A., Richardson D.J.** Highly scalable amplified hybrid TDM/DWDM array architecture for interferometric fiber-optic sensor systems // *Journal of Lightwave Technology*. 2013. Vol. 31. No. 6. Pp. 882–888.

7. **Kersey A.D., Dandridge A., Dorsey K.L.** Transmissive serial interferometric fiber sensor array // *Journal of Lightwave Technology*. 1989. Vol. 7. No. 5. Pp. 846–854.

8. **Brooks J., Moslehi B., Kim B., Shaw H.** Time-domain addressing of remote fiber-optic interferometric sensor arrays // Journal of Lightwave Technology. 1987. Vol. 5. No. 7. Pp. 1014–1023.
9. **Lijuan Gu, Xiangge He, Duo Yi, et al.** Common-mode noise suppression technique in interferometric fiber-optic sensors // Journal of Lightwave Technology. 2019. Vol. 37. No. 21. Pp. 5619–5627.
10. **Yoshida M., Hirayama Y., Takahara A.** Real-time displacement measurement system using phase-shifted optical pulse interferometry: Application to a seismic observation system // Japanese Journal of Applied Physics. 2016. Vol. 55. Vol. 2. P. 022701.

*Статья поступила в редакцию 16.04.2020, принята к публикации 25.04.2020.*

### СВЕДЕНИЯ ОБ АВТОРАХ

**КОСТРОМИТИН Алексей Олегович** — инженер АО «Концерн «ЦНИИ «Электроприбор», Санкт-Петербург; аспирант Высшей школы прикладной физики и космических технологий Санкт-Петербургского политехнического университета Петра Великого, Санкт-Петербург, Российская Федерация.

197046, Российская Федерация, г. Санкт-Петербург, Малая Посадская ул., 30.  
kostromitin.aleksei@yandex.ru

**ЛИОКУМОВИЧ Леонид Борисович** — доктор физико-математических наук, профессор Высшей школы прикладной физики и космических технологий Санкт-Петербургского политехнического университета Петра Великого, Санкт-Петербург, Российская Федерация.

195251, Российская Федерация, г. Санкт-Петербург, Политехническая ул., 29  
leonid@spbstu.ru

**СКЛЯРОВ Филипп Владимирович** — начальник группы АО «Концерн «ЦНИИ «Электроприбор», Санкт-Петербург; аспирант Высшей школы прикладной физики и космических технологий Санкт-Петербургского политехнического университета Петра Великого, Санкт-Петербург, Российская Федерация.

197046, Российская Федерация, г. Санкт-Петербург, Малая Посадская ул., 30.  
sklyarov.fil@gmail.com

**КОТОВ Олег Иванович** — доктор физико-математических наук, профессор Высшей школы прикладной физики и космических технологий Санкт-Петербургского политехнического университета Петра Великого, Санкт-Петербург, Российская Федерация.

195251, Российская Федерация, г. Санкт-Петербург, Политехническая ул., 29  
kotov@rphf.spbstu.ru

DOI: 10.18721/JPM.13211

УДК 539.126.3

## PRODUCTION OF $K^*$ -MESONS IN THE COPPER-GOLD NUCLEI COLLISIONS AT $\sqrt{s_{NN}} = 200$ GeV

*V.S. Borisov, Ya.A. Berdnikov, A.Ya. Berdnikov,  
D.O. Kotov, Iu.M. Mitrانков*

Peter the Great St. Petersburg Polytechnic University, St. Petersburg, Russian Federation

This paper presents invariant transverse momentum spectra and nuclear modification factors of  $K^*(892)$ -mesons measured in the Cu + Au collisions at  $\sqrt{s_{NN}} = 200$  GeV. The measurements were performed in five centrality bins in the range of transverse momentum from 2.00 to 5.75 GeV/c in the PHENIX experiment at the RHIC. Nuclear modification factors were compared with previously obtained PHENIX data in Cu + Cu collisions at  $\sqrt{s_{NN}} = 200$  GeV. The nuclear modification factors of  $K^*$ -mesons in Cu + Cu and Cu + Au collisions at the same values of a number of participants  $N_{part}$  were found to have similar values (within uncertainties).

**Keywords:** quark gluon plasma, jet quenching, heavy ion collision, strangeness, nuclear modification factor

**Citation:** Borisov V.S., Berdnikov Y.A., Berdnikov A.Y., Kotov D.O., Mitrانков I.M., Production of  $K^*$ -mesons in the copper-gold nuclei collisions at  $\sqrt{s_{NN}} = 200$  GeV, St. Petersburg Polytechnical State University Journal. Physics and Mathematics. 13 (2) (2020) 121–129. DOI: 10.18721/JPM.13211

This is an open access article under the CC BY-NC 4.0 license (<https://creativecommons.org/licenses/by-nc/4.0/>)

## РОЖДЕНИЕ $K^*$ -МЕЗОНОВ В СТОЛКНОВЕНИЯХ ЯДЕР МЕДИ И ЗОЛОТА ПРИ ЭНЕРГИИ $\sqrt{s_{NN}} = 200$ ГЭВ

*В.С. Борисов, Я.А. Бердников, А.Я. Бердников,  
Д.О. Котов, Ю.М. Митранков*

Санкт-Петербургский политехнический университет Петра Великого,  
Санкт-Петербург, Российская Федерация

В статье приведены результаты измерений инвариантных спектров рождения и факторов ядерной модификации  $K^*(892)$ -мезонов в столкновениях ядер меди и золота (Cu + Au) при энергии  $\sqrt{s_{NN}} = 200$  ГэВ. Измерения выполнены в пяти классах событий по центральности в диапазоне поперечных импульсов от 2,00 до 5,75 ГэВ/с в эксперименте PHENIX на коллайдере RHIC. Значения факторов ядерной модификации сравнивались с ранее полученными данными на PHENIX в (Cu + Cu)-столкновениях при такой же энергии (200 ГэВ). Установлено, что факторы ядерной модификации  $K^*$ -мезонов в столкновениях Cu + Cu и Cu + Au, при одинаковом числе участников  $N_{part}$ , имеют одинаковые значения (в пределах неопределенностей).

**Ключевые слова:** кварк-глюонная плазма, эффект гашения струй, странность, фактор ядерной модификации

**Ссылка при цитировании:** Борисов В.С., Бердников Я.А., Бердников А.Я., Котов Д.О., Митранков Ю.М. Рождение  $K^*$ -мезонов в столкновениях ядер меди и золота при энергии  $\sqrt{s_{NN}} = 200$  ГэВ // Научно-технические ведомости СПбГПУ. Физико-математические науки. 2020. Т. 13. № 2. С. 142–151. DOI: 10.18721/JPM.13211

Статья открытого доступа, распространяемая по лицензии CC BY-NC 4.0 (<https://creativecommons.org/licenses/by-nc/4.0/>)



## Introduction

Studies on the properties of nuclear matter under extreme conditions, where quarks and gluons become deconfined, are aimed at solving an important problem in high energy physics. It is hypothesized that deconfinement existed in the early Universe [1].

Quantum chromodynamics (QCD) predicts for high energy densities of approximately 1 GeV/fm<sup>3</sup> that a phase transition occurs from ordinary hadronic matter, described in terms of color-neutral hadrons, to a new state of matter called the quark-gluon plasma (QGP), where the degrees of freedom are quarks and gluons leaving the confinement region about 1 fm in radius [2]. Matter with extremely high energy density can be produced in the laboratory by colliding heavy ions at ultrarelativistic energies.

One of the key signatures for QGP production is jet quenching, which consists in strong suppression of particle yields in central collisions of heavy nuclei due to energy losses of quarks and gluons in the medium [3, 4].

An intriguing effect observed in collisions of heavy nuclei is an increased yield of strange hadrons. Since quark-antiquark pairs  $s\bar{s}$  are mainly produced in gluon-gluon interactions ( $gg \rightarrow s\bar{s}$ ), the probability of the process in QGP increases for the following reason. Restoration of chiral symmetry in QGP results in decreasing the strange quark mass, which in turn reduces the energy threshold for strangeness production, making the production of an  $s\bar{s}$  pair energetically more favorable than that of  $u\bar{u}$  and  $d\bar{d}$  pairs [5]. Therefore, extracting the yields of vector  $K^*(892)$  mesons (whose rest mass is equal to  $0.8916 \text{ GeV}/c^2 \approx 892 \text{ MeV}/c^2$ ) with open strangeness ( $d\bar{s}$ ) is an effective method for studying the properties of QGP [6].

Our study presents the data on the yields of  $K^*$  mesons, their invariant spectra depending on transverse momentum ( $p_T$ ), and the nuclear modification factors  $R_{AB}$ . The observables were measured experimentally in collisions of copper and gold nuclei (denoted as Cu + Au) at  $\sqrt{s_{NN}} = 200 \text{ GeV}$  at midrapidity in the transverse momentum range from 2.00 to 5.75 GeV/c using the PHENIX detector at the Relativistic Heavy Ion Collider (RHIC) at Brookhaven National Laboratory, USA [7–9].

## Measurement procedure

Extracting  $K^*$  meson yields, we used two procedures to generate independent sources of systematic uncertainties. Experimental data from different detectors were combined

to cover different  $p_T$  bins, providing the widest range of transverse momenta possible in this collision system. The procedures have different sources of systematic uncertainties; importantly, both procedures were used in the range of intermediate transverse momenta, making it possible to check the validity of the results obtained.

$K^*$  and  $\bar{K}^*$  meson yields were extracted using the following subsystems of the PHENIX experiment: drift chamber (DC), third-layer pad chamber (PC3) [10] and time-of-flight (TOF) detector [11].

The transverse momenta of  $K$  and  $\pi$  mesons are measured in DC and PC. The TOF detector is used to reconstruct  $K$  and  $\pi$  mesons, as well as protons.  $K^*$  and  $\bar{K}^*$  meson yields are reconstructed from hadronic decays into  $K^+\pi^-$  and  $K^-\pi^+$  pairs. Unlike-sign particles detected in one collision are combined into pairs for this purpose. Only particles with transverse momenta exceeding 0.3 GeV/c are extracted. A charged particle is assumed to be either a  $K$  or a  $\pi$  meson, and, depending on the given decay channel and the particle's charge, it is assigned the mass of a charged  $K$  or  $\pi$  meson. Two procedures described below are used to reconstruct the invariant mass spectra of  $(K\pi)$  meson pairs, increasing the statistical significance of the experimental data in a wide range of transverse momenta.

The first procedure, ToF-PC3, assumes that the transverse momenta of  $K$  mesons are measured in DC, and  $K$  mesons are reconstructed in the TOF detector, while the transverse momenta of  $\pi$  mesons are measured in DC and in PC3. This procedure allows to detect and calculate the kinematic characteristics of  $K^*$  mesons at low  $p_T$  (1.9–2.9 GeV/c).

The second procedure, PC3-PC3, assumes that the transverse momenta of  $K$  and  $\pi$  mesons are measured in DC and in PC3. This procedure allows to extract  $K^*$  meson yields at intermediate and high  $p_T$  (2.6–6.5 GeV/c). The drawback of the second procedure is that the combinatorial background is much larger compared with that for the first procedure, which means that  $K^*$  meson yields cannot be extracted at transverse momenta below  $p_T = 2.0 \text{ GeV}/c$  in Cu + Au interactions.

Fig. 1 shows examples of approximated invariant mass distributions for  $(K\pi)$  meson pairs in central collisions; the results were obtained using both procedures.

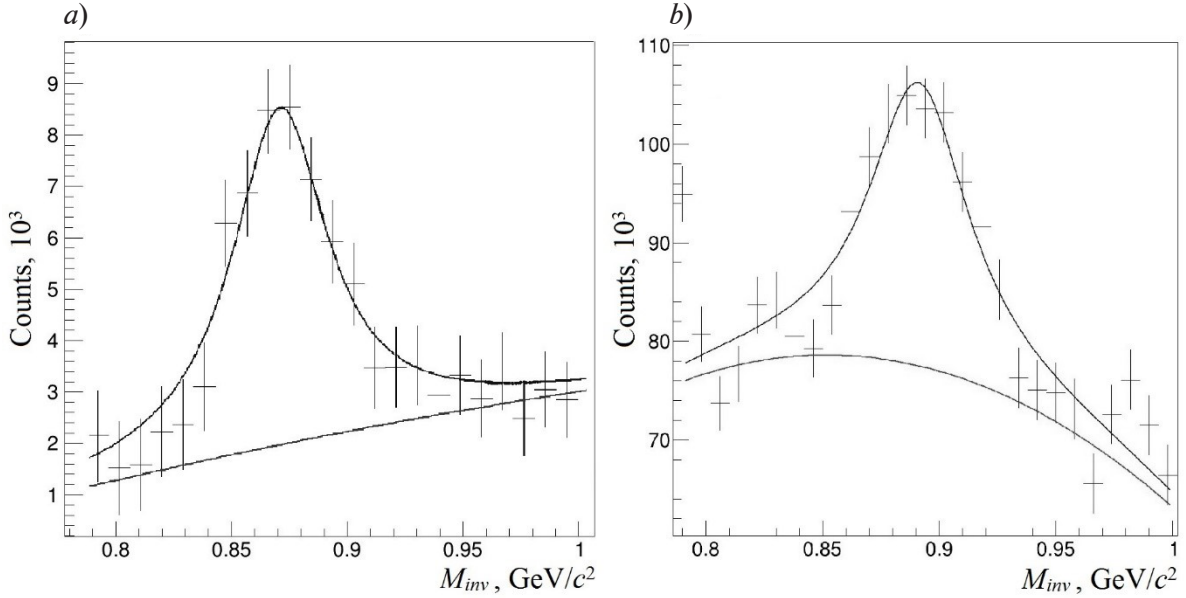


Fig. 1. Invariant mass distributions of  $K$  and  $\pi$  meson production in central Cu + Au collisions, obtained by two procedures: ToF-PC3 (a) and PC3-PC3 (b) in  $p_T$  ranges of 2.3–2.6 and 2.9–3.4 GeV/c, respectively

Because  $K$  and  $\pi$  mesons produced in  $K^*$  meson decays cannot be distinguished from other particles of the same kind, all tracks of these particles from each event satisfying the acceptance criteria are combined into like-sign or unlike-sign pairs. The components of the three-momentum vector  $\mathbf{p}$  for each track are measured using DC:

$$p_y = p \sin \theta_0 \sin \phi_0,$$

$$p_z = p \cos \theta_0.$$

The invariant mass and transverse momentum are then calculated for a pair of  $(K\pi)$  mesons based on two-body decay kinematics.

$$m_{K\pi}^2 = (E_K + E_\pi)^2 - (\mathbf{p}_K + \mathbf{p}_\pi)^2,$$

$$p_{T_{K\pi}}^2 = (p_{x_K} + p_{x_\pi})^2 + (p_{y_K} + p_{y_\pi})^2,$$

where  $E_K = \sqrt{\mathbf{p}_K^2 + m_K^2}$  and  $m_K = 0.43667$  GeV;

$E_\pi = \sqrt{\mathbf{p}_\pi^2 + m_\pi^2}$  and  $m_\pi = 0.13957$  GeV.

The invariant mass spectrum for a pair of unlike-sign mesons contains both the  $K^*$  meson signal and the combinatorial background. The latter includes two components: the correlated and the uncorrelated background. Event mixing is used to estimate the

combinatorial background. Analysis is aimed at extracting the yields of  $K^*$  mesons from the yields of inclusive  $(K\pi)^\pm$  pairs.  $K^*$  meson yields were obtained in all reconstructions by integrating the invariant mass distribution within  $\pm 100$  MeV/ $c^2$  of the  $K^*$  meson mass (892 MeV/ $c^2$ ) after subtracting the combinatorial background.

The experimental data are reconstructed as two-dimensional distributions of  $K^*$  meson yields as functions of invariant mass and transverse momentum, divided into transverse momentum bins and fitted with a relativistic Breit–Wigner distribution (RBW) convoluted with a Gaussian plus a second-order polynomial accounting for the residual background:

$$RBW = \frac{1}{2\pi} \cdot \frac{MM_0\Gamma}{(M^2 - M_0^2)^2 + M_0^2\Gamma^2},$$

where  $M_0$ , GeV/ $c^2$  and  $\Gamma$ , GeV/ $c^2$ , are the mass and the decay width of  $K^*$  mesons, respectively, according to the data from PDG (Particle Data Group);  $M$ , GeV/ $c^2$ , is the experimental value of particle mass.

The residual background is mostly generated by decay of other types of mesons.

The invariant production spectrum of  $K^*$  mesons is calculated as follows for each transverse momentum bin:

$$\frac{1}{2\pi p_T} \cdot \frac{d^2 N}{dp_T dy} = \frac{1}{2\pi p_T} \times$$

$$\times \frac{1}{2} \cdot \frac{1}{N_{events}} \cdot \frac{1}{Br} \cdot \frac{1}{\varepsilon_{eff}(p_T)} \cdot \frac{N(\Delta p_T)}{\Delta p_T \Delta y},$$

where  $p_T$  and  $\Delta p_T$ , GeV/c, are the meson transverse momentum and its bin width;  $y$  and  $\Delta y$  are the rapidity and its bin width;  $N(\Delta p_T)$  is the number of mesons reconstructed by the detector (meson yields);  $N_{events}$  is the total number of events reconstructed for a given centrality bin;  $\varepsilon_{eff}(p_T)$  is the  $K^*$  meson reconstruction efficiency, obtained by Monte Carlo simulation of decay, passage, and regeneration of mesons in the PHENIX detector;  $Br = 0.666$  is the probability of meson decay in the given channel. The coefficient  $1/2$  is taken in the formula for averaging the invariant  $K^*$  and  $\bar{K}^*$  meson yields.

The nuclear modification factors of particles in heavy ion collisions, used to analyze the collective effects governing the particle spectra depending on transverse momentum, are calculated by the formula:

$$R_{CuAu} = \frac{d^2 N_{CuAu}(p_T) / dy dp_T}{N_{coll} / \sigma_{pp}^{inel} \cdot d^2 \sigma_{pp} / dy dp_T},$$

where the numerator is the quantity characterizing the invariant spectrum of meson production in collisions of heavy copper and gold

nuclei;  $d^2 \sigma_{pp} / dy dp_T$  is the invariant differential cross section for production of these particles in collisions of the given nuclei at the same center-of-mass energy;  $N_{coll}$  is the average number of binary collisions per event in Cu + Au collisions;  $\sigma_{pp}^{inel}$  is the inelastic cross section for proton-proton scattering (here  $\sigma_{pp}^{inel} = 42.2$  mb).

### Measurement results and discussion

The reconstructed invariant spectra for the production of  $K^*$  mesons as a function of transverse momentum are shown in Fig. 2. The measurements were performed in five centrality bins with the transverse momenta ranging from 2.00 to 5.75 GeV/c. The given spectra were approximated by the Levy function for  $K^*$  mesons [12].

Fig. 3 shows the measured nuclear modification factors  $R_{AB}$  with systematic uncertainties, depending on transverse momentum, obtained for  $K^*$  mesons in Cu + Au interactions at  $\sqrt{s_{NN}} = 200$  GeV for different centrality bins. The results were obtained using two procedures: ToF-PC3 and PC3-PC3. We found that the results for the same transverse momenta are in good agreement.

The nuclear modification factors  $R_{AB}$  for  $K^*$  mesons in central Cu + Au collisions take values less than unity at high transverse momenta ( $R_{AB}$  values for  $p_T = 5-6$  GeV/c lie in the range from 0.4 to 0.7). As collision centrality increases, there is less suppression of  $K^*$  meson yields, and  $R_{AB}$  values approach unity.

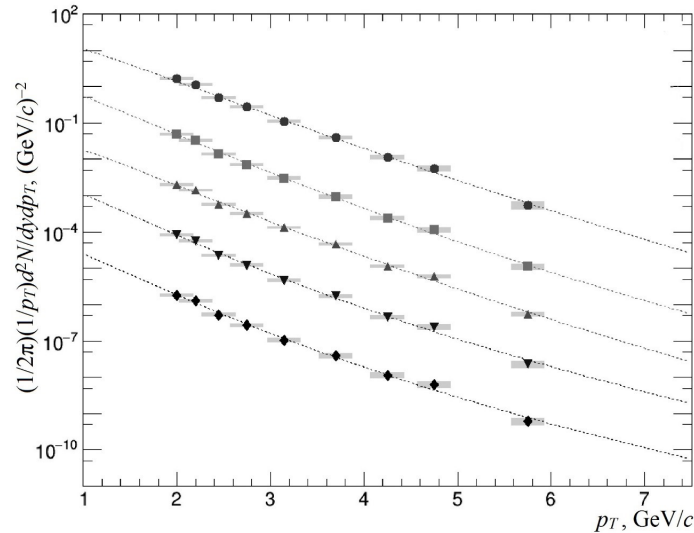


Fig. 2. Invariant spectra for production of  $K^*$  mesons in Cu + Au collisions at  $\sqrt{s_{NN}} = 200$  GeV for five centrality bins, %:

0–80 (●); 0–20 (■); 20–40 (▲); 40–60 (▼); 60–80 (◆).

The statistical uncertainties of the measurements are no larger than the symbols.

The boxes correspond to systematic uncertainties.

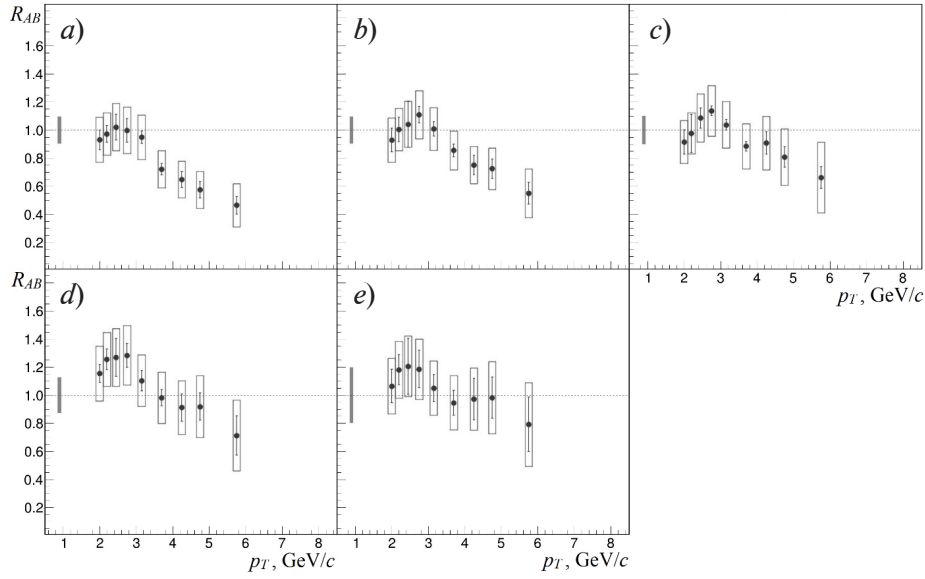


Fig. 3. Distributions of nuclear modification factors as functions of transverse momentum for  $K^*$  mesons in Cu + Au collisions at  $\sqrt{s_{NN}} = 200$  GeV for five centrality bins, %: 0–20 (a), 20–40 (b), 0–80 (c), 40–60 (d), 60–80 (e). Bars and boxes correspond to statistical and systematic uncertainties

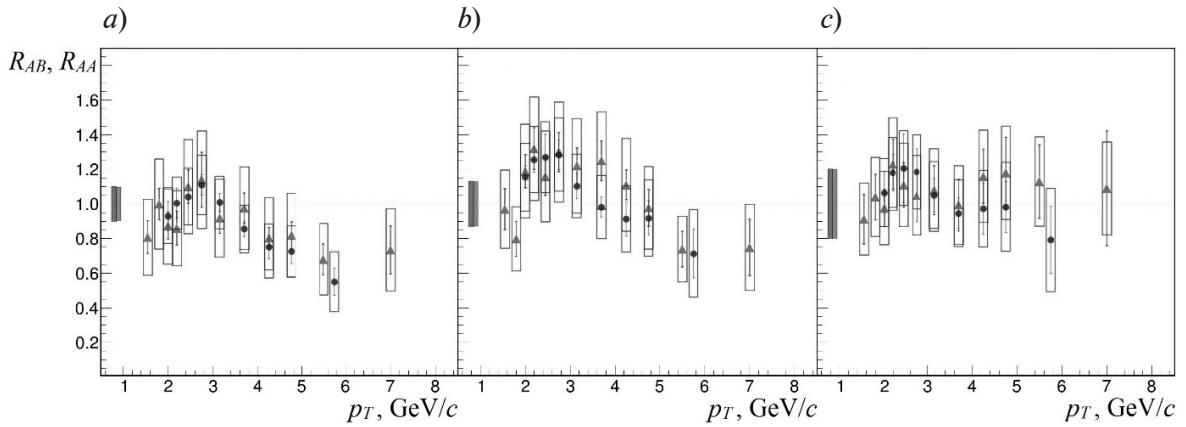


Fig. 4. Comparison of nuclear modification factors  $R_{AB}$  for  $K^*$  mesons in Cu + Au collisions (circles) with nuclear modification factors  $R_{AA}$  for Cu + Cu collisions (triangles) at the same  $\sqrt{s_{NN}} = 200$  GeV and with similar numbers of participants  $N_{part}$ : 80.37 (Cu + Au) and 85.9 (Cu + Cu) (a); 34.92 and 45.2 (b); 11.54 and 6.40 (c). Bars and boxes correspond to statistical and systematic uncertainties

Fig. 4 compares the nuclear modification factors  $R_{AB}$  for  $K^*$  mesons, measured in collisions of Cu + Au nuclei, with the nuclear modification factors  $R_{AA}$ , measured in collisions of identical nuclei (Cu + Cu) at the same energy of 200 GeV. Evidently, the results are in good agreement given a similar number of participants (within the uncertainties).

Fig. 5 compares the data for  $p_T$  distributions of nuclear modification factors of  $K^*$ ,  $\phi$ ,  $\pi^0$ ,

$\eta$ ,  $K_S$  and  $\omega$  mesons in Cu + Au collisions at 200 GeV. Evidently, the nuclear modification factors  $R_{AB}$  of  $K^*$  and  $\phi$  mesons equal unity in central collisions at intermediate  $p_T$  values, while the nuclear modification factors  $R_{AB}$  of  $\pi^0$ ,  $\eta$ ,  $K_S$  and  $\omega$  mesons are suppressed in central collisions over the entire range of  $p_T$  values. All light mesons exhibit the same level of suppression at high  $p_T$  in the most central collisions. The nuclear modification factors

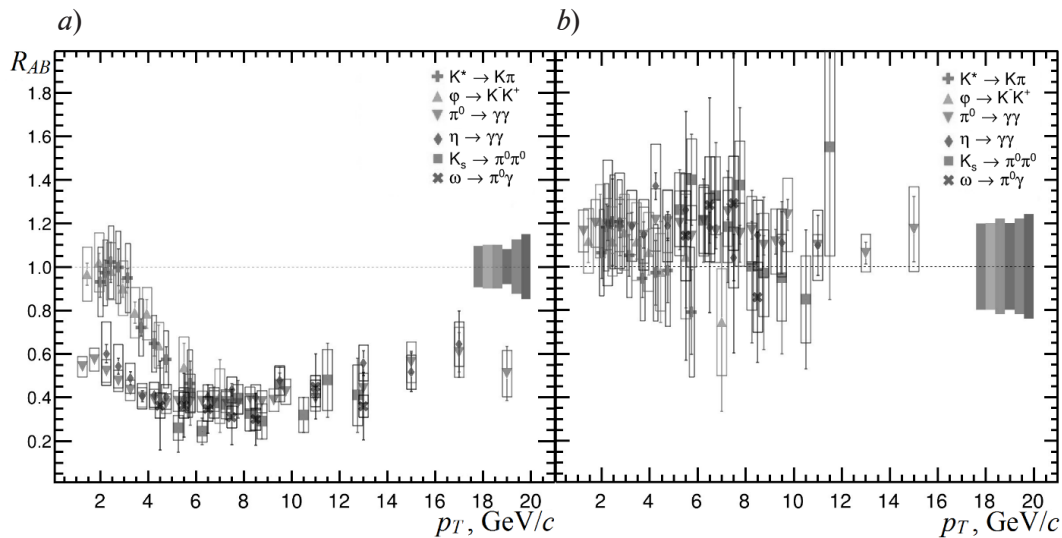


Fig. 5. Collisions of Cu + Au nuclei at  $\sqrt{s_{NN}} = 200$  GeV. Data are compared for distributions of nuclear modification factors as functions of transverse momentum for different light mesons in central (a) and peripheral (b) collisions. Bars and boxes correspond to statistical and systematic uncertainties

$R_{AB}$  equal unity in peripheral collisions for all mesons considered (within uncertainties). The same behavior was also observed for light mesons in Cu + Cu collisions at  $\sqrt{s_{NN}} = 200$  GeV [12].

### Conclusion

We have measured the invariant production spectra and nuclear modification factors of  $K^*$  mesons in collisions of copper and gold (Cu + Au) nuclei at  $\sqrt{s_{NN}} = 200$  GeV, in the pseudorapidity range  $|\eta| < 0.35$ , at transverse momenta in the range of  $2.00 < p_T < 5.75$  GeV/c and for five centrality bins. All data for the measurements were obtained at the PHENIX experiment in 2012.

We have carried out comparative analysis of the nuclear modification factors of  $K^*$  mesons in Cu + Cu and Cu + Au interactions at the same energy  $\sqrt{s_{NN}} = 200$  GeV and the nuclear modification factors of  $K^*$ ,  $\phi$ ,  $\pi^0$ ,  $\eta$ ,  $K_S$  and  $\omega$

mesons in Cu + Au collisions at  $\sqrt{s_{NN}} = 200$  GeV. We have found that  $K^*$  meson yields in Cu + Au and Cu + Cu collisions at the same energy  $\sqrt{s_{NN}} = 200$  GeV have the same values over the entire range of transverse momenta given similar numbers of participants.

Thus, suppression of mesons depends on the size of the nuclear overlap region but does not depend on the shape of the nuclei for a large number of participants [13–15].

$K^*$  and  $\phi$  meson yields in central Cu + Au collisions are less suppressed in the range of intermediate  $p_T$  compared to mesons consisting only of first-generation quarks, which points to excessive production of strangeness. The yields of  $K^*$  mesons and other light mesons are suppressed in the range of high transverse momenta in central collisions of copper and gold, which confirms the presence of the jet quenching effect.

### REFERENCES

1. Adcox K., Adler S.S., Afanasiev S., et al., Formation of dense partonic matter in relativistic nucleus-nucleus collisions at RHIC: experimental evaluation by the PHENIX Collaboration, Nuclear Physics. A. 757 (1–2) (2005) 184–283.
2. Accardi A., Gyulassy M. Cronin effect vs. geometrical shadowing in d+ Au collisions at RHIC // Phys. Lett. B. 586 (3–4) (2004) 244–253
3. Berdnikov A., Berdnikov Ya., Kotov D., et al., Phi meson measurements in Cu+Au collisions at 200 GeV and in U+U collisions at 192 GeV // J. Phys.: Conf. Ser. 1135 (1) (2018) 012044.
4. A. Adare, S. Afanasiev, C. Aidala, et al., Measurement of  $K_S^0$  and  $K^{*0}$  in  $p+p$ ,  $d+Au$ , and Cu+Cu collisions at  $\sqrt{s_{NN}} = 200$  GeV, Physical Review. C. 90 (5) (2014) 054905.
5. Kondratiev V.P., Feofilov G.A., Strange particles production in relativistic heavy-ion





collisions, *Physics of Elementary Particles and Atomic Nuclei*. 42 (6) (2011) 1721–1803 (in Russian).

6. **Ilner A., Cabrera D., Markert C., et al.**,  $K^*$  vector meson resonance dynamics in heavy-ion collisions // *Phys. Rev. C*. 95 (1–2) (2017) 014903.

7. **Arsene I., Dearden I.G., Beavis D., et al.**, Quark gluon plasma and color glass condensate at RHIC? The perspective from the BRAHMS experiment, *Nuclear Physics. A*. 757 (1–2) (2005) 1–27.

8. **Back B.B., Baker M.D., Ballintijn M., et al.**, The PHOBOS perspective on discoveries at RHIC // *Nucl. Phys. A*. 757 (1–2) (2005) 28–101.

9. **Adams J., Aggarwal M.M., Ahammed Z., et al.**, Experimental and theoretical challenges in the search for the quark gluon plasma: the STAR Collaboration's critical assessment of the evidence from RHIC collisions, *Nuclear Physics. A*. 757 (1–2) (2005) 102–183.

10. **Lokesh K.**,  $K^*(892)$  and  $\phi(1020)$  resonance

production at RHIC // *EPJ Web of Conferences*. 97 (1–2) (2015) 00017.

11. **Ghiglieri J.**, Energy loss at NLO in a high-temperature quark-gluon plasma, *Nuclear Physics, A*. 956 (December) (2017) 801–804.

12. **Adler S.S., Afanasiev S., Aidala C., et al.**, Nuclear modification of electron spectra and implications for heavy quark energy loss in Au+Au collisions at  $\sqrt{s_{NN}} = 200$  GeV // *Phys.Rev.Lett.* 96 (1–2) (2006) 032301.

13. **Adare A., Aidala C., Ajitanand N.N., et al.**, Low-mass vector-meson production at forward rapidity in  $p+p$  collisions at  $\sqrt{s_{NN}} = 200$  GeV // *Phys. Rev. D*. 90 (5) (2014) 052002.

14. **Adare A., Afanasiev S., Aidala C., et al.**, Measurement of neutral mesons in  $p+p$  collisions at  $\sqrt{s_{NN}} = 200$  GeV and scaling properties of hadron production // *Phys. Rev. D*. 83 (5) (2011) 052004.

15. **Mitrankov I.**, Scaling properties of high- $p_T$  light hadrons from small to large systems by PHENIX // *Proceedings of Science*. 345 (1) (2018) 0108.

*Received 26.03.2020, accepted 08.04.2020.*

## THE AUTHORS

### **BORISOV Vladislav S.**

*Peter the Great St. Petersburg Polytechnic University*

29 Politechnicheskaya St., St. Petersburg, 195251, Russian Federation

borisov\_vs@spbstu.ru

### **BERDNIKOV Yaroslav Ya.A.**

*Peter the Great St. Petersburg Polytechnic University*

29 Politechnicheskaya St., St. Petersburg, 195251, Russian Federation

berdnikov@spbstu.ru

### **BERDNIKOV Alexander A.Ya.**

*Peter the Great St. Petersburg Polytechnic University*

29 Politechnicheskaya St., St. Petersburg, 195251, Russian Federation

alexber@phmf.spbstu.ru

### **KOTOV Dmitry O.**

*Peter the Great St. Petersburg Polytechnic University*

29 Politechnicheskaya St., St. Petersburg, 195251, Russian Federation

dmitriy.kotov@gmail.com

### **MITRANKOV Iurii M.**

*Peter the Great St. Petersburg Polytechnic University*

29 Politechnicheskaya St., St. Petersburg, 195251, Russian Federation

mitrankovy@gmail.com

## СПИСОК ЛИТЕРАТУРЫ

1. Adcox K., Adler S.S., Afanasiev S., et al. Formation of dense partonic matter in relativistic nucleus-nucleus collisions at RHIC: experimental evaluation by the PHENIX Collaboration // Nuclear Physics A. 2005. Vol. 757. No. 1–2. Pp. 184–283.
2. Accardi A., Gyulassy M. Cronin effect vs. geometrical shadowing in d+ Au collisions at RHIC // Phys. Lett. B. 2004. Vol. 586. No. 3–4. Pp. 244–253.
3. Berdnikov A., Berdnikov Ya., Kotov D., et al. Phi meson measurements in Cu+Au collisions at 200 GeV and in U+U collisions at 192 GeV // J. Phys.: Conf. Ser. 2018. Vol. 1135. No. 1. P. 012044.
4. Adare A., Afanasiev S., Aidala C., et al. Measurement of  $K_S^0$  and  $K^0$  in  $p + p$ ,  $d + Au$ , and  $Cu + Cu$  collisions at  $\sqrt{s_{NN}} = 200$  GeV // Physical Review. C. 2014. Vol. 90. No. 5. P. 054905.
5. Кондратьев В.П., Феофилов Г.А. Рождение странных частиц в релятивистских столкновениях тяжелых ионов // Физика элементарных частиц и атомного ядра. 2011. Т. 42. Вып. 6. С. 1721–1803.
6. Ilners A., Cabrera D., Markert C., et al.  $K^*$  vector meson resonance dynamics in heavy-ion collisions // Phys. Rev. C. 2017. Vol. 95. No. 1–2. P. 014903.
7. Arsene I., Dearden I.G., Beavis D., et al. Quark gluon plasma and color glass condensate at RHIC? The perspective from the BRAHMS experiment // Nuclear Physics A. 2005. Vol. 757. No. 1–2. Pp. 1–27.
8. Back B.B., Baker M.D., Ballintijn M., et al. The PHOBOS perspective on discoveries at RHIC // Nucl. Phys. A. 2005. Vol. 757. No. 1–2. Pp. 28–101.
9. Adams J., Aggarwal M.M., Ahammed Z., et al. Experimental and theoretical challenges in the search for the quark gluon plasma: the STAR Collaboration's critical assessment of the evidence from RHIC collisions // Nuclear Physics A. 2005. Vol. 757. No. 1–2. Pp. 102–183.
10. Lokesh K.  $K^*(892)$  and  $\phi(1020)$  resonance production at RHIC // EPJ Web of Conferences. 2015. Vol. 97. No. 1–2. P. 00017.
11. Ghiglieri J. Energy loss at NLO in a high-temperature quark-gluon plasma // Nuclear Physics. A. 2016. Vol. 956. December. Pp. 801–804.
12. Adler S.S., Afanasiev S., Aidala C., et al. Nuclear modification of electron spectra and implications for heavy quark energy loss in Au+Au collisions at  $\sqrt{s_{NN}} = 200$  GeV // Phys. Rev. Lett. 2006. Vol. 96. No. 1–2. P. 032301.
13. Adare A., Aidala C., Ajitanand N.N., et al. Low-mass vector-meson production at forward rapidity in  $p+p$  collisions at  $\sqrt{s_{NN}} = 200$  GeV // Phys. Rev. D. 2014. Vol. 90. No. 5. P. 052002.
14. Adare A., Afanasiev S., Aidala C., et al. Measurement of neutral mesons in  $p+p$  collisions at  $\sqrt{s_{NN}} = 200$  GeV and scaling properties of hadron production // Physical Review. D. 2011. Vol. 83. No. 5. P. 052004.
15. Mitrankov I. Scaling properties of high- $p_T$  light hadrons from small to large systems by PHENIX // Proceedings of Science. 2018. Vol. 345. No. 1. P. 0108.

Статья поступила в редакцию 26.03.2020, принята к публикации 08.04.2020.

## СВЕДЕНИЯ ОБ АВТОРАХ

**БОРИСОВ** Владислав Сергеевич – инженер *Вышей инженерно-физической школы Санкт-Петербургского политехнического университета Петра Великого*, Санкт-Петербург, Российская Федерация.

195251, Российская Федерация, г. Санкт-Петербург, Политехническая ул., 29  
borisov\_vs@spbstu.ru

**БЕРДНИКОВ** Ярослав Александрович – доктор физико-математических наук, профессор *Вышей инженерно-физической школы Санкт-Петербургского политехнического университета Петра Великого*, Санкт-Петербург, Российская Федерация.

195251, Российская Федерация, г. Санкт-Петербург, Политехническая ул., 29  
berdnikov@spbstu.ru



**БЕРДНИКОВ** Александр Ярославич — кандидат физико-математических наук, доцент Высшей инженерно-физической школы Санкт-Петербургского политехнического университета Петра Великого, Санкт-Петербург, Российская Федерация.

195251, Российская Федерация, г. Санкт-Петербург, Политехническая ул., 29  
alexber@phmf.spbstu.ru

**КОТОВ** Дмитрий Олегович — кандидат физико-математических наук, доцент Высшей инженерно-физической школы Санкт-Петербургского политехнического университета Петра Великого, Санкт-Петербург, Российская Федерация.

195251, Российская Федерация, г. Санкт-Петербург, Политехническая ул., 29  
dmitriy.kotov@gmail.com

**МИТРАНКОВ** Юрий Михайлович — ассистент Высшей инженерно-физической школы Санкт-Петербургского политехнического университета Петра Великого, Санкт-Петербург, Российская Федерация.

195251, Российская Федерация, г. Санкт-Петербург, Политехническая ул., 29  
mitrankovy@gmail.com

DOI: 10.18721/JPM.13212

УДК: 539.12

## MEASUREMENT OF $\phi$ -MESON'S NUCLEAR MODIFICATION FACTORS IN THE COLLISIONS OF PROTON BEAMS WITH ALUMINUM NUCLEI AT AN ENERGY OF 200 GeV

*M.M. Larionova, Ya.A. Berdnikov, A.Ya. Berdnikov,  
Iu.M. Mitrانkov, D.O. Kotov*

Peter the Great St. Petersburg Polytechnic University, St. Petersburg, Russian Federation

The  $\phi$ -mesons production in the relativistic collisions of proton beams with aluminum nuclei ( $p + \text{Al}$ , small system) at  $\sqrt{s_{NN}}$  energy of 200 GeV has been studied. The PHENIX experiment was carried out at the RHIC. The  $\phi$ -mesons' invariant transverse momentum spectra and their nuclear modification factors were measured in four centrality bins of the range of transverse momentum (%): 0 – 20, 20 – 40, 40 – 72, 0 – 72. The obtained results were compared with similar data on the  $\pi^0$ -mesons production. The experimental data analysis led to the conclusion that the  $\phi$ -mesons' nuclear modification factors were equal to one (within the measurement uncertainties) over all available ranges of centrality and transverse momenta. The findings of the work testified that quark-gluon plasma did not produce in the performed collisions.

**Keywords:** quark-gluon plasma, cold nuclear matter effect, nuclear modification factor, relativistic ion collision

**Citation:** Larionova M.M., Berdnikov Ya.A., Berdnikov A.Ya., Mitrانkov I.M., Kotov D.O., Measurement of  $\phi$ -meson's nuclear modification factors in the collisions of proton beams with aluminum nuclei at an energy of 200 GeV, St. Petersburg Polytechnical State University Journal. Physics and Mathematics. 13 (2) (2020) 130–136. DOI: 10.18721/JPM.13212

This is an open access article under the CC BY-NC 4.0 license (<https://creativecommons.org/licenses/by-nc/4.0/>)

## ИЗМЕРЕНИЕ ФАКТОРОВ ЯДЕРНОЙ МОДИФИКАЦИИ $\phi$ -МЕЗОНА В СТОЛКНОВЕНИЯХ ПРОТОННЫХ ПУЧКОВ С ЯДРАМИ АЛЮМИНИЯ ПРИ ЭНЕРГИИ 200 ГЭВ

*М.М. Ларионова, Я.А. Бердников, А.Я. Бердников,*

*Ю.М. Митранков, Д.О. Котов*

Санкт-Петербургский политехнический университет Петра Великого,

Санкт-Петербург, Российская Федерация

В работе изучено рождение  $\phi$ -мезонов в релятивистских столкновениях пучков протонов с ядрами алюминия ( $p + \text{Al}$ , малая система) при энергии  $\sqrt{s_{NN}} = 200$  ГэВ, проведенных в эксперименте PHENIX на коллайдере RHIC. Измерены инвариантные спектры  $\phi$ -мезонов по поперечному импульсу и их факторы ядерной модификации для четырех классов событий по центральности, %: 72 – 0, 72–40, 40 – 20, 20 – 0. Проведено сравнение полученных результатов с аналогичными данными по рождению  $\pi^0$ -мезонов. Анализ полученных экспериментальных данных привел к заключению, что во всех доступных диапазонах по центральности и поперечному импульсу факторы ядерной модификации  $\phi$ -мезонов равны единице в пределах неопределенностей измерения. Полученный результат свидетельствует в пользу того, что в рассматриваемых столкновениях кварк-глюонная плазма не образуется.

**Ключевые слова:** кварк-глюонная плазма, эффект холодной ядерной материи, фактор ядерной модификации



**Ссылка при цитировании:** Ларионова М.М., Бердников Я.А., Бердников А.Я., Митранков Ю.М., Котов Д.О. Измерение факторов ядерной модификации  $\phi$ -мезона в столкновениях протонных пучков с ядрами алюминия при энергии 200 ГэВ // Научно-технические ведомости СПбГПУ. Физико-математические науки. 2020. Т. 13. № 2. С. 152–159. DOI: 10.18721/JPM.13212

Статья открытого доступа, распространяемая по лицензии CC BY-NC 4.0 (<https://creativecommons.org/licenses/by-nc/4.0/>)

### Introduction

Quantum chromodynamics predicts the existence of a state of matter known as quark-gluon plasma (QGP), where quarks and gluons are deconfined. Ultrarelativistic heavy ion collisions provide an opportunity for studying the behavior of nuclear matter at temperatures and pressures sufficient for QGP production [1]. Exploring the properties of QGP produced in controlled conditions and its evolution into hadron gas is the main purpose of the PHENIX experiment [2] at RHIC (Relativistic Heavy Ion Collider located at Brookhaven National Laboratory, USA) [3].

One method for studying the properties of QGP experimentally is measuring final-state particle yields. In particular,  $\phi$  mesons have a range of distinctive properties, such as small cross section for interaction with non-strange hadrons and much longer lifetimes (42 fm/c) than those of QGP [4]. Thanks to these properties, hadron interactions have less effect on  $\phi$  meson production at the late stages in the evolution of the system formed in heavy ion collisions; furthermore,  $\phi$  meson daughter particles are not rescattered in the hadron phase.

Thus, the properties of  $\phi$  mesons mainly depend on the conditions in the early parton phase, and measuring  $\phi$  meson yields can be regarded as a clean test for the behavior of the matter produced in collisions of relativistic nuclei.

Measuring  $\phi$  meson yields can be used to study the so-called cold nuclear matter (CNM) effects in small collision systems [5]. Cold nuclear matter effects are understood as modifications of parton distributions in the nucleus [6], the Cronin effect [7] associated with multiple rescattering of incoming partons inside the target nucleus, and other effects.

Analysis of CNM effects by measuring  $\phi$  meson production in small systems can explain whether the effects observed in heavy ion collisions are connected with the effects of cold or hot nuclear matter. In particular,

results of such studies can help understand the difference between nuclear modification factors of  $\pi^0$  mesons,  $\phi$  mesons, and protons obtained in collisions of gold (Au+Au), copper (Cu+Cu), copper-gold (Cu+Au) nuclei at  $\sqrt{s_{NN}} = 200$  GeV, as well as uranium nuclei (U+U) collisions at  $\sqrt{s_{NN}} = 192$  GeV [8, 9].

### Measurement procedure

We used the measurement results obtained with the PHENIX detector at RHIC. Our goal consisted in reconstructing the production of  $\phi$  mesons decaying into charged kaons ( $\phi \rightarrow K^+ K^-$ ) in collisions of proton and aluminum nuclei ( $p+Al$ ) at  $\sqrt{s_{NN}} = 200$  GeV.

We primarily focused on obtaining invariant transverse momentum spectra and nuclear modification factors  $R_{AB}$  for  $\phi$  mesons in  $p+Al$  collisions.

As kaons produced in  $\phi$  meson decay are indistinguishable from other kaons, so all kaon tracks from each event are combined into unlike-sign pairs. The components of the three-momentum vector  $\mathbf{p}$  for each track were measured using the drift chamber. Invariant mass and transverse momentum are calculated for kaon pairs based on two-body decay kinematics.

The invariant mass spectrum for unlike-sign kaon pairs contains both the signal of  $\phi$  mesons and the combinatorial background. The latter includes two components: correlated and uncorrelated background. The event-mixing technique is used to estimate combinatorial background [12]. After subtracting the uncorrelated background from the total spectrum, the correlated background is estimated by fitting the invariant mass distributions to a Breit–Wigner distribution convoluted with a Gaussian (where the dispersion equals the experimental mass resolution of the detector) to describe the signal, plus a polynomial to describe the background.

The experimental mass resolution of the detector is estimated by Monte Carlo simulation of the spectrometer with zero width for  $\phi \rightarrow K^+ K^-$ , where  $\phi$  mesons have infinite lifetimes. We obtained  $\phi$  meson yields



by integrating the invariant mass distribution within  $\pm 9$  MeV/c<sup>2</sup> of the  $\phi$  meson mass (1.019 GeV/c<sup>2</sup> [13]) after subtracting the combinatorial background.

The invariant spectrum of  $\phi$  meson production is calculated as follows in each transverse momentum bin:

$$\frac{1}{2\pi p_T} \frac{d^2 N}{dp_T dy} = \frac{1}{2\pi p_T} \frac{1}{N_{event}} \frac{1}{Br} \frac{1}{\epsilon_{eff}(p_T)} \frac{N(\Delta p_T)}{\Delta p_T \Delta y}, \quad (1)$$

where  $p_T$  and  $\Delta p_T$ , GeV/c, are the meson transverse momentum and its bin width respectively;  $y$  and  $\Delta y$  are the rapidity and its bin width;  $N(\Delta p_T)$  is the number of mesons reconstructed with the experimental detector (meson yields);  $N_{event}$  is the total number of events reconstructed in the given centrality bin;  $\epsilon_{eff}(p_T)$  is the  $\phi$  meson reconstruction efficiency obtained using Monte Carlo models of decay, passage and regeneration of mesons in the PHENIX experiment; Br is the probability of meson decay via the given channel.

Suppression of particle yields in relativistic heavy ion collisions is studied by finding the nuclear modification factors  $R_{AB}$ , calculated as a ratio of invariant particle yields measured in relativistic heavy ion collisions to the yields of the same particles measured

in elementary collisions of protons ( $p+p$ ). The yield for  $A+B$  collision is normalized to the number of inelastic nucleon-nucleon collisions.

Nuclear modification factors of particles in collisions of different nuclei are used to account for the collective effects governing the transverse momentum spectra of particle production, and are calculated by the formula:

$$R_{AB}(p_T) = \frac{f_{bias} \sigma_{pp}^{inel}}{N_{coll}} \frac{dN_{AB}(p_T)}{d\sigma_{pp}(p_T)}, \quad (2)$$

where

$$dN_{AB}(p_T) = \frac{1}{2\pi p_T} \frac{d^2 N_{AB}(p_T)}{dp_T dy}$$

is the invariant spectrum of meson production in heavy ion collisions;

$$d\sigma_{pp}(p_T) = \frac{1}{2\pi p_T} \frac{d^2 \sigma_{pp}}{dp_T dy}$$

is the invariant differential cross-section for production of these particles in  $p+p$  collisions at the same center-of-mass energy;  $f_{bias}$  is the Bayes factor correcting for the bias in centrality measurements;  $\sigma_{pp}^{inel} = 42.2$  mb is the cross section for inelastic proton-proton scattering;  $N_{coll}$  is the number of binary collisions in the given centrality bin.

If  $R_{AB}(p_T) \approx 1$ , collective effects are probably absent in heavy ion interactions, and the interactions may be represented by superposition of individual nucleon interactions.

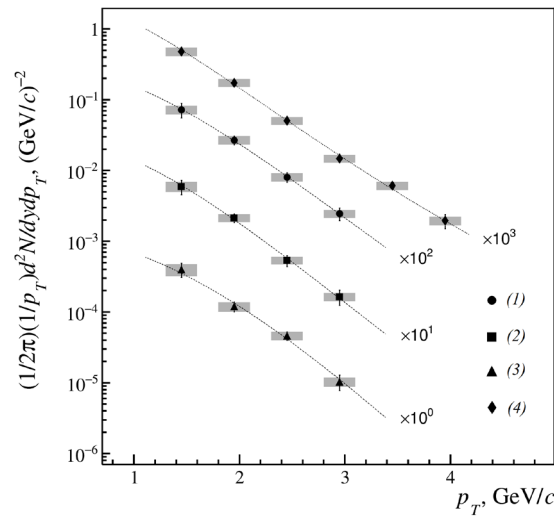


Fig. 1. Invariant transverse momentum spectra of  $\phi$  meson production in  $p+Al$  collisions at  $\sqrt{s_{NN}} = 200$  GeV in four centrality bins, %: 0–20 (1), 20–40 (2), 40–72 (3), 0–72 (4).

The dotted curves were fitted with the Lévy function.

Bars and boxes correspond to statistic and systematic uncertainty, respectively

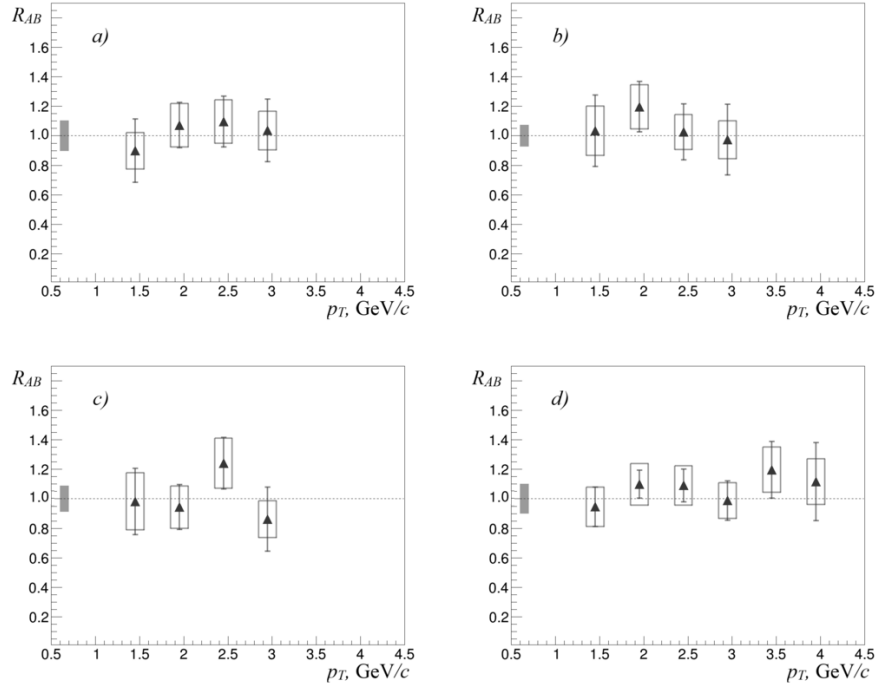


Fig. 2. Distributions of nuclear modification factors as function of transverse momentum for  $\phi$  meson production in  $p$ +Al collisions at  $\sqrt{s_{NN}} = 200$  GeV in four centrality bins, %: 0–20 (a), 20–40(b), 40–72(c), 0–72(d);  $|y| < 0.35$

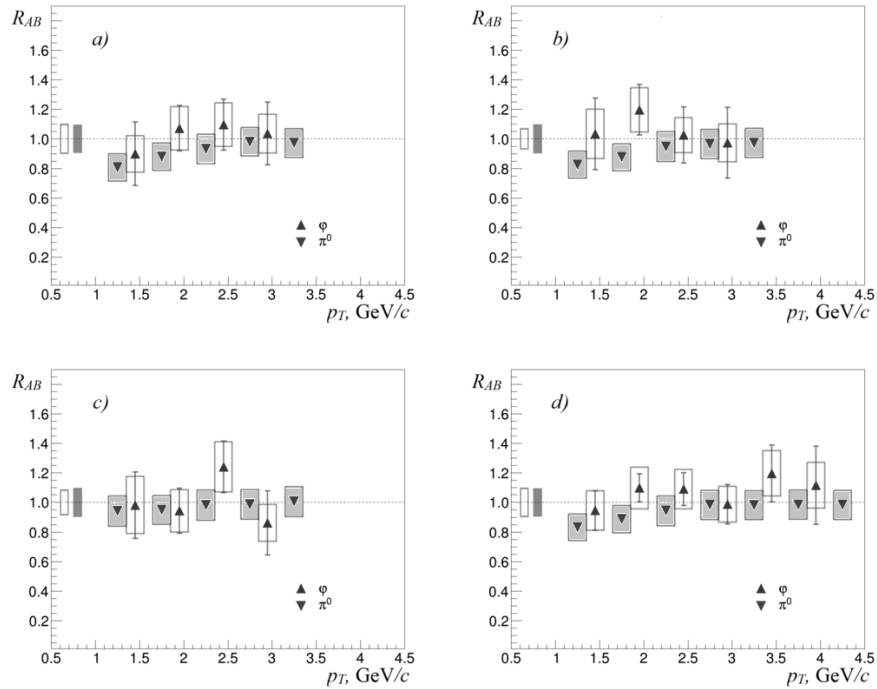


Fig. 3. Distributions of nuclear modification factors as function of transverse momentum for  $\phi$  and  $\pi^0$  meson production in  $p$ +Al collisions at  $\sqrt{s_{NN}} = 200$  GeV in four centrality bins, %: 0–20 (a), 20–40 (b), 40–72 (c), 0–72 (d);  $|y| < 0.35$

If  $R_{AB}(pT) < 1$  ( $> 1$ ), particle yields are suppressed (or, respectively, excessive), which may confirm the presence of collective effects in heavy ion interactions.

### Experimental results and discussion

Fig. 1 shows invariant transverse momentum spectra of  $\phi$  meson production in  $p$ +Al collisions at  $\sqrt{s_{NN}} = 200$  GeV. These spectra were measured in four centrality bins, %: 0–72, 0–20, 20–40 и 40–72, with transverse momenta ranging from 1.0 to 4.0 GeV/c, and fitted with the Lévy distribution:

$$\frac{1}{2\pi p_T} \frac{d^2 N}{dp_T dy} = \frac{m}{2\pi} \times \times \frac{(n-1)(n-2)}{(k+m_\phi(n-1))(k+m_\phi)} \left( \frac{k + \sqrt{p_T^2 + m_\phi^2}}{k+m_\phi} \right), \quad (3)$$

where  $m_\phi$ , GeV/c<sup>2</sup>, is the invariant mass of the  $\phi$  meson,  $k$ ,  $m$ ,  $n$  are free parameters.

The transverse momentum spectra obtained were used to calculate nuclear modification factors of  $\phi$  mesons in  $p$ +Al collisions at  $\sqrt{s_{NN}} = 200$  GeV.

Fig. 2 shows the distributions of nuclear modification factors  $R_{AB}$  depending on transverse momentum, measured for  $\phi$

mesons in  $p$ +Al interactions at  $\sqrt{s_{NN}} = 200$  GeV in different centrality bins. Evidently, the nuclear modification factors  $R_{AB}$  for  $\phi$  mesons equal unity in all centrality bins over the entire range of transverse momenta within uncertainties.

Fig. 3 shows a comparison of nuclear modification factors for  $\phi$  and  $\pi^0$  mesons in  $p$ +Al collisions at  $\sqrt{s_{NN}} = 200$  GeV. Apparently, the nuclear modification factors for  $\phi$  and  $\pi^0$  mesons take the same values in all centrality bins over the entire range of transverse momenta within uncertainties. This may indicate that CNM effects have no impact on the difference between the nuclear modification factors for  $\phi$  and  $\pi^0$  mesons in collisions of gold, copper and uranium nuclei (Au+Au, Cu+Cu, Cu+Au, U+U) [8, 9].

### Conclusion

We have measured the invariant transverse momentum spectra and nuclear modification factors for  $\phi$  mesons in  $p$ +Al collisions at  $\sqrt{s_{NN}} = 200$  GeV.

The nuclear modification factors for  $\phi$  mesons equal unity in all available centrality bins and over the entire range of transverse momenta within the uncertainties. The results obtained confirm that the collisions under consideration produce no quark-gluon plasma.

### REFERENCES

1. Adcox K., Adler S.S., Afanasiev S., et al., Formation of dense partonic matter in relativistic nucleus-nucleus collisions at RHIC: experimental evaluation by the PHENIX Collaboration, Nuclear Physics. A. 757 (1–2) (2005) 184–283.
2. Adcox K., Adler S. S., Aizama M., et al. (PHENIX Collaboration), PHENIX detector overview, Nuclear Instruments and Methods in Physics Research, Section A: Accelerators, Spectrometers, Detectors and Associated Equipment. 499 (2–3) (2003) 469–479.
3. Harrison M., Ludlam T., Ozaki S., RHIC project overview, Nuclear Instruments and Methods in Physics Research, A., 499 (2–3) (2003) 235–244.
4. Koch P., Müller B., Rafelski J., Strangeness in relativistic heavy ion collisions, Physics Reports. 142 (4) (1986) 167–262.
5. Armesto N., Small collision systems: theory overview on cold nuclear matter effects, EPJ Web of Conferences. 171 (2018) 11001.
6. Arneodo M., Nuclear effects in structure functions, Physics Reports. 240 (5–6) (1994) 301–393.
7. Kopeliovich B.Z., Nemchik J., Schurfer A., Tarasov A.V., Cronin effect in hadron production of nuclei // Physical Review Letters. 88 (23) (2002) 232303.
8. Adare A., Afanasiev S., Aidala C., et al. Nuclear modification factors of  $\phi$  mesons in  $d + Au$ ,  $Cu + Cu$  and  $Au + Au$  collisions at  $\sqrt{s_{NN}} = 200$  GeV// Physical Review. C. 2011. Vol. 83 (2) (2011) 024909.
9. Berdnikov A., Berdnikov Ya., Kotov D., et al., Phi meson measurements in  $Cu + Au$  collisions at 200 GeV and in  $U + U$  collisions at 192 GeV, J. Phys.: Conf. Ser. 1135 (1) (2018) 012044.
10. Adcox K., Ajitanand N.N., Alexander J., et al. (PHENIX Collaboration). PHENIX central arm tracking detectors, Nuclear Instruments and Methods in Physics Research, A. 499 (2–3) (2003) 489–507.
11. Ikematsu K., Iwata Y., Kaimi K., et al., A start-timing detector for the collider experiment



PHENIX at RHIC-BNL, Nuclear Instruments and Methods in Physics Research. Section, A. 411 (2–3) (1998) 238–248.

12. **L'Hôte D.**, About resonance signal extraction from multiparticle data: combinatorics and event mixing methods,

Nuclear Instruments and Methods in Physics Research. Section, A. 337 (2–3) (1994) 544–556.

13. **Beringer J., et al.** (Particle Data Group), Review of particle physics, Physical Review, D. 86 (1) (2012) 010001.

*Received 31.03.2020, accepted 20.04.2020.*

## THE AUTHORS

**LARIONOVA Mariia M.**

*Peter the Great St. Petersburg Polytechnic University*

29 Politechnicheskaya St., St. Petersburg, 195251, Russian Federation

mashalario@gmail.com

**BERDNIKOV Yaroslav A.**

*Peter the Great St. Petersburg Polytechnic University*

29 Politechnicheskaya St., St. Petersburg, 195251, Russian Federation

berdnikov@spbstu.ru

**BERDNIKOV Alexander Ya.**

*Peter the Great St. Petersburg Polytechnic University*

29 Politechnicheskaya St., St. Petersburg, 195251, Russian Federation

alexber@phmf.spbstu.ru

**MITRANKOV Iurii M.**

*Peter the Great St. Petersburg Polytechnic University*

29 Politechnicheskaya St., St. Petersburg, 195251, Russian Federation

mitrankovy@gmail.com

**KOTOV Dmitry O.**

*Peter the Great St. Petersburg Polytechnic University*

29 Politechnicheskaya St., St. Petersburg, 195251, Russian Federation

dmitriy.kotov@gmail.com

## СПИСОК ЛИТЕРАТУРЫ

1. **Adcox K., Adler S.S., Afanasiev S., et al.** Formation of dense partonic matter in relativistic nucleus-nucleus collisions at RHIC: experimental evaluation by the PHENIX Collaboration // Nuclear Physics A. 2005. Vol. 757. No. 1–2. Pp. 184–283.

2. **Adcox K., Adler S. S., Aizama M., et al.** (PHENIX Collaboration), PHENIX detector overview // Nuclear Instruments and Methods in Physics Research. Section A: Accelerators, Spectrometers, Detectors and Associated Equipment. 2003. Vol. 499. No. 2–3. Pp. 469–479.

3. **Harrison M., Ludlam T., Ozaki S.** RHIC project overview // Nuclear Instruments and Methods in Physics Research. A. 2003. Vol. 499. No. 2–3. Pp. 235–244.

4. **Koch P., Müller B., Rafelski J.** Strangeness in relativistic heavy ion collisions // Physics

Reports. 1986. Vol. 142. No. 4. Pp. 167–262.

5. **Armesto N.** Small collision systems: theory overview on cold nuclear matter effects // EPJ Web of Conferences. 2018. Vol. 171. P. 11001.

6. **Arneodo M.** Nuclear effects in structure functions // Physics Reports. 1994. Vol. 240. No. 5–6. Pp. 301–393.

7. **Kopeliovich B.Z., Nemchik J., Schafner A., Tarasov A.V.** Cronin effect in hadron production of nuclei // Physical Review Letters. 2002. Vol. 88. No. 23. P. 232303.

8. **Adare A., Afanasiev S., Aidala C., et al.** Nuclear modification factors of  $\phi$  mesons in  $d + Au$ ,  $Cu + Cu$  and  $Au + Au$  collisions at  $\sqrt{s_{NN}} = 200$  GeV // Physical Review. C. 2011. Vol. 83. No. 2. P. 024909.

9. **Berdnikov A., Berdnikov Ya., Kotov D., et al.** Phi meson measurements in Cu+Au collisions at

200 GeV and in U+U collisions at 192 GeV // J. Phys.: Conf. Ser. 2018. Vol. 1135. No. 1. P. 012044.

10. **Adcox K., Ajitanand N.N., Alexander J., et al.** (PHENIX Collaboration). PHENIX central arm tracking detectors // Nuclear Instruments and Methods in Physics Research. A. 2003. Vol. 499. No. 2–3. Pp. 489–507.

11. **Ikematsu K., Iwata Y., Kaimi K., et al.** A start-timing detector for the collider experiment PHENIX at RHIC-BNL // Nuclear Instruments

and Methods in Physics Research. Section A. 1998. Vol. 411. No. 2–3. Pp. 238–248.

12. **L'Hôte D.** About resonance signal extraction from multiparticle data: combinatorics and event mixing methods // Nuclear Instruments and Methods in Physics Research. Section A. 1994. Vol. 337. No. 2–3. Pp. 544–556.

13. **Beringer J., et al.** (Particle Data Group). Review of particle physics // Physical Review. D. 2012. Vol. 86. No. 1. P. 010001.

*Статья поступила в редакцию 31.03.2020, принята к публикации 20.04.2020.*

### СВЕДЕНИЯ ОБ АВТОРАХ

**ЛАРИОНОВА Мария Максимовна** — аспирантка Высшей инженерно-физической школы Санкт-Петербургского политехнического университета Петра Великого, Санкт-Петербург, Российская Федерация.

195251, Российская Федерация, г. Санкт-Петербург, Политехническая ул., 29  
mashalario@gmail.com

**БЕРДНИКОВ Ярослав Александрович** — доктор физико-математических наук, профессор Высшей инженерно-физической школы Санкт-Петербургского политехнического университета Петра Великого, Санкт-Петербург, Российская Федерация.

195251, Российская Федерация, г. Санкт-Петербург, Политехническая ул., 29  
berdnikov@spbstu.ru

**БЕРДНИКОВ Александр Ярославич** — кандидат физико-математических наук, доцент Высшей инженерно-физической школы Санкт-Петербургского политехнического университета Петра Великого, Санкт-Петербург, Российская Федерация.

195251, Российская Федерация, г. Санкт-Петербург, Политехническая ул., 29  
alexber@phmf.spbstu.ru

**МИТРАНКОВ Юрий Михайлович** — ассистент Высшей инженерно-физической школы Санкт-Петербургского политехнического университета Петра Великого, Санкт-Петербург, Российская Федерация.

195251, Российская Федерация, г. Санкт-Петербург, Политехническая ул., 29  
mitrankovy@gmail.com

**КОТОВ Дмитрий Олегович** — кандидат физико-математических наук, доцент Высшей инженерно-физической школы Санкт-Петербургского политехнического университета Петра Великого, Санкт-Петербург, Российская Федерация.

195251, Российская Федерация, г. Санкт-Петербург, Политехническая ул., 29  
dmitriy.kotov@gmail.com



DOI: 10.18721/JPM.13213

УДК 539.3

## **DETERMINATION OF THE EFFECTIVE YOUNG'S MODULUS OF MEDIUM WITH MICROSTRUCTURE TYPICAL FOR HYDROGEN DEGRADATION**

*K.P. Frolova*

Institute for Problems of Mechanical Engineering RAS, St. Petersburg, Russian Federation;  
Peter the Great St. Petersburg Polytechnic University, St. Petersburg, Russian Federation

The paper aims at calculation of the effective elastic properties of metals with a microstructure typical for hydrogen-enhanced degradation. For the purpose of this study, we use the Maxwell homogenization scheme and explicit expression for compliance contribution tensor to determine the overall Young's moduli. The model introduces oblate spheroids to describe intergranular microcracks and spheres to describe pores. Within the frame of the paper, we consider random orientations of the microcracks, certain preferential orientation accompanied by random scatter with the scattering parameter and random orientations of the spheroids' axes in the same plane. The dependences of the effective Young's moduli on the porosity and aspect ratio of the spheroid have been studied.

**Keywords:** effective Young's modulus, Maxwell homogenization scheme, hydrogen degradation, spheroidal inhomogeneity

**Citation:** Frolova K.P., Determination of the effective Young's modulus of medium with microstructure typical for hydrogen degradation, St. Petersburg Polytechnical State University Journal. Physics and Mathematics. 13 (2) (2020) 137–149. DOI: 10.18721/JPM.13213

This is an open access article under the CC BY-NC 4.0 license (<https://creativecommons.org/licenses/by-nc/4.0/>)

## **ОПРЕДЕЛЕНИЕ ЭФФЕКТИВНОГО МОДУЛЯ ЮНГА СРЕДЫ С МИКРОСТРУКТУРОЙ, ХАРАКТЕРНОЙ ДЛЯ ВОДОРОДНОЙ ДЕГРАДАЦИИ**

*К.П. Фролова*

Институт проблем машиноведения РАН, Санкт-Петербург, Российская Федерация;  
Санкт-Петербургский политехнический университет Петра Великого,  
Санкт-Петербург, Российская Федерация

Работа посвящена определению эффективных упругих свойств металлов с микроструктурой, характерной для водородной деградации. С целью определения эффективных модулей Юнга решается задача гомогенизации по схеме Максвелла в терминах тензоров вклада. Микротрещины, возникающие по границам зерен, моделируются сплюснутыми сфероидами, поры – сферами. Рассматривается три варианта ориентации осей симметрии сфероидов в материале: произвольная, преимущественная ориентация с параметром рассеяния, произвольная ориентация в одной плоскости. Исследуются зависимости эффективных модулей Юнга от пористости материала и от соотношения длин полуосей сфероидов.

**Ключевые слова:** эффективный модуль Юнга, схема гомогенизации Максвелла, водородная деградация, сфероидальная неоднородность

**Ссылка при цитировании:** Фролова К.П. Определение эффективного модуля Юнга среды с микроструктурой, характерной для водородной деградации // Научно-технические ведомости СПбГПУ. Физико-математические науки. 2020. Т. 2 № 13. С. 160–174. DOI: 10.18721/JPM.13213

Эта статья открытого доступа, распространяемая по лицензии CC BY-NC 4.0 (<https://creativecommons.org/licenses/by-nc/4.0/>)

## Introduction

Hydrogen dissolved in metals may lead to degradation of mechanical properties and premature fracture of metal workpieces. The impact of hydrogen on the properties and character of material fracture largely depends on both external factors, and the features of the internal structure and characteristics of materials. This is why the phenomenon of hydrogen degradation, comprising an entire range of negative effects induced by hydrogen, remains an important topic in materials science demanding further comprehensive studies [1, 2].

Many works considered the effects of hydrogen on the material microstructure [3–9]. Hydrogen is assumed to diffuse through the metal lattice and interact with the defects of the structure, such as dislocations, pores, vacancies, etc., thus inducing microcracks. The defects develop in workpieces during production, and are typically located along the boundaries of grains or inclusions in alloys (the defects are also found inside the grains, but to a lesser extent). Ultimately, if there are no significant internal or external stresses, hydrogen-induced microcracks form, propagating along the grain boundaries [3–5, 9] or blisters that lead to embrittlement of the surface [7, 9]. At the same time, microcracks can be observed at grain boundary triple junctions as well [4, 5, 8, 9]. Microcracks are often seen to initiate with a preferential orientation, which is parallel to the rolling direction [3, 7].

Several papers [10–12] studied hydrogen diffusion along the grain boundaries, finding the effective diffusion coefficient in a composite material, where one phase consisted of grain boundaries with a high diffusion coefficient, and the other phase included the actual grains with a low diffusion coefficient. However, hydrogen-induced changes in the microstructure were not simulated in these studies. For example, [13] used phenomenological approaches to solve a related problem of hydrogen transfer and changes in the defects structure of the material. The effect of hydrogen on the material was accounted for within the cumulative damage theory. A number of papers discussed hydrogen-induced degradation of elastic properties of

material [9, 14, 15]; in particular, [9] dealt with hydrogen degradation in low carbon steels at different levels. The authors found that long-term hydrogen saturation leads to a reduction in bulk elastic modulus. Microstructural analysis revealed that the reasons for this may lie in the deformation of larger grains, cracks, and blisters caused by hydrogen penetration. As observed in [14], prolonged hydrogen charging may decrease the value of Young's modulus by up to 15% in a gamma titanium aluminide alloy. The experiments in [15] were conducted for three different grades of high-strength steel. Hydrogen charging of steels resulted in degradation of mechanical properties and changes in the microstructure in all cases.

Summarizing the above, we can remark that analytical models of hydrogen degradation generally tend to account for diffusion assumed to be the primary process leading to changes in microstructure and to degradation of mechanical properties. The degradation of elastic properties due to the actual changes in the microstructure has received much less attention.

The goal of our study consisted in determining the effective elastic moduli for a material whose microstructure is assumed to have formed as a result of hydrogen degradation.

For this purpose, we solve the problem of homogenization which allows to estimate the contribution of inhomogeneities to a given property. We consider the influence that the potential shape and orientation of microcracks in the material, as well as its porosity have on effective Young's moduli.

## Microstructure of the material

This paper studies the influence of coin-like microcracks, as well as pores on the effective properties of materials, assuming that the former accounts for intergranular cracking, and the latter for the impact of the pores which did not merge into microcracks, and the voids near grain boundary triple junctions. It was found in [16] that jagged boundaries of planar cracks or deviations from circular shape are unimportant for elastic properties of the material, so these inhomogeneities can be simulated as elliptical.



Microcracks were modelled by oblate spheroids and pores by spheres in our study. We consider three cases of inhomogeneities in the material.

In the first case, we assumed that microcracks have random (isotropic) distribution in the bulk. This pattern is characteristic for metal products weakly deformed during production.

In the second case, we assumed that microcracks have preferential orientation (for instance, in case of rolling and layered structure of material). A factor that we took into account was that microcracks may deviate from the preferential orientation in this instance.

Finally, to complete the picture, we considered the case when the symmetry axes of spheroid microcracks have random orientation in a certain plane. This situation is observed, for example, when a material is compressed and there are no cracks forming in the plane of loading.

### Compliance tensor of spheroid microcrack

Contribution tensors are used within the homogenization method to describe the contributions of individual inhomogeneities into the given properties [17].

Taking a homogenous elastic material (matrix) with the compliance tensor  $\mathbf{S}^0$ , let us consider a representative volume  $V$ , containing an isolated inhomogeneity of volume  $V_1$  with the compliance tensor  $\mathbf{S}^1$ . The volume  $V$  should be, on the one hand, large enough to reflect the characteristic microstructure, and, on the other hand, small enough compared with the entire volume of the material so that the variations of the macroscopic fields are negligible.

Correct choice of representative volume is discussed, for example, in [17]. The effective elastic properties of the material are estimated by means of a tensor accounting for the contribution of inhomogeneities to compliance: it is a fourth-rank tensor  $\mathbf{H}$ , which describes extra strain  $\Delta\epsilon$  generated in volume  $V$  due to inhomogeneity:

$$\Delta\epsilon = \frac{V_1}{V} \mathbf{H} : \sigma_0, \quad (1)$$

where  $\sigma_0$  is the stress field depending on boundary conditions, which would be generated in the volume in the absence of inhomogeneities.

The tensor accounting for the contribution of an ellipsoidal inhomogeneity to compliance can be expressed in terms of compliance tensors of the matrix, inhomogeneities characterizing the material properties, and the second Hill's tensor  $\mathbf{Q}$  reflecting the influence of inhomogeneity shape:

$$\mathbf{H} = \left[ (\mathbf{S}^1 - \mathbf{S}^0)^{-1} + \mathbf{Q} \right]^{-1}. \quad (2)$$

The fourth-rank tensor  $\mathbf{Q}$  is related to the first Hill's tensor  $\mathbf{P}$  by

$$\mathbf{Q} = \mathbf{C}^0 - \mathbf{C}^0 : \mathbf{P} : \mathbf{C}^0,$$

where  $\mathbf{C}^0$  is the matrix stiffness tensor.

In turn, the fourth-rank tensor  $\mathbf{P}$  is expressed in terms of derivatives of Green's function  $\mathbf{G}$  for displacements as

$$\mathbf{P} = \left( \nabla \int_{V_1} \mathbf{G}(\mathbf{x} - \mathbf{x}') \nabla dV' \right)_{(1,2)(3,4)}^S, \quad (3)$$

where  $( )_{(1,2)(3,4)}^S$  indicates symmetry with respect to permutation of subscripts in the first and the second pair.

Pores and microcracks are characterized by zero elastic moduli. Then  $\mathbf{S}^1 \rightarrow \infty$ , and expression (2) is reduced to  $\mathbf{H} = \mathbf{Q}^{-1}$ . Tensors  $\mathbf{H}$  and  $\mathbf{Q}$  are transversely isotropic for a spheroidal microcrack in an isotropic matrix (the symmetry axis is codirectional to the inhomogeneity symmetry axis), and can be expressed as linear combinations of the tensor basis elements  $\mathbf{T}_1, \mathbf{T}_2, \dots, \mathbf{T}_6$  [18]:

$$\mathbf{H} = \sum_{k=1}^6 h_k \mathbf{T}_k, \quad \mathbf{Q} = \sum_{k=1}^6 q_k \mathbf{T}_k. \quad (4)$$

The basis elements have the following form:

$$\begin{aligned} \mathbf{T}_1 &= \boldsymbol{\theta}\boldsymbol{\theta}, \quad \mathbf{T}_2 = \frac{1}{2} \left( (\boldsymbol{\theta}\boldsymbol{\theta})_{(1,4)}^T + (\boldsymbol{\theta}\boldsymbol{\theta})_{(2,4)}^T - \boldsymbol{\theta}\boldsymbol{\theta} \right), \\ \mathbf{T}_3 &= \mathbf{I} - \mathbf{nn}, \quad \mathbf{T}_4 = \mathbf{nn}, \\ \mathbf{T}_5 &= \frac{1}{4} \left( \mathbf{n}\boldsymbol{\theta}\mathbf{n} + (\mathbf{n}\boldsymbol{\theta}\mathbf{n})_{(1,2)(3,4)}^T + (\boldsymbol{\theta}\mathbf{nn})_{(1,4)}^T + (\boldsymbol{\theta}\mathbf{nn})_{(2,3)}^T \right), \\ \mathbf{T}_6 &= \mathbf{nnnn}, \end{aligned} \quad (5)$$

where  $\boldsymbol{\theta} = \mathbf{I} - \mathbf{nn}$  ( $\mathbf{I}$  is the second-rank unit tensor) is the projection to the plane normal to the unit vector  $\mathbf{n}$  along the symmetry axis.

The basis introduced allows to represent the transversely isotropic tensor  $\mathbf{B} = \sum b_i \mathbf{T}_i$  (summation over repeated indices from 1 to 6) and its inverse in one basis [17]:

$$\begin{aligned} \mathbf{B}^{-1} &= \frac{b_6}{2\Delta} \mathbf{T}_1 + \frac{1}{b_2} \mathbf{T}_2 - \frac{b_3}{\Delta} \mathbf{T}_3 - \\ &\quad - \frac{b_4}{\Delta} \mathbf{T}_4 + \frac{4}{b_5} \mathbf{T}_5 + \frac{2b_1}{\Delta} \mathbf{T}_6, \end{aligned} \quad (6)$$

where  $\Delta = 2(b_1 b_6 - b_3 b_4)$ .

Thus, determining the tensors  $\mathbf{Q}$  and  $\mathbf{H}$  for a pore or a microcrack is reduced to determining the components of tensor  $\mathbf{Q}$ , which are calculated as follows in case of a spheroidal inclusion [19]:

$$\begin{aligned} q_1 &= \mu^0 [4\kappa - 1 - 2(3\kappa - 1)f_0 - 2\kappa f_1], \\ q_2 &= 2\mu^0 [1 - (2 - \kappa)f_0 - \kappa f_1], \\ q_3 &= q_4 = 2\mu^0 [(2\kappa - 1)f_0 + 2\kappa f_1], \\ q_5 &= 4^{1/4} [f_0 + 4\kappa f_1], \\ q_6 &= 8\mu^0 \kappa [f_0 - f_1], \quad \kappa = (1 - \nu^0)/2, \end{aligned} \quad (7)$$

where  $\mu^0$  and  $\nu^0$  are the shear modulus and Poisson's ratio of the matrix, respectively.

Parameters  $f_0$  and  $f_1$  depend on the aspect ratio of spheroid semi-axes  $\gamma = a_3/a$  ( $a_3$  is the axis of rotation) as follows:

$$\begin{aligned} f_0 &= \frac{1 - g}{2(1 - \gamma^{-2})}, \\ f_1 &= \frac{1}{4(1 - \gamma^{-2})^2} [(2 + \gamma^{-2})g - 3\gamma^{-2}], \end{aligned}$$

where

$$g = \begin{cases} \frac{1}{\gamma\sqrt{1 - \gamma^{-2}}} \arctan \frac{\sqrt{1 - \gamma^{-2}}}{\gamma}, & \gamma \leq 1; \\ \frac{1}{2\gamma\sqrt{\gamma^2 - 1}} \ln \left( \frac{\gamma + \sqrt{\gamma^2 - 1}}{\gamma - \sqrt{\gamma^2 - 1}} \right), & \gamma \geq 1. \end{cases}$$

For a spheroidal inhomogeneity,  $\gamma = 1$ ,  $g = 1$ ,  $f_0 = 1/3$ ,  $f_1 = 1/15$ . The compliance tensor of a spheroidal pore  $\mathbf{H}_p$  is isotropic and takes the following form:

$$\begin{aligned} \mathbf{H}_p &= \frac{15(1 - \nu)}{2\mu} \times \\ &\times \left[ \frac{1}{10(1 + \nu)} \frac{1}{3} \mathbf{I} + \frac{1}{7 - 5\nu} \left( \mathbf{J} - \frac{1}{3} \mathbf{I} \right) \right], \end{aligned} \quad (8)$$

where  $\mathbf{I}$  is the second-rank unit tensor,

$$\mathbf{J} = \frac{1}{2} \left( (\mathbf{I})_{(1,4)}^T + (\mathbf{I})_{(2,4)}^T \right)$$

is the fourth-rank unit tensor.

Tensors  $\mathbf{I}$  and  $\mathbf{J}$  can be represented as follows in the transversely isotropic basis [17]:

$$\begin{aligned} \mathbf{I} &= \mathbf{T}_1 + \mathbf{T}_3 + \mathbf{T}_4 + \mathbf{T}_6, \\ \mathbf{J} &= \frac{1}{2} \mathbf{T}_1 + \mathbf{T}_2 + 2\mathbf{T}_5 + \mathbf{T}_6. \end{aligned} \quad (9)$$

### Effective properties of metals with spheroidal microcracks and pores

Effective properties of heterogeneous materials can be determined by different methods. A historical review of these methods can be found, for example, in [20], while [17] presents analysis of the current situation. All analytical methods are approximate solutions, while the exact solution can be obtained only numerically for specific materials with a known microstructure. The best-known analytical methods include:

non-interaction approximation,  
effective media schemes,  
differential scheme,

effective field methods (including both Mori–Tanaka and Kanaun–Levin methods),

Maxwell scheme.

These methods differ in their approaches to accounting for the mutual influence of multiple inhomogeneities, while their applicability is limited by material symmetry, shape and orientation of inclusions. The Maxwell scheme seems to be an optimal method to describe the contributions of inhomogeneities of different shape and orientation [21].

Let us find an effective compliance tensor using the Maxwell scheme in terms of contribution tensors:

$$\mathbf{S}^{eff} = \mathbf{S}^0 + \left\{ \left[ \frac{1}{V_\Omega} \sum_i V_i \mathbf{H}_i \right]^{-1} - \mathbf{Q}_\Omega \right\}^{-1}, \quad (10)$$

where  $\mathbf{Q}_\Omega$  is the second Hill's tensor determined for a homogenized region  $\Omega$  which contains isolated inhomogeneities and possesses the required effective properties.

In the absence of  $\mathbf{Q}_\Omega$ , the effective compliance tensor coincides with the value determined neglecting the interaction of inhomogeneities.

Let us determine the total contribution of isolated inhomogeneities to compliance. If the inhomogeneities have the same shape and size but different orientation, then their total contribution can be determined as the product of the averaged contribution by volume fraction of inhomogeneities [17]. The averaged value of the contribution tensor for spheroidal inclusions coincides with the contribution tensor of a separate spheroidal pore  $\mathbf{H}_p$  due to symmetry. If spheroidal microcracks and spherical pores are present in the material, their total contribution is determined as

$$\frac{1}{V} \sum_i V_i \mathbf{H}_i = \varphi_{mc} \langle \mathbf{H}_{mc} \rangle + \varphi_p \mathbf{H}_p, \quad (11)$$



where  $\varphi_{mc}$  and  $\varphi_p$  are the volume fractions of oblate spheroids and spheres, respectively,  $\langle \mathbf{H}_{mc} \rangle$  is the value of the averaged total tensor describing the contribution of microcracks to compliance.

It is sufficient to average the elements of the tensor basis to determine  $\langle \mathbf{H}_{mc} \rangle$ , i.e.,

$$\langle \mathbf{H}_{mc} \rangle = \sum_{k=1}^6 h_{mc(k)} \langle \mathbf{T}_k \rangle.$$

If there is a preferential orientation  $\mathbf{m}$ , the symmetry axes  $\mathbf{n}$  of spheroidal microcracks tend to coincide with  $\mathbf{m}$  with a certain deviation depending on the scatter parameter  $\lambda$ .

Let us introduce a probability density function for the orientation distribution of spheroid axes of symmetry over a semisphere ( $0 \leq \theta \leq \pi/2$ ) in accordance with [22]:

$$\psi_*(\theta) = \frac{1}{2\pi} \left[ (\lambda^2 + 1) e^{-\lambda\theta} + \lambda e^{-\lambda\pi/2} \right]. \quad (12)$$

If  $\lambda = 0$ , the microcracks have a random orientation in the representative volume and the material is isotropic. If  $\lambda \rightarrow \infty$ , the symmetry axes of the microcracks are oriented strictly along the preferential direction and the material is transversely isotropic with the symmetry axis coinciding with  $\mathbf{m}$ . To average the elements of the tensor basis, let us integrate them with respect to the surface of a semisphere  $\tilde{\Omega}_{1/2}$  of unit radius:

$$\langle \mathbf{T}_i \rangle = \frac{1}{2\pi} \int_{\tilde{\Omega}_{1/2}} \mathbf{T}_i d\tilde{\Omega}_{1/2}. \quad (13)$$

If the spheroid axes of symmetry  $\mathbf{n}$  are randomly oriented in a certain plane normal to  $\mathbf{m}$ , the material is transversely isotropic and its axis of symmetry is co-directional to  $\mathbf{m}$ . To average the tensor basis elements, let us integrate them with respect to a unit circle  $l_1$  lying in a plane normal to  $\mathbf{m}$ :

$$\langle \mathbf{T}_i \rangle = \frac{1}{2\pi} \int_{l_1} \mathbf{T}_i dl_1. \quad (14)$$

The averaged values of the elements of transversely isotropic basis are given in the Appendix.

The choice of homogenized domain  $\Omega$  used in the Maxwell scheme to account for the interactions of inhomogeneities is discussed in detail in [22].

In case of spheroidal inhomogeneities, this domain is also a spheroid with the aspect ratio of semiaxes expressed as

$$\tilde{a}_\Omega = \begin{cases} \sum_i V_i Q_{3333}^{(i)} / \sum_i V_i Q_{1111}^{(i)}, & \text{if } \sum_i V_i Q_{3333}^{(i)} / \sum_i V_i Q_{1111}^{(i)} \leq 1, \\ \sum_i V_i P_{1111}^{(i)} / \sum_i V_i P_{3333}^{(i)}, & \text{if } \sum_i V_i Q_{3333}^{(i)} / \sum_i V_i Q_{1111}^{(i)} > 1, \end{cases} \quad (15)$$

where  $Q_{ijkl}$ ,  $P_{ijkl}$  are Hill's tensor components  $\mathbf{Q}$  and  $\mathbf{P}$ , respectively.

In general, the shape of homogenized domain depends on concentration, orientation and shapes of inhomogeneities. If the inhomogeneities have isotropic orientation distribution, the shape is spherical. Otherwise, if the material contains spherical pores of the same size and spheroidal microcracks of the same size and shape, we need to define the quantity

$$\frac{1}{V} \sum_i V_i \mathbf{Q}_i = \varphi_{mc} \langle \mathbf{Q}_{mc} \rangle + \varphi_p \mathbf{Q}_p, \quad (16)$$

$$\langle \mathbf{Q}_{mc} \rangle = \sum_{k=1}^6 q_{mc(k)} \langle \mathbf{T}_k \rangle.$$

After we find the components of the effective compliance tensor,  $S_{ijkl}^{eff}$ , we can determine effective Young's moduli. To be definite, let us assume that the symmetry axis of the material coincides with the direction  $\mathbf{e}_3$  of the Cartesian basis ( $\mathbf{e}_1, \mathbf{e}_2, \mathbf{e}_3$ ).

Then the effective Young's moduli of the transversely isotropic material  $E_{11}^{eff} = E_{22}^{eff}, E_{33}^{eff}$  can be calculated as follows:

$$E_{11}^{eff} = E_{22}^{eff} = \frac{1}{S_{1111}^{eff}}, E_{33}^{eff} = \frac{1}{S_{3333}^{eff}}. \quad (17)$$

## Results and discussion

In this study, we found the effective elastic properties of steel with shear modulus  $\mu^0 = 80$  GPa and Poisson's ratio  $\nu^0 = 0.3$ . Young's modulus of steel  $E^0$  follows the expression

$$E^0 = 2 \mu^0 (1 + \nu^0).$$

If the inhomogeneities have random orientation distribution, the material is isotropic, i.e.,

$$\mathbf{S}^{eff} = K^{eff} \mathbf{\Pi} + \mu^{eff} \left( \mathbf{J} - \frac{1}{3} \mathbf{\Pi} \right), \quad (18)$$

where  $K^{eff}$  and  $\mu^{eff}$  are the effective values of the coefficient of compressibility and shear modulus respectively.



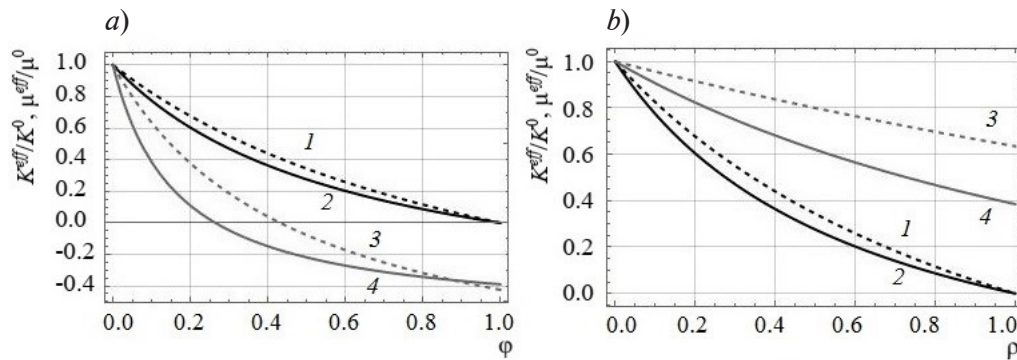


Fig. 1. Dependences of moduli  $K^{eff}/K^0$  (solid lines) and  $\mu^{eff}/\mu^0$  (dashed lines) on porosity of material (a) and density of cracks (b). Pores are modeled by spheres (1, 2), microcracks by spheroids with aspect ratio of semiaxes  $\gamma = 0.1$  (3, 4)

Fig. 1, a shows the dependencies of moduli  $K^{eff}/K^0$ ,  $\mu^{eff}/\mu^0$  on porosity of the material  $\phi$  for a spherical pore ( $\gamma = 1$ ) and a spheroidal microcrack (at  $\gamma = 0.1$ ). Evidently, the porosity of the material with spherical inhomogeneities may theoretically reach 100% (the material disappears). In case of microcracks of oblate spheroidal shape, the elastic moduli approach zero at porosities less than 100% (around 26% at  $\gamma = 0.1$ ). Negative values of elastic moduli at high concentrations of inhomogeneities indicate that the problem of homogenization cannot be solved correctly for this material.

Thus, the acceptable porosity of the material is defined by a relation between the aspect ratio of the microcrack semiaxes. To take this correlation into account, we can introduce crack density into the model

$$\rho = (4/3)\pi a^3 N/V$$

( $N$  is the number of microcracks) [17], related to porosity  $\phi$  as  $\phi = \rho\gamma$ .

Fig. 1, b shows the dependences of moduli  $K^{eff}/K^0$  and  $\mu^{eff}/\mu^0$  on crack density.

To find a possible explanation for the limited acceptable porosity, we studied the dependence of effective shear modulus  $\mu^{eff}_{12}/\mu^0$  on porosity for different scatter parameters  $\lambda$ . We considered spheroidal microcracks with  $\gamma = 0.10$  and  $0.05$ . The results are shown in Fig. 2.

The results indicate that given the same aspect ratio of spheroid semiaxes  $\gamma$ , the porosity of the material may theoretically reach 100% if it contains parallel oriented microcracks ( $\lambda \rightarrow \infty$ ), or, if the microcracks deviate from the preferential orientation, the acceptable porosity decreases, reaching the minimum with an isotropic distribution ( $\lambda = 0$ ). As evident from comparing Figs. 2, a and b, spheroids with a high value of  $\gamma$  have a higher value of acceptable

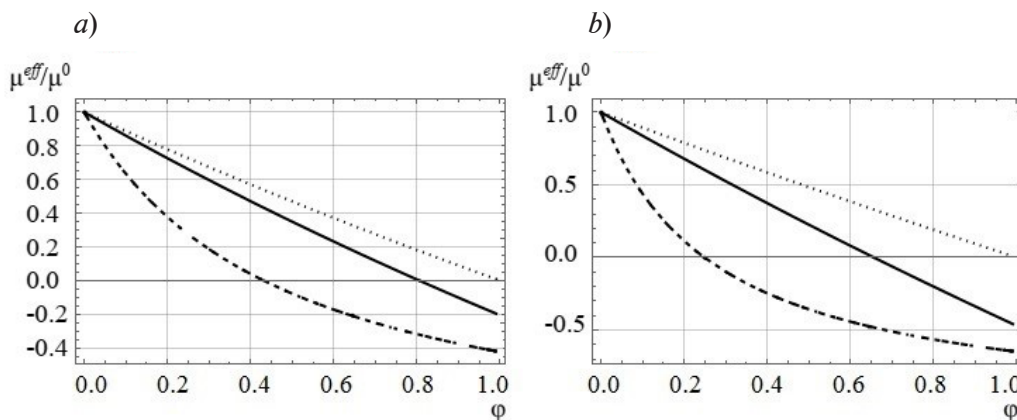


Fig. 2. Dependence of effective shear modulus  $\mu^{eff}_{12}/\mu^0$  on porosity of material at aspect ratio of spheroid semiaxes  $\gamma = 0.10$  (a) and  $\gamma = 0.05$  (b). Scatter parameter  $\lambda = 0$  (dashed lines),  $\lambda = 10$  (solid lines) and  $\lambda \rightarrow \infty$  (dotted lines)



porosity. Apparently, when porosity reaches a certain value depending on the degree of deviation of spheroid microcracks from the preferential orientation, as well as on their degree of oblateness, multiple narrow microcracks cannot be regarded as isolated. Since this assumption is actually adopted for self-consistent schemes (which also include the Maxwell method), more accurate methods need to be found to account for the mutual influence of inhomogeneities.

We determined the dependences of effective Young's moduli  $E_{ij}^{eff}/E^0$  on porosity of material  $\varphi$  for three case of orientation distribution of inhomogeneities:

- isotropic distribution (I),
- preferential orientation with the scatter parameter  $\lambda$  (II),
- random distribution of symmetry axes of inhomogeneities in a certain plane (III).

We assumed that the material contained two types of inhomogeneities: oblate spheroidal microcracks with  $\gamma = 0.1$  and spherical pores.

Total porosities  $\varphi$  of all inhomogeneities were taken in the range between 0 and 10%.

Materials with the following types of microstructure were considered:

only oblate spheroids are present ( $\varphi_{mc} = \varphi$ ,  $\varphi_p = 0$ );

ratio of total volume of oblate spheroids to total volume of pores is 2 : 1 ( $\varphi_{mc} = 2\varphi/3$ ,  $\varphi_p = \varphi/3$ );

total volume of oblate spheroids equals total volume of pores ( $\varphi_{mc} = \varphi/2 = \varphi_p$ );

only pores are present ( $\varphi_{mc} = 0$ ,  $\varphi_p = \varphi$ ).

Fig. 3 shows the computational results taking into account the given conditions. As expected, an increase in porosity leads to a decrease in elastic moduli in all cases. Evidently,

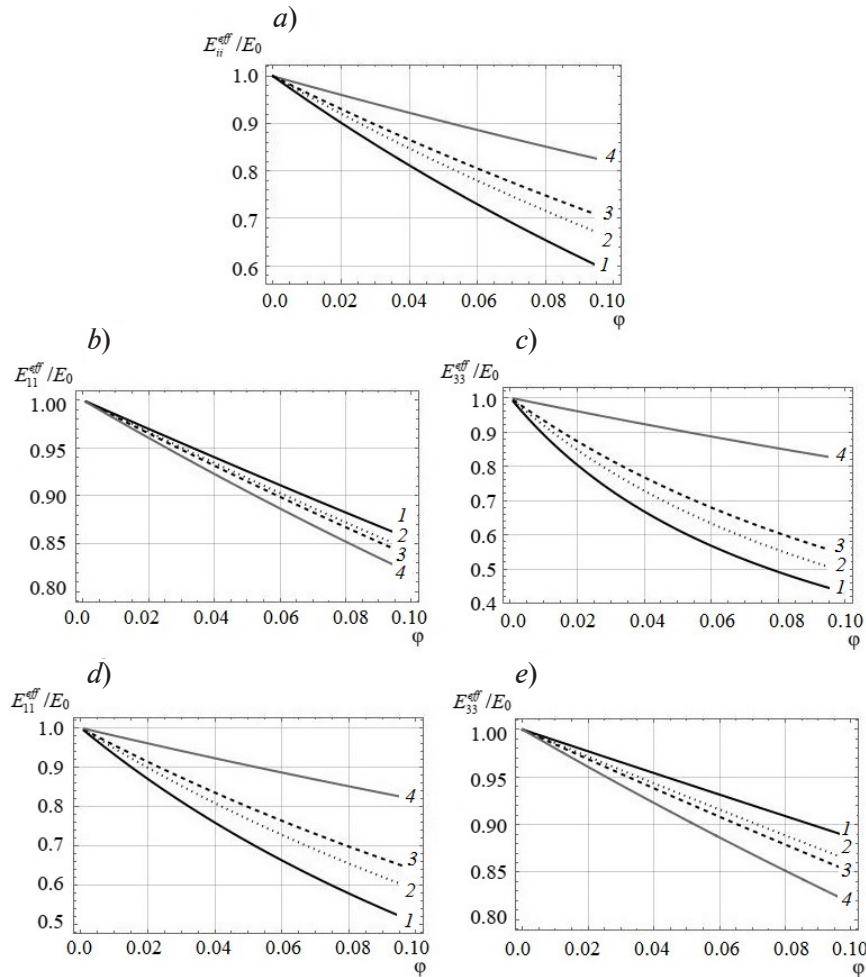


Fig. 3. Dependence of moduli  $E_{ij}^{eff}/E^0$  on porosity of material for different orientation distributions of inhomogeneities ( $\gamma = 0.1$ ): I (a), II (при  $\lambda = 10$ ) (b, c) and III (d, e) (see explanations in the text).

The following types of microstructures were considered:  $\varphi_{mc} = \varphi$ ,  $\varphi_p = 0$  (1);

$\varphi_{mc} = 2\varphi/3$ ,  $\varphi_p = \varphi/3$  (2);  $\varphi_{mc} = \varphi/2 = \varphi_p$  (3);  $\varphi_{mc} = 0$ ,  $\varphi_p = \varphi$  (4)

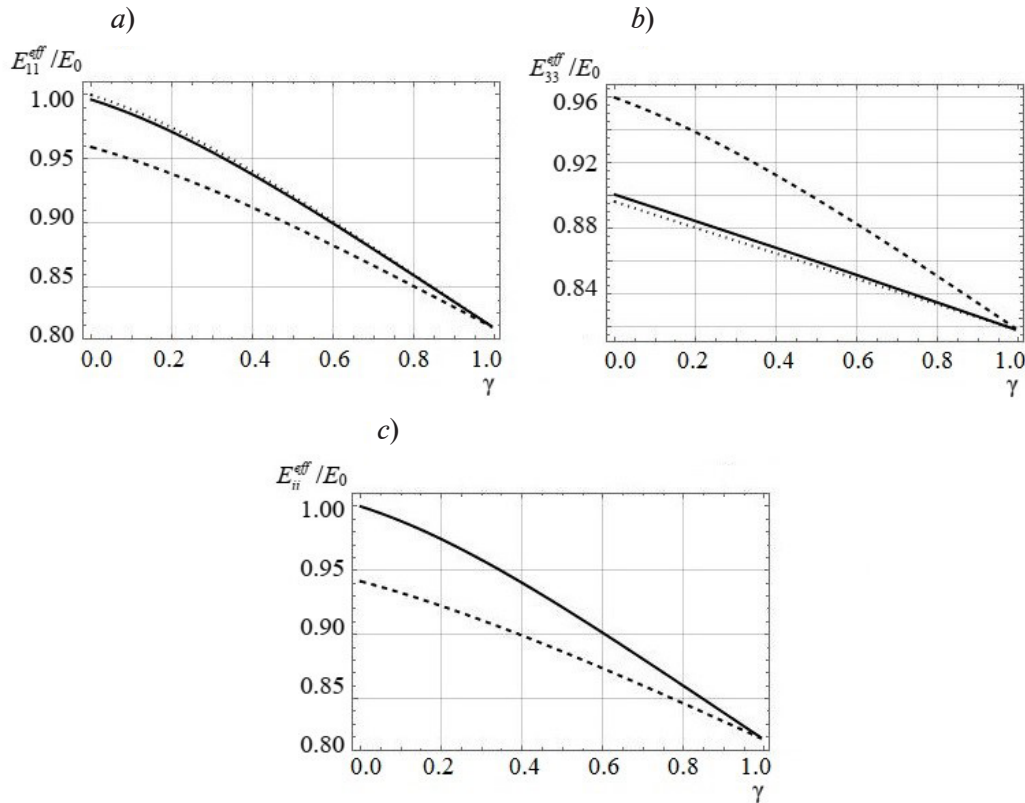


Fig. 4. Dependences of moduli  $E_{ij}^{eff}/E_0$  on parameter  $\gamma$  at different orientation distributions of inhomogeneities (crack density  $\rho = 0.1$ ): I, II (a, b) and III (c) (see explanations in the text); a, b correspond to the scatter parameters  $\lambda = 0$  (dashed lines),  $\lambda = 10$  (solid lines) and  $\lambda \rightarrow \infty$  (dotted-dashed lines); c corresponds to the moduli  $E_{11}^{eff}/E_0$  (dashed lines) and  $E_{33}^{eff}/E_0$  (solid lines)

pores have less effect on Young's modulus than microcracks at the same value of  $\varphi$  for an isotropic distribution (Fig. 3, a). For example, if  $\varphi = 0.10$ , then the value of modulus  $E_{ii}^{eff}/E_0 \approx 0.82$  at  $\varphi_{mc} = 0$ ,  $\varphi_p = \varphi$  and  $E_{ii}^{eff}/E_0 \approx 0.58$  at  $\varphi_{mc} = \varphi$ ,  $\varphi_p = 0$ .

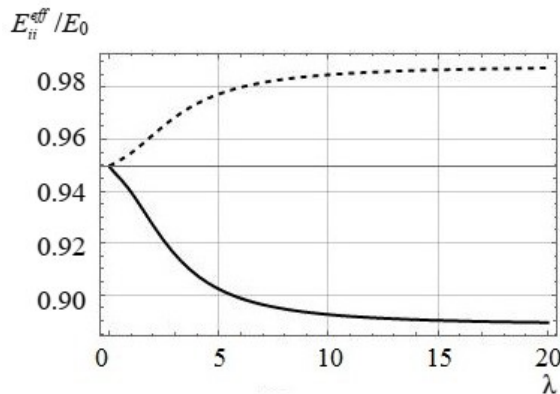


Fig. 5. Dependences of moduli  $E_{11}^{eff}/E_0$  (dashed line) and  $E_{33}^{eff}/E_0$  (solid line) on scatter parameter; parameter values  $\gamma = 0.1$ ,  $\varphi = 0.01$  were taken

If microcracks have a preferential orientation in the material (Fig. 3, b, c), Young's modulus along the material axis decreases more than Young's modulus in the isotropic plane. Narrow cracks make a larger contribution to  $E_{33}^{eff}$  compared to pores, and a smaller contribution to  $E_{11}^{eff}$ . Conversely, if the symmetry axes of microcracks are distributed in the isotropic plane (Fig. 3, d, e), Young's modulus along the material axis decreases less than Young's modulus in the isotropic plane. Narrow cracks make a larger contribution to  $E_{11}^{eff}$  compared to pores, and a smaller contribution to  $E_{33}^{eff}$ .

Next, we studied the dependence of effective Young's moduli  $E_{ij}^{eff}/E_0$  on the aspect ratio of spheroid semiaxes  $\gamma$ . An increase in the parameter  $\gamma$  from 0 to 1 describes the change in the shape of the spheroid from a disk to a sphere. As established above, the total porosity cannot be random in case of narrow microcracks, so the concentration of cracks was assumed to be constant and, thus, the total porosity varied due to varying  $\gamma$ .



It was assumed that crack density  $\rho = 0.1$ ; in this case, if  $\gamma = 0.1$ , the total porosity of material amounts to 1%, which provides the best agreement with the experimental data.

Fig. 4 shows the computational results for the considered cases of orientation distribution of inhomogeneities. Evidently (see Figs. 4, *a*, *b*), if  $\lambda > 0$ , the presence of oblate spheroids leads to a larger decrease in Young's modulus along the material axis and to a smaller decrease in the isotropic plane. For example, the values of the moduli are  $E_{11}^{eff}/E_0 \approx 0.86$ ,  $E_{33}^{eff}/E_0 \approx 0.92$  at  $\lambda = 10$ ,  $\gamma = 0.5$ . If the symmetry axes of microcracks have random orientations in a certain plane (see Fig. 4, *c*), Young's modulus in the isotropic plane of the material is more sensitive to the decrease of the aspect ratio  $\gamma$  of spheroid semiaxes than Young's modulus along the material axis. For example, we obtained  $E_{11}^{eff}/E_0 \approx 0.89$ ,  $E_{33}^{eff}/E_0 \approx 0.92$  at  $\gamma = 0.5$ . A decrease in Young's moduli was observed with an increase in  $\gamma$  for all orientation distributions of inhomogeneities, because the total porosity of material depends linearly on the parameter  $\gamma$ .

We considered a separate case of preferential orientation of spheroids and studied the dependence of effective properties of the material on the scatter parameter  $\lambda$ , taking  $\gamma = 0.1$ ,  $\varphi = 0.01$ . Fig. 5 shows the computational results. The material is isotropic at  $\lambda = 0$ , characterized by effective Young's modulus  $E_{11}^{eff}/E_0 \approx 0.95$ . As seen from Fig. 5, the more the symmetry axis of inhomogeneities deviate from the preferential orientation (with decreasing  $\lambda$ ), the more significantly the effective moduli change. Different patterns are observed in the changes in Young's moduli along the material axis and in the isotropic plane: Young's modulus along the material axis decreases if inhomogeneities smooth out ( $\lambda \rightarrow \infty$ ), while Young's modulus in the isotropic plane conversely decreases with increasing scatter ( $\lambda \rightarrow 0$ ).

### Conclusion

We have analyzed the variation in effective Young's moduli of metals with microstructures typical for hydrogen-enhanced degradation, specifically, for the microstructures containing intergranular microcracks and pores. Microcracks were modeled by oblate spheroids, and pores were modeled by spheres. The homogenization problem was solved using the Maxwell problem in terms of contribution tensors. We have studied the dependences of

effective elastic properties on porosity, degree of oblateness of spheroids and orientation distribution of inhomogeneities. We have established that effective Young's moduli heavily depend on the aspect ratio of semiaxes of spheroidal microcracks and porosity of the material. Effective Young's moduli along different directions can change to a greater or lesser degree depending on the orientation of microcracks in the material. This proves that it is essential to account for the structure of metal products (for example, layered structure of metal) and, consequently, the method by which they were produced (for example, rolling) when determining the characteristics of metals charged with hydrogen. Moreover, depending on orientation, microcracks can make smaller or greater contributions compared to pores, with the same concentration of microcracks and pores. In addition, we have found that the correlation between the porosity of material and the shape of microcracks should be taken into account in solving the homogenization problem.

### Appendix

#### Averaged values of transversely isotropic basis elements

If inhomogeneities have isotropic orientation distribution, the averaged values of the transversely isotropic basis elements have the following form [16]:

$$\langle \mathbf{T}_1 \rangle = \frac{1}{15} [7\mathbf{T}_1 + 2\mathbf{T}_2 + 6(\mathbf{T}_3 + \mathbf{T}_4) + 4\mathbf{T}_5 + 8\mathbf{T}_6],$$

$$\langle \mathbf{T}_2 \rangle = \frac{1}{15} [\mathbf{T}_1 + 6\mathbf{T}_2 - 2(\mathbf{T}_3 + \mathbf{T}_4) + 12\mathbf{T}_5 + 4\mathbf{T}_6],$$

$$\langle \mathbf{T}_3 \rangle = \langle \mathbf{T}_4 \rangle = \frac{1}{15} [3\mathbf{T}_1 - 2\mathbf{T}_2 + 4(\mathbf{T}_3 + \mathbf{T}_4) - 4\mathbf{T}_5 + 2\mathbf{T}_6],$$

$$\langle \mathbf{T}_5 \rangle = \frac{1}{30} [\mathbf{T}_1 + 6\mathbf{T}_2 - 2(\mathbf{T}_3 + \mathbf{T}_4) + 12\mathbf{T}_5 + 4\mathbf{T}_6],$$

$$\langle \mathbf{T}_6 \rangle = \frac{1}{15} [2(\mathbf{T}_1 + \mathbf{T}_2) + \mathbf{T}_3 + \mathbf{T}_4 + 4\mathbf{T}_5 + 3\mathbf{T}_6].$$

If the symmetry axes of inhomogeneities have a preferential orientation along the axis  $\mathbf{m}$  with the scatter parameter  $\lambda$ , the averaged values of transversely isotropic basis elements are expressed as

$$\begin{aligned} \langle \mathbf{T}_1 \rangle = & (1 - 2g_1(\lambda) + g_3(\lambda))\mathbf{T}_1 + g_3(\lambda)\mathbf{T}_2 + \\ & + (1 - g_1(\lambda) - g_2(\lambda) + g_4(\lambda))(\mathbf{T}_3 + \mathbf{T}_4) + \end{aligned}$$

$$\begin{aligned}
 & +4g_4(\lambda)\mathbf{T}_5 + (1-2g_2(\lambda)+g_5(\lambda))\mathbf{T}_6, \\
 \langle \mathbf{T}_2 \rangle &= \frac{g_3(\lambda)}{2}\mathbf{T}_1 + \left(1-2g_1(\lambda)+\frac{g_3(\lambda)}{2}\right)\mathbf{T}_2 + \\
 & +\frac{1}{2}(g_1(\lambda)+g_2(\lambda)+g_4(\lambda)-1)(\mathbf{T}_3+\mathbf{T}_4) + \\
 & +2(g_4(\lambda)-g_1(\lambda)-g_2(\lambda)+1)\mathbf{T}_5 + \\
 & +\frac{1}{2}(g_5(\lambda)-2g_2(\lambda)+1)\mathbf{T}_6, \\
 \langle \mathbf{T}_3 \rangle &= (g_1(\lambda)-g_3(\lambda))\mathbf{T}_1 - g_3(\lambda)\mathbf{T}_2 + \\
 & + (g_2(\lambda)-g_4(\lambda))\mathbf{T}_3 + (g_1(\lambda)-g_4(\lambda))\mathbf{T}_4 - \\
 & -4g_4(\lambda)\mathbf{T}_5 + (g_2(\lambda)-g_5(\lambda))\mathbf{T}_6, \\
 \langle \mathbf{T}_4 \rangle &= (g_1(\lambda)-g_3(\lambda))\mathbf{T}_1 - g_3(\lambda)\mathbf{T}_2 + \\
 & + (g_1(\lambda)-g_4(\lambda))\mathbf{T}_3 + (g_2(\lambda)-g_4(\lambda))\mathbf{T}_4 - \\
 & -4g_4(\lambda)\mathbf{T}_5 + (g_2(\lambda)-g_5(\lambda))\mathbf{T}_6, \\
 \langle \mathbf{T}_5 \rangle &= \left(\frac{g_1(\lambda)}{2}-g_3(\lambda)\right)\mathbf{T}_1 + \\
 & + (g_1(\lambda)-g_3(\lambda))\mathbf{T}_2 - g_4(\lambda)(\mathbf{T}_3+\mathbf{T}_4) + \\
 & + (g_1(\lambda)+g_2(\lambda)-4g_4(\lambda))\mathbf{T}_5 + \\
 & + (g_2(\lambda)-g_5(\lambda))\mathbf{T}_6, \\
 \langle \mathbf{T}_6 \rangle &= g_3(\lambda)(\mathbf{T}_1+\mathbf{T}_2) + \\
 & + g_4(\lambda)(\mathbf{T}_3+\mathbf{T}_4+4\mathbf{T}_5) + g_5(\lambda)\mathbf{T}_6.
 \end{aligned}$$

Here

$$\begin{aligned}
 g_1(\lambda) &= \frac{18-\lambda e^{-\frac{\pi\lambda}{2}}(\lambda^2+3)}{6(\lambda^2+9)}, \\
 g_2(\lambda) &= \frac{\left(3+\lambda e^{-\frac{\pi\lambda}{2}}\right)(\lambda^2+3)}{3(\lambda^2+9)},
 \end{aligned}$$

$$\begin{aligned}
 g_3(\lambda) &= \frac{30}{(\lambda^2+9)(\lambda^2+25)} - \\
 & - \lambda e^{-\frac{\pi\lambda}{2}} \frac{(7\lambda^4+178\lambda^2+435)}{60(\lambda^2+9)(\lambda^2+25)}, \\
 g_4(\lambda) &= \frac{3(5+\lambda^2)}{(\lambda^2+9)(\lambda^2+25)} + \\
 & + \lambda e^{-\frac{\pi\lambda}{2}} \frac{(\lambda^4+19\lambda^2+30)}{15(\lambda^2+9)(\lambda^2+25)}, \\
 g_5(\lambda) &= \frac{(\lambda^4+22\lambda^2+45)}{(\lambda^2+9)(\lambda^2+25)} + \\
 & + \lambda e^{-\frac{\pi\lambda}{2}} \frac{(\lambda^4+34\lambda^2+105)}{5(\lambda^2+9)(\lambda^2+25)}.
 \end{aligned}$$

If the symmetry axes of inhomogeneities have a random orientation along the plane normal to the axis  $\mathbf{m}$ , the averaged values of transversely isotropic basis elements are expressed as follows [16]:

$$\begin{aligned}
 \langle \mathbf{T}_1 \rangle &= \frac{1}{4}[\mathbf{T}_1 + \mathbf{T}_2 + 2(\mathbf{T}_3 + \mathbf{T}_4) + 4\mathbf{T}_6], \\
 \langle \mathbf{T}_2 \rangle &= \frac{1}{8}[\mathbf{T}_1 + \mathbf{T}_2 - 2(\mathbf{T}_3 + \mathbf{T}_4) + 8\mathbf{T}_5 + 4\mathbf{T}_6], \\
 \langle \mathbf{T}_3 \rangle &= \frac{1}{4}[\mathbf{T}_1 - \mathbf{T}_2 + 2\mathbf{T}_4], \\
 \langle \mathbf{T}_4 \rangle &= \frac{1}{4}[\mathbf{T}_1 - \mathbf{T}_2 + 2\mathbf{T}_3], \\
 \langle \mathbf{T}_5 \rangle &= \frac{1}{4}[\mathbf{T}_2 + 2\mathbf{T}_5], \\
 \langle \mathbf{T}_6 \rangle &= \frac{1}{4}[\mathbf{T}_1 + \mathbf{T}_2].
 \end{aligned}$$





## REFERENCES

1. **Koyama M., Akiyama E., Lee Y.K., et al.**, Overview of hydrogen embrittlement in high-Mn steels, *International Journal of Hydrogen Energy*. 42(17) (2017) 12706–12723.
2. **Yakovlev Yu.A., Tretyakov D.A., Frolova K.P.**, Hydrogen diagnostics structural elements and engineering constructions, *Methods of Control and Diagnostics in Mechanical Engineering*. (3) (2019) 117–120.
3. **Shen C.H., Shewmon P.G.**, A mechanism for hydrogen-induced intergranular stress corrosion cracking in alloy 600, *Metallurgical Transactions A*. 21(5) (1990) 1261–1271.
4. **Koyama M., Springer H., Merzlikin S.V., et al.**, Hydrogen embrittlement associated with strain localization in a precipitation-hardened Fe–Mn–Al–C light weight austenitic steel, *International Journal of Hydrogen Energy*. 39 (9) (2014) 4634–4646.
5. **Kuhr B., Farkas D., Robertson I.M.**, Atomistic studies of hydrogen effects on grain boundary structure and deformation response in FCC Ni, *Computational Materials Science*. 122 (September) (2016) 92–101.
6. **Villalobos J.C., Serna S.A., Campillo B., Lypcz-Martinez E.** Evaluation of mechanical properties of an experimental microalloyed steel subjected to tempering heat treatment and its effect on hydrogen embrittlement, *International Journal of Hydrogen Energy*. 42(1) (2017) 689–698.
7. **Merson E.D., Myagkikh P.N., Klevtsov G.V., et al.**, Effect of fracture mode on acoustic emission behavior in the hydrogen embrittled low-alloy steel, *Engineering Fracture Mechanics*. 210 (1 April) (2019) 342–357.
8. **Sun B., Krieger W., Rohwerder M., et al.**, Dependence of hydrogen embrittlement mechanisms on microstructure-driven hydrogen distribution in medium Mn steels, *Acta Materialia*. 183 (15 January) (2020) 313–328.
9. **Wasim M., Djukic M.B.**, Hydrogen embrittlement of low carbon structural steel at macro-, micro- and nano-levels, *International Journal of Hydrogen Energy*. 45 (3) (2020) 2145–2156.
10. **Jothi S., Croft T.N., Wright L., et al.**, Multi-phase modelling of intergranular hydrogen segregation/trapping for hydrogen embrittlement, *International Journal of Hydrogen Energy*. 40 (43) (2015) 15105–15123.
11. **Hoch B.O., Metsue A., Bouhattate J., Feaugas X.**, Effects of grain-boundary networks on the macroscopic diffusivity of hydrogen in polycrystalline materials, *Computational Materials Science*. 97 (1 February) (2015) 276–284.
12. **Knyazeva A.G., Grabovetskaya G.P., Mishin I.P., Sevostianov I.**, On the micromechanical modelling of the effective diffusion coefficient of a polycrystalline material, *Philosophical Magazin*. 95 (19) (2015) 2046–2066.
13. **Arkhangelskaya E.A., Lepov V.V., Larionov V.P.**, The connected model for delayed fracture of damaged media, *Physical Mesomechanics*. 4 (5) (2001) 75–80.
14. **Ruales M., Martell D., Vazquez F., et al.**, Effect of hydrogen on the dynamic elastic modulus of gamma titanium aluminide, *Journal of Alloys and Compounds*. 339 (1–2) (2002) 156–161.
15. **Rahman K.M., Mohtadi-Bonab M.A., Ouellet R., Szpunar J.A.**, Comparative study of the role of hydrogen on degradation of the mechanical properties of API X60, X60SS, and X70 pipeline steels, *Steel Research International*. 90 (8) (2019) 1900078.
16. **Kachanov M., Sevostianov I.**, On quantitative characterization of microstructures and effective properties, *International Journal of Solids and Structures*. 42 (2) (2005) 309–336.
17. **Kachanov M., Sevostianov I.**, *Micromechanics of materials, with applications*, Vol. 249, Springer, Berlin, Germany, 2018.
18. **Kanaun S.K., Levin V.M.**, *Metod effektivnogo polya v mekhanike kompozitnykh materialov* [Effective field method in the mechanics of composite materials], Petrozavodsk State University, Petrozavodsk, 1993 (in Russian).
19. **Sevostianov I., Kachanov M.**, Compliance tensors of ellipsoidal inclusions, *International Journal of Fracture*. 96 (1) (1999) 3–7.
20. **Markov K.Z.**, Elementary micromechanics of heterogeneous media, In the book: *Heterogeneous Media*, Birkhäuser, Boston, MA, 2000.
21. **Sevostianov I., Kachanov M.**, On some controversial issues in effective field approaches to the problem of the overall elastic properties, *Mechanics of Materials*. 69 (1) (2014) 93–105.
22. **Sevostianov I.**, On the shape of effective inclusion in the Maxwell homogenization scheme for anisotropic elastic composites, *Mechanics of Materials*. 75 (August) (2014) 45–59.

*Received 30.03.2020, accepted 20.04.2020.*

## THE AUTHOR

**FROLOVA Ksenia P.**

*Institute for Problems of Mechanical Engineering RAS,*

*Peter the Great St. Petersburg Polytechnic University*

61 Bolshoi Ave. of V. Isl., St. Petersburg, 199178, Russian Federation

kspfrolova@gmail.com

## СПИСОК ЛИТЕРАТУРЫ

1. Koyama M., Akiyama E., Lee Y.K., Raabe D., Tsuzaki K. Overview of hydrogen embrittlement in high-Mn steels // *International Journal of Hydrogen Energy*. 2017. Vol. 42. No. 17. Pp. 12706–12723.
2. Яковлев Ю.А., Третьяков Д.А., Фролова К.П. Водородная диагностика элементов конструкций и инженерных конструкций // *Мехатроника, автоматика и робототехника*. 2019. № 3. С. 117–120.
3. Shen C.H., Shewmon P.G. A mechanism for hydrogen-induced intergranular stress corrosion cracking in alloy 600 // *Metallurgical Transactions. A*. 1990. Vol. 21. No. 5. Pp. 1261–1271.
4. Koyama M., Springer H., Merzlikin S.V., Tsuzaki K., Akiyama E., Raabe D. Hydrogen embrittlement associated with strain localization in a precipitation-hardened Fe–Mn–Al–C light weight austenitic steel // *International Journal of Hydrogen Energy*. 2014. Vol. 39. No. 9. Pp. 4634–4646.
5. Kuhr B., Farkas D., Robertson I.M. Atomistic studies of hydrogen effects on grain boundary structure and deformation response in FCC Ni // *Computational Materials Science*. 2016. Vol. 122. September. Pp. 92–101.
6. Villalobos J.C., Serna S.A., Campillo B., Lypetz-Martinez E. Evaluation of mechanical properties of an experimental microalloyed steel subjected to tempering heat treatment and its effect on hydrogen embrittlement // *International Journal of Hydrogen Energy*. 2017. Vol. 42. No. 1. Pp. 689–698.
7. Merson E.D., Myagkikh P.N., Klevtsov G.V., Merson D.L., Vinogradov A. Effect of fracture mode on acoustic emission behavior in the hydrogen embrittled low-alloy steel // *Engineering Fracture Mechanics*. 2019. Vol. 210. 1 April. Pp. 342–357.
8. Sun B., Krieger W., Rohwerder M., Ponge D., Raabe D. Dependence of hydrogen embrittlement mechanisms on microstructure-driven hydrogen distribution in medium Mn steels // *Acta Materialia*. 2020. Vol. 183. 15 January. Pp. 313–328.
9. Wasim M., Djukic M.B. Hydrogen embrittlement of low carbon structural steel at macro-, micro- and nanolevels // *International Journal of Hydrogen Energy*. 2020. Vol. 45. No. 3. Pp. 2145–2156.
10. Jothi S., Croft T.N., Wright L., Turnbull A., Brown S.G.R. Multi-phase modelling of intergranular hydrogen segregation/trapping for hydrogen embrittlement // *International Journal of Hydrogen Energy*. 2015. Vol. 40. No. 43. Pp. 15105–15123.
11. Hoch B.O., Metsue A., Bouhattate J., Feaugas X. Effects of grain-boundary networks on the macroscopic diffusivity of hydrogen in polycrystalline materials // *Computational Materials Science*. 2015. Vol. 97. 1 February. Pp. 276–284.
12. Knyazeva A.G., Grabovetskaya G.P., Mishin I.P., Sevostianov I. On the micromechanical modelling of the effective diffusion coefficient of a polycrystalline material // *Philosophical Magazin*. 2015. Vol. 95. No. 19. Pp. 2046–2066.
13. Архангельская Е.А., Лепов В.В., Ларионов В.П. Связная модель замедленного разрушения повреждаемой среды // *Физическая мезомеханика*. 2001. Т. 4. № 5. С. 81–87.
14. Ruales M., Martell D., Vazquez F., Just F.A., Sundaram P.A. Effect of hydrogen on the dynamic elastic modulus of gamma titanium aluminide // *Journal of Alloys and Compounds*. 2002. Vol. 339. No. 1–2. Pp. 156–161.
15. Rahman K.M., Mohtadi-Bonab M.A., Ouellet R., Szpunar J.A. Comparative study of the role of hydrogen on degradation of the mechanical properties of API X60, X60SS, and X70 pipeline steels // *Steel Research International*. 2019. Vol. 90. No. 8. P. 1900078.
16. Kachanov M., Sevostianov I. On quantitative characterization of microstructures and effective properties // *International Journal of Solids and Structures*. 2005. Vol. 42. No. 2. Pp. 309–336.
17. Kachanov M., Sevostianov I. *Micromechanics of materials, with applications*. Berlin, Germany: Springer, 2018. Vol. 249. 712 p.

18. **Канаун С.К., Левин В.М.** Метод эффективного поля в механике композитных материалов. Петрозаводск: Изд-во Петрозаводского гос. ун-та, 1993. 598 с.
19. **Sevostianov I., Kachanov M.** Compliance tensors of ellipsoidal inclusions // International Journal of Fracture. 1999. Vol. 96. No. 1. Pp. 3–7.
20. **Markov K.Z.** Elementary micromechanics of heterogeneous media // Heterogeneous Media. Birkhäuser, Boston, MA, 2000. Pp. 1–62.
21. **Sevostianov I., Kachanov M.** On some controversial issues in effective field approaches to the problem of the overall elastic properties // Mechanics of Materials. 2014. Vol. 69. No. 1. Pp. 93–105.
22. **Sevostianov I.** On the shape of effective inclusion in the Maxwell homogenization scheme for anisotropic elastic composites // Mechanics of Materials. 2014. Vol. 75. August. Pp. 45–59.

*Статья поступила в редакцию 30.03.2020, принята к публикации 20.04.2020.*

### **СВЕДЕНИЯ ОБ АВТОРЕ**

**ФРОЛОВА Ксения Петровна** — младший научный сотрудник Института проблем машиноведения РАН, Санкт-Петербург, Российская Федерация; аспирантка Высшей школы теоретической механики Санкт-Петербургского политехнического университета Петра Великого, Санкт-Петербург, Российская Федерация.

199178, Российская Федерация, г. Санкт-Петербург, Большой проспект В.О., 61.  
kspfrolova@gmail.com